Lattice Matching of Epitaxial Rare-Earth-doped Dielectric PLD-Films

Dissertation

zur Erlangung des Doktorgrades
des Department Physik
der Universität Hamburg

vorgelegt von

Bilge İleri

aus Hamburg

Hamburg
2007

Gutachter der Dissertation:	Prof. Dr. G. Huber Prof. Dr. W. Hansen
Gutachter der Disputation:	Prof. Dr. G. Huber Priv. Doz. Dr. V. Baev
Datum der Disputation:	14.02.2008
Vorsitzender des Prüfungsausschusses:	Dr. K. Petermann
Dekan der Fakultät für Mathematik, Informatik und Naturwissenschaften:	Prof. Dr. A. Frühwald
Vorsitzender des Promotionsausschusses	Prof. Dr. G. Huber

Soli Deo Gloria

ὁ Θεὸς γάρ ἐστιν ὁ ἐνεργῶν ἐν ὑμῖν καὶ τὸ θέλειν καὶ τὸ ἐνεργεῖν ὑπὲρ τῆς εὐδοκίας.

(Phil 2:13)

Abstract

Bilge İleri, *Lattice Matching of Epitaxial Rare-Earth-doped Dielectric PLD-Films*

The increasing demand of integrated optical devices requires the fabrication of high-quality optically active thin films. This work focuses on lattice matched dielectric oxide thin films. The investigated film materials include sesquioxides, orthovanadates and aluminum garnets, which are promising materials as they are well-known hosts for rare-earth-doped solid-state lasers with superior mechanical and thermal properties (e. g. low phonon energies, large thermal conductivity).

Highly crystalline rare-earth-doped films of optical quality were grown by the pulsed laser deposition (PLD) technique on single-crystal substrates of α-Al_2O_3, $LiYF_4$, Y_2O_3, $ScLuO_3$, YVO_4, and $Y_3Al_5O_{12}$. Different possibilities of lattice matching were investigated by heteroepitaxy of Al_2O_3–$ScLuO_3$, $ScLuO_3$–Al_2O_3 and $LiYF_4$–Lu_2O_3 substrate–film systems and by homo- and quasi-homoepitaxy of Y_2O_3–RE_2O_3, YVO_4–$REVO_4$ and $Y_3Al_5O_{12}$–$RE_3Al_5O_{12}$ substrate–film systems. The lattice matching in the quasi-homoepitaxial systems was realized by admixing the (Gd, Lu)-amount to match the yttrium-based substrate material. Lattice matching of up to 99.88% (heteroepitaxy) and 99.79% (quasi-homoepitaxy) was realized.

The film growth was studied by in-situ reflection high-energy electron diffraction (RHEED). Continuous layer-by-layer growth was observed for all three quasi-homoepitaxial substrate–film systems. The crystal structure of the films was determined by ex-situ X-ray diffraction (XRD) analysis. These measurements reveal that the films are highly textured along the default substrate direction. However, subplantation effects of high-energy plasma species and subsequent particle interdiffusion into the substrate matrix are indicated in heteroepitaxy at too high deposition temperatures.

Besides in-situ RHEED monitoring and ex-situ XRD analysis, the surface morphology of the thin films was studied by atomic force microscopy (AFM). For better comparison and in order to achieve an arranged atomically flat surface with terraces of monolayer step height (2 – 5 Å), the substrates were annealed prior to deposition. The annealing duration, atmosphere and temperature differed according to the substrate material. In general, the resulting film surface was very smooth. In some cases three-dimensional island formation could be verified in good agreement with the corresponding RHEED measurements. A multi-level surface morphology with monolayer step heights of 5 Å each (half the film lattice constant) was observed for a 1 µm two-dimensional layer-by-layer grown lattice matched Nd:$(Gd, Lu)_2O_3$ film on (100) Y_2O_3 substrate.

Optical properties of the rare-earth-doped films were studied by spectroscopic measurements in the (vacuum-) ultraviolet and visible spectral-range. The emission and excitation spectra of the Eu^{3+}-doped films look similar to those of the corresponding single-crystalline bulk materials, i. e. the symmetry around the Eu^{3+} ions is preserved. Depending on the film matrix and its number of different lattice sites and symmetries available for the rare-earth ions, the existence of additional ions in mixed (Gd, Lu)-films can in some cases disturb the band structure (CTS and ES) of the film lattice.

Kurzfassung

Bilge İleri, *Gitteranpassung von epitaktischen SE-dotierten dielektrischen PLD-Schichten*

Das Interesse an neuen Bauteilen für die integrierte Optik erfordert zunehmend die Herstellung dünner, optisch aktiver Schichten. Da dielektrische Oxide wie Sesquioxide, Orthovanadate und Aluminium-Granate aufgrund ihrer mechanischen und thermischen Eigenschaften für ein solches Aufgabengebiet sehr gut geeignet und bereits als Wirtsgitter für die Seltenen Erden (SE) in Festkörperlasern im Einsatz sind, wird in dieser Arbeit die Gitteranpassung dünner dielektrischer Oxidschichten untersucht.

Mit dem Pulsed Laser Deposition (PLD)-Verfahren konnten kristalline Selten-Erd-dotierte Sesquioxid-, Orthovanadat-, und Aluminium Granatschichten von optischer Qualität auf α-Al_2O_3-, $LiYF_4$-, Y_2O_3-, $ScLuO_3$-, YVO_4- und $Y_3Al_5O_{12}$-Substraten hergestellt werden. Die verschiedenen Möglichkeiten der Gitteranpassung wurden bei Substrat–Schicht Systemen in der Heteroepitaxie von Al_2O_3–$ScLuO_3$, $ScLuO_3$–Al_2O_3 und $LiYF_4$–Lu_2O_3 sowie der Homo- und Quasihomoepitaxie von Y_2O_3–RE_2O_3, YVO_4–$REVO_4$ und $Y_3Al_5O_{12}$–$RE_3Al_5O_{12}$ untersucht. Durch Abmischung des (Gd, Lu)-Anteils wurde in quasihomoepitaktischen Systemen eine Gitteranpassung zu dem Yttrium-basierten Substratmaterial erzielt. Gitteranpassungen von bis zu 99.88% (Heteroepitaxie) und 99.79% (Quasihomoepitaxie) konnten somit realisiert werden.

Durch Einsatz von in-situ Reflection High-Energy Electron Diffraction (RHEED) konnte das Schichtwachstum untersucht werden. Kontinuierliches Frank-van-der-Merve-Wachstum (layer-by-layer) konnte bei allen drei quasihomoepitaktischen Systemen beobachtet werden. Mit Röntgenbeugung (XRD) wurde die Kristallstruktur der Schichten bestimmt und ein hochtexturiertes Wachstum in die jeweilige, vom Substrat vorgegebene Richtung festgestellt. In der Heteroepitaxie konnte in Zusammenhang mit zu hohen Substrattemperaturen Subplantation von hochenergetischen Teilchen aus dem Plasma mit anschließender Interdiffusion in die Substratmatrix zugeordnet werden.

Die Oberflächenbeschaffenheit der Schichten wurde mit Rasterkraftmikroskopie (AFM) untersucht. Zum besseren Vergleich der Schichtoberfläche erfolgte eine thermische Vorbehandlung der Substrate, mit der geordnete, atomar glatte Oberflächen erzielt wurden. Anhand einer Stufenbildung konnte die Aufteilung der jeweiligen Einheitszelle in verschiedene Lagen (2 – 5 Å) beobachtet werden. Die Schichtoberflächen waren in der Regel atomar glatt, wobei in Übereinstimmung mit RHEED in einigen Fällen auch 3D-Inselbildung beobachtet wurde. Für eine gitterangepasste, 1 µm dicke Nd:$(Gd, Lu)_2O_3$-Schicht ergab sich eine Oberfläche mit Stufenbildung von jeweils 5 Å, welches der Hälfte einer Einheitszelle entspricht.

Die optischen Eigenschaften der Selten-Erd-dotierten Schichten wurden durch spektroskopische Messungen im (Vakuum-)Ultravioletten und sichtbaren Spektralbereich bestimmt. Dabei entsprechen die Emissions- und Anregungsspektren denen eines Volumenkristalls, d. h. die lokale Symmetrie der Eu^{3+}-Ionen ist erhalten. In Abhängigkeit von der Kristallmatrix und der Anzahl an verschiedenen Symmetrieplätzen im Gitter führte das Hinzufügen eines zusätzlichen Ions in (Gd, Lu)-Schichten zu einer Störung der Bandstruktur (CTS und ES) in der kristallinen Schicht.

Contents

Abstract i
Kurzfassung ii

List of Symbols and Abbreviations **vii**

1 Introduction **1**
1.1 Motivation 1
1.2 Structure of this Thesis 3

2 Materials **5**
2.1 Sesquioxides 5
2.2 Corundum 10
2.3 Yttrium Aluminum Garnet 11
2.4 Orthovanadates of Yttrium and Gadolinium 12
2.5 Lithium Yttrium Fluoride 13

3 Lanthanide Dopants **17**
3.1 The Free Ion 18
3.2 The Lanthanide Ion in a Crystal Matrix 21
3.2.1 Intraconfigurational 4f-4f Transitions 22
3.2.2 Interconfigurational 4f-5d Transitions 23
3.2.3 Charge Transfer Transitions 24
3.2.4 Vibrations of the Host Lattice 25
3.3 Europium as Probe Ion 28

4 Pulsed Laser Deposition **31**
4.1 Laser-Target Interactions 33
4.2 The Plasma Plume 39

5 Lattice Matched Thin Films **45**
5.1 Growth Mechanisms 46
5.2 Combination of Different Lattices 50
5.3 Investigated Systems 53

6 Thin Film Preparation **57**
6.1 Pre-Deposition Substrate Treatment 65
6.2 Reflection High-Energy Electron Diffraction 67

7 Analytical Techniques **75**
7.1 X-Ray Diffraction . . . 75
7.2 Ellipsometry and Reflectometry . . . 80
7.3 Atomic Force Microscopy . . . 83
7.4 Optical Spectroscopy . . . 84
7.4.1 Fluorescence and Excitation Measurements . . . 85
7.4.2 Lifetime Measurements . . . 86
7.4.3 VUV Measurements . . . 87

8 Characterization of Heteroepitaxial Thin Films **89**
8.1 Composite Sesquioxide Films on Sapphire . . . 89
8.1.1 Lattice Matching . . . 89
8.1.2 Structural Characterization . . . 90
8.1.3 Surface Structure and Topography . . . 95
8.1.4 Spectroscopic Analysis . . . 97
8.2 Sapphire Films on Composite Sesquioxide . . . 103
8.2.1 Lattice Matching and Structural Characterization . . . 103
8.2.2 Surface Structure and Topography . . . 105
8.2.3 Spectroscopic Analysis . . . 106
8.3 Lutetia Films on Lithium Yttrium Fluoride . . . 107
8.3.1 Lattice Matching and Structural Characterization . . . 107
8.3.2 Surface Structure and Topography . . . 109
8.3.3 Spectroscopic Analysis . . . 110
8.4 Summary and Discussion . . . 112

9 Characterization of Homo- and Quasi-Homoepitaxial Thin Films **115**
9.1 Sesquioxide Films on Yttria . . . 115
9.1.1 Lattice Matching . . . 115
9.1.2 Structural Characterization . . . 116
9.1.3 Surface Structure and Topography . . . 124
9.1.4 Spectroscopic Analysis . . . 127
9.2 Orthovanadate Films on YVO_4 . . . 130
9.2.1 Lattice Matching and Structural Characterization . . . 130
9.2.2 Surface Structure and Topography . . . 135
9.2.3 Spectroscopic Analysis . . . 138
9.3 Garnet Films on YAG . . . 142
9.3.1 Lattice Matching and Structural Characterization . . . 142
9.3.2 Surface Structure and Topography . . . 147
9.3.3 Spectroscopic Analysis . . . 150
9.4 Summary and Discussion . . . 154
9.4.1 Lattice Defects and Lattice Expansion . . . 156

10 Conclusions **157**
10.1 Summary of Results 157
10.2 Résumé 159
10.3 Outlook and Future Work 160

A List of Fabricated Films **163**

B Sellmeier Equations **167**

Bibliography **168**

List of Publications **187**

Acknowledgement **191**

Index **193**

List of Symbols and Abbreviations

Constants

ε_0	vacuum permittivity
a_B	Bohr radius
c_0	speed of light in vacuum
e	elementary charge
h	Planck constant
$\hbar$	$= h/2\pi$
k	Boltzmann constant
m_e	electron mass

Variables

$\alpha(\lambda)$	absorption coefficient
β	propagation constant
γ	adiabatic exponent
γ_A	surface energy of the growing film
γ_B	surface energy of the substrate
γ^*	interface energy film–substrate
γ_m	multi-photon absorption coefficient
ε_av	avalanche coefficient
θ	diffraction angle
λ	wavelength
ν	frequency
ϱ	charge density
τ	pulse duration
φ	wetting angle of a nucleus on the substrate
Φ	laser fluence

Φ_{thr}	threshold laser fluence
Ψ_0	wavefunction of a free ion in the central field approximation
χ_{opt}	optical electronegativity
ω	$= 2\pi\nu$ angular frequency
a	lattice constant
$\mathbf{a}$	primitive lattice vector
$\mathbf{B}$	magnetic field
c	speed of light in a medium
C_{v}	specific heat
d_{hkl}	inter planar spacing
D_{th}	thermal diffusivity
$\mathbf{D}$	electric displacement
E_0	energy eigenvalue of an ionic state
$\mathbf{E}$	electric field
$\mathbf{E}(\mathbf{r})$	electrostatic field of the ligands
g_0	statistical weight of a neutral atom
g_i	statistical weight of an electron–ion pair
$\mathbf{G}$	reciprocal lattice vector
$\mathcal{H}$	Hamiltonian for a free ion
$\mathcal{H}_0$	Hamiltonian for a free ion in the central field approximation
$\mathcal{H}_{ee}$	pertubation term for $\mathcal{H}_0$: non radial.symmetric part of the electron-electron interaction
$\mathcal{H}_{\mathrm{SO}}$	pertubation term for $\mathcal{H}_0$: spin-orbit coupling
$\mathcal{H}_{\mathrm{Stark}}$	pertubation term for $\mathcal{H}_0$: interaction of the 4f electrons of a lanthanide ion with the electrostatic field of the ligands
$\mathbf{H}$	magnetic flux density
ΔH_{v}	vaporization energy
I_{thr}	threshold power intensity
$\mathbf{j}$	current density
$\mathbf{j}_i$	angular momentum vector of the i^{th} electron
$\mathbf{J}$	total angular momentum quantum number
$\mathbf{k}$	$= 2\pi/\lambda$ wavevector
K	thermal conductivity
l_i	orbital angular momentum quantum number of the i^{th} electron
$\mathbf{l}_i$	orbital angular momentum vector of the i^{th} electron

L_{th}	thermal diffusion length
m_l	magnetic quantum number of an electron
m_s	spin quantum number
M	Mach number
n_0	density of neutral atoms
n_e	density of electrons
n_i	density of ions
n_i	principal quantum number of the i^{th} electron
$n_{\mathrm{s/f/c}}$	refractive index of the substrate, film, and superstrate
n_{eff}	effective refractive index
N	number of electrons in an ion
N_e	electron density in the conduction band
p	mode number
$p(\mathrm{O_2})$	oxygen partial pressure
r_i	position of the i^{th} electron relative to the nucleus
r_{ij}	position of the electrons i and j relative to each other
$R(\lambda)$	reflectivity
R_{RMS}	surface roughness (root-mean-square)
$\mathbf{s}_i$	spin vector of the i^{th} electron
$\mathbf{S}$	total spin quantum number
T_0	initial temperature
$V(\mathbf{r})$	effective spherically potential in the central field approximation
w_0	beam radius
W_i	ionization potential
Z	atomic number

Abbreviations

AFM	atomic force microscope
AI	avalanche ionization
CTS	charge transfer state
EBV	electron beam evaporation
ED	electric dipole
ES	excitonic state

FWHM	full width at half maximum
LuAG	lutetium aluminum garnet ($Lu_3Al_5O_{12}$)
MD	magnetic dipole
MPA	multi-photon absorption
NA	numerical aperture
PLD	pulsed laser deposition
RE	rare earth
RHEED	reflection high-energy electron diffraction
RMS	root-mean-square
SXRD	surface X-ray diffraction
TE	transverse electric polarization
TEM	transmission electron microscope
TM	transverse magnetic polarization
XRD	X-ray diffraction
VUV	vacuum ultraviolet
YAG	yttrium aluminum garnet ($Y_3Al_5O_{12}$)

1 Introduction

1.1 Motivation

In the last two decades computer-based processes and internet applications created an exponentially growing data transfer. Since the information transmission rate of purely electronic devices is limited due to fundamental physical reasons, this development led to an increased use of optical fibres and advanced photonic technologies. As the operation of these new devices incorporates optics and electronics as well, a mixed discipline was born called *integrated photonics*. The basic difference in this discipline is the substitutionary use of photons instead of electrons, whereas the integrated optical circuits are very similar to those in conventional electronics and focus on fabrication and integration of several photonic components on a common planar substrate.

In integrated photonics, optical signals propagate through non-conducting dielectric media and operate in highly transparent wavelength ranges of the used materials. As this transparency window is generally located in the visible and near-infrared range of the electromagnetic spectrum corresponding to light frequencies around 300 THz (10^6 times higher compared to electrical transmission frequencies), the resultant bandwidth is very large and allows the transport of huge amounts of information. Although a variety of optical elements is required for integrated optics, the key element of all devices are optical waveguides which provide guiding, coupling, switching, splitting, and (de-)multiplexing of optical signals. Despite the increasing number of proposed, modelled and fabricated integrated photonic devices, basic components still are the straight waveguide, the bend waveguide and the power splitter. All optical components in integrated photonics are composed of these three building blocks. An overview on several basic components can be found in [Lif03].

The fabrication of high quality thin films constitutes the basic technology for these waveguides with diffusion and deposition techniques being the most widely used methods for such thin film production. However, photolithographic processes can be used for the integration of multiple functions on a planar circuit requiring structures with lateral dimensions of a few microns [Hai01]. Suitable materials for the fabrication of functional devices in integrated photonics can be found in semiconductors like indium phosphide (InP) and gallium arsenide (GaAs) or in dielectrics like polymers, glasses or lithium niobate ($LiNbO_3$). Another way of realizing the required integrated optics components is developed in *photonic crystals*, as this class of materials allows the individual design of its optical properties. In photonic crystals, the periodic arrangement of refractive index

variation determines the photon flux through the crystal. Due to the defined multiple directions in which the photons may escape, photonic crystal microcavities are more efficient than conventional semiconductor diode lasers.

Dielectric Oxides

Besides the wide use of semiconductor compounds, crystalline oxide dielectrics are also very promising materials for integrated optics because of their advantageous properties. Dielectric oxides offer a wide transparency range from the ultraviolet to the mid-infrared part of the electromagnetic spectrum and are well-known hosts for rare-earth doping. By incorporating different rare-earth ions, the optical properties can be selectively influenced. The refractive index of dielectric oxides is moderate compared to semiconductors. In case of endfaces designed for light coupling in and out of the device, considerably reduced fresnel reflections can be obtained, which is important as the reflections determine the efficiency of the system. At normal incidence of near-infrared light the reflectivity of dielectric oxides is less than 10%, whereas for semiconductors the reflectivity is around 30%. Responsible for this difference is the refractive index difference between the used material and air, which is $\Delta n < 1$ for dielectric oxides and $\Delta n \approx 2.5$ for semiconductors.

Thus, the aim of this thesis is the preparation and characterization of lattice matched dielectric oxide thin films, i. e. sesquioxides (e. g. Y_2O_3), orthovanadates (e. g. YVO_4), and aluminum garnets (e. g. $Y_3Al_5O_{12}$). A diverse range of potential applications can be envisioned for these materials. Y_2O_3 is an important material for semiconductors and also for optical applications such as phosphors or waveguide lasers due to the possibility of rare-earth doping with atoms like europium or neodymium. Its large bandgap (5.8 e V) and dielectric constant (14-18) make the use of Y_2O_3 favorable in metal–insulator–semiconductor (MIS) diodes, metal–oxide–semiconductor (MOS) capacitors, transistor gates, and dynamic random access memory (DRAM) gate dielectrics. Moreover, high power laser operation of sesquioxides Yb:Lu_2O_3 and Yb:Sc_2O_3 in a thin-disk laser geometry has recently been realized by R. Peters et al. [Pet07]. Another application of rare-earth-doped oxide films is the fabrication of planar waveguide structures including passive elements and active waveguides (amplifiers and lasers), as these oxide materials are well-known bulk hosts for laser ions. Waveguides of Nd:YAG [Bon00] and of Er:Y_2O_3 [Hoe92, Kor01, Lec02] have already been fabricated.

These applications demand high quality crystalline materials. For film growth, this presupposes very low densities of defects especially at the interface between substrate and film, which is achievable by minimizing the lattice mismatch of the film in regard to the substrate. In previous crystalline films fabricated by pulsed laser deposition, a lattice matching of around 95% could be realized [Bur02, Bär04]. However, following the standards of 'lattice matched' film preparation in semiconductor physics, the mismatch should only amount 0.1 – 1.0%. Therefore the preparation and characterization of substrate–film systems which meet these requirements of lattice matching, high crystallinity, low defect densities, and a refractive index variation well-suited for waveguide application are subject of this work.

Advantages of Pulsed Laser Deposition

Apart from the pulsed laser deposition technique, many other technologies are available for the fabrication of optical thin films. Various chemical and physical methods have already been used for the synthesis of dielectric oxide film, e. g. chemical vapor deposition (CVD) [Sha93, McK00], ion-assisted evaporation [Cho99], electron-beam evaporation (EBV) [Fuk89, Rab04], and sol-gel techniques [Rao96, Lou01] – to mention just a few. Due to many reasons pulsed laser deposition (PLD) has proven to be a very attractive and practical method for the fabrication of thin films. Although a detailed description of the PLD process will be given in chapter 4, some advantages that explain the attractiveness of this technique are anticipated in the following:

1. Film growth in which the target stoichiometry is preserved;
2. Accurate control of the film thickness by the number of pulses;
3. Possibility of exact growth monitoring by in-situ reflection high-energy electron diffraction (RHEED);
4. Deposition in reactive gas environments in contrast to conventional evaporation in which hot filaments or crucibles could oxidize;
5. Benefit from a high ionization degree of the plasma flux of up to 80%, which positively influences the film properties;
6. High-energies of the plasma species often ranging from 5 to $\geq 100\,\mathrm{eV}$, which can have positive effects on the film properties like good film adhesion at low substrate temperatures;
7. Possibility to use small targets in contrast to large targets required for sputtering. By using alternate-targets versatile thin film deposition can be realized [Ser99].

1.2 Structure of this Thesis

This introduction is followed by the description of the crystallographic and physical properties of the used substrate and film materials in chapter 2. Electronic transitions and optical characteristics of the lanthanide ions, which are incorporated in the thin films as luminescent probes, are summarized in chapter 3.

The fundamental physical mechanisms involved in the pulsed laser deposition process and experimental aspects of thin film fabrication by pulsed laser deposition are set forth in chapter 4. An introduction of lattice matching with possible combinations of different materials are given in chapter 5. Further, a detailed description of target and substrate preparation, the used pulsed laser deposition setup as well as pre-deposition substrate treatment and a brief introduction of the RHEED theory and setup are given in chapter 6.

The different analytical tools for examining the structural and optical properties of the deposited films are described in chapter 7. These include X-ray diffraction (crystallinity), reflectometry (film thickness) and atomic force microscopy (surface morphology) for the structural characterization, and fluorescence measurements (including VUV excitation) as well as lifetime measurements to determine the optical properties.

In the following two chapters the deposited thin films are characterized, with heteroepitaxial film analysis being described in chapter 8 and (quasi-)homoepitaxial film analysis detailed in chapter 9. Finally, chapter 10 presents the conclusions drawn from the experimental results and gives an outlook on improvements as well as on future work.

Peculiarities

During the completion of this work, 'progress' and 'change' were the key words. Many materials were prepared as films and different substrate–film combinations were investigated. In addition, several setup improvements regarding the PLD device were undergone, especially with regard to the substrate heating capabilities. Therefore, the deposition parameters were varied and the attempt to obtain optimum parameters for each investigated system was made. Crucial information on the pre-deposition treatment of the used substrates together with the initial operation of a new reflection high-energy electron diffraction (RHEED) device were introduced by T. Gün in early 2007 [Gün07].

Therefore, in different stages of this work the preparation of thin films differed according to the current state of knowledge, which implies difficulties for the direct comparison of films. For instance, a RHEED analysis could only be performed for the last twelve fabricated films denoted with 'SR'. Despite the steadily improved knowledge in pulsed laser deposition and its different appliance in hetero- and (quasi-)homoepitaxy, further parameter optimization is possible and required due to the diversity of the investigated materials. A definite analysis of the prepared and characterized lattice matched films was not always possible for the same reason. Future work will include deposition parameter and film composition improvements as well as incorporation of additional characterization methods like high resolution transmission electron microscopy (HRTEM) and surface X-ray diffraction (SXRD).

2 Materials

In this chapter an overview of the materials used for thin film production by pulsed laser deposition and their properties is given. This covers the materials used as substrates as well as the ones utilized for thin film growth. As the achievement of lattice matched thin films grown by pulsed laser deposition is the primary aim of this thesis, the spectroscopic and structural properties of various materials, such as the sesquioxides, will be the main field of investigation.

The sesquioxides yttria, scandia, lutetia, and gadolinia will be the starting point in the first part, as – with the exception of the latter – they were the subject of prior scientific work in this field. Some of these materials were also grown as bulk crystals and were used as substrates in the current work. The description will focus on the key properties relevant to this work. Additional data can be found in the theses of E. Mix, L. Fornasiero, V. Peters and P. Burmester [Mix99, For99a, Pet01, Bur02]. The properties of corundum as well as yttrium aluminum garnet, also chosen as substrate materials, are detailed in the next two sections. Finally, this chapter deals with the properties of yttrium and gadolinium orthovanadates as well as lithium yttrium fluoride, used as new substrate materials in order to achieve better lattice matching.

2.1 Sesquioxides

The term sesquioxide denotes oxide materials with an anion to cation ratio of 3 : 2 (lat. sesqui = one and a half). In the context of this thesis, however, when referring to sesquioxides, only the oxides of the rare-earth elements, which are found in the third main group of the periodic table (cp. figure 2.1), will be considered.

Even though the rare-earth elements readily oxidize, they do so with varying strength [Hol92]. Cerium metal, in the presence of air, oxidizes completely to CeO_2, whereas praseodymium occurs naturally as Pr_6O_{11}, showing a slightly oxygen deficient fluorite structure. The rare-earth oxides from neodymium onward all occur naturally as sesquioxides RE_2O_3, except for terbium naturally occurring as Tb_4O_7 and under positive oxygen pressure transforming into TbO_2. However, only cerium, praseodymium and terbium form dioxides[1].

[1] Though still unclear why dioxides exist only for Ce, Pr, and Tb, the favoring of this structure can be explained by the less tightly bound *f* electrons in the lighter lanthanides, resulting in compounds that display a larger oxygen coordination number. In terbium the extra electron on top of the half-filled shell is less tightly bound, resulting in a valency larger than 3+.

Rare-earth sesquioxides are known to be excellent laser host materials due to high thermal conductivities, low phonon energies, and high damage thresholds [Mor82]. Their structural and optical properties have therefore been thoroughly studied for several years resulting in the wide application of the europium-doped sesquioxide yttria as a red phosphor and the sesquioxides scandia and lutetia as possible laser host matrices [For99b].

Sesquioxides can be found in several crystallographic structures depending on the cation radius, the temperature, and the pressure [Rot60, Hoe66]. Below 2000 °C, three different structure types are adopted by the rare-earth sesquioxides.

1. Light rare-earth elements crystallize in the hexagonal A-type structure with space group $P\overline{3}\,m1$;
2. Middleweight rare-earth elements can be found either in the C-type structure (see below) or in the B-type structure with space group $C2/m$ (C_{2h}^3), which is a monoclinic distortion of the C-type structure;
3. Heavy rare-earth elements crystallize in the cubic C-type bixbyite structure with body centered space group $Ia3$ (T_h^7).

Under specific temperature and pressure conditions, conversions between the different structure types are induced. At room temperature, the sesquioxides of the rare-earth elements ranging from lanthanum (La_2O_3) to terbium (Tb_2O_3) form a thermodynamically favored monoclinic structure, whereas the sesquioxides of dysprosium (Dy_2O_3) to lutetium (Lu_2O_3) as well as of yttrium (Y_2O_3) and scandium (Sc_2O_3) crystallize in the cubic C-type

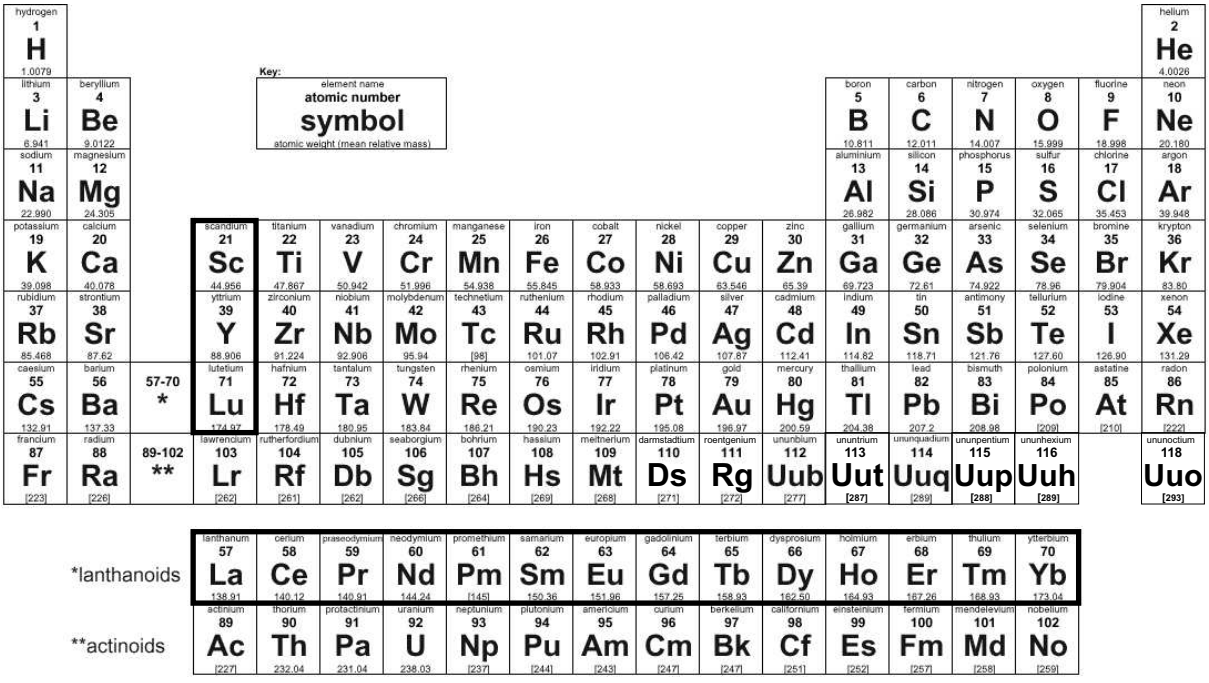

Figure 2.1: *Periodic table of elements. The rare-earths are highlighted.*

bixbyite structure with body-centered space group $Ia3\,(T_h^7)$ [Wyc86]. This structure, as depicted in figure 2.2, remains stable up to the melting point with the exception of yttria, which changes to a hexagonal high-temperature phase a little below the melting point [For99a, Mix99]. Due to the *lanthanide contraction* there is a slight decrease in the lattice constants of the sesquioxides ranging from Dy_2O_3 to Lu_2O_3. A typical scaling, however, is 10 Å depending on the type of cation.

A unit cell of the bixbyite structure contains 16 formula units with a total of 80 atoms. The 32 cations, each coordinated sixfold with oxygen, form two different symmetry sites: 24 sites with point group symmetry C_2 (non-centrosymmetric), labelled RE1 below, and 8 sites with C_{3i} symmetry (centrosymmetric), labelled RE2. The twofold axes of the C_2 sites are oriented parallel to the $\langle 100 \rangle$ directions, the threefold axes of the C_{3i} sites are parallel to $\langle 111 \rangle$ (cp. figure 2.2). Furthermore the crystals have a cleavage plane parallel to the $\{111\}$ - plane [Sch70].

In sesquioxides the chemical bonds between the metal and the oxygen ions are dominated by ionic bonding character with an admixing of covalent bonding. The bond lengths for the two cation sites in the different sesquioxide matrices are given in table 2.1 (page 15). It is noticeable that three different pairs of RE1–O bonds with varying distances exist, whereas all six RE2–O bonds have the same bonding length.

The geometric arrangement of the cation and its surrounding anions described above determines the electronic structure of the sesquioxides. Because of the identical structure and small variations concerning the ionic cation radii, it is possible to grow mixed sesquioxide crystals, such as $(Sc_{1-x}Lu_x)_2O_3$. These crystals are well-suited for the tuning of specific parameters as for example the lattice constant.

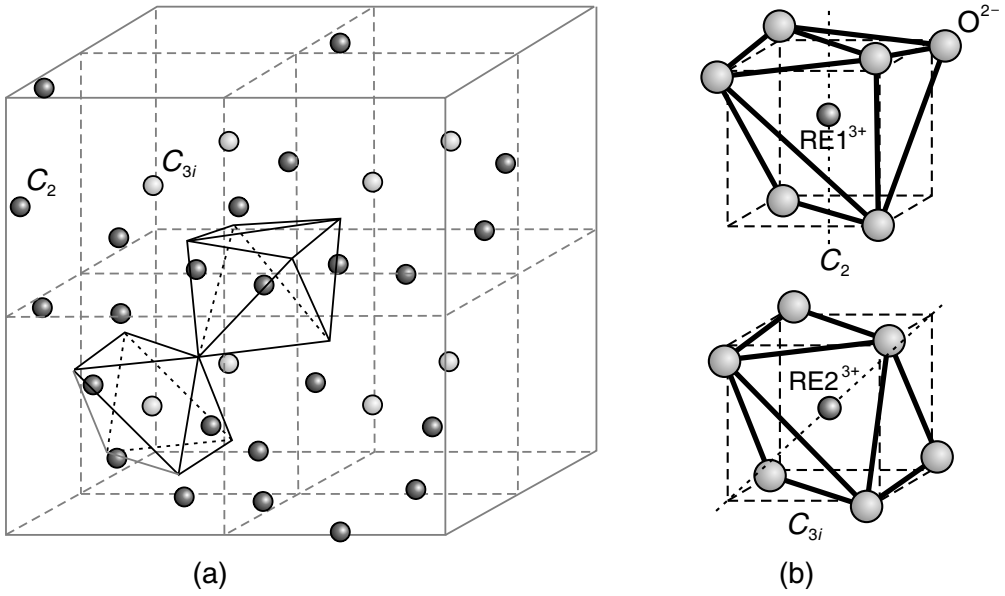

Figure 2.2: *Crystallographic structure of bixbyite: (a) unit cell with 24 sites with point group symmetry C (non-centrosymmetric) and 8 sites with C symmetry (centrosymmetric), (b) the two different cation sites.*

When activated with luminescent ions, the structural and electronic properties of the sesquioxides have important implications on the spectroscopic properties by determining the crystal field and thus defining the energetic positions of the electronic states. It was found that, in general, trivalent rare-earth ions are randomly distributed in sesquioxide RE_2O_3 single-crystals, occupying different symmetry sites [Man63]. As a result of the differences between these two symmetry sites the spectroscopic characteristics of the $RE^{3+}(C_2)$ and $RE^{3+}(C_{3i})$ ions differ from each other. The intraconfigurational *f-f* electric dipole transitions are forbidden for centrosymmetric C_{3i} sites and only magnetic dipole transitions can occur, whereas the crystal field interaction with non-centrosymmetric C_2 sites introduces an opposite-parity part to the potential energy of the crystal levels, also making possible the electric dipole transitions.

Compared with other dielectric oxide materials like $YAlO_3$ or $Y_3Al_5O_{12}$, sesquioxides have a considerably smaller phonon energy $E_{\mathrm{ph}} = \hbar\omega_{\mathrm{eff}}$ insuring good laser efficiency by minimizing energy loss due to non-radiative processes. The phonon energy, already low in YAG with 700 cm^{-1}, is even weaker in rare-earth oxides with 420 cm^{-1} for Gd_2O_3 and 377 cm^{-1} for Y_2O_3. With non-radiative processes suppressed, this class of materials is interesting for upconversion processes. However, up to now, besides the interest in the electronic properties of crystalline yttria, no further investigation of the electronic structures of scandia, lutetia or gadolinia are found in literature.

Growth of Sesquioxide Crystals

The main reason for sesquioxides not widely being used in industry is their complicated growth. Unlike other materials of equal suitability as laser hosts, sesquioxide bulk crystals or substrates are not commercially available up to now. Although sesquioxides, like yttria, are well investigated and their optical properties are quite favorable for laser applications, the extremely high melting point of approximately 2400 °C hinders the growth of large-volume single-crystals that are free of stress and impurities.

Until the end of the nineties experiments with various crystal growth techniques have been carried out, but none of them met the needs required for high-quality sesquioxides. Though, with these crystals grown, most properties of sesquioxides could be investigated. Then finally, much better results were obtained using a new growth method called heat exchange method (HEM) derived from the Bridgeman technique.

This technique was employed in the course of this work to grow sesquioxide bulk crystals which were then prepared as substrates for pulsed laser deposition and reference measurements. More information on the developed HEM growth technique and various other growth methods can be found in [Mix99, For99a, Pet01, Pet02a, Pet02b].

Yttrium-, Lutetium- and Scandiumoxide

Y_2O_3 is an insulator with a bandgap energy of approximately 6.1 e V [Abr78], meaning that it is transparent up to the ultraviolet region of approximately 200 nm. Consequently, the absorption rises steeply at wavelengths smaller than 220 nm. The fundamental absorption starts off with a sharp maximum at 5.9 e V, which is considered an excitonic state

[Abr78, Tom86]. As the short wavelength edge of the exciton band is superimposed by the interband absorption, the binding energy of this exciton is considerably low (0.1 e V) [Abr78].

As self-consistent band structure calculations of Y_2O_3 by Xu et al. [Xu97] have shown, the upper valence band is mainly formed by *2p* orbitals of oxygen electrons and some admixing of yttrium *4d* and *5p* orbitals, whereas the lower conduction band states are predominantly formed by yttrium *4d* and *5p* states. Based on the work of Ephraim and Bloch [Eph26], who found that the values of the interelectronic repulsion parameters separating the multiplet terms of $4f^q$ (*nephelauxetic effect*, cp. page 18) are smaller in more covalent compounds than in ionic compounds, and from the observed values of the interelectronical repulsion parameters between the metal ion and the oxygen ligands, Jørgensen et al. predicted that a substantial degree of covalency is mixed with the predominant ionic bonding character between Y and O [Jør64]. The effective charges of Y1 and Y2 were determined to be +2.08 and +2.10, while the effective charge of the oxygen ions is −1.39 [Xu97].

The sesquioxides Lu_2O_3 and Sc_2O_3 are isostructural to Y_2O_3. Consequently, the three crystals are well comparable with regard to their optical properties. Lutetia shows a reflectivity decrease related to interband transitions at an energy of 5.7 e V with a resulting bandgap energy of 6.1 e V. The excitonic state in lutetia is indicated via the sharp peak in the reflectivity spectrum at 5.8 e V [Kir03, Kuz03]. The valence band energy levels in Y-based compounds are formed predominantly by oxygen *2p* orbitals. However, in lutetia crystals the top of the valence band is composed mainly by lutetium *4f* orbitals [Moi97]. Abramov et al. determined the bandgap energy of Sc_2O_3 to be 6.3 e V [Abr83] and performed additional calculations that indicated a predominance of the ionic bond and a slightly greater contribution of covalency compared to Y_2O_3 ($q_{Sc} < q_Y$).

One interesting difference between these three sesquioxides is the lack of an exciton detection for Sc_2O_3, whereas in Y_2O_3 as well as in Lu_2O_3 an excitonic state can be observed [Abr83]. However, due to the inconsistency of different literature values, uniformly measured bandgap energies will be considered in this work. E. Mix determined the bandgap energies of Sc_2O_3, Y_2O_3, and Lu_2O_3 to be 5.91 e V, 5.64 e V, and 5.51 e V, respectively [Mix99].

Gadoliniumoxide

The sesquioxide Gd_2O_3 differs from the others mentioned above. At room temperature it crystallizes not in the C-type bixbyite structure but in the monoclinic B-type structure with space group $C2/m$ (C_{2h}^3). This side-centered cell contains six fomula units with lattice constants having the values $a = 14.08$ Å, $b = 3.567$ Å, $c = 8.743$ Å and $\beta = 100°$. Lanthanide atoms are located in three non-equivalent sevenfold coordinated C_S symmetry sites. Although the bandgap energy of Gd_2O_3 was investigated by Petit et al. to be 5.3 e V [Pet05], more detailed information on the electronic structure was not available up to today.

In the context of this thesis Gd_2O_3 is not used as an isolated crystal but primarily as a compound of mixed sesquioxide $(Gd_{1-x}Lu_x)_2O_3$ crystals. Therefore the structure is considered cubic with the lattice constant value $a = 10.813$ Å . This assumption is justified by X-ray measurements of the grown composite films (cp. section 9.1).

2.2 Corundum

Depending on the conditions, aluminum oxide crystallizes in many different structures of which the α-form (corundum) is the best known. This crystal is commercially available in epitaxial high-quality with regard to crystal purity, precise orientation and surface polishing. It is used as substrate material for pulsed laser deposition [Bur02, Bär04, Kuz06]. Although the matrix itself is colorless, natural corundum often contains impurities causing coloration. Pure α-Al_2O_3 is sometimes referred to as sapphire, despite the fact that the expression sapphire is more precisely defining Al_2O_3 doped with Fe^{2+} and Ti^{4+} resulting in blue colored crystals. With Cr^{3+} as dopant the crystal appears red and is commonly known as ruby. It is probably due to the various forms of Al_2O_3 in nature that the mineralogical term sapphire is widely used as a synonym for colorless pure α-Al_2O_3, alongside the term corundum.

Figure 2.3 shows the unit cell of α-Al_2O_3. It contains two Al_2O_3 units, as α-Al_2O_3 crystallizes in a ditrigonal-scalenohedral structure with space group $R\bar{3}c\,(D_{3d}^5)$. A hexagonal close-packed structure (hcp) is formed by the oxygen ions with the Al^{3+} ions located in the octahedrally coordinated interstices. Every aluminum ion is surrounded by six oxygen ligands and has each three bonds in the length of 1.969 Å and 2.278 Å.

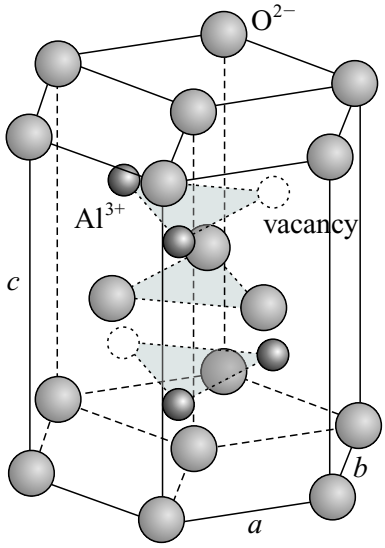

Figure 2.3: *Unit cell of α-alumina*

A simple hexagonal Bravais lattice, built by stacking two-dimensional triangular nets directly on top of each other, is underlying the hcp structure. This stacking occurs in the direction of the c-axis of the crystal, whereas the triangular lattice in the x-y-plane is generated by the lattice constants a and b [Ash76].

Corundum is an insulator with a bandgap energy of 9.5 e V (130 nm), which is about 3.5 e V higher than that of yttria. However, the fundamental absorption edge is overlapped by an absorption of an excitonic state. Absorption into a charge-transfer state was observed below the bandgap of α-Al_2O_3 [Fre90], which is due to the always present Cr^{3+} impurities. More details regarding the electronic structure of aluminum oxide are given in [Bat82] and [Xu91].

2.3 Yttrium Aluminum Garnet

Favorable spectroscopic properties, high thermal conductivity, mechanical stability, and high optical damage threshold were some of the features that made yttrium aluminum garnet one of the most important host materials for laser application. Many commercially produced solid-state lasers are based on this material, referred to as YAG. Up to now, well-known laser performances have been obtained by rare-earth-doped YAG crystals, such as Nd:YAG and Yb:YAG.

It was Menzer who in 1928 pioneered the investigating of this new material class, later named garnets [Men28]. The crystals categorized in this class belong to the cubic, body-centered space group $Ia3d\,(O_h^{10})$.

A unit cell of the garnet structure contains 160 atoms in eight identical $C_3A_2D_3O_{12}$ units, with C, A and D denoting crystallographic sites (cp. figure 2.4). Depending on their symmetry site, the 64 cations are either coordinated eightfold, sixfold or fourfold with oxygen, each forming an oxygen polyhedron in the crystal. There are 24 eightfold oxygen-coordinated C-sites with point group symmetry D_2, 12 sixfold oxygen-coordinated A-sites with point group symmetry C_{3i} and 24 fourfold oxygen coordinated D-sites with point group symmetry S_4.

An octant in the garnet structure of YAG is denoted $Y_3Al_2Al_3O_{12}$, as the C-site is occupied with trivalent yttrium ions and the A- and D-sites with trivalent aluminum ions. The three oxygen polyhedrons in the YAG crystal are slightly distorted and therefore cannot obtain a regular geometry. This distortion causes the loss of inversion symmetry in the dodecahedral C-site, whereas the octahedral A-site remains inversion-symmetrical. Optical transitions are influenced by the inversion symmetry of crystallographic sites.

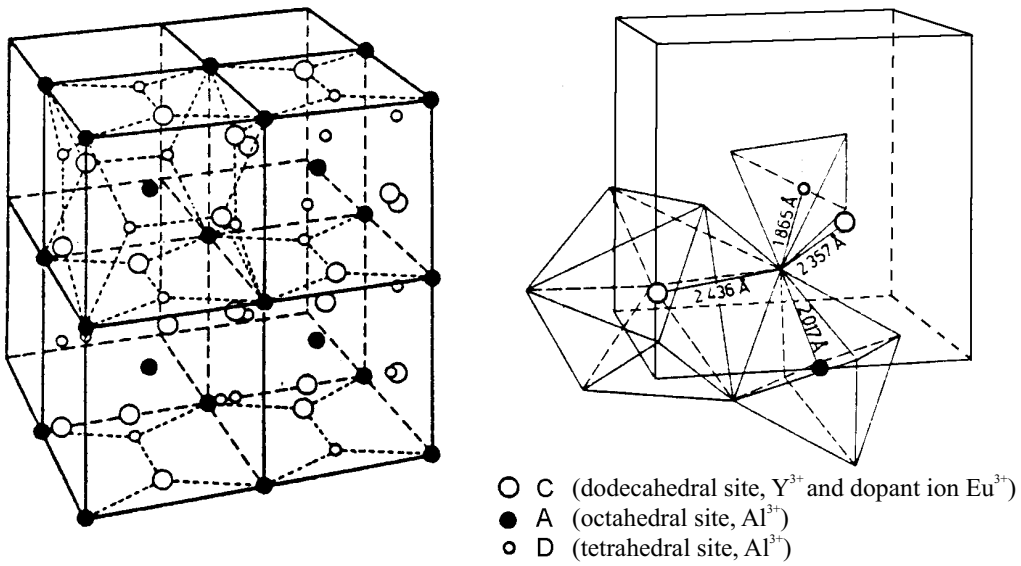

Figure 2.4: Unit cell of garnet crystals [Win81]

YAG is an insulator with a bandgap energy of 6.5 eV. Calculations of its electronic structure were performed recently by Xu and Ching [Xu99, Chi99].

One can also consider YAG as a congruent mixture of two oxides – Y_2O_3 and Al_2O_3. Other congruent compositions of the same compounds are $YAlO_3$ (YAP) with a perovskite orthorhombic lattice and $Y_4Al_2O_9$ (YAM) with a monoclinic structure. Although YAP is sometimes utilized as a host for rare-earth dopants, both, YAP and YAM, are not widely used.

2.4 Orthovanadates of Yttrium and Gadolinium

Both materials, yttrium vanadate and gadolinium vanadate, belong to the group of oxide compounds crystallizing in the $ZrSiO_4$ zircon structure with tetragonal space group $I4_1/_{amd}$ (D^{19}_{4h}). The undistinguishable a and b axes are perpendicular to the crystallographic c axis with fourfold symmetry. As the crystals YVO_4 and $GdVO_4$ are isostructural, the description below is valid for both.

A unit cell of yttrium vanadate contains four YVO_4 molecules with a total of 24 atoms. The trivalent rare-earth ion is coordinated eightfold with oxygen and has the point group symmetry D_{2d}. It is arranged at the center of a tetrahedron formed by four oxygen ions.

This tetrahedron is shorter along the c axis than the corresponding dimensions perpendicular to the c axis and thus irregular, causing the reduction to D_{2d} symmetry. In addition, it is surrounded by four yttrium ions and their oxygen tetrahedra, located in duplicate below and above the site in question (cp. figure 2.5). With this site at the center, a larger irregular tetrahedron is formed by the mentioned four Y-O tetrahedra. This large tetrahedron is rotated 90° from the orientation of the Y-O tetrahedron at its center. In the first approximation, the vanadium ions are not seen by the yttrium ions since each

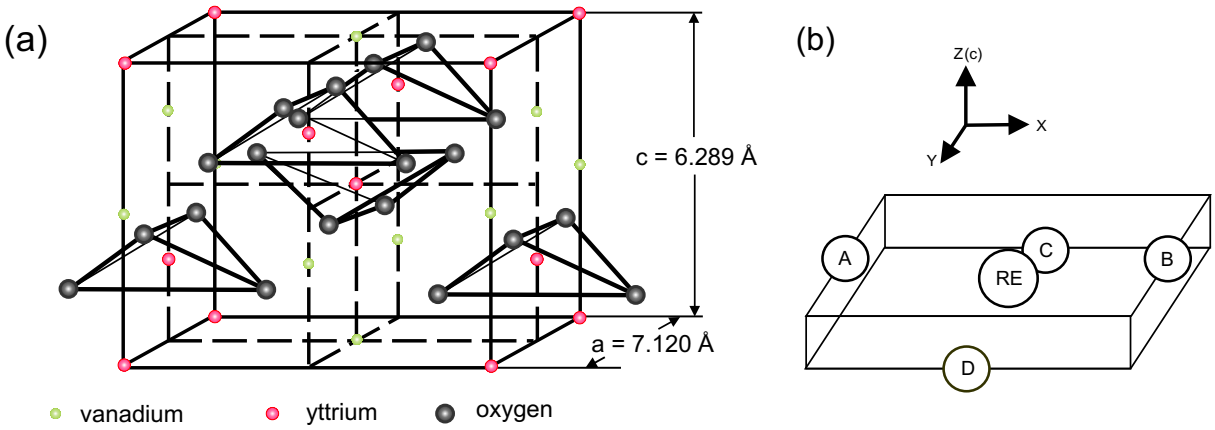

Figure 2.5: *A unit cell of YVO_4 – isostructural to $GdVO_4$ – according to (a) [Yan76] and (b) [And94]. The oxygen ions forming an irregular tetrahedron are labelled with A to D.*

vanadium ion, due to its small size of 0.59 Å, is completely shielded by a tetrahedron of oxygen ions [Yan76].

The lattice constants of YVO_4 have the values $a = 7.120$ Å and $c = 6.289$ Å. In comparison, replacing trivalent yttrium ions by larger gadolinium ions increases the distances between dodecahedral lattice sites, causing a decrease of ion-ion interaction between neighboring ions and also making the segregation coefficient closer to unity. The lattice parameters of $GdVO_4$ are $a = 7.211$ Å and $c = 6.350$ Å.

2.5 Lithium Yttrium Fluoride

Fluoride crystals are favorable laser materials due to some physical properties. Being non-hygroscopic, their low phonon energies recommend them for upconversion lasers.

The lithium yttrium fluoride crystal is uniaxial and crystallizes in the tetragonal scheelite structure of $CaWO_4$ with space group $I4_1/_a$ (C_{4h}^6). Figure 2.6 shows a tetragonal unit cell which contains four stoichiometric $LiYF_4$ units with eight trivalent cations and sixteen anions. The rare-earth ions occupy the eightfold dodecahedrally coordinated lattice site with point group symmetry S_4, which is non-inversion symmetrical. The lithium ions occupy the fourfold tetrahedrally coordinated lattice site, with the corresponding polyhedrons being distorted.

$LiYF_4$ has a melting point of approximately 840° C and a Mohs hardness of 4-5. Lattice constants are $a = 5.16$ Å and $c = 10.75$ Å, the low phonon energy being in the range of 442-460 cm^{-1}.

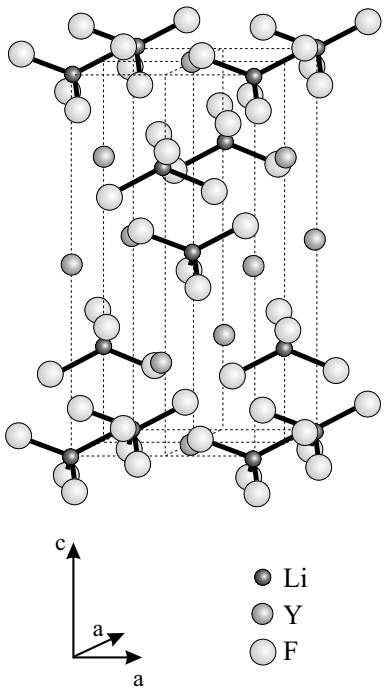

Figure 2.6: *Unit cell of $LiYF_4$ [Win81]*

Material properties

Some important parameters and properties of the substrate and film materials are summarized in the table below. Appendix B summarizes the associated Sellmeier equations.

	Sc_2O_3	Y_2O_3	Lu_2O_3	Gd_2O_3
Crystal structure	cubic	cubic	cubic	monoclinic[2]
Symmetry	$Ia3$ (T_h^7)	$Ia3$ (T_h^7)	$Ia3$ (T_h^7)	$C2/m$ (C_{2h}^3)
Lattice constants (Å)	$a = 9.844$	$a = 10.603$	$a = 10.391$	$a = 14.08$ $b = 3.567$ $c = 8.743$
Density ($\frac{\mathrm{g}}{\mathrm{cm}^3}$)	3.847	5.03	9.42	7.100
Hardness (Mohs)	6.8	6.8	≈ 7	6.9
Melting temperature (K)	≈ 2703	2703	≈ 2723	2693
Thermal conductivity κ $\left(\frac{\mathrm{W}}{\mathrm{m\,K}}\right)$ @ 300 K	17	14	13	≈ 13
Thermal expansion α ($10^{-6}\,\mathrm{K}^{-1}$)	9.6	8.6	7.9	8.2
Phonon energy $\hbar\omega_{\max}$ (cm^{-1})	672	597	618	604
Possible dopant	RE	RE	RE	RE
Site symmetry (coordination number)	$C_2(6)$ $C_{3i}(6)$	$C_2(6)$ $C_{3i}(6)$	$C_2(6)$ $C_{3i}(6)$	$C_S(7)$
Transparency range (µm)	0.21 . . . 8	0.21 . . . 8	0.22 . . . 8	0.22 . . . 8
Refractive index n @ 1 µm	1.967	1.890	1.911	1.950
$\frac{\mathrm{d}n}{\mathrm{d}T}$ ($10^{-6}\,\mathrm{K}^{-1}$) @ 589 nm		1.0		
Bandgap energy (e V)	5.9	5.6	5.5	5.3

[2] Though Gd_2O_3 crystallizes in monoclinic structure at room temperature, the cubic form is of interest in this thesis. As it is used in mixed sesquioxide compositions with lutetia, it also crystallizes in cubic $Ia3(T_h^7)$ structure with lattice $a = b = c = 10.813$ Å.

α-Al_2O_3	$Y_3Al_5O_{12}$	YVO_4	$GdVO_4$	$LiYF_4$
hexagonal	cubic	tetragonal	tetragonal	tetragonal
$R\,\bar{3}c$ (D_{3d}^5)	$Ia3d$ (O_h^{10})	$I4_1/amd$ (D_{4h}^{19})	$I4_1/amd$ (D_{4h}^{19})	$I4_1/a$ (C_{4h}^6)
$a = 4.762$ $c = 12.995$	$a = 12.01$	$a = 7.120$ $c = 6.289$	$a = 7.211$ $c = 6.350$	$a = 5.16$ $c = 10.75$
3.987	4.5	4.22	5.47	3.95
9	8.5	5	5	$4 - 5$
2313	2223	2083	≈ 2083	1098
35	11	5		6
5.3 ($\parallel$ c) 4.5 ($\perp$ c)	6.9	4.43 ($\parallel$ c) 11.37 ($\perp$ c)		8.3 ($\parallel$ c) 13.3 ($\perp$ c)
950	857	850		450
TM	RE, TM	RE	RE	RE
$O_h(6)$	$D_2(8)$ $C_{3i}(6)$ $S_4(4)$	$D_{2d}(8)$	$D_{2d}(8)$	$S_4(8)$
$0.14 \ldots 6.5$	$0.24 \ldots 6$	$0.4 \ldots 5$		$0.18 \ldots 6.7$
$n_o = 1.756$ $n_e = 1.747$	1.816	$n_o = 1.960$ $n_e = 2.169$	$n_o = 1.988$ $n_e = 2.202$	$n_o = 1.448$ $n_e = 1.471$
13.6 (n_o) 14.7 (n_e)	7.3 – 8.9	8.5 (n_o) 3.0 (n_e)		-2.0 (n_o) -4.1 (n_e)
9.5	6.5	3.7		10.3

Table 2.1: *Material properties of Sc_2O_3, Y_2O_3, Lu_2O_3, Gd_2O_3, α-alumina, $Y_3Al_5O_{12}$, YVO_4, $GdVO_4$ and $LiYF_4$ [Bar57, Ber74, Con69, For99a, Mix99, Sam82, Web82, Cze02, Zyc02, Win07]*

3 Lanthanide Dopants

In order to study the properties of thin films, lanthanide ions are used as luminescent probes. This is due to the sensitivity of their emission characteristics to the crystallographic environment. Electronic transitions and characteristic optical properties of rare-earth ions, reviewed in this chapter, are required to interpret the optical data of the presented systems. When introduced by substitution of another non-luminescent unit, it is essential that the probe perturbs the investigated material as little as possible.

The elements used for doping can be found in the third main group of the periodic table (cp. figure 2.1). First introduced in this work in section 2.1, the term rare-earth (RE) usually refers to the elements lanthanum (atomic no. 57) through lutetium (atomic no. 71) also known as lanthanides, and the chemically similar elements scandium (atomic no. 21) and yttrium (atomic no. 39) [Gre87]. However, the following discussion will only address the lanthanides.

As also known from other element groups in the periodic table, the lanthanides of increasing atomic number show a periodic behavior with regard to some of their properties, like density, melting and boiling points, while other properties, like ionic radii, change aperiodically. This aperiodic phenomenon is referred to as *lanthanide contraction*.

The similarity in chemical properties stems from the electron configuration of rare-earth atoms, denoted[1] [Xe] $(4f)^n(5d)^x(6s)^2$ with $x = 1$ in the case of lanthanum ($n = 0$), gadolinium ($n = 7$), lutetium ($n = 14$) and $x = 0$ with $n = 2$ through $n = 14$ for cerium through ytterbium. Although the incorporation of the rare-earth ions into a crystal matrix uses the stable trivalent form with the electron configuration [Xe] $(4f)^{n+x-1}$, divalent rare-earths can appear in crystals with divalent lattice sites. Another occasion for divalent rare-earth ions is local charge compensation provided either by crystal defects, such as color centers in sesquioxides and garnets, or by the presence of quadrivalent co-dopants in the crystal matrix [Kap62, Loh69].

[1] [Xe] represents the electron configuration of the noble gas xenon.

The spectroscopic properties of the trivalent rare-earth atoms are dominated by intra-configurational *4f-4f* transitions and interconfigurational *4f-5d* transitions. Because the *5s* and *5p* shells are completely filled in the [Xe] configuration, the *4f* shell electrons are effectively shielded from influences of the chemical environment, e. g. the surrounding crystal field. Therefore, only low variations of the *4f* states can be observed in different local environments [Bur62, Ray63]. This insensitivity to the surrounding offers the advantage of easily determining the energy levels by adding the influence of the crystal field as a perturbation to the free ion energy level terms. In case of the investigated *4f-4f* electric dipole transitions, this results in narrow transition line-widths, compared to those observed in transition metals, in divalent rare-earths, and between RE^{3+} *5d* states [Hen89]. The strength of the shielding decreases with increasing atomic numbers [Ste66, Erd72].

Due to the influence of the crystal matrix, the peak positions of the *4f-4f* transitions perform a little shift. This behavior is known as the *nephelauxetic effect* (Greek: cloud expanding). As interelectronic repulsion and spin-orbit coupling primarily determine the energies of the excited levels, a shift of the peak positions towards lower energy with increasing covalency of the surrounding media is expected. This behavior recommends the rare-earths as suitable probe ions, which is also due to the crystallographic properties of their lattice sites. A detailed discussion of the nephelauxetic effect is given in [Sin66].

Aside from europium, which can be used as a red light emitter in phosphors and is utilized as the main probe ion within the context of this thesis, there are also other rare-earths that are very promising as dopant ions for sesquioxides. Neodymium doping in scandia for operation at 1486 nm is recommendable for the telecommunications industry while erbium in lutetia may prove to be suitable for high power operation at 2.7 µm in medical applications [Pet01]. Besides, high power laser operation was recently demonstrated with Yb:Lu_2O_3 and Yb:Sc_2O_3 in a thin-disk laser geometry [Pet07].

3.1 The Free Ion

In order to calculate the electronic states together with their energies, the Hamiltonian must be determined and the Schrödinger equation solved. For a free ion with a nucleus of charge Ze and N electrons of mass m_e the Hamiltonian is

$$\mathcal{H} = \sum_{i=1}^{N} \left(-\frac{\hbar^2}{2m_e}\Delta_{r_i} - \frac{Ze^2}{4\pi\varepsilon_0 r_i} \right) + \sum_{i<j=1}^{N} \frac{e^2}{4\pi\varepsilon_0 r_{ij}} \,. \tag{3.1}$$

The kinetic energy of the electrons $-(\hbar^2\Delta_{r_i}/2m_e)$ as well as their Coulomb interaction $-(Ze^2/4\pi\varepsilon_0 r_i)$ with the nucleus is described in the first summation. The distance between the electron i and the nucleus is denoted r_i. Represented in the second summation is the electrostatic repulsion between the electrons which are separated by the distance $r_{ij} = |\mathbf{r}_i - \mathbf{r}_j|$. Obviously, a separation of the Schrödinger equation in N one-particle-problems is not possible because of this two-particle-operator, and hence no analytical solution can be found.

The system has to be reduced to a radial, effective central field without electron-electron interaction. In this central field approximation, where each electron moves in an effective spherically symmetric potential $V(\mathbf{r})$ created by the nucleus and the remaining $(N-1)$ electrons, the Hamiltonian is given by

$$\mathcal{H}_0 = \sum_{i=1}^{N} \left(-\frac{\hbar^2}{2m_e} \Delta_{r_i} + V(\mathbf{r}_i) \right) \ . \tag{3.2}$$

The Hamiltonian is now separable and the time-independent Schrödinger equation can be obtained with the energy eigenvalues E_0

$$\mathcal{H}_0 \Psi_0 = E_0 \Psi_0 \ . \tag{3.3}$$

The solution Ψ_0 is the product of the eigenstates of the single-electron wavefunctions $|n_i l_i m_l m_s\rangle$

$$\Psi_0 = \prod_{i=1}^{N} |n_i l_i m_l m_s\rangle \ , \tag{3.4}$$

with n_i denoting the principal quantum number and l_i the orbital angular momentum of the electron i. The wavefunction Ψ_0 has to be completely anti-symmetric, since according to the Pauli exclusion principle two electrons cannot share the same single-particle-state. Consequently, Ψ_0 is built up as a Slater determinant out of one-electron spin orbitals. The energy eigenvalues of these eigenstates are only dependent on the quantum numbers n and l and are degenerated with respect to m_l and m_s.

It is possible to iteratively determine a self-consistent central-potential by the Hartree-Fock method. Once started with a chosen potential, the calculated potentials converge by successive iteration with the Hartree-Fock equations towards the self-consistent potential $V(\mathbf{r})$ of the system.

Two corrections have to be considered in the central field approximation: First, the non-spheric and non-symmetric part of the Coulomb repulsion interaction between the electrons

$$\mathcal{H}_{ee} = \sum_{i<j=1}^{N} \frac{e^2}{4\pi\,\varepsilon_0\, r_{ij}} - \sum_{i=1}^{N} \left(-\frac{Ze^2}{4\pi\,\varepsilon_0\, r_i} + V(\mathbf{r}_i) \right) \ , \tag{3.5}$$

that results in a splitting of the *4f* states into ${}^{2S+1}L$ states, in which the total orbital angular momentum is $L = |\mathbf{L}|$ with $\mathbf{L} = \sum_i \mathbf{l}_i$ and $S = |\mathbf{S}|$ is the total spin with $\mathbf{S} = \sum_i \mathbf{s}_i$. The resulting wavefunctions are described by the quantum numbers L, S, M_L, and M_S. Typically, the energy splitting of the LS-terms is of the order of 10^4 cm^{-1}.

The second correction due to the spin-orbit interaction is given by

$$\mathcal{H}_{\mathrm{SO}} = -\sum_{i=1}^{N} \frac{1}{2m^2c_0^2} \frac{1}{r_i} \frac{\mathrm{d}V(\mathbf{r}_i)}{\mathrm{d}r_i} \left(\mathbf{s}_i \cdot \mathbf{l}_i\right) \ , \tag{3.6}$$

with $\mathbf{s}_i$ the spin-vector of the i^{th} electron and $\mathbf{l}_i$ the orbital angular momentum vector of the i^{th} electron. c_0 is the speed of light in vacuum. With the two perturbations considered, the Hamiltonian for the free ion can now be written as

$$\mathcal{H} = \mathcal{H}_0 + \mathcal{H}_{ee} + \mathcal{H}_{\mathrm{SO}} \ . \tag{3.7}$$

The further energy level splitting is depending on the coupling of the electrons. To gain a better understanding of how the perturbation terms are effecting the central field, three different cases are compared:

1. In the case of very heavy elements, $\mathcal{H}_{\mathrm{SO}}$ is the dominating part. Consequently, the spin and the orbital angular momentum of each electron couple to the angular momentum $\mathbf{j}_i = \mathbf{s}_i + \mathbf{l}_i$ resulting in the total angular momentum $\mathbf{J} = \sum_i \mathbf{j}_i$. This case is termed *jj*- coupling.

2. If in the opposite case $\mathcal{H}_{\mathrm{ee}}$ is the dominating term, the individual spins couple to the total spin $\mathbf{S} = \sum_i \mathbf{s}_i$, and the individual orbital angular momentums couple to the total orbital angular momentum $\mathbf{L} = \sum_i \mathbf{l}_i$. This coupling mechanism, in which the influence of the spin-orbit interaction effects a splitting of the LS-terms in J-multiplets, is termed LS-coupling or Russell-Saunders-coupling.

3. Taking to account the influence of the perturbation terms in lanthanide ions, both correction terms are of comparable magnitude resulting in an intermediate coupling scheme. The eigenstates are linear combinations of several LS states of the same total angular momentum J, named according to the state with the strongest influence. Though the total angular momentum J remains a non-degenerate quantum number, different ${}^{2S+1}L$ manifolds may energetically overlap with regard to the J-components. The eigenstates are designed by the quantum numbers L, S, and J. Because the ${}^{2S+1}L_J$ states are $(2J+1)$-fold degenerated in regard to M_J [Hen89], it is common to label the energy eigenstates following the Russell-Saunders approximation (${}^{2S+1}L_J$). A detailed discussion of the intermediate coupling can be found in the books of Sobelman [Sob79] as well as Condon and Shortley [Con51]. The energetic splitting of the ${}^{2S+1}L_J$ is typically in the range of 10^3 cm^{-1}.

Several orders of magnitude smaller than the observed interactions are additional perturbations, such as spin-spin interactions or orbit-orbit interactions as well as hypersensitive interactions, and can therefore be neglected. Of more importance is the influence of the crystal field and its effect on the positions of energy levels of rare earth ions. This will be discussed in the following section.

3.2 The Lanthanide Ion in a Crystal Matrix

When an ion is incorporated into a crystal lattice – any other chemical environment like glass or solution will also do –, it is subject to the electrostatic field of the neighboring ions, also called ligands. By the interaction of the *4f* electrons of a lanthanide ion with the mentioned electrostatic field of the ligands, the spherical symmetry of the free ion is destroyed. This is referred to as Stark effect. The influence of the local electric field $\mathbf{E}$ introduced as an additional perturbation term is represented by the Hamiltonian

$$\mathcal{H}_{\text{Stark}} = -e \sum_{k=1}^{N} \mathbf{E}(\mathbf{r}_k) \cdot \mathbf{r}_k \ . \tag{3.8}$$

The crystal field has two effects on the energy level structure of the free ion.

1. It induces a red shift on the free ion levels that can be explained by a reduction of the free ion parameters [Jør77] referred to as nephelauxetic effect (cp. page 18).

2. It causes a Stark splitting of the ${}^{2S+1}L_J$ manifolds of the free ion and thus repeals the degeneracy with respect to M_J. For lanthanide ions having an odd number of electrons, the Kramers theorem asserts a splitting in $(2J+1)/2$ twofold degenerated Stark levels. This Kramers degeneration is a consequence of the time-reversal invariance. Ions with an even number of electrons are split into $(2J+1)$ levels [Mes90].

The Hamiltonian for a rare-earth ion arranged in a crystal field is concludingly given by

$$\mathcal{H} = \mathcal{H}_0 + \mathcal{H}_{ee} + \mathcal{H}_{\text{SO}} + \mathcal{H}_{\text{Stark}} \ , \tag{3.9}$$

with the influence of the perturbation $\mathcal{H}_{\text{Stark}}$ being one order of magnitude smaller than the contributions of $\mathcal{H}_{\text{SO}}$ and $\mathcal{H}_{ee}$, as the *4f* electrons are shielded from the crystal field by the *5s* and *5p* electrons. As the interaction with the ligand field or with vibrational states mixes electronic states of different parity into the *4f*-wavefunctions, the regularly forbidden electric dipole transitions within the *4f* shell are now partially allowed (cp. section 3.2.1).

3.2.1 Intraconfigurational 4f-4f Transitions

The excitation of an ion via an electron transition from the ground state to a higher energy level can be initiated by an oscillating electromagnetic field of appropriate frequency. As higher order transitions like electric or magnetic quadrupole processes can generally be neglected due to reduced transition probabilities [Die68, Pea75], the transitions between two energy levels may be categorized in having either electric dipole or magnetic dipole character.

In expressing the electric field in terms of a multipole expansion, the first terms of order n of this expansion are denoted monopole ($n = 0$), dipole ($n = 1$), quadrupole ($n = 3$), and octupole ($n = 4$). The Laporte selection rules for electric multipole transitions of order n in a symmetric central field are:

1. For $n = 0, 2, 4, \ldots$ only transitions between states of the same parity are allowed.
2. For $n = 1, 3, 5, \ldots$ only transitions between states of different parity are allowed.

As electric dipole transitions require a change of parity of the electron wavefunction, they are forbidden within the *4f* shell, due to the Laporte selection rules above, and only magnetic dipole transitions are expected [Hen89]. Usually these transitions are weaker than electric dipole transitions by a factor of 10^5.

However, under the influence of crystal fields without inversion symmetry, a configurational mixing of opposite-parity states – like $4f^{n-1}5d$ – into the $4f^n$ states can occur partly allowing electron dipole transitions in the *4f* states and retensioning the Laporte rules. In the case of crystallographic sites with inversion symmetry the Laporte selection rule is weakened by rare-earth ions occupying acentric sites in the matrix, reintroducing intraconfigurational *4f-4f* transitions observed as forced electric dipole transitions. Though, the weakening of inversion symmetrical sites is considerably smaller than of non-inversion sites. The selection rules for these forced electric dipole transitions between $4f^n$ states are [Hen89, Kam90]

1. $\Delta l = \pm 1$
2. $\Delta S = 0$
3. $\Delta L = 2\,l = 6$
4. $\Delta J = 2\,l = 6$

In the case of rare-earth ions with an even number of electrons some additional selection rules apply as follows

1. $J = 0 \leftrightarrow J' = 0$ forbidden
2. $J = 0 \leftrightarrow J' = 2, 4, 6, \ldots$ strong
3. $J = 0 \leftrightarrow J' = 1, 3, 5, \ldots$ weak .

Intensive investigation on the admixing of states with opposite parity to the *4f* states was done by Judd and Ofelt [Jud62, Ofe62].

As mentioned earlier, two different lattice sites with symmetry C_2 and symmetry C_{3i} are provided by the matrix of the sesquioxides (cp. chapter 2.1). As the C_{3i}-sites show

inversion symmetry, the effect of admixing is considerably smaller compared to the C_2-sites, due to the lack of a center symmetry. Thus, the Laporte selection rule is stronger for ions occupying the C_{3i}-site, resulting in a reduced transition probability compared with transitions of ions in the C_2-site.

After having described the intraconfigurational, parity forbidden *4f-4f*-transitions (weak) and the applying selection rules, we will now focus on the parity allowed transitions of the lanthanide ions (strong), which appear as broad bands in optical spectra. These parity allowed transitions are the interconfigurational $4f^n \rightarrow 4f^{n-1}5d$ and the charge transfer (CT) transitions.

3.2.2 Interconfigurational 4f-5d Transitions

The outer electrons situated in the *5d*-orbitals are not shielded by other electrons as the ones in the *4f*-levels and therefore energetically very sensitive to the environment. Thus, the crystal field is the primary influence of these *5d*-orbitals, being more relevant than the Stark effect or the Coulomb interaction [Loh73]. The position of the energy levels and the splitting due to the crystal field with respect to the site symmetry [Sch67] is given by the *ligand-field theory*.

This model contributes an extension to the crystal field theory to allow covalent interactions and is valid for electrons in non-completely filled shells. The bonding is generally explained by molecular orbital theory [Sch67, Sch73, Bal62].

Assumptions regarding the ligand field theory are that the motion of the electrons occurs in the potential of the metal ion core as well as in the electrostatic potential of the ligands. The interaction among the electrons of the central ion and the electrons of the ligands can be neglected, as the ligands are regarded as point charges. The energy splitting is therefore explained as a consequence of this electrostatic interaction, with the premise of purely ionic bonding between the metal ion and the ligands having no covalent admixture.

The orientation of the *d*-orbital wavefunctions either increases or decreases the electron energy depending on the orbital extended into a region of high or low electron density. This results in a splitting of energy levels.

Applying this electrostatic model for example to an octahedrally coordinated d^1 electron which is – due to the angular part of the crystal field potential – degenerated twofold in an E_g state and threefold in a T_{2g} state, the energy difference of the splitting is given by

$$10\,\mathrm{Dq}_{Okt} = \frac{q\langle r^4\rangle}{6\,R^5}\,. \tag{3.10}$$

The total energy splitting $10\,\mathrm{Dq}$ is named *crystal field stabilization energy*, with $\langle r\rangle$ being the radial probability density of the electron and R the metal-ligand internuclear distance. Because of the destabilizing effect of the center symmetrical part of the ligand field, an energetic increase $\varepsilon_{0,\,Okt}$ is induced on the d^1 electron levels, with the resulting influence of the ligand field on a single d^1 electron of

$$\Delta\varepsilon_{Okt} = \varepsilon_{0,Okt} + \begin{cases} +6\,\mathrm{Dq}_{Okt} & \text{for} \quad \mathrm{E}_g \\ -4\,\mathrm{Dq}_{Okt} & \text{for} \quad \mathrm{T}_{2g} \end{cases} . \tag{3.11}$$

It has to be mentioned though, that the excitation of an *4f* electron into a *5d* orbital presents a $4f^{\,n} \rightarrow 4f^{\,n-1}5d$ transition and thus cannot be described as a one-particle-problem. All electrons, *4f* and *5d* orbitals have to be taken into account in order to obtain an exact calculation of the energy levels.

In general, a large crystal field splitting energy is provided by ligands with high negative charge and small radius and by metal cations with large oxidation number. In section 3.2.4 a more illustrative description of the *4f-5d* transitions is given, as the single configurational coordinate model is introduced.

3.2.3 Charge Transfer Transitions

Interconfigurational transitions which involve a ligand-to-metal charge transfer transition and the reverse process, a metal-to-ligand charge transfer transition, are referred to as charge transfer transitions. An electronic state in which a large fraction of the electronic charge is transferred from one molecular entity (electron donor) to another (electron acceptor) is generally defined as charge transfer state (CTS) [McN97]. The charge center between the central ion and the ligands is considerably shifted with respect to the ground state. This is due to the displacement of electronic charge across a typical interatomic distance. The shifted charge center produces a large transition dipole moment and a concomitant large oscillator strength.

An often given description of a ligand-to-metal charge transfer process is the transfer of an electron from the ligands to the central metal ion ($\mathrm{M^{n+}L^{m-}} \rightarrow \mathrm{M^{(n-1)+}L^{(m-1)-}}$) resulting in an excitation of an electronic state, which is called charge transfer state [Pie01]. This model then interprets a charge transfer state as a hole which is transferred from the $\mathrm{RE^{3+}}$ ion to the ligands, moving around the $\mathrm{RE^{2+}}$ core in a potential field produced by the lattice because of the effective negative charge [Hos77].

The energy of a charge transfer band E_{CT} is dependent on the donor ionization energy, the acceptor electron affinity and on the extent of the charge displacement. As the CT band energy correlates well with the Pauling scale of electronegativities, Jørgensen introduced the concept of optical electronegativity [Jør70]. According to this model, the energy E_{CT} can be estimated by the optical electronegativity of the anion $\chi_{\mathrm{opt}}(\mathrm{L})$ and of the central metal ion $\chi_{\mathrm{opt}}(\mathrm{M})$ as follows:

$$E_{\mathrm{CT}} = [\chi_{\mathrm{opt}}(\mathrm{L}) - \chi_{\mathrm{opt}}(\mathrm{M})] \times 30\,000\,\mathrm{cm^{-1}} . \tag{3.12}$$

For the corresponding values $\chi_{\mathrm{opt}}(\mathrm{Eu^{3+}}) = 1.8$ and $\chi_{\mathrm{opt}}(\mathrm{O^{2-}}) = 3.2$ of the investigated $\mathrm{Eu^{3+}}$ ion in an oxide host matrix, the average CT band position equals $42\,000$ $\mathrm{cm^{-1}}$, being anti-proportional to the Eu-O distance. The band shifts to lower energies with increasing bond length [Hoe75].

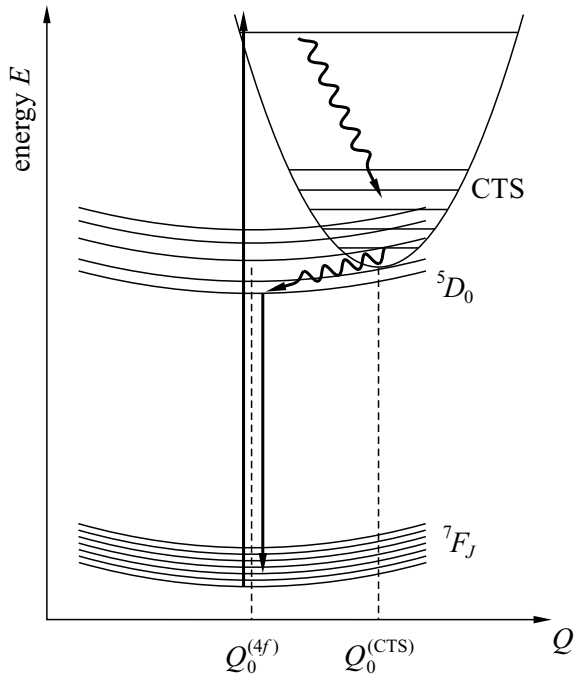

Figure 3.1: *CT excitation of Eu^{3+}:Y_2O_3*

The involvement of a charge transfer state in either absorption or emission processes can be observed. However, luminescence from a charge transfer state is only possible if this state is lower in energy than the lowest energy level of an excited $4f^{n-1}5d$ state. Moreover, no *4f* energy levels are allowed to be present at energies comparable to the charge transfer state, because of the resulting fast intersystem crossing to the lower energy $4f^n$ states and $4f^n \rightarrow 4f^n$ emission. In figure 3.1 this mechanism is shown for Eu^{3+}:Y_2O_3 and the case that UV radiation is efficiently absorbed by a transition to the charge transfer state of the Eu^{3+} ion. No emission is taking place from the charge transfer state, because of the relaxation to the lower *4f* levels in the ^5D_J manifold. Instead, luminescence from the $^5D_0$ state of Eu^{3+} occurs [Nak79].

3.2.4 Vibrations of the Host Lattice

Host lattice vibrations have significant influence on the optical transitions of the rare-earth ions. Again, it is necessary to expand the Hamiltonian operator of two additional terms in order to describe the electron-phonon interactions. The first considers the kinetic energy of all ions and the second takes into account the interionic potential energy due to the movements off the equilibrium positions.

In comparison, the electron-phonon coupling of the *5d* electrons is significantly stronger than the one of the *4f* electrons because of the wider ranging radial expansion and unshielded interaction of the *5d* orbitals. While the *4f-4f* transitions are quite narrow banded, the electron-phonon interaction leads to a strong broadening of the interconfigurational transitions.

A more illustrative description of these phenomenons is given by the *single-configurational coordinate model* [Bar74, Hen89]. In this model radiative and non-radiative transitions, the shape of an optical transition (narrow or broad lines), as well as the Stokes' Law are explained. It is based on the *Born-Oppenheimer approximation* [Bor27], separating the motion of the electrons from the one of the nuclei (lattice vibrations). The eigenvalues $\phi(r_i, R_l)$ of the electron-phonon coupling can be written be

$$\phi(r_i, R_l) = \psi(r_i)\chi(R_l) \; , \tag{3.13}$$

with the position of the l^{th} ion R_l, the electronic part $\psi(r_i)$ describing the eigenvalues of the Hamilton operator in a static lattice and $\chi(R_l)$ describing the dynamics of the lattice. Further, this model introduces symmetrical stretching mode (or *breathing mode*) which

preserves the symmetry of the ligands around the metal ion and represents all vibrational modes of the lattice (*phonons*).

Illustrated in the corresponding configurational coordinate diagram (cp. figure 3.2) are the potential energy curves of a *4f* ground state, a *4f* excited state, and a *5d* excited state of a localized lanthanide ion as a function of the configurational coordinate Q. This coordinate describes the average distance between the central ion and the ligands.

The vibrational motion being of harmonic nature is displayed in the diagram by parabolic curves with the well-known quadratic dependence of the potential energy V_{pot} on Q

$$V_{\text{pot}} = \tfrac{1}{2}\, k\, (Q - Q_0)^2 \ . \tag{3.14}$$

The restoring force constant of the vibrational motion is represented by the factor k. The horizontal lines in the diagram refer to the discrete, vibrational levels of energy $E_m = (m+\frac{1}{2})\hbar\omega_m$ which are yielded by the quantum mechanical solution of this equation.

The strength of the electron-phonon coupling is symbolized by the slope of the parabola. Parabola with wider aperture have smaller electron-phonon coupling and vice versa. This effect is shown for the *4f* and *5d* states in a lanthanide ion in the aforementioned figure 3.2. More influenced by lattice vibrations are the *5d* states, with their restoring forces being therefore larger than those of the *4f* states, i. e. $k(5d) > k(4f)$.

Each active ion configuration has a certain spatial dimension because of different radial

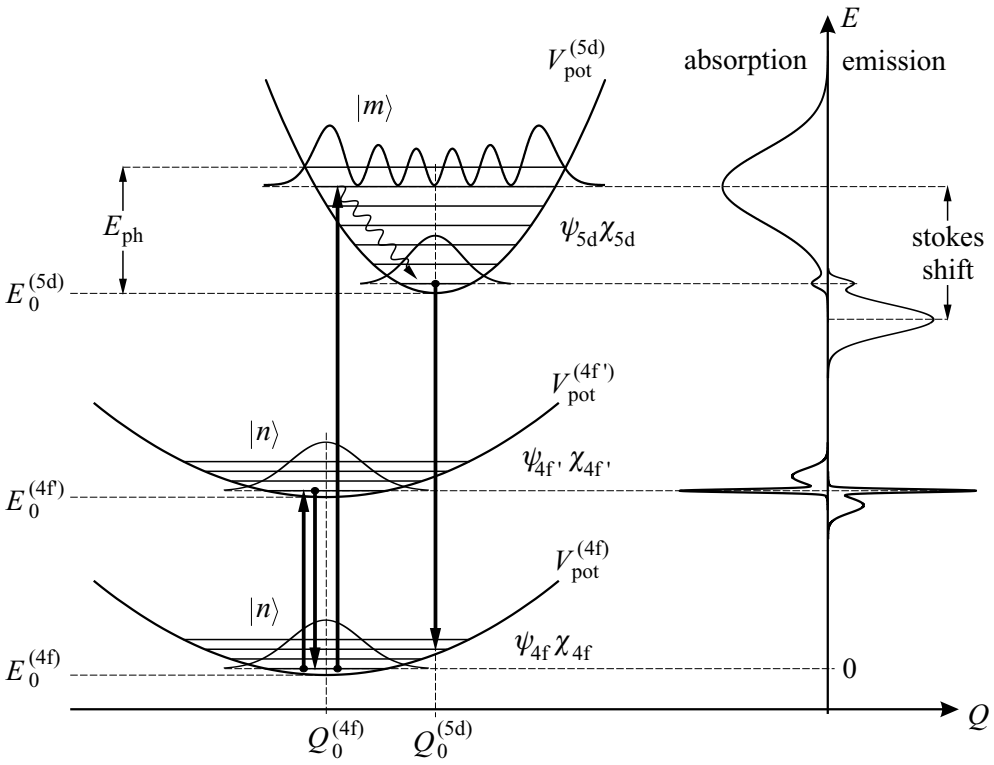

Figure 3.2: *Configurational coordinate diagram of the 4f and 5d states in a lanthanide ion*

probability densities, resulting in a characteristic equilibrium configurational coordinate Q_0, which denotes the shifting of parabolas due to different equilibrium configurations. This emphasizes that the minimum of the excited state energy may deviate in position from the one of the ground state energy.

Treating the transitions between electronic energy levels according to the Born-Oppenheimer approximation, the *Franck-Condon principle* [Con28] must be considered, stressing that electronic transitions occur much faster than nuclei can respond to their new equilibrium positions. A transition from the m^{th} into the n^{th} vibrational level of two different electronic states $|a\rangle$ and $|b\rangle$ has the transition probability

$$P_{|an\rangle\to|bm\rangle} = P^{\text{el}}_{|a\rangle\to|b\rangle}|\langle m|n\rangle|^2 \,, \tag{3.15}$$

with the purely electronic transition probability denoted by $P^{\,\text{el}}$. The Franck-Condon-principle is considered in the configurational coordinate diagram by drawing radiative transitions as vertical lines, i. e. Q remains constant during the transition.

Also illustrated in figure 3.2 is the broadening of the interconfigurational transitions and their huge Stokes shift compared to the intraconfigurational transitions. The figure shows a displacement of the parabolas involved in interconfigurational transitions. Therefore, the absorption from state $|n\rangle$ does not occur into the minimum, but into the side wing of parabola $5d$, occupying the vibrational state $|m\rangle$, which can relax non-radiatively into the minimum of parabola $5d$ (cp. figure 3.2). In intraconfigurational transitions the equilibrium positions Q_0 are identical and thus very sharp absorption and emission bands are displayed.

The vibrational states $|n\rangle$ and $|m\rangle$ are occupied thermally at temperatures $T > 0$, with non-radiative transitions being possible despite the broadening of the transition bands. It can occur through an intercrossing if a relaxed excited electronic state intersects the parabola of a less energetic excited electronic state or the electronic ground state. A non-radiative return to a less energetic excited state or the ground state is possible as well by the process of a multi-phonon relaxation. The energy difference between two levels must not exceed more than five times the vibrational frequency of the host (effective phonon energy) in order to excite vibrations of the host through multi-phonon decay.

3.3 Europium as Probe Ion

The Eu^{3+} ion was chosen for use as a structural probe for the sites occupied by the RE^{3+} in the given materials. The reasons for this choice were its high emission quantum yield and its relatively simple energy level scheme [Bün89]. Although the structural investigation of thin films often requires complex analytical tools, the local crystal structure is more easily determined by the luminescence spectrum of a dopant or probe ion.

Because of the advantages mentioned above and the fact that the transitions are mainly in the visible spectrum and thus easy to detect, throughout this thesis Eu^{3+} is used as dopant ion for the introduced materials (cp. chapter 2) in order to investigate and compare the spectroscopic properties.

Depending on the material, Eu^{3+} substitutes for rare-earth ions in the lattice – like Y^{3+}, Sc^{3+}, Lu^{3+}, or Gd^{3+}. Comparable ionic radii are very useful but not obligatory, as the rare-earth ions are of similar kind. The spectroscopic properties depend on the populated crystallographic sites and their symmetries, which vary in different materials. For better comparison, the ionic radii contingent on the oxygen coordination of the used element compounds and four dopants are shown in table 3.1.

The Eu^{3+} spectrum shows the transitions between energy levels of the *4f* electrons. The influence of the dopant on the regular crystal lattice should be as small as possible, i. e. the ionic radii of Y^{3+} and Eu^{3+} do not differ much. Therefore, the Eu^{3+} ions in Y_2O_3 populate the two sites of different symmetry with equal probability [Heb70]. The surrounding crystal field strongly influences the position and intensity of these transitions (cp. section 3.2).

It is particularly the site symmetry of the dopant ion that will be seen in the fluorescence spectrum. The symmetry of the local crystal field results in a splitting of the Eu^{3+} energy levels in a set of $(2J + 1)$ sublevels, while the host lattice does not affect the global electronic structure of Eu^{3+}.

Coordination	**Element**					**Dopant**			
Number	Al^{3+}	Sc^{3+}	Y^{3+}	Lu^{3+}	Gd^{3+}	Cr^{3+}	Nd^{3+}	Eu^{3+}	Yb^{3+}
[4]	0.39	—	—	—	—	—	—	—	—
[6]	0.54	0.75	0.92	0.86	0.94	0.62	0.98	0.95	0.87
[8]	—	0.87	1.02	0.98	1.06	—	1.11	1.06	0.99

Table 3.1: Ionic radii (Å) of the used trivalent rare-earths, aluminum, and common dopants dependent on their oxygen coordination [Kam90, Sha76]

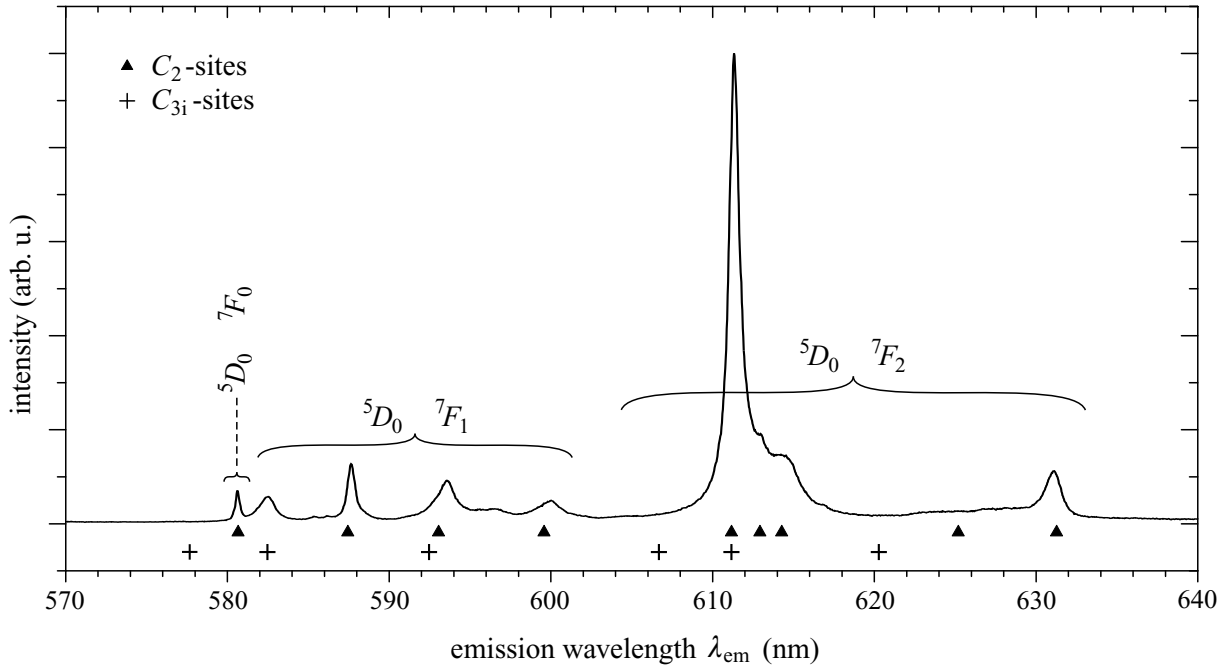

Figure 3.3: *Emission spectrum of Eu(1%):Y_2O_3 bulk crystal ($\lambda_{ex} = 243\,nm$, spectral resolution 0.08 nm). The symbols indicate the emission from the two symmetry sites C_2(▲) and C_{3i}(+).*

transition	Di	range (nm)	I	comments
$^5D_0 \rightarrow {}^7F_0$	ED	577 - 581	vw	forbidden, non-degenerate; J-mixing gains intensity
$^5D_0 \rightarrow {}^7F_1$	MD	585 - 600	s	allowed; intensity independent from environment
$^5D_0 \rightarrow {}^7F_2$	ED	610 - 625	s-vs	hypersensitive ($\Delta J = 2$); absent on inversion center
$^5D_0 \rightarrow {}^7F_3$	ED	640 - 655	vw	forbidden; J-mixing adds allowed MD character
$^5D_0 \rightarrow {}^7F_4$	ED	680 - 710	m-s	sensitive to the Eu-environment ($\Delta J = 4$)
$^5D_0 \rightarrow {}^7F_5$	ED	740 - 770	vw	forbidden, seldom observed
$^5D_0 \rightarrow {}^7F_6$	ED	810 - 840	vw	seldom observed

Table 3.2: *Europium $^5D_0 \rightarrow {}^7F_J$ transitions;* Di *indicates the dipole character,* range *gives the approximate wavelength range of the transition, I gives the intensity of the transition* (vw – *very weak,* m – *medium,* s – *strong,* vs – *very strong).*

As the most intense transitions originate from the excited $^5D_0$ state, which is not split into sublevels due to the crystal field, the characteristic emission spectrum of the Eu^{3+} ion is easily analyzed. As an example of the used materials, the energy level scheme for Eu:Y_2O_3 is depicted in figure 3.4. Energy level schemes of trivalent europium in the other used materials are similar to the addressed one. The spectroscopic peculiarities of each film material will be discussed in chapters 8 and 9.

When the Eu^{3+} ion is excited into the charge transfer band, the electrons are promoted into the ^5D_J manifold due to non-radiative processes (cp. figure 3.4). It is the $4f \rightarrow 4f$ electronic relaxation to the ^7F_J ground state manifold that leads to the characteristic emission. Although the excitation mechanism in the charge transfer band is the same for all investigated Eu-doped materials, the center wavelength may slightly differ. For instance, the charge transfer band of Eu^{3+} in YAG is located around 228 nm [Zho03] in comparison to 243 nm in Y_2O_3.

A typical emission spectrum regarding Eu^{3+} in a crystalline Y_2O_3 matrix is depicted in figure 3.3. The intense, narrow peak at 611 nm, arising from the hypersensitive $^5D_0 \rightarrow {}^7F_2$ transition of Eu^{3+} in the C_2-site, is characteristic. Almost insensitive to the environment due to its purely magnetic dipole character is the $^5D_0 \rightarrow {}^7F_1$ transition of Eu^{3+}, occupying both the C_2 and C_{3i}-sites, whereas in contrast the intensities of the $^5D_1 \rightarrow {}^7F_{0,1,2}$ transitions are quite weak and respond very sensitively to the Eu-environment. An overview of the $^5D_0 \rightarrow {}^7F_J$ transitions is given in table 3.2.

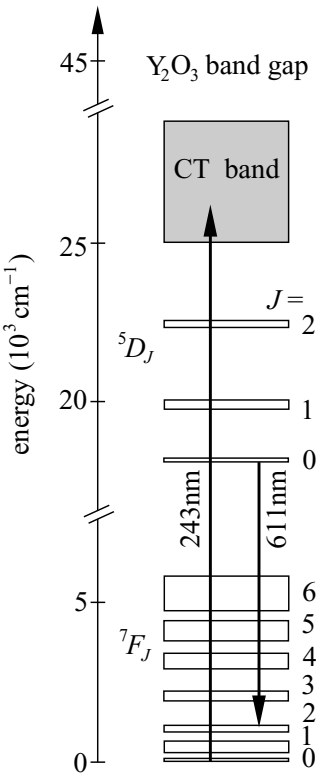

Figure 3.4: *Energy level scheme of Eu^{3+} in Y_2O_3*

As the energy gap between $^5D_0$ and $^7F_6$ in Eu:Y_2O_3 is about 11 500 cm^{-1} large, the probability of a depopulation of the excited $^5D_0$ state by a non-radiative multiphonon process is very small. Consequently, 30 phonons with an energy of 400 cm^{-1} each would be involved in these processes, while a non-radiative deexcitation of the $^5D_1$ state to the luminescent $^5D_0$ state would only require 4 phonons due to the energy difference of only 1700 cm^{-1}.

4 Pulsed Laser Deposition

Apart from the material and the substrate, the utilized fabrication method significantly determines the properties of a thin film. As there is a vast variety of film fabrication methods one distinguishes different categories according to the phase of the deposited material. Waveguide fabrication methods based on modification of the substrate material can be regarded as a separate group. The following table 4.1 presents an overview of these techniques. More detailed information can be obtained in the theses of [Bur02, Rab04, Kuz06]. The pulsed laser deposition (PLD) technique has been the standard method for this work and will be described in detail in this chapter. It can be categorized as re-sublimation method, meaning that the film growth occurs in the gas phase.

Category	**Fabrication Method**
Solid	Direct Bonding Thermal Bonding
Liquid	Liquid Phase Epitaxy (LPE) Sol-Gel Process
Gas / Plasma	Chemical Vapor Deposition (CVD) Molecular Beam Epitaxy (MBE) *Pulsed Laser Deposition (PLD)* Sputtering Thermal Evaporation: Resistive Heating Electron Beam Evaporation (EBV) Ion Assisted Deposition (IAD)
Modification of Material	Indiffusion Ion Exchange Ion Implantation Direct Laser Writing Reactive Ion Etching

Table 4.1: *Film fabrication methods and waveguide structuring techniques.*

The history of pulsed laser deposition (PLD) began in 1965 when Smith and Turner demonstrated the deposition of thin films by ablating material with a pulsed ruby laser [Smi65]. Not long before, in 1962, Breech and Cross had shown that material could be ablated by laser radiation [Bre62] – laying the foundation for the development soon to come in 1965. In the first PLD experiment, Smith and Turner were able to produce 'optically satisfactory' films of different sorts, like Sb_2S_3, ZnTe, and $PbCl_2$.

However, it was not before 1987 that stronger attention was drawn to PLD when Dijkamp et al. applied this technique to fabricate thin films of $YBa_2Cu_3O_{4-\delta}$ (YBCO), which was at that time considered a promising new high-temperature superconductor [Dij87]. The newly risen attraction was due to the successful demonstration of depositing a complex material like YBCO and because the degree of stoichiometric control in PLD was superior to the one achieved by evaporation or sputtering techniques. Today, pulsed laser deposition is not only employed to produce crystalline films of epitaxial quality but also to create nanostructures at atomic scale, combining for instance conductor and isolator materials. Also strong efforts are made to achieve improving waveguide materials by PLD.

The principle of PLD is quite simple as the technique is based on physical processes that arise from the impact of high-power pulsed laser radiation on solid targets, leading to the removal of partially ionized material from the impact zone (plasma). In short, the pulsed laser beam is focused on solid target material that is evaporated due to the deposited energy. The evaporated material expands from the target surface and is deposited on a substrate which is placed on the opposite side (cp. figure 4.1). Vacuum condition or reduced ambient atmosphere is required for the ablation process, since the ablated material can not reach the substrate under atmospheric pressure. The PLD process takes place far away from equilibrium and involves a large number of complex physical and chemical mechanisms with lots of variables. It should be emphasized that, in spite of the simplicity of the general idea and its realization, the processes taking place during ablation and deposition are complex and not fully understood up to now. Most of the research in this area is empirical due to the fact that analytical descriptions of the processes involved are extremely difficult.

A brief introduction to these mechanisms is given in this section, also referring to a variety of published articles and books analyzing this technique in more detail, e. g. [Bäu00, Chr94]. Two review articles dealing with the processes of pulsed laser deposition by K. L. Saenger are worth noticing [Sae93a, Sae93b]. Therein, a precise overview of the history of PLD is given as well as the physical mechanisms.

The deposition process can be subdivided into four stages:

1. Interaction of laser radiation with the target leading to ablation;
2. Spatial expansion of the ablation products (plasma) –
   including interaction and chemical reaction within the plasma;
3. Interaction of the ablation products with the substrate;
4. Nucleation and growth of thin film on the substrate surface.

A simplified scheme of these four stages is shown in figure 4.1. The different processes will be described in the following sections, as the properties like crystallinity, stoichiometry, and surface roughness of the obtained films are influenced by each stage.

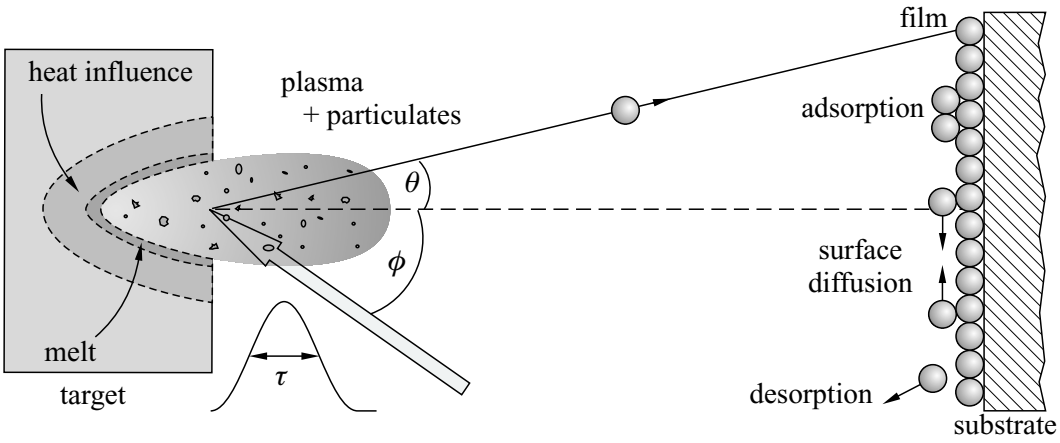

Figure 4.1: *Illustration of ablation and deposition processes [Bäu00, Sae93a]*

4.1 Laser-Target Interactions

The mechanisms of laser-induced material removal are almost entirely dependent on the target properties and laser parameters of wavelength, power density, and pulse duration. They can be identified in the limits of a continuum between 'thermal' and 'non-thermal'. In a simple thermal process the absorbed laser photons generate heat, which results in the vaporization of material. A removal of non-thermal kind can occur by several mechanisms, like the emission of atoms, molecules, and / or ions resulting from bond-breaking due to photon excitation of specific bonds. Sometimes these processes are categorized as 'desorption induced by electronic transitions' [Mat89]. It is also possible that materials nominally transparent to low power irradiation at a specific wavelength may be vaporized at higher power densities due to the presence of non-linear absorption mechanisms or laser-generated absorbing defect sites. Less useful for PLD are other mechanisms for material removal including 'hydrodynamic sputtering' and 'fracto-emission'. Target surface melt by laser energy and droplet ejection induced by transient shock or pressure waves are mechanisms referred to as hydrodynamic sputtering [Kel85]. If light particles, atomic particles, and sometimes macroscopic particulates are emitted from surfaces freshly fractured by thermal or mechanical stresses, fracto-emission takes place [Don88]. Exfoliation can be regarded as a variant of fracto-emission, in which macroscopic flakes of material detach as a result of repeated thermal shocks.

Laser-induced Breakdown

The laser radiation into a target of weak absorbing material such as dielectrics may lead to its destruction due to the energy transfer. This is known as *laser-induced breakdown*, describing the increase of the electron density in the conduction band N_e due to the laser irradiation [Blo74]. Consequently a larger number of electron-phonon interactions takes place leading finally to the destruction of the material if the critical value N_e^{cr} is exceeded. Depending on the material is the duration of the energy transfer between the excited electron system and the lattice τ_{e-ph}, being of the order of $1-100\,ps$.

The above described effect is based on 'free' electrons in the conduction band. These are present only in small numbers of $10^8 - 10^{10}\,\mathrm{cm}^{-3}$ in dielectrics [Blo74] and can be obtained in two ways when using high radiation intensities in the range of $10^{11} - 10^{14}\,\mathrm{W/cm}^2$:

1. By non-linear multi-phonon absorption leading to ionization (MPA),
2. By absorption of the laser radiation by present electrons in the conduction band (free-carrier-absorption) and subsequent avalanche ionization (AI).

In the latter case, the large electric field of the radiation accelerates the free electrons in the conduction band. The surrounding atoms are ionized by these high-energy electrons creating new free electrons that are also accelerated. The result is an avalanche-like production of electrons.

The following rate equation describes the time dependence of the electron density N_e in the conduction band in the near-surface region during the presence of a laser pulse with intensity $I(t)$ [Stu96]

$$\frac{\mathrm{d}N_\mathrm{e}}{\mathrm{d}t} = \underbrace{\varepsilon_\mathrm{av}\, I(t)\, N_\mathrm{e}(t)}_{\mathrm{AI}} + \underbrace{\gamma_m\, I^m(t)}_{\mathrm{MPA}}\,, \tag{4.1}$$

with ε_av denoting the avalanche coefficient, γ_m being the multi-phonon absorption coefficient for the absorption of m photons, and m being the minimum number of photons for a transition between valence band and conduction band. An important experimental parameter is the threshold intensity I_thr for which the critical electron density N_e^cr is reached. Because the laser fluence Φ is defined as the total energy per unit area per pulse

$$\Phi = \int_0^\tau I(t)\,\mathrm{d}t\,, \tag{4.2}$$

it is obvious with regard to equation 4.1 that the threshold fluence is independent of the pulse duration τ, thus having a constant value if only considering the avalanche ionization;

$$\Phi_\mathrm{thr}(\tau) = \frac{1}{\varepsilon_\mathrm{av}} \ln\left(\frac{N_\mathrm{e}^\mathrm{cr}}{N_0}\right)\,. \tag{4.3}$$

Though assuming a square-wave pulse, in the case of pure m-photon absorption the threshold fluence scales with $\tau^{\frac{m-1}{m}}$. This underlines the importance and the gain of an experimental determination of Φ_thr in order to obtain a more detailed insight into the physical mechanisms leading to damage in dielectrics.

In case of long pulse durations with a laser-target interaction being in the range of nanosecond pulses, the heating of the lattice during the pulse has to be considered ($\tau \gg \tau_{\mathrm{e-ph}}$). Changed plasma properties are the result because of the expanding plasma interacting with the incoming laser beam (shielding effect) and this leading to a reduced energy transfer into the target.

Under the premise of nanosecond pulses with $\tau \gg \tau_{\mathrm{e-ph}}$ being valid, the material removal caused by heat will be briefly investigated in the following.

Heat-induced Material Removal

Through electron-phonon coupling the deposited energy leads to the heating of the target material. By assuming that the laser irradiance I on the target has a constant power density per unit area during the pulse duration τ, one can investigate the maximum surface temperature and the volume of the heated region. These two quantities are indicators of probability and amount of target vaporization and depend on the optical properties of the target, namely the reflectivity $R(\lambda)$ and the absorption coefficient $\alpha(\lambda)$, and on the thermal properties of the target, namely the specific heat C_v, the vaporization energy ΔH_v, and the thermal conductivity K.

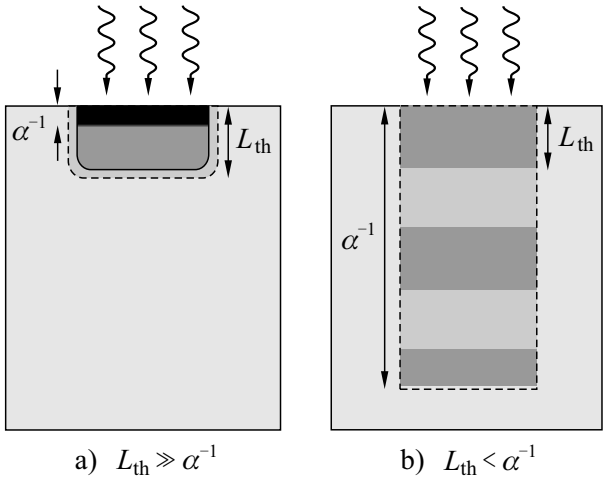

Figure 4.2: *Scheme of radiation absorption and target heating. The deposited heat at the end of the laser pulse is confined approximately to the region within the dotted lines.*

The heating mechanism is characterized by the thermal diffusion length L_th of the target which is related to the thermal diffusivity $D_\mathrm{th} = K/\varrho\, C_\mathrm{v}$ by

$$L_\mathrm{th} = \sqrt{2D_\mathrm{th}\tau} = \sqrt{2\frac{K}{\varrho\, C_\mathrm{v}}\tau} \qquad (4.4)$$

and describes the spatial extension of the heat influenced zone, in which the temperature is reduced by a factor of $e^{-1/2}$ with respect to the maximum value [Sae93b].

The target surface peak temperature responsible for evaporation and thus ablation of material can be estimated by the two limiting cases of very strong and very weak absorption (cp. figure 4.2).

Considering the first case (a), the optical penetration depth α^{-1} is small compared to the thermal diffusion length, i. e. $\alpha\sqrt{2D_\mathrm{th}\tau} \gg 1$. Since the laser wavelength for PLD is often chosen to coincide with strong target absorption, this case covers many of the materials deposited by PLD. As this strong absorption occurs in the UV region for most of these materials, excimer lasers at either 248 nm (KrF) or 193 nm (ArF) are favored for the ablation process.

The thermal diffusion length for a 20 ns pulse are typically of the order of 1-2 µm for silicium as well as for many metals, while the α^{-1} values for visible wavelength are usually a factor of 10^2 lower. Thus, for $L_\mathrm{th} \gg \alpha^{-1}$ the fluence absorbed during the laser pulse, $(1-R)I\tau$, is used to heat a layer of thickness L_th. The average temperature rise in this layer, with $\varrho\, C_\mathrm{v}$ being the heat capacity per unit volume, is given by [Sae93b]

$$\Delta T \simeq \frac{(1-R)I\tau}{\varrho\, C_\mathrm{v} L_\mathrm{th}} = \frac{(1-R)I\tau}{\varrho\, C_\mathrm{v}\sqrt{2D_\mathrm{th}\tau}}\,. \qquad (4.5)$$

Regarding for example the sesquioxides described in this thesis, the thermal diffusion length can be calculated using equation 4.4 with the material parameters in table 2.1 and

a pulse duration of $\tau = 15\,\mathrm{ns}$. As no values are available for C_v, C_p is used instead and since $C_\mathrm{p} \leq C_\mathrm{v}$[1], the lower limit of L_th is determined to be

$$L_\mathrm{th} = \sqrt{\frac{2K\tau}{\varrho\, C_\mathrm{v}}} > \sqrt{\frac{2K\tau}{\varrho\, C_\mathrm{p}}} \approx 30\,\mu\mathrm{m}\,.$$

The optical absorption depth α^{-1} for the KrF-laser can be estimated by an absorption spectrum ($\alpha^{-1} \ll 10\,\mu\mathrm{m}$) [Mix99], whereas the values of n and k are calculated by [Pal85]. The relation between α and k is [Bor75]

$$\alpha = \frac{4\pi k}{\lambda}\,, \tag{4.6}$$

resulting in $\alpha^{-1} \approx 46\,\mathrm{nm}$ at $\lambda = 248\,\mathrm{nm}$ and $k = 0.427$.

The optical absorption length α^{-1} in the other case (b) is larger than the thermal diffusion length, i. e. $\alpha\sqrt{2D_\mathrm{th}\tau} < 1$. An exponential temperature profile along the depth z is created by the absorption of radiation that corresponds to the absorption profile, i. e. [Sae93b]

$$\Delta T(z) = \frac{(1-R)\,\alpha\, I\, e^{-\alpha z}\tau}{\varrho\, C_\mathrm{v}}\,. \tag{4.7}$$

As described by this equation, the heat is rapidly transported away from the ablation area. This leads to melting and, in some cases, to the evaporation of the target material, both preventing the desired congruent evaporation. At very high fluences even the superheating of a large volume due to large absorption depths is possible. This heating results in molten droplets or particulates as the heated volume will be transformed into the melting phase and ejected from the surface due to rapid expansion.

However, in both cases (a) and (b) macroscopic material removal by vaporization is expected if the heat absorbed per unit volume exceeds the energy density corresponding to the latent heat of vaporization, $\varrho\,\Delta H_\mathrm{v}$. In the first case (a) the condition yields that a threshold fluence of

$$\Phi_\mathrm{thr} > \frac{\varrho\,\Delta H_\mathrm{v}\, L_\mathrm{th}}{(1-R)} \tag{4.8}$$

has to be reached before material vaporization to a depth L_th is initiated. Though, the experimentally observed threshold values might be lower than the calculated ones, due to the non-perfect target morphology. Non-homogeneous evaporation mechanisms (ablation of clusters or particles, multiple pulse effects) also affects the threshold fluence and is responsible for differing experimentally observed values Φ_thr.

As a direct consequence of one-dimensional heat flow for pulse durations $> \tau_\mathrm{e-ph}$, the equations 4.4 and 4.8 show that the threshold fluence Φ_thr defined in equation 4.2 is proportional to $\sqrt{\tau}$ for vaporization. It becomes obvious in this relation that in using very short pulse-lasers with pico- or femtosecond pulses instead of nanosecond pulses either the same material vaporization should be possible at lower laser fluences or higher

[1] C_v equals C_p solely for $T = 0$

vaporization rates should be accessed for identical fluence. Nevertheless an implication of fs-lasers being more suitable for the ablation of material would be wrong because, as it is shown in the following, the interaction of the laser pulse with the developing plasma can also have beneficial effects on the plume species.

Influence of Target Morphology

The material removal is affected by the target surface and its morphology in various ways. The expanding vapor plume has a preferred direction being perpendicular to the target surface, as section 4.2 will show in detail. A rough surface will cause the direction of the plume to change during the ablation process, resulting in non-uniform films on the substrate. Another problematic occurrence is the change of the target morphology after irradiation with many laser pulses due to recrystallization or development of macroscopic features such as craters. A bending of the plasma plume towards the incident laser beam is caused by structures like this, which again will lead to non-uniform material deposition [Bäu00].

Thermal properties are additionally influencing the ablation process. Though being of the same material, the thermal diffusion length may vary regarding a sintered target versus a single-crystal. Bulk materials as single-crystals or amorphous materials are usually applied as targets in order to reduce the generation of particulates. Nevertheless, if the corresponding bulk material is transparent to the laser length, a compressed and sintered powder target may be preferred. The absorption of the target will then be enhanced by scattering effects [San85].

Stoichiometry of Removed Material

In pulsed laser deposition the material flux from the target usually matches the target stoichiometry. This 'congruent' vaporization, pertinent to targets which incorporate multiple components like Eu:$(\mathrm{Gd},\mathrm{Lu})_3\mathrm{AL}_5\mathrm{O}_{12}$, is a very important benefit of the pulsed laser deposition technique. It is explained by the pulsed laser heating, which is a highly non-equilibrium process. A very high heating rate ($10^8\,\mathrm{K/s}$) of the surface is caused by the pulsed ns-laser irradiation due to the large optical absorption coefficient and, in the case of sintered material, due to the poor thermal conductivity [Bec88]. Thus, qualitatively explaining, material removal occurs before the individual components of the target material can segregate into low and high vapor pressure components [Che88].

Particulate Generation

The deposition of particulates which are produced together with the vapor during the ablation process is one of the major drawbacks of PLD. These particulates, ranging from several hundred nanometers to a few tens of micrometers in size, are responsible for poor film quality because of their adverse effect on the growth of the subsequent

layers. There are various reasons for the appearance of particulates. Some mechanisms for particulate production are illustrated schematically in figure 4.3.

- In the *splashing effect* (a), a sub-surface layer of the target superheats above its vaporization temperature and blows off the molten overlayer resulting in liquid droplets. Heat removal by evaporation can only occur at the top surface, therefore the maximum temperature in the solid lies below the surface. This mechanism was first proposed by Ready [Rea63] and has then been examined further by other authors. In contrast, Miotello and Kelly have shown that absorption in combination with surface evaporation does not lead to sub-surface layer superheating [Mio95].

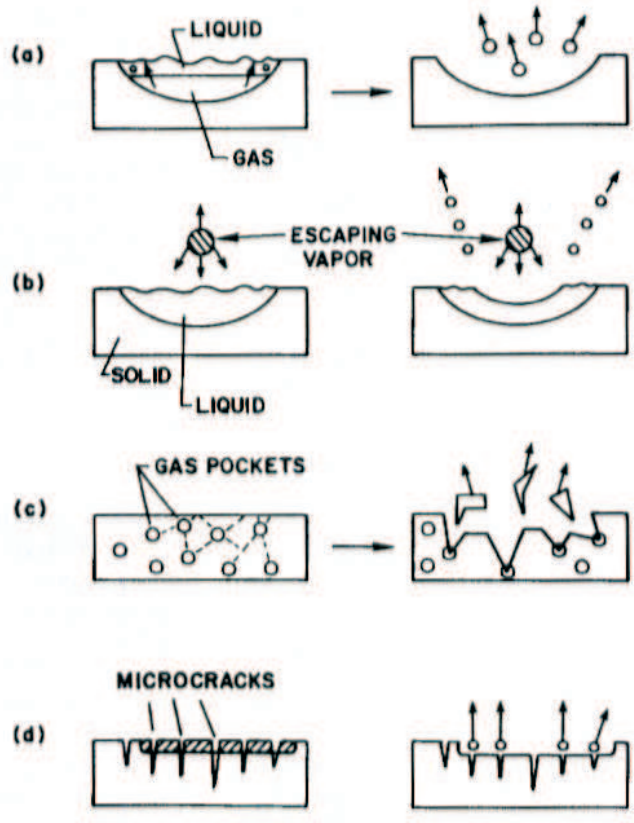

Figure 4.3: *Mechanisms for particulate production: (a) splashing, (b) recoil pressure, (c) target outgassing and (d) fracto-emission [Sae93b].*

- The *recoil pressure mechanism* (b) for particle production resembles splashing. Vaporized material that leaves the target surface acts like a piston, forcing the liquid droplets to be ejected from the periphery of the molten 'lake' produced by the laser irradiation [Sae93b].
- In the case of *target outgassing* (c), an expansion of encapsulated gas leads to the ejection of particles from the sintered target, whereas the emission of particles from microcracks in the target is referred to as *fracto-emission* (d). Both effects can be minimized if single-crystal targets are used instead of sintered ceramics.

Koren et al. investigated a strong dependence between the size / content of the particulates and the wavelength used for ablating the material [Kor89]. For shorter laser wavelengths, a reduction of the particulates in size and density can be observed. This wavelength-dependent effect can be explained by the reduced energy deposition depth. Consequently, a thinner layer at the surface reaches the ablation threshold and a hotter plume of finer species develops.

There is a necessity in irradiating different parts of the target surface with each laser shot in order to avoid problems associated with changes in the composition of the target

surface [Auc88, Coh91] or with crater formation in the target, which results in a skewed plume direction and a higher concentration of particulates [Bec88]. Different techniques have been developed to achieve this, like rotating the target while keeping the laser spot in a fixed position slightly displaced from the rotation axis resulting in ring-shaped ablation tracks. Another option can be found in scanning the laser beam over the target surface by using mirrors to control this laser scan while keeping the target in a fixed position.

As this brief overview made clear, there is a variety of processes involved in particulate generation. This implies even more complexity due to the fact that these processes may be operative at the same time [Ugl77]. Thus, no 'simple' correlation between film particulate content and target thermal properties could be found [Dup89]. However, a good possibility to eliminate particulates is given by a high-speed velocity filter due to the velocities of particulates being one order of magnitude smaller than those of atoms and ions [Dup89, Bar69].

4.2 The Plasma Plume

The previous section described the absorption of the incident laser radiation by the target leading to the evaporation of material. Initially, this hot and dense vapor is confined to a very small volume near the target surface that may contain many species as atoms, molecules, ions, free electrons, and in some cases also large particulates. Once the content of charged particles in this vapor exceeds a critical value, it is called plasma, being of quasi-neutral manner in general with as many positive charges as negative ones.

Applying the Boltzmann distribution in order to derive the degree of ionization in thermal equilibrium, i. e. the ratio of the density of ions n_i and the density of neutral atoms n_0, the Eggert–Saha equation can be obtained [Egg19, Sah21]

$$\frac{n_i\, n_e}{n_0} = 2\,\frac{g_i}{g_0}\left(\frac{2\pi m_e kT}{h^2}\right)^{3/2} e^{-W_i/k_B T}\,. \tag{4.9}$$

In this equation n_e denotes the electron number density, m_e the electron mass, k_B is the Boltzmann constant, h is Planck's constant, and g_i as well as g_0 are the statistical weights for the electron-ion pair and the neutral atom, respectively. W_i is the ionization potential, i. e. the energy necessary to remove an electron from an atom.

The equation 4.9 of Eggert–Saha is derived on the premise of isolated and non-interacting atoms. Thus, its applicability does not include high plasma densities, in which the effective ionization energy is lowered by the overlap of the neighboring ion potentials. Consequently the degree of ionization is higher than predicted by equation 4.9. Another limitation of the Eggert–Saha equation is the counter case of having low densities, in which the condition of a thermodynamic equilibrium may not be fulfilled.

Although there is no thermodynamic transition defined between the gas phase and the plasma phase in general, equation 4.9 reveals that at temperatures of several 1000 K the degree of ionization increases from nearly 0 to 1. Assuming typical values of $W_i \approx 10\,\mathrm{eV}$

and $T \approx 10\,000\,\mathrm{K}$, the plasma is initially characterized by neutral particle densities of $10^{19} - 10^{20}\,\mathrm{cm}^{-3}$ and electron densities of $10^{17} - 10^{20}\,\mathrm{cm}^{-3}$ [Sae93b].

Laser-Plume Interactions

The interaction between the expanding plasma and the incoming radiation has to be considered at laser pulse durations of the order of nanoseconds. This may have negative as well as positive effects on the film growth process.

It has already been mentioned in section 4.1 that the fraction of laser fluence reaching the target can be attenuated by these laser-plume interactions. This should be taken into consideration when using laser fluences high above the threshold fluence, whereas at fluences near the threshold value the plasma plume size is very small and the plasma localizes at the substrate surface. An increasing of the fluence leads to a larger ablation volume and consequently results in an enlarged and denser plume, which interacts strongly with the incident laser radiation before reaching the target. If sub-picosecond pulses are used, these interactions are ignorable due to plasma velocities of $\lesssim 10^6$ cm/s [Bäu00].

Nevertheless, it is also possible that these interactions have a positive influence on the deposition process in modifying the composition of the plume species. As the dissociation, ionization and/or electronic excitation of the atoms and molecules in the plume is possible due to the absorption of one or more laser photons, the relative amount of ions increases with respect to neutral molecules and atoms. Free electrons in the plume can also be heated by the *inverse bremsstrahlung* [2] in which the absorption of a laser photon increases the electrons' kinetic energy in a collision process.

Plasma Expansion

Investigating the plasma expansion, its general dynamic behavior is comparable with the dynamics of a free-jet adiabatic expansion [Kel92, Zhe89]. A highly forward-peaked material flux and an average particle speed many times higher than the mean random thermal speed characterize both expansions. It is the kinetic energy of the arriving plume species that is regarded as one of the key parameters of film growth on the substrate. In thermodynamic gas theory this can be described by temperature. The local temperature

[2] The term 'bremsstrahlung' refers to emitted radiation by charged particles under decelerations when passing through the field of atomic nuclei. With m denoting the rest mass of the particle, the energy emitted by an accelerated particle is proportional to $1/m^2$, which is the reason why bremsstrahlung plays an influential role for light particles such as electrons. Thus, scattering of two electrons results in emission of radiation (1) and the inverse process termed 'inverse bremsstrahlung' can occur using intense radiation (2)

$$e^- + e^- \rightarrow e^- + e^- - \Delta E_{\mathrm{kin}} + h\nu \qquad (1)$$

$$h\nu + e^- + e^- \rightarrow e^- + e^- + \Delta E_{\mathrm{kin}} \qquad (2)\,.$$

In the latter case, a photon is absorbed and the kinetic energy of the electrons is increased correspondingly.

$T(z)$ and density $n(z)$ are related to

$$\frac{T(z)}{T_0} = \left[\frac{n(z)}{n_0}\right]^{\gamma-1} , \tag{4.10}$$

when assuming the adiabatic expansion of a high-pressure gas and the one-dimensional character of the expansion. Therein, T_0 and n_0 are the initial temperature and density, and $\gamma = C_\mathrm{V}/C_\mathrm{p}$ is the ratio of constant volume and constant pressure specific heats. It is estimated that in laser-produced plasmas with temperatures up to $10^5\,\mathrm{K}$ γ is about 1.2 - 1.3 [Sin90, Sae93b]. A fall-off regarding the temperature as well as the density of the plume can be observed during the spatial plasma expansion, the latter as the inverse cube of the distance from the target, i. e. $n(z)/n_0 \propto d^{-3}$, in a simplified spherical model [Sin90].

Thus, the collision rate of the plume species decreases and the random kinetic energy of the particles is converted to a directed motion away from the target. This behavior is not valid for effusive sources, e. g. in EBV processes. It can only be applied to supersonic sources, such as laser-produced plasmas.

Effects of the Background Gas

The expansion of the plume is not completely described by the considerations made in the last section, as the expansion strongly depends on the presence of a background gas often used during the deposition process. Any type of background gas significantly influences the plume transport and its appearance. The scattering of the plume species, for example, reduces the velocity and amount of material reaching the substrate. Another example are chemical reactions that change the initial composition of species, result in different optical emission characteristics and finally change the shape of the plume due to physical confinement.

Reactive oxygen has been used as background gas for all depositions presented in this thesis. Consequently, when growing a sesquioxide such as Y_2O_3, the formation of Y^* and YO^* takes place with the asterisk indicating electronic excitation [Dye91]. The latter byproduct YO^* is not an effect of the ablation process, but directly related to the exothermic $Y + O_2$ plasma-background gas reaction. These transformations all have an effect on the growth mechanism of the substrate–film. Having very low oxygen pressure or even an inert atmosphere during the deposition of oxides like Y_2O_3, the grown films are in general not matching the correct stoichiometric composition inter alia due to oxygen deficiencies.

After the plume-dynamics have been successfully described by K. L. Sänger using the similarity to adiabatic supersonic expansion of gaseous jets and giving an explanation of the plume angular distribution [Sae89], Bulgakov and Bulgakova have developed a simplified model for the plume expansion in an ambient gas [Bul98]. It is based on the theory of a supersonic jet that is formed when a high-pressure gas streams through a nozzle into a low-pressure gas, thus being also termed ‘underexpanded jet’.

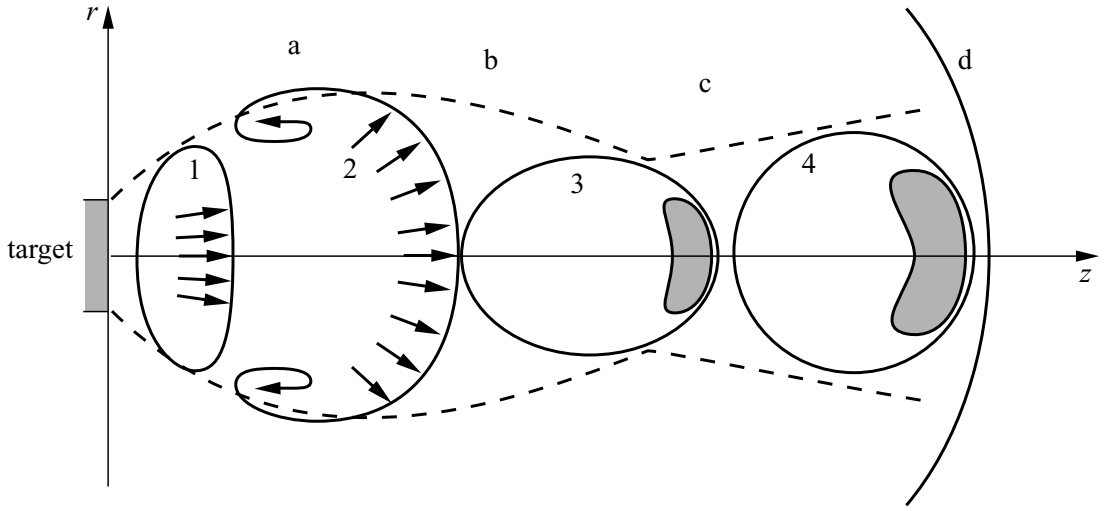

Figure 4.4: *Different stages of plasma expansion in a background gas environment. (1)-(4) indicate the consecutive positions of the plume; (a) denotes the vortical motion arising at the plume periphery; broken line (b) shows the motion of the plume boundary point farthest from the plume axis z; (c) are the regions with the pressure increase in the front part of the plume and (d) is the shock wave ahead of the plume [Bul98].*

There are two physical regimes which the gas-dynamic behavior of the plume can be divided into and which can be observed during the ablation process: first a nearly spherical plume expansion and second a mainly forward directed plume. Thus, the flow of the ablated particles is aligned with the plume axis. The two expansion regimes are both directly connected to the chosen experimental conditions. Short laser pulses with $\lesssim 20\,\mathrm{ns}$ and large spot radii of $\gtrsim 1\,\mathrm{mm}$ characterized the deposition setup which was used in the experiments. In this case the forward directed plasma is the result, with the initial form of the plume being like a thin disc under these conditions. The expansion of the plasma is illustrated in figure 4.4.

A broadening of the disc-like cloud along the disc axis is observed when moving away from the target. This is due to the velocity distribution of the particles and perpendicular to the axis because of the plasma underexpansion (position 1 in figure 4.4). The plasma cloud slightly overexpands after passing the region in which the cloud pressure becomes equal to the one of the background gas (position 2). Now the plume size decreases (position 3) and the plasma passes the pressure equilibrium once more. Its pressure exceeds the pressure of the background gas, and the plume re-expands (position 4) with the same velocity as the background gas in the shock front, illustrated by line (d) in figure 4.4. Being generated by the rapid plume expansion at the beginning, the shock front can be described analogously to the *Mach disk* observed in supersonic[3] molecular beams. The increasing interaction

[3] The ratio of the flow velocity u to the local speed of sound a is known as the Mach number $M \equiv \frac{u}{a} = u(\frac{\gamma kT}{m})^{-1/2}$. Expansions with $M > 1$ are termed *supersonic*.

with the background gas finally stops the plume expansion with

$$R_{\max} \sim \left(\frac{m_{\mathrm{abl}} E}{\pi \rho_b p_b} \right)^{1/6} \tag{4.11}$$

giving the maximum propagation length of the plume from the target $R_{\max}$ in a background gas of mass density ρ_b and at pressure p_b [Bul95]. In this formula, m_{abl} is the ejected mass and E the absorbed laser energy. The deposition will proceed by diffusion resulting in low deposition rates, if the final propagation length of the plume is shorter than the target-substrate distance.

The regions (c) in figure 4.4 show that the particle flow is decelerated during the expansion process by the background gas leading to an increased pressure in the front part of the plume. It can be assumed that at this stage a mixing of the cloud material with the ambient gas takes place [Ani83] resulting in the strong red YO^* chemiluminescence, which can be observed in experiments dealing with yttrium compounds [Fri93].

Plume Angular Distribution

Usually, the plume is oriented along the surface normal of the target, as depicted in the model of the plume expansion in an ambient gas. Since the irradiated surface of a perfectly planar, isotropic target has no 'memory' of the direction from which the absorbed photons originated, this is also valid for non-normal incident laser radiation. Because real targets are not perfectly planar in most cases, the plume tilting cannot be avoided in practice. One has to take into account too that the laser beam intensity profile may be asymmetric or non-uniform. A good illustration is a hot spot at the center of the laser beam profile, introducing asymmetries in target irradiance due to the shadowing effects of the denser plasma above the corresponding hot spot on the target [Sae93b].

Different contributions to the plasma distribution with distinct physical origins can be related besides these experimental deviations of the plume direction. It is possible to treat the source of the evaporation, i. e. the irradiated spot on the target, as a small area effusive source. It is defined by the ratio $d/h \ll 1$ with d representing the diameter of the source (approximately the laser spot size) and h denoting the target-substrate distance. The emission distribution of such source is described by a $\cos\theta$ law [Mai83].

As the single cosine fit holds only for the broad structure seen in the plume angular distribution, the enhanced forward peaking of the plume is commonly approximated by a $\cos^n\theta$ function. Therein, the values for the exponent range between $1 < n \leq 200$. In application, a superposition of a cosine and a $\cos^n$ function in the following form is used to fit the angular distribution:

$$a\cos(\phi - \varepsilon) + b\cos^n(\phi - \varepsilon)\ . \tag{4.12}$$

It is this two-component structure usually being applied to all species, neutral atoms and ions, in the plasma plume though A. Thum-Jäger and K. Rohr [Thu99] found out that the angular profiles depend on the degree of ionization and that for ions with a charge

$q \geq 2$ the emission can be well described by a single $\cos^n$ fit. For species of different mass the shape of the distribution varies, observing a relative enrichment of the lower mass elements near $\theta = 0$.

As a possibility the narrow angular distribution of the ejected plume towards the substrate may lead to high deposition rates, preventing extensive chamber contamination. However, this can result in non-uniform film thickness and inhomogeneous stoichiometries over large deposition areas, which are major drawbacks of pulsed laser deposition.

5 Lattice Matched Thin Films

Thin films can show a different behavior in comparison to bulk crystals of the same chemical composition. This would indicate a different inner structure. Film growth on a substrate can be of epitaxial, polycrystalline or amorphous kind. The structures arising during this process may be homogenous, pillar-like or porous. These structures do not absorb light as they measure some tens of nanometers [Flo04]. However, they may strongly influence the optical properties of the grown film. The mechanical properties and the long-term stability are also of influence.

The fabrication of epitaxially grown crystalline dielectric oxide films is of great technological interest as these materials may be used as active waveguide devices, compact microlasers [Gri04], and as crystalline coatings in a thin-disk laser setup [Kuz06]. For all these applications high-quality thin films are required. Film quality is mainly determined by the interface between the substrate and the grown film. Thus, lattice matching in film growth and its requirements will be thoroughly explained in the following sections.

Another objective in film growth is that the refractive index difference of substrate and film should be preferably high. Even though a great difference between the refractive indexes is advantageous for waveguide usage [Bur02, Bär04, Kuz06], this usually presupposes the epitaxy of different materials with varying lattice constants and structures. In turn, non-epitaxial growth is induced, including stress in the film and point defects, especially at the interface between the substrate and the grown film. In the case of perfect lattice matched films no interface defects are expected and thus high-quality crystalline growth can be obtained, which is beneficial for waveguide materials as well as for crystalline coatings.

As it is the aim of this thesis to investigate crystalline film growth using various lattice matched systems, this chapter first deals with growth mechanisms and particularly with epitaxial growth in section 5.1. In section 5.2 different crystal structures are presented with the possibilities of combining them. Thereby, different ways to achieve lattice matching are shown. Section 5.3 presents the investigated substrate–film systems.

5.1 Growth Mechanisms

The term epitaxy (Greek; epi 'above' and taxis 'in ordered manner') describes an ordered crystalline growth on a monocrystalline substrate. Therein, the substrate can be regarded as seed crystal and its lattice structure and orientation are continued by the deposited film. Three forms of epitaxial growth are distinguished[1] in the course of this work:

i) **Homoepitaxy**: Epitaxial growth performed with only one material. Here, a crystalline film is grown on a crystalline substrate or film of the same material, for instance Eu:Y_2O_3 grown on Y_2O_3. It is evident that the dopant is not considered since its concentration is very low.

ii) **Quasi-Homoepitaxy**: Epitaxial growth performed with materials of the same class, in which only one component is replaced by another or, in order to achieve perfect lattice matching, by two species. However, these changes do not affect the material properties significantly as all the replaced species belong to the same chemical group, e. g. Eu:Lu_2O_3 or also Eu:$(Sc_{1-x}Lu_x)_2O_3$ grown on Y_2O_3.

iii) **Heteroepitaxy**: Epitaxial growth performed with materials that are different from each other. In this case, a crystalline film is grown on a crystalline substrate or film of another material class, for instance Eu:Y_2O_3 grown on α-Al_2O_3.

When the pulsed laser deposition technique (cp. chapter 4) is employed in film growth, the kinetic adsorption and diffusion processes of the plume species on the substrate surface result in thin-film formation. Nucleation, coalescence, and subsequent thickness growth are intermediate states of this thin-film formation and can all be influenced by the deposition parameters. The mechanisms underlying nucleation and film growth are summarized in this section. More detailed descriptions can be found in [Kai02, Met94].

High degrees of supersaturation (10^5 J/mole) and ionization as well as a high kinetic energy of the plume species characterize the vapor in pulsed laser deposition, which is responsible for film growth on the substrate. Initially, these energies range from 10 to several 10^4 eV, depending on the laser parameters and the used background gas. When these high-energy species hit the surface they affect the film growth. They can either improve or deteriorate the overall morphology, stoichiometry, and microstructure of the growing film. In the worst case, the occurrence of bond-breaking generates subsurface vacancies and displacement or removal of atoms. However, at energies which are usually achieved during the deposition process, the kinetic energy of the species enhances the surface diffusion of adsorbed atoms; the adatom diffuses through several atomic distances on the substrate until it sticks to a stable position within the forming film. If the bonding forces between the atoms do not suffice, the atoms are abandoned from the surface. Referred to as desorption effect, it depends on the substrate surface condition but also on the atom character. It can be concluded that the surface morphology during the growth process is

[1] Despite varying definitions in literature, the subdivisions of epitaxy chosen in this thesis are beneficial due to structural consideration.

determined by interaction of deposition, diffusion, and desorption. Figure 5.1 illustrates the various atomic processes which may occur during film growth. The morphology of the grown film is determined by these interactions.

When a background gas is used during the deposition process, the plume species undergo collisions not only within the plasma but also with the ambient gas. These collisions reduce the ion fraction as well as the kinetic energy of the evaporated target material. Thus, it is possible that the energy of the species is reduced to thermal levels when reaching the substrate and the adatoms lack sufficient mobility to migrate to the correct lattice site. For the right crystalline structure to emerge, substrate heating is required in order to increase the adatom mobility at the substrate surface (cp. chapter 6.1).

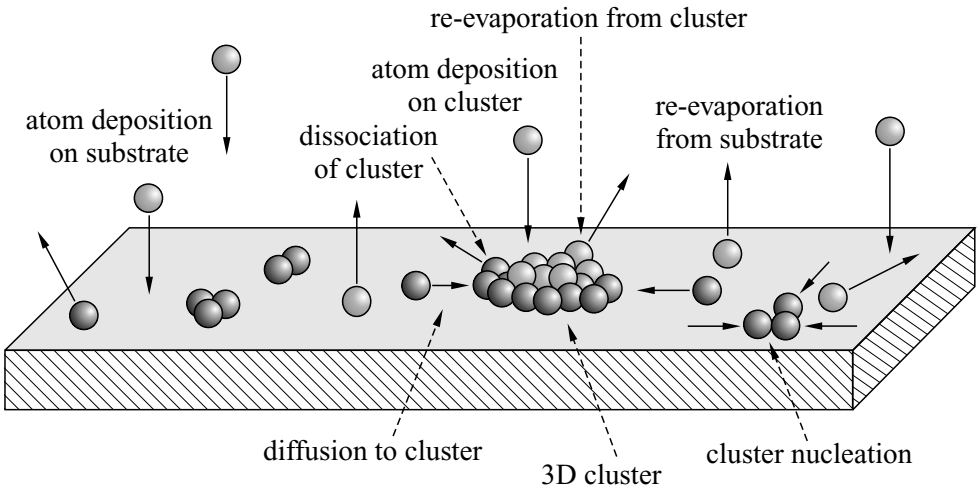

Figure 5.1: *Possible mechanisms during film growth*

Taking the ratio of the substrate temperature T_{sub} and the melting temperature of the material T_{m} as an indicator, different ranges of $T_{\mathrm{sub}}/T_{\mathrm{m}}$ can be distinguished with different basic processes being dominant. This concept has been extended to the *structure zone model* that expects the real structure to be made up of three zones [Kai02]. The first zone is characterized by lower substrate temperatures, i. e. $T_{\mathrm{sub}}/T_{\mathrm{m}} < 0.3$. Consequently, the adatoms have only low mobility and stick to the substrate in which they impact on the surface. A fine-grained porous structure is the result in this case. The temperature region $0.3 < T_{\mathrm{sub}}/T_{\mathrm{m}} < 0.5$ corresponds to activation energies of $0.1 - 0.3\,\mathrm{eV}$, which leads to surface diffusion and finally a columnar structure. The growth of large crystalline grains is facilitated by bulk diffusion at high substrate temperatures $T_{\mathrm{sub}}/T_m > 0.5$. Continuative considerations are made in chapter 6.1 based on equation 6.3. However high temperatures T_{sub} in combination with large film thicknesses may result in the process of recrystallization, completely changing the crystal orientation, or in a phase transition.

Better crystal structures are in general obtained by higher substrate temperatures. This is regarded valid until reaching a point in which re-evaporation of the more volatile elements in the film will result in non-stoichiometric growth. However, the formation of the nuclei and their growth does not only depend on the substrate temperature but mainly on the interaction energies of substrate and film atoms. Since flat surfaces without defects do

not exist in nature, defects, e. g. dislocations, kinks, vacancies, and ledges, act as favored nucleation sites [Ven00]. Therefore, the initial stage of film growth is determined by the adatom bond strength to the substrate compared to the bond strength between its surrounding neighbors. Young's equation described the relation between the surface energy of the substrate γ_B and the surface energy of the growing film γ_A

$$\gamma_B = \gamma^* + \gamma_A \cos\varphi \ , \tag{5.1}$$

with γ^* denoting the film–substrate interface energy and φ the wetting angle of a nucleus on the substrate (cp. figure 5.2). Different modes of film formation (cp. figure 5.3) can be distinguished depending on these interaction energies [Bau58]:

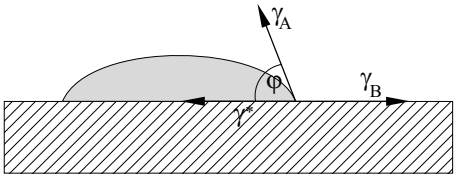

Figure 5.2: *Wetting angle φ of a liquid nucleus on a substrate*

a) **Layer-by-layer growth (Frank-van-der-Merwe mode)**: The interaction between substrate and film atoms is greater than between adjacent film atoms ($\gamma_B > \gamma_A + \gamma^*$) and the layers grow one on top of the other. The nucleation on the monolayer of order $(n+1)$ only takes place, if the monolayer of order n is entirely closed.

b) **Step-flow growth**: This is an alternative monolayer growth mode, which occurs if the diffusion energy is sufficiently high for the surface atoms to quickly move to the atomic step edges and perform step-bonding. This presupposes thermal substrate treatment (chapter 6.1) prior to deposition and requires the diffusion length to be greater than the atomic terrace widths ($l_D > L$).

c) **Island growth (Volmer-Weber mode)**: The interaction between film atoms is greater than between adjacent film and substrate atoms ($\gamma_B < \gamma_A + \gamma^*$). Consequently, separate three-dimensional islands are formed on the substrate.

d) **Layer-plus-island growth (Stranski-Krastanov mode)**: In this hybrid form of the above mentioned growth modes (a) and (c), one or two monolayers form first, followed by individual islands due to the increase of the interface energy with film thickness; typically the layer on top of the substrate is strained to fit the substrate's lattice constant.

Intensive research in the field of active opto-electronic elements consisting of island films has been carried out in recent years. The Stranski-Krastanov layer-plus-island growth

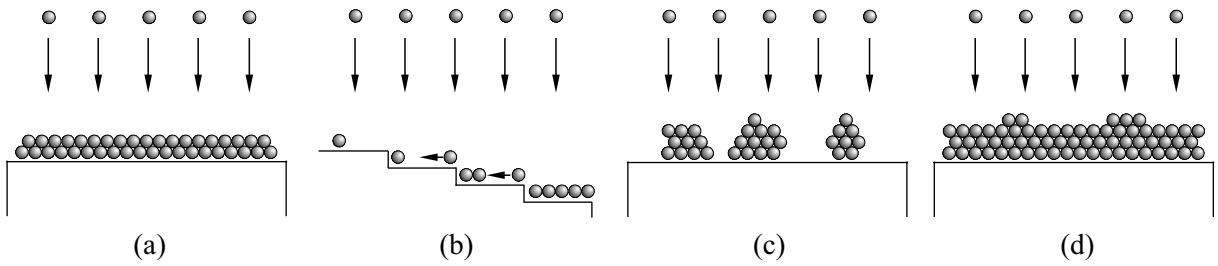

Figure 5.3: *Different modes of film formation: (a) layer-by-layer growth, (b) step-flow growth, (c) island growth, and (d) layer-plus-island growth.*

of Ge-islands upon Si-substrates for the production of self-assembled quantum dots may serve as an example of optically active molecules [Vin00].

The quality of epitaxially grown films is strongly influenced by the substrate, and in general, single-crystalline growth is only possible on substrates with a similar lattice spacing. The definition of the lattice mismatch f between film and substrate is given by

$$f := \frac{a_{0,\mathrm{f}} - a_{0,\mathrm{s}}}{a_{0,\mathrm{f}}} \,, \tag{5.2}$$

with a_0 denoting the lattice spacing and subscripts 'f' and 's' refer to the film and substrate, respectively. The crystal lattice of the substrate is continued in the growing film in cases of homoepitaxy and quasi-homoepitaxy and no dislocations and stress due to lattice mismatch are expected. A low rate of growth defects at the interface is necessary especially for waveguides, thus homoepitaxy or quasi-homoepitaxy is favored. With homoepitaxy, however, only a small difference in the refractive indices is achieved by the dopant, which is a major disadvantage for waveguides. As this alteration is of the order of $\Delta n \approx 3 \times 10^{-4}$ per percent of doping [Iva75], the growth of quasi-homoepitaxial films may offer a solution for this problem and enable higher refractive index deviations.

By heteroepitaxy an even higher Δn can be obtained (cp. table 5.1). Epitaxy between materials with different chemical character and lattice constant is possible, as Frank and van der Merwe have shown [Fra59]. In this growth process, which is termed *pseudomorph*, the lattice parameters of the growing film fit to the substrate lattice constant by elastic deformations in the potential field of the substrate. Different types of stress can be distinguished, depending on the lattice constant of the deposit compared to that of the substrate: compressive stress ($a_{0,\mathrm{f}} > a_{0,\mathrm{s}}$) and tensile stress ($a_{0,\mathrm{f}} < a_{0,\mathrm{s}}$).

Usually in the case of small lattice mismatch and small film thickness elastic deformation occurs. The stress in thin films of a few monolayers can accommodate lattice mismatches of up to 7% depending on the used materials and their properties. However, with increasing mismatch and film thickness the formation of a substrate–film interface due to point defects and dislocations becomes energetically favorable in order to relax stress. If the film cannot compensate the stress by elastic deformations, it relaxes partly or completely (cp. figure 5.4). As these plastic deformations are often of irreversible kind and lead to the Stranski-Krastanov growth mode, this results in polycrystalline film growth or the growth of small 'micro-crystallites' [Tan98].

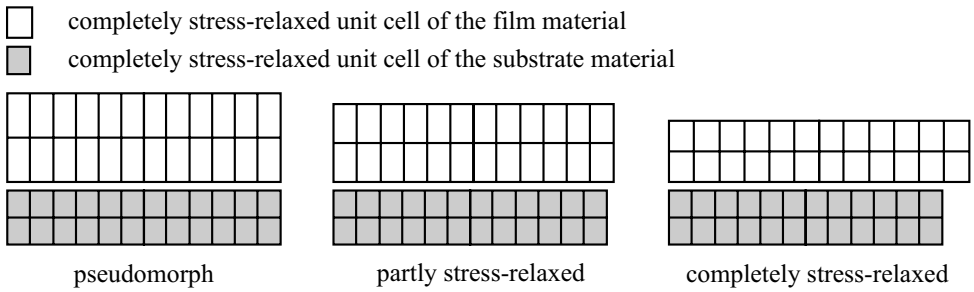

Figure 5.4: *Schematic illustration of elastic (pseudomorph) and plastic deformations (stress-relaxed) during the initial states of film growth.*

It has been observed that in some systems the orientation of the substrate for the growth of a certain crystalline phase is not of primary importance. In these cases polycrystalline growth [Che01] or even single-crystalline growth [Hu96] may be possible on completely amorphous substrates if enough adatom mobility is provided. This growth mode, observed in yttria films on silica [Pon02, Zha98], can be regarded as an exception which only occurs if a certain growth direction is energetically heavily favorable compared to elastic and plastic deformation [Seo02]. Regarding this unusual growth behavior one can conclude that there is no general rule to predict the film growth based solely on the value of the lattice mismatch. Besides the lattice parameters, many variables such as the mechanical properties of substrate and film material as well as the formation energies of different dislocations, have considerable influence and play an important role in the film growing process.

5.2 Combination of Different Lattices

Different lattices can epitaxially combine in various ways. The lattice constant and crystal structure of the materials determine the lattice matching in terms of matching symmetries. Beginning with 'natural' combinations[2], the most prevalent ways of lattice matching with gradually increasing intricacy are introduced in the following .

Direct

The direct lattice constant matching of a_f and a_s can be regarded as the most basic epitaxial growth. It requires nearly equal lattice constants and includes cases of cubic-cubic, hexagonal-hexagonal and tetragonal-tetragonal symmetries as well as mixtures thereof, e. g. cubic-tetragonal (cp. table 5.1). No change of crystal orientation takes place. The elemental and simplistic lattice matching, which perpetuates the given crystal lattice with a minimum variation between substrate and grown film, is beneficial. Therefore the amount of growth defects and dislocations is expected to be very low, stress in the grown film can be neglected [Gün07]. Of course, the advantages diminish with increasing lattice constant deviation of the used materials.

An example of direct lattice matching is given by the hexagonal materials SnO_2 and α-Al_2O_3. The data in table 5.1 emphasize that the lattice constants deviate very little and that this epitaxy would be well-suited for coating applications due to the obvious refractive index variation. Symmetry matching of cubic and tetragonal lattices is exemplified by HfO_2 and $LiYF_4$ with an even greater difference in refraction.

Integer Multiples

Epitaxy of materials which achieve lattice matching by integer multiples of each other can be denoted by $a_1 \approx n \times a_2$. n is of integer value, with either the substrate material having

[2] The term 'natural' refers to the substrate material that defines the norm. It is used to quantify the extent in which the grown film deviates from the substrate material with regard to structure and orientation.

Material	**Crystal Structure**		**Lattice Constant (Å)**	**Lattice Matching**	**Refraction Index** @ 1 µm
SnO_2	hexagonal	D_8^4	$a_{h_1} = 4.740$	$a_{h_2} \approx a_{h_1}$	$n = 2.00$
α-Al_2O_3	hexagonal	D_{3d}^5	$a_{h_2} = 4.762$	$f = 0.4\,\%$	$n = 1.76$
YVO_4	tetragonal	D_{4h}^{19}	$a_{t_1} = 7.123$	$a_{t_2} \approx a_{t_1}$	$n = 1.96$
SiO_2 *cristobalite*	tetragonal	O_h^7	$a_{t_2} = 7.130$	$f = 0.1\,\%$	$n = 1.49$
HfO_2	cubic	O_h^5	$a_c = 5.125$	$a_t \approx a_c$	$n \approx 2.2$
$LiYF_4$	tetragonal	C_{4h}^6	$a_t = 5.160$	$f = 0.68\,\%$	$n = 1.45$
ZrO_2	cubic	O_h^5	$a_{c_1} = 5.08$	$a_{c_2} \approx 2\,a_{c_1}$	$n \approx 2.2$
$YScO_3$	cubic	T_h^7	$a_{c_2} = 10.20$	$f = 0.39\,\%$	$n \approx 1.89$
YAG	cubic	O_h^{10}	$a_{c_1} = 11.930$	$2\,a_{c_2} \approx a_{c_1}$	$n = 1.82$
PbF_2	cubic	O_h^5	$a_{c_2} = 5.939$	$f = 0.44\,\%$	—
GGG	cubic	O_h^{10}	$a_{c_1} = 12.376$	$2\,a_{c_2} \approx a_{c_1}$	$n = 1.97$
BaF_2	cubic	O_h^5	$a_{c_2} = 6.196$	$f = 0.13\,\%$	$n = 1.47$
YN	cubic	O_h^5	$a_{c_1} = 4.877$	$a_{c_2} \approx 2\,a_{c_1}$	—
Sc_2O_3	cubic	T_h^7	$a_{c_2} = 9.844$	$f = 1.06\,\%$	$n = 1.87$
LaN	cubic	O_h^5	$a_{c_1} = 5.295$	$a_{c_2} \approx 2\,a_{c_1}$	—
Y_2O_3	cubic	T_h^7	$a_{c_2} = 10.603$	$f = 0.12\,\%$	$n = 1.89$
C *diamond*	cubic	O_h^7	$a_c = 3.567$	$a_t \approx 2\,a_c$	$n = 2.42$
YVO_4	tetragonal	D_{4h}^{19}	$a_t = 7.123$	$f = 0.15\,\%$	$n = 1.96$
YVO_4	tetragonal	D_{4h}^{19}	$a_t = 7.123$	$a_c \approx \sqrt{2}\,a_t$	$n = 1.96$
$ScLuO_3$	cubic	T_h^7	$a_c = 10.098$	$f = 0.24\,\%$	$n \approx 1.91$
ZrO_2	cubic	O_h^5	$a_c = 5.080$	$\sqrt{2}\,a_t \approx 2\,a_c$	$n \approx 2.2$
YVO_4	tetragonal	D_{4h}^{19}	$a_t = 7.123$	$f = 0.85\,\%$	$n = 1.96$
GGG	cubic	O_h^{10}	$a_c = 12.376$	$\sqrt{3}\,a_t \approx a_c$	$n = 1.97$
YVO_4	tetragonal	D_{4h}^{19}	$a_t = 7.123$	$f = 0.31\,\%$	$n = 1.96$
YVO_4	tetragonal	D_{4h}^{19}	$a_t = 7.123$	$2\,a_c \approx \sqrt{3}\,a_t$	$n = 1.96$
BaF_2	cubic	O_h^5	$a_c = 6.196$	$f = 0.44\,\%$	$n = 1.47$
C *diamond*	cubic	O_h^7	$a_c = 3.567$	$a_h \approx \sqrt{2}\,a_c$	$n = 2.42$
SiO_2 *tridymite*	hexagonal	D_{6h}^4	$a_h = 5.030$	$f = 0.29\,\%$	$n = 1.47$
Y_2O_3	cubic	T_h^7	$a_c = 10.603$	$3\,a_h \approx \sqrt{2}\,a_c$	$n = 1.89$
GeO_2	hexagonal	D_8^4	$a_h = 4.972$	$f = 0.53\,\%$	$n = 1.7$

Table 5.1: *Possible systems to be combined as substrate and film materials [Hub04]. The table is structured according to the subdivision in section 5.2.*

a lattice n-times smaller than the grown film or vice versa (cp. table 5.1). In special cases n may also denote a fraction of two integer values, e. g. $n = 2/3$. Symmetry combinations are cubic-cubic, tetragonal-tetragonal as well as cubic-tetragonal. Regarding this category of lattice matching one can conclude that although some changes in structure take place at the interface during the initial film growth, the crystal orientation remains the same and no rotation of the film planes has to take place. This is an advantage in comparison to lattice matching of non-integer multiples.

For instance, symmetry matching in integer multiples can be obtained by using ZrO_2 and $YScO_3$, both having cubic structure. In this case, the lattice of ZrO_2 is about two times smaller than the one of $YScO_3$, indicating a lattice matching according to $a_{YScO_3} \approx 2\, a_{ZrO_2}$. A combination of varying symmetries may be obtained by using diamond C and YVO_4. Therein, the cubic lattice of C is about two times smaller than the tetragonal lattice of YVO_4, presumably resulting in a symmetry matching in the way of $a_{YVO_4} \approx 2\, a_C$. In both examples the refractive indices of substrate and film would be quite different, recommending the application as waveguide devices or coatings.

Non-Integer Multiples

Combining the lattices of two different materials by non-integer multiples of each other is another way of lattice matched growth. This class presents the highest complexity in combining different materials and can be described by $\sqrt{m}\, a_1 \approx n \times a_2$, with m and n being integer values. It includes different symmetry combinations as well and can be subdivided in two categories (cp. table 5.1):

i) When combining cubic-cubic, cubic-tetragonal or tetragonal-tetragonal symmetries, only an *in-plane rotation* of the film-lattice is required in order to match the substrate (cp. figure 5.5).

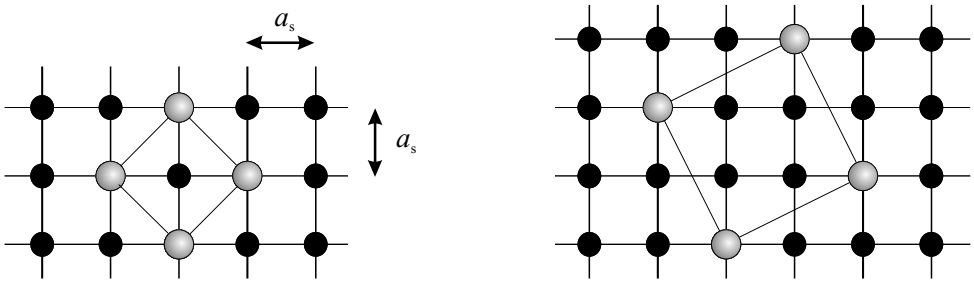

Figure 5.5: *Symmetry matching of non-integer multiples by in-plane rotation. Both cases incorporate cubic-cubic, cubic-tetragonal and tetragonal-tetragonal symmetries. The lattice constants have the relation (a)* $a_f \approx \sqrt{2} a_s$ *and (b)* $a_f \approx \sqrt{3} a_s$.

ii) When combining cubic-hexagonal symmetries, a *change of crystal orientation* is involved as the cubic lattice offers a hexagonal structure in the cubic {111}-planes. Lattice matching is thus achieved due to different crystallographic orientations (cp. figure 5.6).

The non-integer multiple symmetry matching with in-plane rotation can be seen by tetragonal YVO_4 combined with cubic GGG, whereas cubic and hexagonal lattice matching is exemplified using Y_2O_3 with cubic structure and GeO_2 consisting of a hexagonal matrix. As depicted in figure 5.6, the cubic lattice of the sesquioxides offers a hexagonal structure in the cubic {111}-planes. For this system one gets the relation $3 \times a_{GeO_2} \approx \sqrt{2}\, a_{Y_2O_3}$.

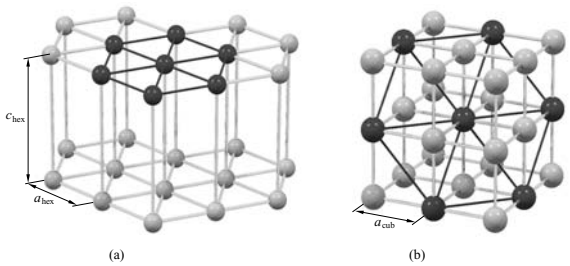

Figure 5.6: *Illustration of symmetry matching with hexagonal (a) and cubic (b) lattices.*

In summary, it can be said that with increasing deviation from the substrate lattice, the film growth becomes more and more energetically unfavorable. Thus, lattice matching which requires the combination of different crystallographic orientation is more likely to result in crystal defects.

5.3 Investigated Systems

Due to the fact that this work is a continuation of previous research on thin films fabricated by pulsed laser deposition at the Institute of Laser-Physics, a short retrospection shall both give insight into the experience and knowledge obtained in this scientific field but also retrace the objective of this thesis and comprehend the materials selected for investigation. Table 5.2 gives an overview of the investigated PLD-films.

Retrospection

A thorough investigation of Y_2O_3 grown on α-Al_2O_3 with respect to structure and spectroscopy was done by [Bur02, Bär04]. The film dopant was europium and the lattice mismatch was about 4.73 %. Other sesquioxides like scandia and lutetia have also been tried and investigated as film materials grown on sapphire in the works of [Bär04, Kuz06]. Using sesquioxide films grown on α-SiO_2 was subject in the master thesis of [Ehl05]. In general, although the grown films offered a high degree of crystallinity, grain boundaries and defects in the grown matrices were a hindrance to growing thicker films for waveguide application or coatings. Although the films were stress relaxed due to the relatively small grain boundaries (cp. page 49), no monocrystalline films of higher thickness can be obtained. In addition, quartz turned out to be unsuited as substrate material in high-temperature pulsed laser deposition due to the phase transition of α-quartz into β-quartz

at 573°C [Ehl05, Kuz06]. The change in lattice symmetry and structure, i. e. from hexagonal quartz to tetragonal cristobalite and vice versa (cp. table 5.2), negatively affects the grown film during the decrease in temperature after deposition.

One reason for the difficulties can be found in the lattice mismatch which leads to elastic deformations at first. Whether these result in plastic deformations depends on the ability of the growing film to compensate the stress that arises at the substrate interface and propagates further in the grown film material. In macroscopic view, two- and three-dimensional island growth can be observed.

Current Work

In order to realize high-quality thick films the lattice matching of substrate and film material needs to be improved. Guided by this objective, various lattice matched systems have been investigated. Thin films with thicknesses usually in the range of 5 to 100 nm have been grown and analyzed in order to study the lattice matching mechanisms in different materials.

Continuing the work based on the heteroepitaxial Y_2O_3–Al_2O_3 system, the lattice mismatch of 4.7% can be reduced by customizing the lattice constant of the sesquioxide compound. This is achieved by mixing the sesquioxides according to $(Sc_{1-x}Lu_x)_2O_3$ and thus shifting the lattice constant to match the substrate value of $a = 10.102\,\text{Å}$. The technique of admixing ions in a crystal matrix is well-known from the growth of laser crystals according to certain requirements [İle04]. The mixed crystals can be described as solid solutions, in which the substituent distribution in the matrix is completely statistical. However, each substituent occupies the correct lattice site. The full solid-solubility of materials used in this thesis was confirmed by fusion experiments with a regular crystal growth setup. As sesquioxides behave similar in chemical and physical terms, most of their properties remain unchanged in a mixed system. The lattice constant in such binary solutions like $(Sc_{1-x}Lu_x)_2O_3$ is a linear function of x and the new lattice constant a' is calculated from the Vegard law [Veg21] using the lattice constants of the pure single-crystals a_1 and a_2

$$a' = x\,a_1 + (1-x)\,a_2\ . \tag{5.3}$$

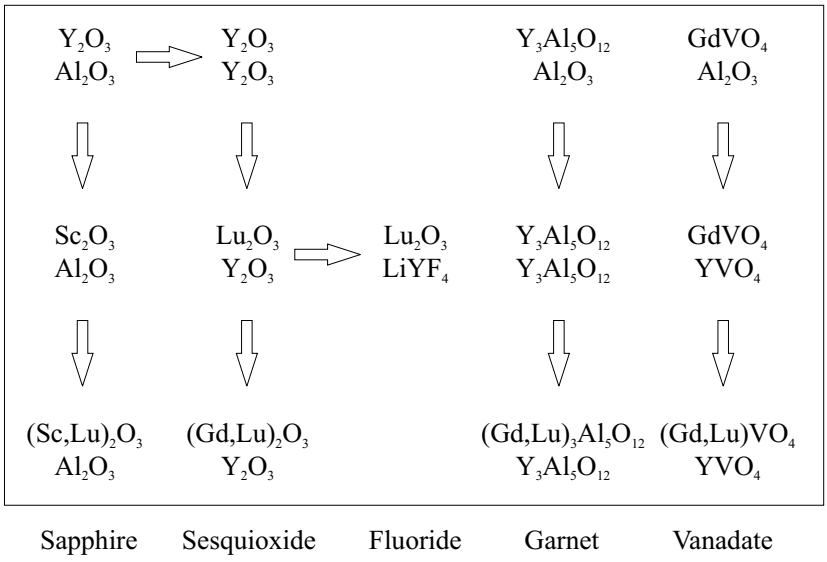

Figure 5.7: *'Map' of studied materials with the* substrate *below and the grown* film *above. No dopants are considered here.*

Material	**Crystal Structure**		**Lattice Constant (Å)**	**Lattice Matching**	**Refraction Index** @ 1µm
Y_2O_3	cubic	T_h^7	$a_c = 10.603$	$3\,a_h \approx \sqrt{2}\,a_c$	$n = 1.89$
α-Al_2O_3	hexagonal	D_{3d}^5	$a_h = 4.762$	$f = 4.73\,\%$	$n = 1.76$
Y_2O_3	cubic	T_h^7	$a_c = 10.603$	$3\,a_h \approx \sqrt{2}\,a_c$	$n = 1.89$
α-SiO_2 *quartz*	hexagonal	$D_8^{4,6}$	$a_h = 4.91$	$f = 1.77\,\%$	$n = 1.54$
Sc_2O_3	cubic	T_h^7	$a_c = 9.844$	$2\,a_t \approx a_c$	$n = 1.87$
SiO_2 *cristobalite*	tetragonal	O_h^7	$a_t = 4.96$	$f = 0.64\,\%$	$n = 1.49$
$(Sc, Lu)_2O_3$	cubic	T_h^7	$a_c = 10.102$	$3\,a_h \approx \sqrt{2}\,a_c$	$n \approx 1.91$
α-Al_2O_3	hexagonal	D_{3d}^5	$a_h = 4.762$		$n = 1.76$
Lu_2O_3	cubic	T_h^7	$a_c = 10.391$	$2\,a_t \approx a_c$	$n = 1.95$
$LiYF_4$	tetragonal	C_{4h}^6	$a_t = 5.16$	$f = 0.68\,\%$	$n = 1.45$
$(Gd, Lu)_2O_3$	cubic	T_h^7	$a_c = 10.603$	direct	$n \approx 1.96$
Y_2O_3	cubic	T_h^7		matching	$n = 1.89$
$(Gd, Lu)_3Al_5O_{12}$	cubic	O_h^{10}	$a_c = 11.93$	direct	$n \approx 1.86$
$Y_3Al_5O_{12}$	cubic	O_h^{10}		matching	$n = 1.823$
$GdVO_4$	tetragonal	D_{4h}^{19}	$a_{t_1} = 7.211$	$a_{t_2} \approx a_{t_1}$	$n = 2.20$
YVO_4	tetragonal	D_{4h}^{19}	$a_{t_2} = 7.123$	$f = 1.22\,\%$	$n = 1.96$
$(Gd, Lu)VO_4$	tetragonal	D_{4h}^{19}	$a_t = 7.123$	direct	$n = 2.10$
YVO_4	tetragonal	D_{4h}^{19}		matching	$n = 1.96$

Table 5.2: *Lattice matching of investigated systems in previous research (first subdivision) and in this thesis (second subdivision).*

This equation delivers the value $x = 0.459$ for $(Sc_{1-x}Lu_x)_2O_3$ approving the lattice matched composition $(Sc_{0.541}Lu_{0.459})_2O_3$.

By changing the substrate material from Al_2O_3 to Y_2O_3 (cp. figure 5.7) a homoepitaxial system is achieved. With only the dopant disturbing the Y_2O_3 film lattice, good matching is expected. A higher refractive index variation is obtained with Lu_2O_3 as film material, although one has to take into account a lattice mismatch increase. This can be diminished by using a dopant with a higher ionic radius than Y^{3+}, for instance Eu^{3+}. Perfect lattice matching is obtained using a $(Gd_{1-x}Lu_x)_2O_3$ film on Y_2O_3.

In addition, the heteroepitaxial growth of Lu_2O_3 on $LiYF_4$ offers a high refractive index variation for applications like Bragg mirrors, antireflex coatings as well as waveguides with a good lattice matching at the same time. The combination of fluorides and oxides is interesting to study but may also incorporate its difficulties due to the possibility of oxyfluoride formation.

Other homo- and quasi-homoepitaxial films based on garnet- and vanadate-materials have been fabricated and characterized. Each of them has been fabricated non-lattice matched by the growth on sapphire in order to estimate the film deposition rate (cp. appendix A). Then the lattice mismatch has gradually been decreased, first by moving to homoepitaxial growth and then to a quasi-homoepitaxial lattice matched film. The last step has always been achieved by admixing gadolinium and lutetium to match the equivalent yttrium-based substrate material (cp. figure 5.7).

6 Thin Film Preparation

A detailed description of the preparation of thin films using the pulsed laser deposition technique is given in this chapter. The films prepared in the course of this work have been deposited at the *Institute of Laser-Physics, University of Hamburg*.

In the previous chapter it has been shown that thin film preparation by pulsed laser deposition involves different physical and chemical processes. Thus, a variety of experimental setup parameters influence the quality and characteristics of the grown films that are enlisted in table 6.1.

Target and Substrate Preparation

Either sintered powders or bulk crystals have been used as targets for ablation. The preparation of sintered targets started with the source materials in powder form (purity $\geq 99.99\,\%$) weighed out in the correct proportion and then cold-pressed into a pellet of 2.3 cm in diameter. The pellet density after applying a pressure of 600 bar using a hydraulic press is about 50 % of the density of the corresponding single-crystal. Of course, this strongly depends on the used powder material properties. In general, higher target densities should result in improved laser evaporation characteristics leading to films with superior properties [Sin92][1]. Thus, in order to increase the density, the pellets were sintered in air for 72 h at a temperature of 1700 °C and then slowly cooled down to room temperature. These sintered pellets of now 2.0 cm in diameter have an estimated density of approximately 90 % of the corresponding single-crystals, again depending on the properties of the powder compounds. In addition, targets of crystalline density have been used in comparison for some PLD-films. Using rhenium crucibles, these targets were prepared by heating up the powder mixtures at temperatures of over 2400 °C and thereby obtaining a homogeneous melt. After cooling down, the melt delivered the polycrystalline target material, processed into the same dimension as the sintered pellets with polished surfaces.

All targets were 'cleaned' prior to deposition by ablation with 500 excimer laser pulses under the same conditions as the subsequent deposition to ensure a homogeneous surface morphology.

The α-Al_2O_3 and YAG substrates, supplied by CrysTec Kristalltechnologie (Berlin, Germany), had a size of 10 mm × 10 mm × 0.5 mm and were single-side polished with an

[1] However, it is still disputed whether or not the use of crystalline, high density targets reduce the amount of particulates, or in how far this parameter is decisive in that quest.

Parameter	Value
laser wavelength, λ_{KrF}	248 nm
laser pulse energy, E_p	0.4 – 1.2 J/pulse
pulse duration, τ_{KrF}	20 ns
laser repetition rate, ν_{rep}	1–50 Hz
type of background gas	N_2, O_2
background gas pressure, p	10^{-8} – 1 mbar
target material property (density and morphology)	crystalline, sintered
target-substrate distance, d	7.5 – 11.5 cm
substrate temperature[2], T_{sub}	20 – 1100 °C

Table 6.1: *Important deposition parameters and their technically possible values.*

RMS-roughness of < 0.4 nm. α-Al_2O_3 substrates were $\langle 0001 \rangle$-oriented to provide good lattice matching with sesquioxides (cp. section 5.2) whereas the YAG substrates were oriented in $\langle 100 \rangle$ and $\langle 111 \rangle$ direction in order to investigate the film growth behavior in dependence of the crystal orientation.

As sesquioxides are not commercially available, they have been grown at the *Institute of Laser-Physics* using the HEM technique. Y_2O_3 substrates have been used for film growth in $\langle 100 \rangle$ and $\langle 111 \rangle$ direction, whereas mixed sesquioxide substrates $(Sc_{0.5}Lu_{0.5})_2O_3$ had (100)-orientation. The $LiYF_4$ substrates were also obtained by crystals grown at the *Institute of Laser-Physics* by the Czochralsky technique. They were oriented in $\langle 100 \rangle$ direction. As orthovanadate single-crystals are difficult to grow [Krä05], the YVO_4 substrates were obtained by a Nd-doped crystal grown at the *Institut für Kristallzüchtung* in Berlin. The dopant concentration was 0.63 at.% and the crystal has been oriented in $\langle 100 \rangle$ direction. The non-commercial crystals Y_2O_3, $(Sc_{0.5}Lu_{0.5})_2O_3$, YVO_4, and $LiYF_4$ were oriented, cut and single-side polished with epitaxial quality by CrysTec Kristalltechnologie. No influence of the Nd-doping in the YVO_4 substrates was observed in preparation and characterization of the thin films.

All the substrates were cleaned with purified air in order to remove dust particles before being loaded into the air-lock chamber. For deposition, the substrates were placed in front of the target holder. The target-substrate distance was varied from 8.0 cm to 9.5 cm depending on other parameters and the film material.

Experimental PLD-Setup

The PLD-machine that has been used throughout this work was built by Pink Vakuumtechnik and is schematically illustrated in figure 6.1. It is constructed as two jointed vacuum chambers that can be isolated by a vacuum valve. As the deposition process takes place in the main chamber, the second chamber is constructed as an air-lock in order to

[2] The maximum substrate temperature has been improved during the course of this work. Different heating techniques were applied.

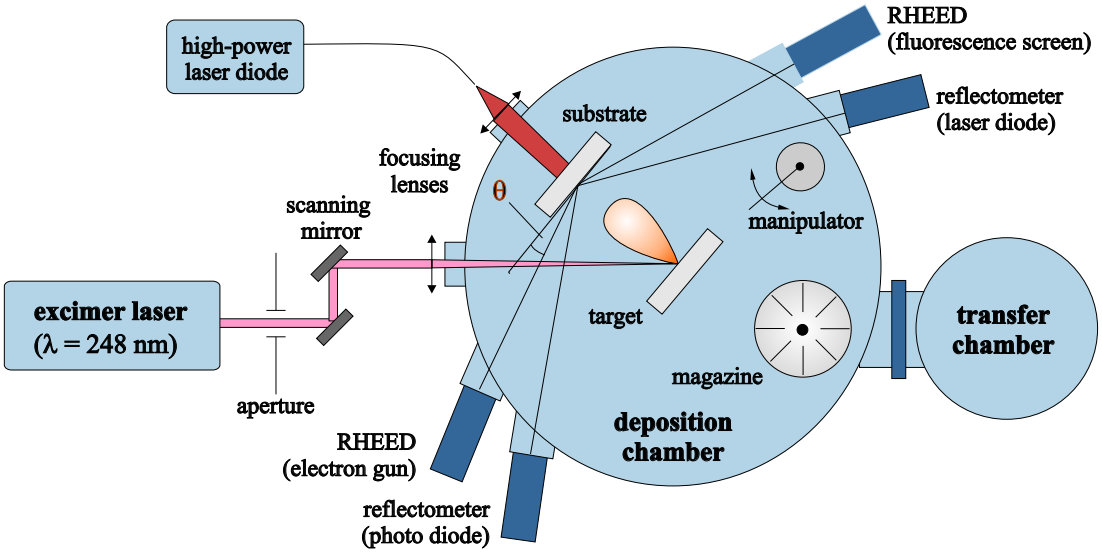

Figure 6.1: *Schematic illustration of the pulsed laser deposition setup.*

transfer substrates and targets without flooding the main chamber with air. Thus, the main chamber is maintained under ultra-high vacuum conditions, also contributing to its purity. With the integrated turbo-molecular pump the pressure in the deposition chamber is in the range of 10^{-8} to 10^{-7} mbar. Mounted in unified metal frames, the substrates and targets are transported from the air-lock chamber into a magazine in the main chamber. From there the frames are transferred by a manipulator arm either to the substrate or the target holder prepared for the deposition process. During the course of this work different heating techniques have been applied. The first one was a resistive heater (Si_3N_4-ceramic) mounted behind the substrate holder with no direct thermal contact. By this means, the effective substrate temperature reached its maximum at 700 – 750 °C, though the heater temperature itself was capable of 1000 °C. As an upgrade in order to reach higher temperatures a laser-based heating was installed. Therein, a heat-spreader (SiC and later Si_3N_4) is mounted beneath the substrate so that the laser spot covers the heat-spreader from behind, thus indirectly heating the substrate. Temperatures of 900 °C could be established using an array of 5×20 W diode lasers. Further improvements were obtained by extending this heater setup to an array of 7×20 W diode lasers. With this last modification the deposition at substrate temperatures of up to 1000 °C was possible. A one-color pyrometer was used to measure the temperature of the substrate. Due to possible thermal problems in the substrate and the grown films, the temperature was increased and decreased with different rates in different temperature regimes. The heating cycle of a substrate if illustrated in figure 6.2. Faster heating rates of 10 °C/min were used up to a temperature of 400 °C, setting the rate to 5 °C/min from then onwards to avoid thermal stress in the substrate. After constant temperature was kept during the deposition, the cooling process was carefully started using a ramp of 5 °C/min and later increasing to 10 °C/min. These low cooling ramps were due to the different thermal expansion coefficients of film and substrate in the depositions. Neither film cracks nor partly flaked-off films have been observed. The temperature processes were all computer-controlled.

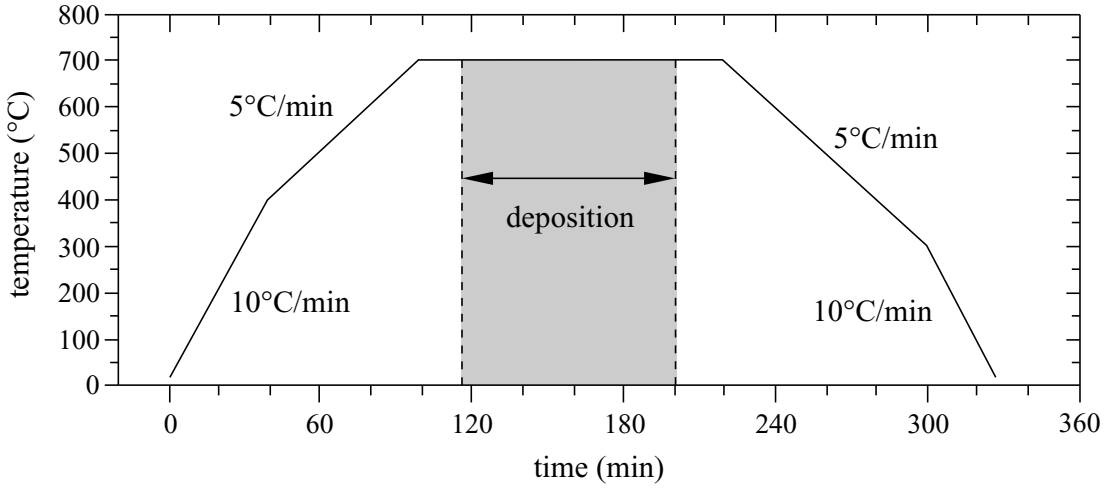

Figure 6.2: *The heating cycle of a substrate.* $T_{\mathrm{sub,max}} = 700\,°C$ *is taken as an example used for the deposition of* $Eu : GdVO_4$ *films on* YVO_4 *substrates.*

A full-range gauge and, in addition, a baratron (capacitance pressure detector) control the gas pressure of the main chamber, the latter one designed for more precise measurements in the range of 10^{-4} to 1 mbar. However, during various deposition experiments the baratron showed a nonlinear behavior in the $< 10^{-2}$ mbar range. As the utilized background gas pressure during deposition had typical values of 10^{-3} to 10^{-2} mbar, the baratron was of no further use, employing the full-range detector instead. Gas flow controllers pour in the selected background gas with the necessary pressure achieved dynamically by balancing the gas inflow and the pumping strength. The entire PLD-machine with the two vacuum chambers, detectors, pumps, motors, and controllers is computer-controlled.

The ablation was carried out by an KrF excimer laser of type Lambda Physik Lpx 305 operating at a wavelength of $\lambda_{\mathrm{KrF}} = 248\,\mathrm{nm}$, a pulse duration of $\tau_{\mathrm{KrF}} = 20\,\mathrm{ns}$ (FWHM) and delivering a laser pulse energy $E_p \leq 1.2\,\mathrm{J/pulse}$ at repetition rates of $\nu_{\mathrm{rep}} \leq 50\,\mathrm{Hz}$. Due to the strongly varying intensity at the laser beam edges, an aperture was used to cut these off and thereby obtain a more homogenous energy distribution in the laser spot on the target. Thus, only the central part of the beam was used for ablation. In order to prevent erratic material removal and crater formation on the target surface (cp. section 4, page 37 et seq.), the laser beam is scanned over the target surface. This also ensures a homogenous film thickness over the entire substrate surface area, since the plasma plume is strongly directed (cp. chapter 4.2). Finally, the beam was focused on the target using a lens ($\mathrm{f} = 400\,\mathrm{nm}$) that was placed in front of the vacuum chamber window. Anti-reflection coatings of lens and window were engineered for wavelength of 248 nm.

The laser beam was originally scanned by a piezoelectric that moved the scanning mirrors. However, this construction had some disadvantages: it was designed for high scanning frequencies and was not able to hold heavy mirrors but only small mirrors with 10 mm in diameter. Thus, a very small aperture was reached for the excimer laser beam. Having a cross section of $\approx 15 \times 30\,\mathrm{mm}$, the beam size had to be reduced by a $\times 2.5$ telescope. Due to these circumstances only about 7% of the laser energy were transmitted into the chamber. Aberrations caused by the telescope lens and the poor quality of the excimer laser

beam resulted in an asymmetrical dash-like spot on the target (cp. figure 6.3) The laser fluence was varied by tuning the energy emitted by the excimer laser while the focusing was kept constant. With this setup an ablation spot size of $1.5\,\mathrm{mm}^2$ was measured. As the laser was typically operating at 700 mJ/pulse, of which 49 mJ (7%) are transmitted into the chamber, a laser fluence of $3.3\,\mathrm{J/cm}^2$ is obtained [Ehl05, Kuz06].

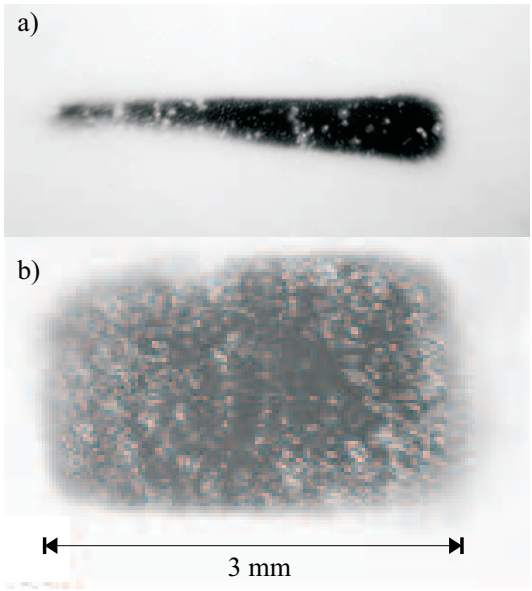

Figure 6.3: *Ablation spots: (a) after execution of 10 pulses with $\Phi = 3.3\,J/cm^2$ using the piezoelectric beam setup on a sintered Y_2O_3 target, (b) after execution of 50 pulses with $\Phi = 2.6\,J/cm^2$ using the galvanometer setup on a sintered Sc_2O_3 target.*

Later, the piezoelectric beam scanner was replaced by a deflection unit with two galvanometer scanners bearing larger mirrors resulting in an aperture of 20 mm in diameter. Therefore, and as the telescope was not needed anymore, the laser spot on the target had rectangular form determined by the aperture, its size being variable by the focusing lens position. With this modification a 20% increase in the laser energy transmitted into the deposition chamber was achieved. When operating at 800 mJ/pulse, 160 mJ are transmitting into the chamber, resulting in a laser fluence of $2.5\,\mathrm{J/cm}^2$ on the target. The upper limit for the threshold fluence has been determined for each material, e. g. being $1.5\,\mathrm{J/cm}^2$ for the sesquioxides. This is also consistent with literature [Kei97, Kuz06]. In order to avoid particulates, it is recommended to use fluences slightly above the threshold, which has been done in this work.

During the deposition process a reflectometer controlled the thickness of the growing film. It will be discussed below in more detail. Another modification made on the PLD-machine in the latter period of this work was the installing of RHEED[3] equipment, including a detecting screen and an electron gun with a double differential pumping stage for operation at high chamber pressures. This facility has been used for the final deposited films.

Film Thickness Control

The film thickness and growth rate of the deposited films were determined in-situ by a reflectometry device, which consisted of a laser diode ($\lambda = 659\,\mathrm{nm}$) and a photo diode (cp. figure 6.1).

For this purpose, the desired films were first grown at room temperature on a substrate with a great refractive index difference with respect to the film. Either silicon or sapphire substrates were used due to the high contrast in the reflectivity signal (cp. figure 6.4). As neither the change of substrate nor the change of substrate temperature have a significant

[3] RHEED stands for 'Reflection High-Energy Electron Diffraction Measurements' (cp. section 6.2).

influence on the growth rate, the results were then applied to the desired lattice matched system. The estimated growth rates do not vary for similar targets (material and density).

In the main chamber, the intensity of the He-Ne laser beam is reflected from the sample and measured by the photo diode, amplified with a DC-amplifier and recorded with a computer during deposition. The real-time control of the film thickness is achieved by means of a special software program that records and instantly analyzes the reflectometer signal. A generic algorithm model is used to fit the signal [Kuz06].

The increasing film thickness during deposition leads to a change in the phase shift between the reflected light from the front film surface and the reflected light from the film-substrate interface. Due to the interference of these reflected beams the detected signal varies in intensity. An infinite number of reflections has to be considered (cp. section 7.2). Ruling out film absorption or scattering, the reflectometer signal can be described by equation 7.14. It can also be written as periodical function of the film thickness d_f

$$R = x\,cos\left(\frac{2\pi\,d_\mathrm{f}}{P_\mathrm{f}}\right) \quad \text{and} \quad P_\mathrm{f} = \frac{\lambda}{2n_\mathrm{f}\,cos(\theta_\mathrm{f})} \tag{6.1}$$

with P_f denoting the period of the function being calculated. Therein, the values for the reflectometer laser wavelength λ, the incident angle θ_f and the refractive index n_f of

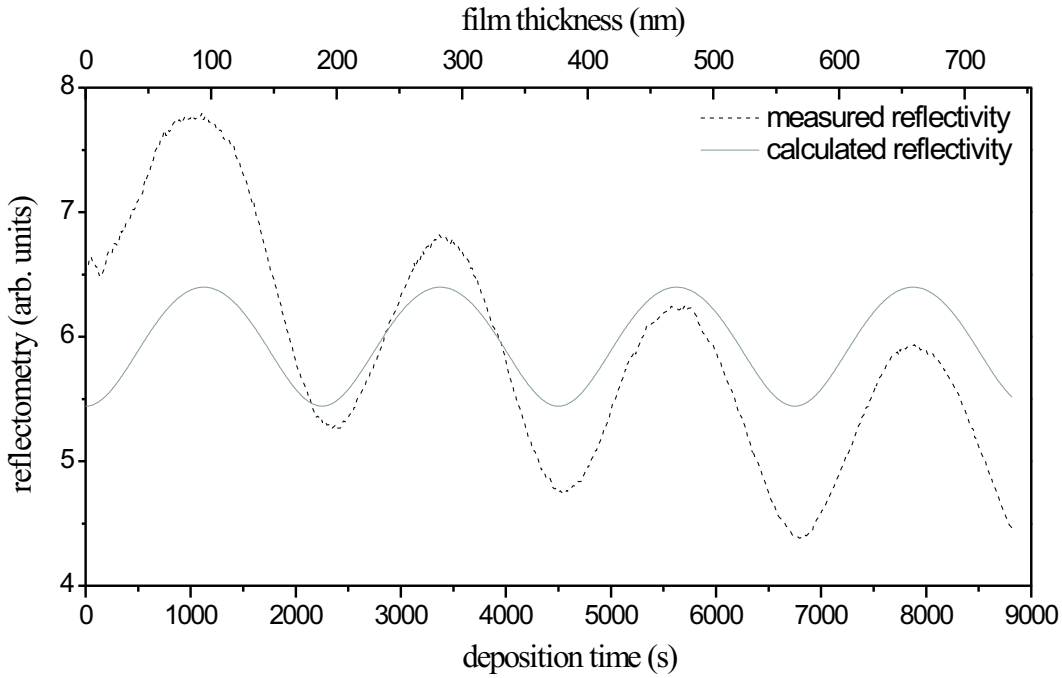

Figure 6.4: *Simulated and measured reflection behavior of a growing Eu:$(Gd, Lu)_2O_3$ film on sapphire. The growth rate was determined to be 0.076 Å per pulse at a laser fluence of $\Phi = 3.3\,J/cm^2$.*

the film must be known. During film deposition the reflectometer signal is recorded as a function of the excimer laser pulse number $I(N_\mathrm{p})$ and the measured signal is fitted using the relation

$$I = c + a\,R\,cos\left(\frac{2\pi\,Z_\mathrm{r}N_\mathrm{p}}{P_\mathrm{f}}\right) \tag{6.2}$$

with R being the reflectometer signal (cp. equation 7.14, page 81), c denoting a constant shift that can result from the amplifier or an incoherent reflection from the substrate backside, a being the amplitude scaling factor, and Z_r representing the deposition rate. By using equation 6.2, the deposition rate Z_r and thus the film thickness $d_\mathrm{f} = Z_\mathrm{r}N_\mathrm{p}$ can be obtained by the measured signal.

An example of simulated and measured reflection behavior is presented in figure 6.4. The intensity decay of the measured signal is due to the increasing film growth causing the reflected beam to slightly drift off the photo diode, whose detection area is only about 1-2 mm in diameter.

Optimization of the Pulsed Laser Deposition Process Parameters

A big advantage of the pulsed laser deposition is the flexibility of the process that enables various different materials to be adapted for deposition. Apart from this beneficial flexibility, the PLD is a quite complex process with many parameters that need to be optimized for every material in order to achieve the desired high film quality. However, systematic investigations concerning the influence of PLD process parameters are rare up to now.

Research on the fabrication of Y_2O_3 films is found in Lancock [Lan04] as well as in the theses of Burmester [Bur02] and Bär [Bär04]. Investigations on the deposition of gadolinium gallium garnet (GGG) and Ti-doped sapphire films can be found in the theses of Barrington [Bar01] and Anderson [And98], whereas the film growth parameters of YAG, Sc_2O_3 and Lu_2O_3 are determined in the thesis of Kuzminykh [Kuz06]. Information on the deposition of RE-doped $GdVO_4$ films on YVO_4 is given in [Bär05]. In addition, general information on deposition behavior in dependence on the process parameters can be found here. However, being a complex process, the deposition success will never depend on the 'correct' setup of one parameter alone, but is an interplay of all crucial deposition parameters enlisted in table 6.1. As the possibilities of lattice matching are investigated using different substrate and film materials, a systematic analysis of the deposition process parameters was performed for materials that have not been investigated for PLD application yet. If possible, the available information has been adapted and adjusted to materials of similar kinds.

The possibilities of lattice matching were primarily investigated by films having a maximum thickness of 100 nm. Thus, although the target density is assumed to influence the amount of particulates and droplets, this effect should only play a negligible role due to the relatively thin film thicknesses. Nevertheless, high density targets (90 – 100% compared to crystal density) have been used. Crystalline targets are claimed to reduce

droplet production [Yos94, Lan05]. All of the used targets had a polished surface leading to a homogeneous plasma plume and thus to a well-distributed film growth behavior.

Larger ablation spots also minimize the droplet density [Yos94]; consequently the ablation laser spot was adjusted to $\approx 6\,\mathrm{mm}^2$. As mentioned before, the ablation should be carried out using a laser fluence Φ slightly above the threshold value [Die92, Kei97]. Therefore the thin-films have mainly been deposited at a laser fluence of about $\Phi = 1.5\,\mathrm{J/mm}^2$.

Higher background pressures during the deposition prevent lattice expansion (cp. figure 5.4) due to the continuous kinetic energy reduction of the atoms before being deposited on the substrate material [Tar96, Che04]. Droplets can primarily be avoided by proper adjustment of the background pressure and the target–substrate distance, as these two parameters mainly define the atom velocity in the plasma plume [Geo95, Tyu98]. Although high background pressures during deposition are favorable in order to achieve epitaxial film growth, the remaining kinetic energy of the atoms is not sufficient to diffuse on the substrate surface in case of too high pressures. Thus, no textured film growth is possible. Predominantly, the target–substrate distance in the course of this work has been $d_{\mathrm{ts}} = 9\ldots9.5\,\mathrm{cm}$ with oxygen pressures between 8.8×10^{-3} and $1 \times 10^{-2}\,\mathrm{mbar}$.

The substrate temperature belongs to the most important process parameters during deposition. In the Einstein diffusion law the influence of substrate temperature T, activation energy E_0, distance a of two neighboring positions on the substrate surface, and the statistic process frequency ν on the diffusion length l_{D} is given [Hen91]

$$l_{\mathrm{D}} = \sqrt{2D\tau} \quad \text{with} \quad D = \nu\, a^2 e^{-E_0/k_B T}\,. \tag{6.3}$$

The average diffusion constant D increases with the temperature resulting in higher mobility of the deposited atoms. In addition to the diffusion constant, the average diffusion

Substrate	**Film**	$\boldsymbol{E_p}$ (J/pulse)	$\boldsymbol{\nu_{\mathrm{rep}}}$ (Hz)	$\boldsymbol{p_{\mathrm{O_2}}}$ (mbar)	$\boldsymbol{d_{\mathrm{ts}}}$ (cm)	$\boldsymbol{T_{\mathrm{sub}}}$ (°C)
Y_2O_3	Eu: Y_2O_3	0.8	1–3	9×10^{-3}	9.5	900
Y_2O_3	Eu: Lu_2O_3	0.8	1–3	9×10^{-3}	9.5	900
Y_2O_3	Eu: $(Gd, Lu)_2O_3$	0.8	1–3	9×10^{-3}	9.5	900
α-Al_2O_3	Eu: $(Sc, Lu)_2O_3$	0.7	1–3	6×10^{-3}	9.5	900
$ScLuO_3$	Cr: Al_2O_3	0.7	1–3	6×10^{-3}	9.5	700
YAG	Eu: YAG	0.8	1–3	1×10^{-2}	9.5	900
YAG	Eu: (Gd, Lu)AG	0.8	1–3	1×10^{-2}	9.5	900
Nd: YVO	Eu: GdVO	0.7	1–3	8×10^{-3}	9.5	800
Nd: YVO	Eu: (Gd, Lu)VO	0.7	1–3	8×10^{-3}	9.5	800
LiYF	Eu: Lu_2O_3	0.4	1–3	4×10^{-3}	9.5	550

Table 6.2: *Optimized deposition parameters for the investigated films.*

length l_D is also influenced by the diffusion time τ being related to the repetition rate of the excimer laser. For higher repetition rates less diffusion time per pulse is available for the atoms leading to smaller values of τ and therefore of l_D. Thus, it can be concluded that single-crystalline film growth requires high temperatures and small laser repetition rates.

A list with all grown films and the corresponding deposition parameters can be found in appendix A. In this context the investigated film materials and their optimized parameters are presented in table 6.2. It is emphasized that these parameters are partly obtained in retrospective. Different parameters have been tried during this work, as seen in appendix A.

6.1 Pre-Deposition Substrate Treatment

Basic requirements for successful RHEED measurements are related to the substrate surface and its quality. In order to achieve epitaxial film growth the substrate surface has to be crystalline and atomically flat. No contaminations should occupy the surface [Bar95, Yos95]. As it is mechanically impossible to cut and polish alongside a single atomic plane, a miscut is introduced [Hen76]. The miscut angle β describes the deviation of the surface plane to the atomic crystal planes and should be small for substrates of good quality.

Under normal conditions at room temperature the substrate surface is atomically disordered. After annealing at high temperatures, atomic steps of monolayer height can be measured with atomic force microscopy (figure 6.5, cp. chapter 7.3) alongside the substrate orientation. The monolayer height depends on the material and the crystal surface orientation. For the materials in this work the step height is typically $2-5\,\text{Å}$. The width L of these atomic terraces depends on the miscut angle β as well as on the annealing time and the temperature. An accurate analysis of the growth process is based on the formation of these atomic steps [Mae97].

The formation of atomic steps after annealing is explained by the Einstein diffusion law (cp. equation 6.3), as the range of the diffusion atoms is depending not only on time τ, but also on the diffusion constant D determined by the Boltzmann distribution. Thus, it becomes obvious that the scope of the surface atoms is determined by the annealing temperature T and its endurance τ. With sufficient time, the surface atoms moving by statistic processes diffuse until an energetically favorable state is achieved through step-bonding.

Experimental Procedure

Due to the described requirements for RHEED and in agreement with the results obtained by [Gün07], the final thin films fabricated in the framework of this thesis were annealed prior to the deposition process. In addition to the possibility of RHEED analy-

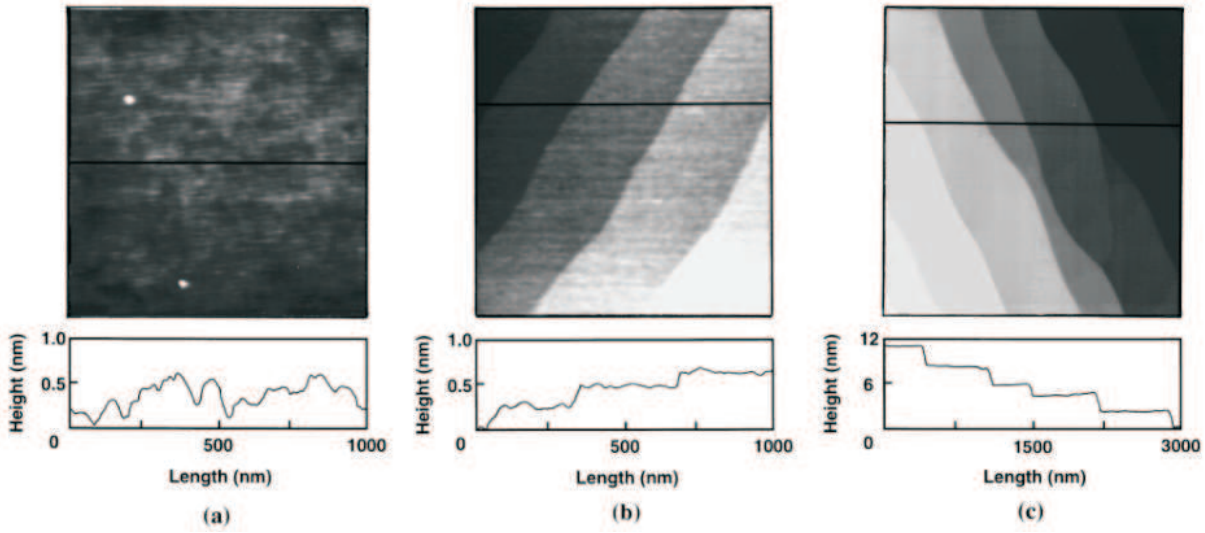

Figure 6.5: *AFM images of (0001) sapphire substrates: (a) as-supplied ($1\times1\,\mu m^2$), (b) annealed at 1000°C for 1 h ($1\times1\,\mu m^2$), and (c) annealed at 1400°C for 1 h ($3\times3\,\mu m^2$). The vertical profile was taken along the line indicated in the image. [Yos95]*

sis, this thermal treatment and the subsequent surface characterization with atomic force microscopy provided additional information regarding the source material condition.

Two devices have been used for thermal substrate treatment. Annealing at temperatures of $T < 1000$°C was done in a pipe furnace, whereas for annealing at higher temperatures a programmable furnace by Agni GmbH was employed. To prevent any surface contamination, the single-side polished substrates were enclosed in a aluminum-ceramic case. After annealing, the substrates were characterized with AFM to determine the atomic step orientation together with the miscut angle. During deposition, the incident electron beam of the RHEED system was oriented parallel to the atomic steps of the substrates. Although film growth monitor with the incident electron beam oriented perpendicular to the atomic steps is possible, better monitoring was achieved in parallel settings [Gün07]. In substrates with high miscut angles *step-bunching* is likely to occur [Joy88, Gün07], which can result in three-dimensional island growth. Thus, substrates with high miscut angles can affect the growth mode of the deposited film [Rij04].

In dependence of the miscut angle and the incorporated trivalent ion, the sesquioxides require annealing at 800 – 1200°C. Surface arrangement of scandia requires higher temperatures compared to the one of yttria [Gün07]. Temperatures of 900°C were used for the thermal treatment of [111] and [100] Y_2O_3 substrates. A relatively high miscut of $\beta \geq 0.15°$ was observed for composite $(Sc, Lu)_2O_3$ substrates. Therefore, lower annealing temperatures of 700 – 800°C were used. Sapphire and YAG substrate were annealed at 1000°C, YVO_4 substrates were annealed at 800°C, and $LiYF_4$ substrates were annealed at 500°C. In order to prevent a reaction with oxygen, the thermal treatment of the fluoride substrates took place in argon atmosphere. In all cases the annealing time was 1 h.

6.2 Reflection High-Energy Electron Diffraction

Since de Broglie first presupposed the wave nature of electrons in his doctoral thesis in 1922 and since his theory was verified by different experiments [Dav21, Dav27, Tho28] the interest in electron diffraction analysis of crystalline materials steadily increased. Besides low-energy electron diffraction (LEED), reflection high-energy electron diffraction (RHEED) is the most established one for surface layer analysis. A thorough account on RHEED and its applications is found in [Lar88, Bra99, Mah90].

A RHEED system consists of an electron source and a photoluminescent detector screen. The generated electron beam has very small incident angles of typically $0.1° < \theta < 3°$ in regard to the sample surface. This results in a high surface sensitivity and makes RHEED an appropriate in-situ method for film growth analysis. Constructive interference occurs at specific angles according to the crystal structure as incident electrons diffract from atoms at the surface of the sample forming regular patterns on the detector screen. Because of the fact that the electrons interfere according to the position of atoms on the sample surface, the diffraction pattern at the detector is a function of the sample surface. Two types of diffraction contribute to this pattern, further referred to as *kinematic diffraction* and *dynamic diffraction*. The first one refers to electrons that are scattered elastically and only once at the crystal surface, while the second denotes electrons that undergo multiple diffraction events in the crystal surface and thereby lose some of their energy. Non-qualitative data, such as the high-intensity spots or rings common to RHEED patterns, are obtained by the kinematically diffracted electrons, whereas qualitative information is gathered by the dynamically diffracted electrons.

Brief Introduction in RHEED Theory

In agreement with the two diffraction types that form the RHEED patterns, the undergirding RHEED theory is subdivided into kinematic and dynamic scattering theory. Both of them are based on the time-independent Schrödinger equation (cp. equations 3.2 and 3.3), assuming that electrons with the relativistic mass m_e, the kinetic energy $E_{\mathrm{kin}} = \hbar^2 k_0^2 / 2m_e$ and the potential energy in the crystal $V(\mathbf{r})$ are scattered. Thus, the Schrödinger equation is modified to

$$\left(\Delta - \frac{2m_e}{\hbar^2} V(\mathbf{r}) + \mathbf{k}_0^2 \right) \Psi(\mathbf{r}) = 0 \,, \tag{6.4}$$

with $V(\mathbf{r})$ describing the Coulomb interaction of the atoms with the incident electron wave (elastic scattering). Therein, the absorption (inelastic fraction) can be taken into account by adding an imaginary potential [Bee88].

Apparently, the kinematic theory only considers single scattering processes. A significant quintessence of the kinematic theory is the possibility to determine the crystal lattice in real-space if the scattering amplitude A is known. Regarding the relation $I(\mathbf{k}) \propto |A(\mathbf{k})|^2$ [Kit86], it becomes obvious that no phase information can be obtained by intensity measurements. This is referred to as 'phase problem'.

Different types of information on the sample are provided by the dynamic theory describing inelastic and multiple scattering events. Intensity of diffraction points is related to dynamic scattering. Inelastically scattered electrons that have already penetrated the surface and subsequently fulfill the Bragg condition yield diffraction patterns called Kikuchi lines [Kik28, Böl88]. Not only are these lines useful for estimating the diffraction conditions. They contain additional information on the surface quality and the crystal orientation of the sample. Narrow Kikuchi lines of distinct intensity suggest high surface quality, as the electrons are scattered at multiple parallel atomic planes and have the same angle when escaping the crystal. However, the Kikuchi lines sometimes interfere with the diffraction points, especially while monitoring film growth, and modify the RHEED image. It is thus commendable to measure diffraction points in an area with no influence of Kikuchi lines.

In the dynamic theory the Schrödinger equation is solved by approximation. Three solving methods are known in literature [Bra99]: the Bethe-Bloch wave method, the parallel-slicing method, and the multiple-slicing formalism. By applying the periodicity of the crystal potential with varying boundary conditions, all methods deliver good results that are strongly related to experimental data. As a detailed and satisfying theoretical description would go beyond the scope of this thesis reference is made to the diversity of literature that provides insight into these RHEED fundamentals [Bra99, Lar88].

Geometrical Considerations

In order to obtain the crystallographic properties of the sample surface, an Ewald sphere is constructed [Her83], indicating the allowed diffraction conditions for kinematically scattered electrons. Thus, knowing the incident electron energy and the distance between detector and sample, the reciprocal sample lattice can be estimated by a diffraction pattern that is related to the constructed Ewald sphere. This is shown schematically in figure 6.6.

Incident high-energy electrons with wave vector $\mathbf{k}_0$ that strike the sample surface with the grazing angle θ are scattered and exit with wave vector $\mathbf{k}_i$. In the kinematic theory, the scattered electrons are describes by the Laue condition $\mathbf{G} = \mathbf{k}_i - \mathbf{k}_0$, with $\mathbf{G}$ denoting the reciprocal lattice vector [Kit86]. An equivalent description is given by the Bragg condition[4] $2d_{hkl} \sin\theta = n\lambda_e$. Since the electrons

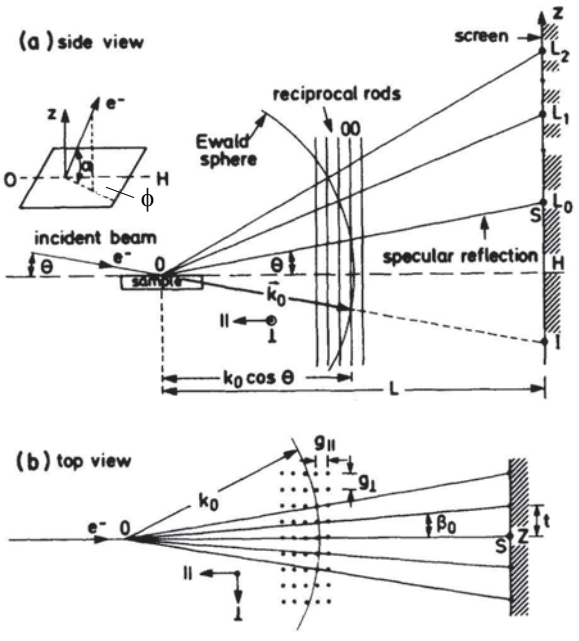

Figure 6.6: *Schematic illustration of (a) the Ewald construction and (b) the projection to the parallel surface plane. [Her83]*

[4] The Bragg diffraction law as well as the Miller indices h, k and l are explained in chapter 7.1

strike the sample surface at very small angles and are scattered at the upper atom layers, they interact with a virtually two-dimensional lattice. The reciprocal lattice forms lattice rods (hk) of infinite length and fineness, which are perpendicular to the ideally assumed surface. Thus, projecting the intersections of the Ewald sphere with radius $k_0 = 2\pi/\lambda_e$ and the reciprocal lattice rods, a diffraction pattern emerges. The intersections are situated on concentric circles called Laue circles with center H and radius L_n (cp. figure 6.6).

The diffraction reflexes are indicated with (n, k) in accordance with the lattice rod indices (hk). For instance, the zero-order diffraction resulting from the intersection of the $(0\,k)$-rod with the Ewald sphere on the zeroth Laue circle of radius L_0 is denoted $(0, k)$-reflex. A special reference is made to the $(0, 0)$-reflex that emerges from the $(0\,0)$-rod intersection with the Laue circle of zeroth order called *specular reflection*. Also important for RHEED analysis is the $(0, 0, 0)$-reflex in the diffraction patterns, which is formed by electrons which are directly detected at the zeroth Laue circle without being scattered at the sample surface.

The incident beam has a very short wavelength due to the high electron energy. Compared to the reciprocal lattice rod spacing[5], the Ewald sphere radius is much larger. Thus, the Ewald sphere is intersected by rows of reciprocal lattice rods forming an approximate plane, as identical rows of parallel reciprocal lattice rods sit directly in front of and behind the single row. These are identified in the diffraction patterns as side maximum resultant from $(0, k)$-reflexes for $k \neq 0$.

The reciprocal lattice vector magnitude g parallel and perpendicular to the beam direction (cp. figure 6.6) follows by geometric considerations for $n \in \mathbb{N}$ and $nt \ll L$ to [Her83, Bra99]

$$n\,g_{\parallel} = k_0 cos\theta - \frac{k_0}{\sqrt{(L_n/L)^2 + 1}} \quad \text{and} \quad n\,g_{\perp} = k_0 \frac{1}{\sqrt{(L/n\,t)^2 + 1}} \simeq k_0 \frac{nt}{L}\,. \tag{6.5}$$

By estimation of the reciprocal lattice g, which is based on the $(0\,0)$-rod diffraction, not only the lattice constants of the used sample materials can be verified, but the beam direction relative to the crystallographic orientation ϕ and the grazing angle θ (cp. figure 6.6) are determined as well. However, as the kinematic theory is applied, these results are not entirely accurate. They help to interpret the diffraction patterns, but may differ in certain degree from experimental data as the strong electron interaction with the surface potential is not taken into account.

Static Surface Structures

When applying the basic principles of ideal conditions with real surfaces, modifications in the diffraction patterns are observed. In general, a broadening of the diffraction reflex takes place because of non-ideal surfaces and non-perfect electron sources. As all

[5] According to the relativistic equation $|\mathbf{k}_i| = |\mathbf{k}_0| \equiv k_0 = \sqrt{2m_0E + (E/c)^2}/\hbar$, electrons of 25 keV have a wave number of $\approx 80\,\text{Å}^{-1}$. In the case of sesquioxide and YAG samples with lattice constants of 10 – 12 Å resulting in reciprocal lattice constants of $0.5 - 0.6\,\text{Å}^{-1}$, the electron wave number is considerably larger in comparison to the reciprocal sample unit cells.

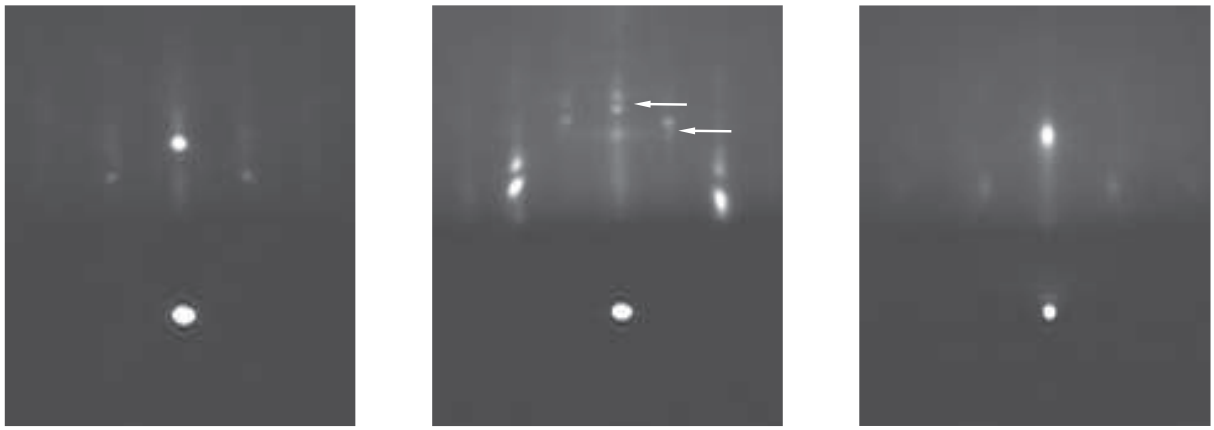

(a) (b) (c)

Figure 6.7: *RHEED images with varying incident electron beam orientation to the atomic steps on the sample surface: (a) YVO_4 substrate (parallel), (b) an YVO_4 substrate (perpendicular), and (c) a 15 nm thin Eu:$(Sc, Lu)_2O_3$ film (parallel).*

wave fractions are incoherent, the experimental intensity I_{ex} is algebraically derived from convolution of the real sample intensity $I_{\mathrm{s}}(\mathbf{k})$ (ideal electron source) with the instrument response function $T_{\mathrm{i}}(\mathbf{k})$ of the electron gun [Hen91]

$$I_{\mathrm{ex}} = I_{\mathrm{s}}(\mathbf{k}) * T_{\mathrm{i}}(\mathbf{k}) \,. \tag{6.6}$$

The autocorrelation function $\phi(\mathbf{r})$, which describes the probability to find two surface atoms at distance r, and the transfer function $t(\mathbf{r})$ are obtained by Fourier transformation $\hat{\mathbf{F}}$ of both components

$$I_{\mathrm{s}}(\mathbf{k}) = \hat{\mathbf{F}}\,\phi(\mathbf{r}) \quad \text{and} \quad T_{\mathrm{i}}(\mathbf{k}) = \hat{\mathbf{F}}\,t(\mathbf{r}) \,. \tag{6.7}$$

Apart from this, inelastically scattered electrons cause another broadening. The finite electron expansion modifies the diffraction points to ellipses, as the correlated theoretical model (e. g. intersection with lattice rods of infinite fineness) are corrected. Thus, RHEED diffraction points often have an elliptic form as shown in figure 6.7 (c) and their degree of circularity gives evidence to the quality of the sample surface.

When reconsidering the atomic surface steps, the electron beam alignment relative to these steps brings forth varying diffraction images in the so-called *off-Bragg condition* (also referred to as *out-of-phase condition*). Parallel alignment results in ordinary patterns as seen in figure 6.7 (a), whereas perpendicular alignment leads to a splitting of the diffraction reflexes as observed in figure 6.7 (b). Based on the kinematic theory and the constraining assumption that electron scattering occurs on the outermost surface atoms only, an autocorrelation function for a two-level system is derived. It describes the stepped surface with step height d and surface coverage $\Theta \in [0, 1]$, the latter being defined as the ratio of occupied to available adsorption sites [Atk87]. With subsequent Fourier transformation the intensity is given by [Len84, Puk88]

$$I(\mathbf{k}) = \left[\Theta^2 + (1-\Theta)^2 + 2\Theta(1-\Theta)\cos(k_z d)\right] 2\pi\delta(k_x) + 2\phi'_{ii}(k_x)\left[1 - \cos(k_z d)\right] \,. \tag{6.8}$$

Therein, ϕ'_{ii} is the Fourier transform of the reduced autocorrelation function between atoms of the same level and depends on the step distribution [Coh86]. Thus, the intensity is an overlay of a delta distribution and a broadened distribution around $k_x = 0$. Based on intensity relation, the different cases of surface coverage must be distinguished to interpret the diffraction reflections correctly.

a) $\mathbf{\Theta = 0}$, $\mathbf{d = 0}$: In the case of atomically flat surfaces without two-dimensional island formations, the delta distribution defines the intensity. Thus, the diffraction point can be regarded as delta peak.

b) $\mathbf{\Theta \neq 0}$ **in-phase**: Fulfilling the Bragg condition $k_z d = 2n\pi$, all delta distributions deliver a RHEED reflex. This is similar to the case with atomically flat surfaces. The steps are not recognized by the electrons.

c) $\mathbf{\Theta \neq 0}$ **out-of-phase**: Fulfilling the off-Bragg condition $k_z d = (2n + 1)\pi$, the intensity is highly sensitive to the surface coverage Θ. The steps are visible in the diffraction pattern, as for $k_z d$ values the delta peak and the broadened peak superimpose.

Apparently, the off-Bragg condition is ideally suited to detect surface derangements. Although the diffraction peak splitting in the off-Bragg condition (perpendicular incident beam) can be used to determine the miscut angle β [Coh86, Puk88], it may disturb the in-situ growth monitoring. Thus, the electron beam was applied in parallel orientation relative to the atomic steps on the surface, and the miscut was determined by AFM.

Gradual Surface Derangement

Since the described effects presupposed high quality substrates being adequately prepared (cp. section 6.1), no strong deviation from the ideal diffraction patterns is expected. The surface arrangements and structures which arise during deposition have an influence on the progress of the film growth. The resulting diffraction patterns with the corresponding reciprocal space are illustrated in figure 6.8 and are well-understood by means of the Ewald construction. Intersections of the reciprocal lattice rods with the Ewald sphere generate the different diffraction images. Case (a) describes the reciprocal lattice and the corresponding diffraction points on the Laue circles for an ideal surface, (b) shows two-dimensional island growth[6] in which the diffraction pattern shows parallel rods due to the island-like though flat surface. In an intermediate state between (a) and (b) with a weaker step structure than in (b) the diffraction points shown in (a) would turn into ellipses on the Laue ring (cp. figure 6.7c). In (c) high three-dimensional islands cause a quasi transmission high-electron diffraction (THEED) image, in which the Laue rings positioned on the Laue circles in (d) symbolize a polycrystalline surface [And96, Lit99].

These are the required fundamentals to interpret the diffraction images that alter during the growth process. The surface roughness is estimated by the root mean square value $R_{\mathrm{RMS}} = (1/N \sum_i^N z_i^2)^{1/2}$, which gives information on the deviation of the measured data z_i relative to an approximated zero level (cp. section 7.3).

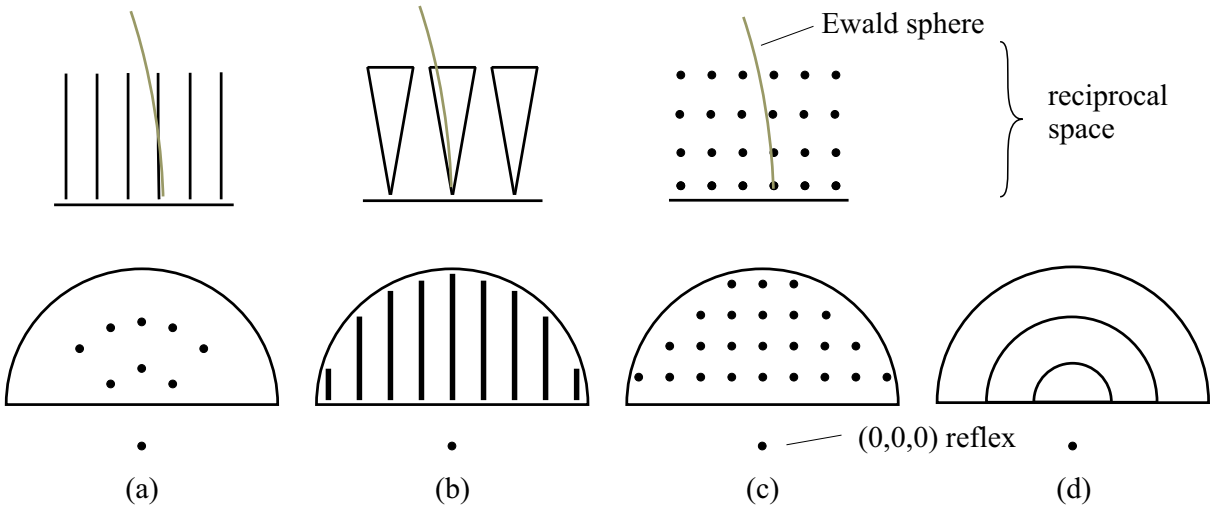

Figure 6.8: *Diffraction pattern and corresponding reciprocal lattice illustration for (a) an ideal surface, (b) a surface with 2D-islands, (c) a surface with 3D-islands, and (d) a polycrystalline surface (not illustrated as reciprocal lattice).*

[6] This describes also the case of atomic planes that are slightly tilted to each other (mosaic structure).

RHEED Oscillations

In film growth the morphology of the surface changes during the deposition process resulting in changing diffraction images as well. An oscillation of the $(0, 0)$-reflex, also referred to as specularly reflected beam, is observed in the layer-by-layer growth mode. A simple explanation is given by the kinematic theory: According to equation 6.8 the maximum intensity in the off-Bragg condition is obtained for completely covered layers ($\Theta = 0$) and the minimum intensity for half-covered surfaces ($\Theta = 0.5$).

The oscillation amplitude is very sensitive to the repetition rate. Higher repetition rates result in stronger damping of the amplitude, as an increase in surface roughness is expectable due to the shorter diffusion time τ and the consequently shorter diffusion length l_D of the deposited atoms. Often a strong decrease in diffraction intensity is observed, which emphasizes the very smooth surface of the sample because of the pre-deposition annealing.

These considerations provide a basic understanding of the RHEED oscillations, but fail to deliver an entire explanation [Bee88, Kaw88]. An enhancement for the inaccuracies of the kinematic model is the *step density model*. Therein, the phase dependence of the electrons' incident angle is considered. An intensity minimum deviation from $\Theta = 0.5$ as well as oscillations in the in-phase condition, which according to the kinematic theory should not occur, can also be explained. Electrons which are diffusely scattered at step edges are takes into account by the step density model. Therefore, the electron beam intensity decreases for higher sample step densities as to the increasing amount of diffusely scattered electrons. This is illustrated in figure 6.9. Applying this model to layer-by-layer growth mode delivers the step density L [Sto88]

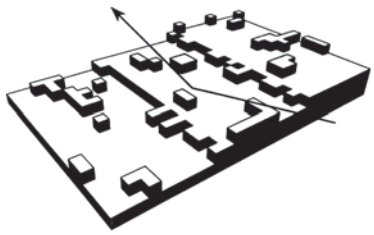

Figure 6.9: *Schematic illustration of the contribution to the step density projected onto the electron beam [Shi92].*

$$L(t) = 2\sqrt{\pi N_0}(1-\Theta)\sqrt{-\ln(1-\Theta)}\,. \tag{6.9}$$

In this equation, N_0 gives the amount of initial nucleation and is a function of the diffusion constant D and the deposition rate ν. As the step density and its maximum depend on the initial nucleation N_0, values of $\Theta \neq 0.5$ are included. The damping of the oscillation amplitude can be explained by expanding this equation for multi-layer systems [Sto88]. At certain incident angles it is observed that the intensity reaches its maximum for half covered layers $\Theta = 0.5$ or that an oscillation with doubled frequency occurs. These effects are explained within the dynamic theory [Joy88].

Experimental Setup

The RHEED setup consists of a STAIB EK-2035-R electron gun, a double-differential pumping system, and a fluorescence screen. In order to filter out light sources other than the high-energy electrons, e. g. the plasma plume or slow electrons, the screen is coated with a thin aluminum film. More information on the used setup is given by [Gün07].

The deposition of oxide materials requires oxygen pressures of $10^{-3} < p < 10^{-2}$ mbar or more. In comparison to the standard application area of RHEED systems, e. g. in molecular beam epitaxy of semiconductor films at $p \approx 10^{-10}$ mbar, the pressure during PLD is considerably high. Taking additionally into account the distance between the electron gun and the fluorescence screen (cp. figure 6.1) as well as the intensity attenuation of the electron beam resulting from electron scattering with oxygen molecules in the deposition atmosphere, double-differential pumping is required.

The electron gun is installed at a deposition chamber flange using electrons accelerated with 25 keV. Scattering losses alongside the tube can be neglected as to the differential pumping system, that ensures a pressure of less than 10^{-7} mbar near the filament and $10^{-4} < p < 10^{-3}$ mbar in the chamber inside the tube. The substrate holder in the PLD setup allows in-plane rotations ϕ of the substrate and rotations θ relative to the electron beam as well. Outside the chamber, the emerging diffraction image is recorded with a charge-coupled device camera (CCD) of type HITACHI KP-M2E/K and digitally processes. It has proved useful to adjust the specularly reflected beam to maximum intensity prior to deposition. All RHEED patterns during the film growth were in direction with the incident electron beam.

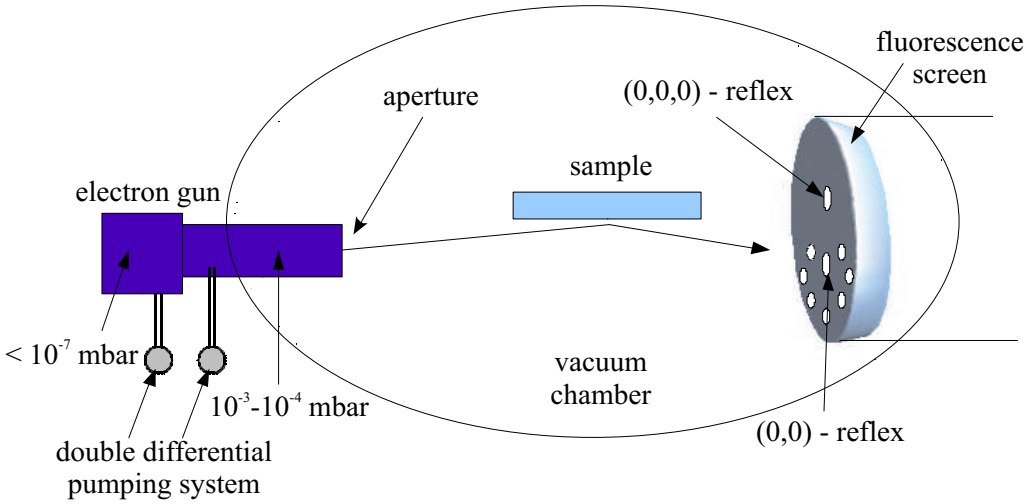

Figure 6.10: *Schematic illustration of the used RHEED setup.*

7 Analytical Techniques

A variety of measuring methods is required to characterize thin crystalline films regarding their structural and optical properties. In this chapter the analytical methods and experimental setups which have been employed throughout this work are described. The characterization process of the films can be subdivided into two parts, namely

i) **in-situ techniques**: The characterization methods in this category include reflectometry (film thickness) and RHEED (surface structure and growth mode analysis; cp. chapter 6.2), both applied during the pulsed laser deposition process of the film.

ii) **ex-situ techniques**: Included therein are analytical tools for examining the structure of the films, such as X-ray diffraction (crystallinity), ellipsometry (refractive index), and atomic force microscopy (surface morphology). The optical properties of the rare-earth-doped films are examined by fluorescence and excitation measurements (including VUV excitation measurements) as well as lifetime measurements.

7.1 X-Ray Diffraction

A non-destructive technique for examining the crystalline structure of the sample material can be found in the X-ray diffraction (XRD) method. It is based on the analysis of the angular intensity distribution of a monochromatic X-ray beam of wavelength λ that is reflected from the sample.

Any given crystal lattice, e. g. cubic, rhombic et cetera, consists of a regular three-dimensional spatial distribution of periodically arranged atoms which form a series of parallel planes separated from each other by a distance d. X-rays propagating through a crystal show a detectable pattern by the varying intensity of the scattered rays. This derives from the interference of the individual X-ray waves scattered at each atom, i. e. at the electrons of the inner atomic shells (Thomson scattering). Two opposite cases can be distinguished.

1. *Amorphous material:* The atoms are randomly arranged in the material, thus the scattered X-rays are incoherent and the resulting intensity is proportional to the total number of scattering centers N.

2. *Crystalline material:* The atoms are arranged in a periodic structure. The optical retardation between the scattered X-rays and the individual atoms is a multitude of the wavelength λ, and positive interference of the scattered X-rays occurs as depicted in figure 7.1. In this case the resulting intensity is proportional to N^2.

Since N is the large amount of atoms, the coherently diffracted X-rays are easily detected in the background of the incoherently scattered X-rays. Thus, the effect of coherency is pronounced. These conditions are summarized in the Bragg diffraction law [Ash76]

$$2d_{hkl}\sin\theta = n\lambda\ , \tag{7.1}$$

in which λ is the X-ray wavelength, n the order of diffraction, θ the incident angle equal to the reflected one, and d_{hkl} the distance between the atomic planes using the Miller indices. The Miller indices[1] are a symbolic vector representation of the orientation of an atomic plane in a crystal lattice. They are defined as the reciprocals of the fractional intercepts of the atomic planes with the crystallographic axes. A set of three integer numbers h, k, and l is the result. The indices find their usage in four different vector notations: (hkl) denoting a crystal plane, $\{hkl\}$ denoting equivalent planes, $[hkl]$ denoting a crystal direction, and $\langle hkl\rangle$ denoting equivalent directions. Atomic plane distances in crystal systems are estimated by

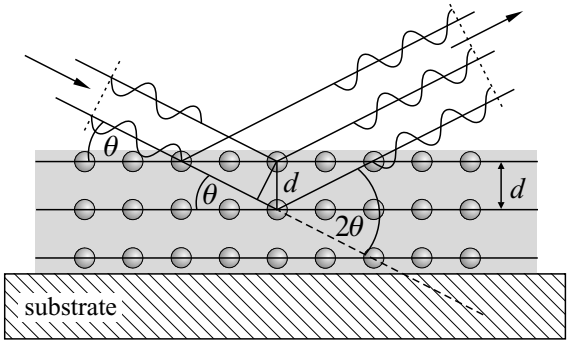

Figure 7.1: *X-ray diffraction*

$$\frac{1}{d_{hkl}} = \sqrt{\left(\frac{h}{a}\right)^2 + \left(\frac{k}{b}\right)^2 + \left(\frac{l}{c}\right)^2} \qquad \text{or} \qquad d_{hkl} = \frac{a}{\sqrt{\frac{4}{3}\left(h^2+hk+k^2\right) + \left(\frac{a}{c}\right)^2 l^2}}\ . \tag{7.2}$$

Therein, the first equation applies to orthogonal and the second to hexagonal systems [Kit86]. For cubic crystals with lattice constant a, as in the case of the investigated sesquioxides and garnets, the interplanar spacing simplifies to $d_{hkl} = a/\sqrt{h^2+k^2+l^2}$. In combination with equation 7.1 the scattering angle of a certain plane in the first diffraction order can be calculated from

$$\sin\theta = \frac{\lambda}{2a}\sqrt{h^2+k^2+l^2}\ . \tag{7.3}$$

Two kinds of diffraction measurements have been carried out in the course of this work. In $\theta - 2\theta$ scans the detector is moved twice the angle compared to the sample movement θ (cp. figure 7.2). Thus, only atomic planes oriented parallel to the incoming rays at $\theta = \omega = 0$ fulfill the Bragg condition of equation 7.1. When applying ω-scans (rocking-curve measurements), the 2θ angle is kept constant and the θ angle is scanned. In doing so, the distribution of crystallite orientations is investigated.

[1] In the case of hexagonal and rhombohedral lattices it is possible to use the Bravais-Miller index, which uses four integer numbers $(hkil)$. Therein, $i = -h-k$ and h, k, and l are the Miller indices.

Many properties of the investigated crystal structures can be derived from the analysis of these diffraction measurements. First of all, a crystalline structure is indicated by the existence of discrete peaks. The peak positions give insight into the directly related atomic planes via the Bragg law 7.1. Moreover, samples of known chemical compositions may easily be examined on phase purity. Having information on the crystal system and the atomic planes, the lattice constants can be calculated using equation 7.2.

Information about the sample texture is contained in the intensity of the diffraction peaks, using the term 'texture' as a synonym for non-random or preferred crystallographic orientation in a polycrystalline material. The more the crystallites are oriented in the same direction, the higher is the detected intensity. One can obtain the texture of a film by comparing the intensities of the corresponding powder diffraction pattern. The intensity $I(h,k,l)$ of a diffraction peak is determined by the distribution of the electrons in the unit cell. It is proportional to the squared absolute value of the structure factor $F(h,k,l)$

$$I(h,k,l) \propto |F(h,k,l)|^2 = \sum\nolimits_r f_r \, e^{2\pi i(hu_r+kv_r+lw_r)} \; . \tag{7.4}$$

In this equation f_r is the atomic form factor, representing the Fourier transform of the charge density of the r^{th} atom, and u_r, v_r, and w_r are the coordinates of the r^{th} atom of the basis.

Apart from peak position and intensity, the width of the diffraction maximum also contains additional information on the crystal system. The relation between the size L of the coherently scattered domains in a sample and the resulting peak width b_L defined as the full width at half maximum (FWHM) is given by the Scherrer equation [Cul78]

$$b_L = \frac{K\,\lambda}{L\,cos(\theta)} \; , \tag{7.5}$$

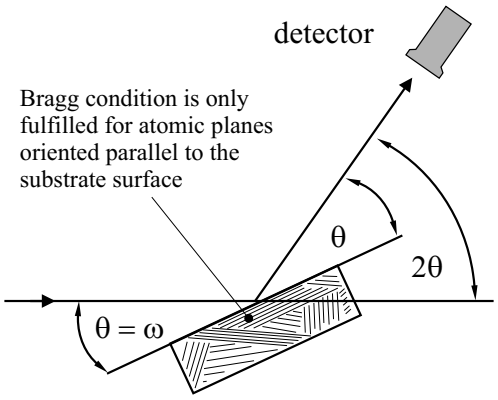

Figure 7.2: *X-ray diffraction measurement: $\theta - 2\theta$ scan*

with $K \approx 0.9 \ldots 1$ being a factor depending on the form of the crystallites, whose size is roughly equal to the ones of the domains. Due to various effects (e. g. stress in the crystal) the observed diffraction peaks are broadened. Assuming that the grown films show no stress, the lower limit of the crystallite size can be estimated by exchanging b_L with the total width of the peaks b_t

$$L = \frac{K\,\lambda}{b_t\,cos(\theta)} \; . \tag{7.6}$$

In addition, the used apparatus also causes a broadening of the peak width due to non-perfect monochromatic radiation and the divergence of the X-rays. The measured peak width b_m is thus a function of the total peak width b_t and of the width b_a (instrumental resolution). Consequently the relation for b_t is [Cul78]

$$b_t = b_m - b_a \; . \tag{7.7}$$

Assuming that both the diffraction peaks as well as the instrumental broadening have a Gaussian profile, the total peak widths are determined by [Bro95]

$$b_t = \sqrt{b_m^2 - b_a^2} \,. \tag{7.8}$$

Though the diffraction lines actually have a form that is described by the Pseudo-Voigt function, which is a mixture of a Gaussian and Lorentzian profile, the line profiles do not deviate much from the Gaussian form and therefore justify the use of this approximation.

The crystallite size of a sample can now be estimated using these two corrections in combination with equation 7.6. For example, when setting $K = 1$, diffraction peaks resulting from X-ray wavelengths of $\lambda_{\mathrm{Cu-K}_{\alpha 1}} = 1.5406$ Å deliver the equation

$$L^{(\mathrm{nm})} = \frac{8.827}{b_t^{(\mathrm{deg})}\, cos(\theta)} \,. \tag{7.9}$$

Although the X-ray measurement technique is mainly used to characterize samples in powder form, it can also be employed for thin film characterization taking into account two limitations:

1. The films need to have a minimum thickness, which grants a certain amount of atomic planes available for diffraction. It is necessary that the intensity of the diffracted X-rays is high enough to be detected.

2. If the film under investigation has no atomic planes parallel to the sample surface, no signal is detected, not even in the case of good crystal quality. It could also be possible that such films are mistaken as amorphous. This worst case is related to films of one predominant crystallite growth direction, especially to single-crystalline samples.

Experimental Setup

As no in-house systems were available, the X-ray diffraction measurements were carried out at the Technische Universität Hamburg-Harburg using a powder X-ray diffraction machine with parallel beam optics of type D8 Advance by the company Bruker Axs.

A copper cathode with monochromatic X-ray radiation of wavelength $\lambda_{\mathrm{Cu-K}_{\alpha 1}} = 1.5406\,$Å is used as X-ray source. Behind the cathode, a Göbel-mirror generates a parallel beam of rays. The samples are arranged on perspex holders and mounted with plasticine. A block of parallel metal plates called Soller-block is located in front of the detector, its geometry defining a tolerance angle. Only rays with a divergence angle smaller than the tolerance angle can pass the Soller-block. Thereby, the fluorescence excited by the X-ray radiation is effectively suppressed without the usage of additional filters. The experimental parameters used in the measurements are 40 kV and 40 mA for the acceleration radiation and the anode current, respectively. The instrumental resolution depends on the selected slit set and is estimated to be $b_a = 0.084°$ for regular scans.

Additional measurements were performed at the Fachhochschule Wedel using a SIEMENS KRISTALLOFLEX 810 diffractometer, which is also supplied with a copper X-ray source operating at 40 kV and 20 mA. This setup provides non-monochromatic X-ray radiation with a removable Ni-screen to filter out the $\lambda_{\mathrm{Cu-K}_\beta}$ emission. Therefore multiple Cu-lines are present in the diffraction spectra: $\mathrm{K}_{\alpha 1}$, $\mathrm{K}_{\alpha 2}$, and a residue of the K_β line. The X-ray radiation occurs at wavelengths of $\lambda_{\mathrm{Cu-K}_{\alpha 1}} = 1.5406\,\text{Å}$, $\lambda_{\mathrm{Cu-K}_{\alpha 2}} = 1.5444\,\text{Å}$, and $\lambda_{\mathrm{Cu-K}_\beta} = 1.3922\,\text{Å}$. However, the Cu-$\mathrm{K}_{\alpha 1}$ and Cu-$\mathrm{K}_{\alpha 2}$ lines are not always resolved because of the reflection broadening.

Overview measurements were performed with the slit set that provided a nominal resolution of 0.15°. High resolution $\theta - 2\theta$ scans, which were used in order to determine the diffraction peak width, and also rocking-curve measurements were done using slit sets with the nominal resolution of 0.05° or 0.018°. An instrumental resolution b_a of 0.04° was determined for the high resolution scans. As the diffraction peaks of lattice matched quasi-homoepitaxial substrate–film materials are closely united in the spectra, it sometimes proved useful to remove the Ni-filter and perform high resolution scans using the Cu-K_β line for analysis.

7.2 Ellipsometry and Reflectometry

The analysis of light reflected from the sample surface is the basis of ellipsometry as well as reflectometry. Both methods are non-destructive measurements and can be performed remotely, especially in situations in which the application of other techniques might be problematic.

Having a thin layer material between two dielectric media, coherent laser light is reflected with an infinite number of reflections to be considered regarding the interference effects. The reflection coefficient of the field amplitude $\tilde{r}$ is defined as

$$\tilde{r} = \frac{\tilde{\varepsilon}_{\mathrm{ref}}}{\tilde{\varepsilon}_{\mathrm{inc}}}, \quad \tilde{\varepsilon} = \varepsilon_0 e^{i\phi} \,, \tag{7.10}$$

with $\tilde{\varepsilon}_{\mathrm{inc}}$ being the complex amplitude for the electric field of the incident light and $\tilde{\varepsilon}_{\mathrm{ref}}$ being the one of the reflected light. For the case presented in figure 7.3, $\tilde{r}$ is given by the infinite progression

$$\tilde{r} = r_{12} + t_{12}\, r_{23}\, t_{21}\, e^{-2i\beta} + t_{12}\, r_{23}^2\, r_{21}\, t_{21}\, e^{-4i\beta} + \ldots \,, \tag{7.11}$$

in which r_{ab} and t_{ab} are the Fresnel reflection and transmission coefficients for the electric field amplitude at the boundary between two dielectric media. The first index denotes the media on the incident side of the boundary, whereas the second index denotes the media on the other side. Variables with 'tilde' emphasize the complex values, containing phase information in addition to the amplitude. The phase shift β between the light being directly reflected from the front surface of the film and the light being reflected from the film-substrate boundary are written as

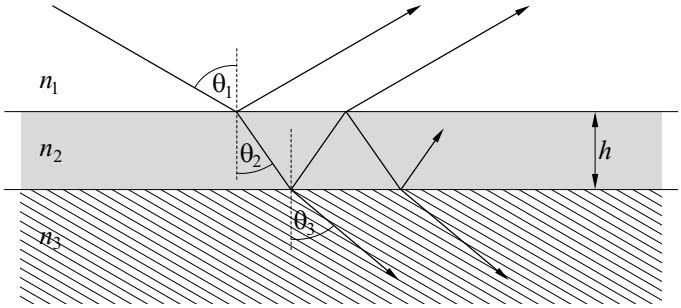

Figure 7.3: *Light reflection from a layered structure*

$$\beta = 2\pi \frac{n_2\, d_2}{\lambda}\, cos(\theta_2) \,, \tag{7.12}$$

with the refractive index of the film material n_1, the film thickness d_1, the wavelength of the light λ, and the light incidence angle inside the film θ_1.

An adaption of equation 7.11 for more complicated cases with more than one layer being present can be done. Considering the case of a single layer between two half-infinite media, i. e. a film on a substrate, the infinite progression of the multiple reflections converges into

$$\tilde{r}^{\sigma,\pi} = \frac{r_{12}^{\sigma,\pi} + r_{23}^{\sigma,\pi}\, e^{2i\beta}}{1 + r_{12}^{\sigma,\pi}\, r_{23}^{\sigma,\pi}\, e^{2i\beta}} \,. \tag{7.13}$$

Here, σ and π denote alternative versions of the same equation for σ- and π-polarizations.

Reflectometry

By reflectometry measurements, the intensity of the reflected light is measured. This is done by determining the intensity reflection coefficient without any phase information. Thus, the intensity reflection coefficient using equation 7.13 can be written as

$$R^{\sigma,\pi} = |\tilde{r}^{\sigma,\pi}|^2 = \frac{(r_{12}^{\sigma,\pi})^2 + (r_{23}^{\sigma,\pi})^2 + 2\, r_{12}^{\sigma,\pi}\, r_{23}^{\sigma,\pi}\, cos(2\beta)}{1 + (r_{12}^{\sigma,\pi})^2\, (r_{23}^{\sigma,\pi})^2 + 2\, r_{12}^{\sigma,\pi}\, r_{23}^{\sigma,\pi}\, cos(2\beta)} \; . \tag{7.14}$$

As intensity measurements have not very high accuracy and contain only little information, single reflection coefficient measurements are rarely used. Instead, the reflection (or transmission) of the sample is measured over a certain wavelength region in order to fit the measured curve with a calculated one. More precise values can be obtained using this systematic for the thickness or refractive index of the film.

It is also possible to continuously monitor the reflection coefficient during the deposition of the film. That was the way in which the reflectometry was used in the context of this thesis: to control the thickness of the deposited films in-situ. Knowing the refractive indices of film and substrate, the absolute intensity is redundant as the form of the signal gives enough information to determine the film thickness. The experimental implementation of this method and the data analysis was already described in chapter 6.

Ellipsometry

The ellipsometry technique is based on the comparison of the polarization states of the incident and reflected light of the sample. Usually the polarization state of the light is named according to the imaginary shape outlined by the end of the electric field vector when looking in the light propagating direction. Knowing linear and circular polarizations as special cases of the polarization states, elliptical polarization is the most general one. Each of these states is described by the ellipticity ε and the orientation θ defining the form of the ellipse as it can be seen in figure 7.4.

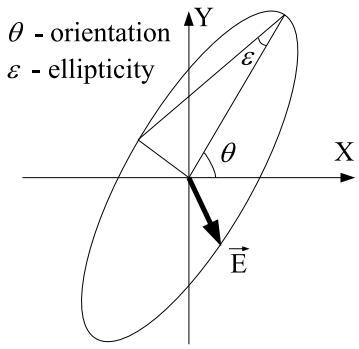

Figure 7.4: *The polarization state of light described by orientation and ellipticity*

The ellipsometry considers the ratio of the reflection coefficients for σ- and π-polarization

$$\rho = \frac{\tilde{r}^{\pi}}{\tilde{r}^{\sigma}} = tan(\Psi)\, e^{i\Delta} \; . \tag{7.15}$$

This complex ratio is more often expressed by two real quantities Ψ and Δ which can be determined by solving the matrix equation

$$\begin{pmatrix} 1 \\ X_{\mathrm{det}} \end{pmatrix} = \begin{bmatrix} 1 & 0 \\ 1 & tan(\Psi)\, e^{i\Delta} \end{bmatrix} \begin{pmatrix} 1 \\ X_{\mathrm{sour}} \end{pmatrix} \; , \tag{7.16}$$

with $X_{\mathrm{det,\,sour}}$ being expressed by experimentally measured $\theta_{\mathrm{det,\,sour}}$ and $\varepsilon_{\mathrm{det,\,sour}}$ in

$$X_{\mathrm{det,\,sour}} = \frac{\tan\theta_{\mathrm{det,\,sour}} + i\,\tan\varepsilon_{\mathrm{det,\,sour}}}{1 - i\,\tan\theta_{\mathrm{det,\,sour}}\,\tan\varepsilon_{\mathrm{det,\,sour}}}\,. \tag{7.17}$$

The ratio of intensities is determined by ellipsometry. In comparison to reflectometry, ellipsometry is the more precise technique, since the experimentally obtained angles ε and θ can be measured with higher accuracy than the intensity. Ellipsometry is thus a more sensitive technique, which maintains the phase value as well. Wavelength-dependent measurements can be used to obtain the dispersion of the material. In conclusion, more information about the sample is gained in such a measurement. A more detailed information about the principles of ellipsometry can be found in [Bas95, Rös90]

Coming to the experimental ellipsometry setup, the commercial ellipsometer EL X-02C of the company DRE was used in the performance of the measurements. It is designed in the rotating analyzer configuration as schematically presented in figure 7.5. A He-Ne laser of wavelength $\lambda = 632.8\,\mathrm{nm}$ makes up the 'left arm' and serves as the light source. No additional polarizer is needed since the laser emission is linearly polarized. With respect to the sample, the laser alignment grants nearly equal light intensities in σ- and π-polarization. The detector and analyzer located in the 'right arm' are rotated by a high-precision step motor with a specified accuracy of 0.002°.

Measurements are performed at different light incidence angles adjusting the position of both arms manually. The reference measurement of the light source is performed by setting both arms horizontally, directly guiding the laser beam into the detector. Controlled by a computer, the ellipsometer data is acquired and analyzed via the supplied software.

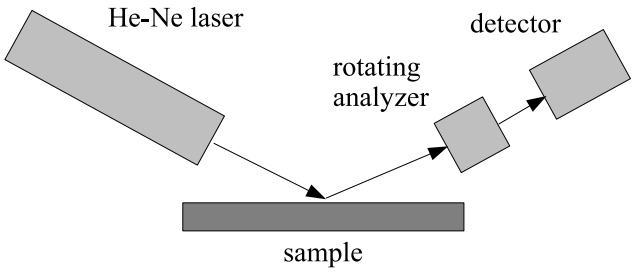

Figure 7.5: *Principle ellipsometer setup*

As mentioned above, ellipsometry is a very sensitive technique. It is therefore possible to examine silica films of several nanometers grown on silicon. However, ellipsometric measurements are not that simple to analyze. As the analysis of the acquired data is based on the comparison of the experimentally obtained values with the ones derived from the simulation, a unique interpretation of the measurements might not be possible. This could be the case if the model parameters deviate substantially from the real ones. Scattering in the investigated samples and substantial deviations of the refractive index can affect the correct analysis of the measurements. Ellipsometry is thus an appropriate technique for precise investigation of the samples with known thickness, refractive indices and extinction coefficients of the film and the substrate. It is not suitable if the parameters are completely unknown or inaccurate. However, reliable data in good consistence with theoretical values can be obtained for the investigated substrates and films. More information on simulation modelling can be found in [Ber66, Rab04].

7.3 Atomic Force Microscopy

With regard to optical properties the surface of substrates and thin films is also of significant importance. If for instance the film interfaces in optical waveguides are of rough nature, the resulting scattering losses may suppress possible waveguiding effects.

By the atomic force microscopy (AFM) technique the film surface can be characterized. This technique applies a probe consisting of a sharp tip with a radius of around 10 nm integrated onto the end of a cantilever, which is raster-scanned across the sample surface using piezoelectric scanners to measure attractive or repulsive forces between the tip and the sample [Bin86]. The AFM technique is thus able to analyze the topography of films, several physical and chemical properties with high lateral and vertical resolution in the nm-range. Detailed information on the AFM technique, its different scanning modes and their theory can be found in the literature [Klu98, Sas00, Mor02, Hof03].

Figure 7.6 illustrates the principle AFM setup. The AFM has three imaging modes to produce topographic images of sample surfaces: contact mode (ionic repulsion forces), non-contact mode (Van der Waals, electrostatic, magnetic or capillary forces), and tapping mode. In all three modes the cantilever is *a)* bent by the tip-sample force interaction and *b)* torsionally deflected by the lateral forces acting between tip and sample. By applying the light pointer principle, in which a laser beam is reflected off the cantilever and onto a segmented photodiode, both movements are detected.

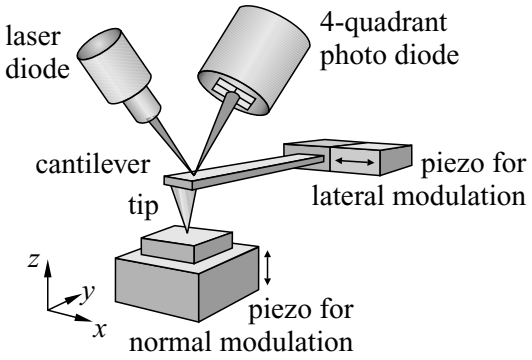

Figure 7.6: *Principle AFM setup*

A particular operating parameter is maintained at a constant level during the scanning process, e. g. the force between tip and sample surface. Through a feedback loop between the optical detection system and the piezoelectric scanners, images are generated. Used for the samples in this work were the contact and non-contact modes. In the contact mode the probe is dragged across the sample surface maintaining a constant bend in the cantilever. A constant deflection is kept through the z-scanner moving the relative position of the sample with respect to the tip as the topography of the sample changes. Under the assumption that the motion of the z-scanner directly corresponds to the sample topography, the feedback mechanism is used to map the topography of the sample during the scan. When applying the contact mode, the sensing of the local mechanical properties of the sample surface, such as the resistance to deformations or frictional forces acting between tip and surface, is also possible. In the non-contact mode the probe is hovering in distances of 10–100 nm to the sample surface. The long-range forces cause the cantilever vibrations as the topography of the sample changes. It can be useful to have a characteristic parameter of the surface roughness in addition to the information on the surface topography. This parameter is generally called root-mean-square roughness R_{RMS} [DIN78] and can be determined by discrete points of the measured surface topography

$z(x_k, y_l)$. It can be written using the number of data points in x- and y-direction N_x and N_y, which are identified by the different indices k and l.

$$R_{\mathrm{RMS}} := \sqrt{\frac{1}{N_x N_y} \sum_{k=1}^{N_x} \sum_{l=1}^{N_y} |z(x_k, y_l) - \bar{z}|^2} \tag{7.18}$$

The value $\bar{z}$ describes a levelled plane with the smallest deviations from the data points (least square fit) [Bra92].

Hard crystalline films, which allow high scanning rates and very sensitive regulation of the tip-surface distance, recommend the contact mode. However, for thin-film layers with flat structures in the atomic scale the non-contact mode leads to better results [Sas00, Gün07].

7.4 Optical Spectroscopy

Employing optical techniques enables the analysis of local structure modifications, which are undetectable with methods based on X-ray diffraction. In the course of this work emission and excitation spectroscopy as well as lifetime measurements were carried out for thin film characterization. The following sections will give an introduction to the employed techniques and the experimental setups.

Absorption spectra of the europium probe ion could not be obtained due to the considerably small film thickness. Absorption cross-sections for interconfigurational transitions are typically in the range of $\sigma_a \approx 10^{-21}$ cm^2. As the produced films have dopant concentrations of a few atomic percents, the density of the optically active ions is approximately 10^{21} cm^{-3}. This results in an absorption length of some millimeters. Therefore, it is not be possible to detect any absorption of the film with thicknesses in the range of $10-500$ nm. Moreover, as the substrate is five orders of magnitude thicker than the grown films, it may heavily influence and overlie any film absorption. Impurities in the substrate, even of minimum size, would be sufficient to dominate the absorption measurements.

Due to these reasons no absolute absorption cross-sections could be determined, and consequently, it was not possible to obtain absolute emission cross-sections by using the reciprocity method as well. Therefore, all the spectra measured in this work only show the spectral photon flux in units of the utilized detector's counting rate.

7.4.1 Fluorescence and Excitation Measurements

A modular fluorescence spectrometer of type Yobin Yvon FL 321 FLUOROLOG-3 was used to carry out fluorescence and excitation measurements of the thin films at room temperature in the ultraviolet and visible spectral region.

In this setup, a high pressure Xenon lamp provides excitation wavelengths between 250 nm and 600 nm, and a double monochromator with a reciprocal linear dispersion of $\Delta\lambda/\Delta x = 2.18$ nm per mm slit width selects the desired wavelengths. Another double monochromator resolves the fluorescence light, this time with a reciprocal linear dispersion of $\Delta\lambda/\Delta x = 2.64$. Depending on the intensity of the fluorescent light, there are three possibilities of light detection: either by a photomultiplier (Hamamatsu R 928P), by a photoncounter (Hamamatsu R 649) or by a CCD camera (Yobin Yvon Spectrum-1 G93). Different band edge filters are used in front of the detection monochromator in order to separate the emitted light from the excitation light. The principle experimental setup is shown in figure 7.7.

The fluorescence spectra are measured at a fixed excitation wavelength. By using the detection monochromator and one of the described detection units, a wavelength-dependent collection of the fluorescence light is achieved. The recorded signal S is corrected by the spectral transmission of the detection monochromator and the spectral sensitivity of the detection units. Excitation spectra are obtained by detecting the spectral photon flux of a particular emission band with respect to the variation of the excitation wavelength. Besides the fluorescence signal S, the signal of the excitation is recorded by a reference diode resulting in a signal R which represents the signal of excitation including the spectral distribution of the lamp and the spectral sensitivity of the monochromator. Thus, the corrected signal of the fluorescence is $S_{\text{corr}} = S/R$.

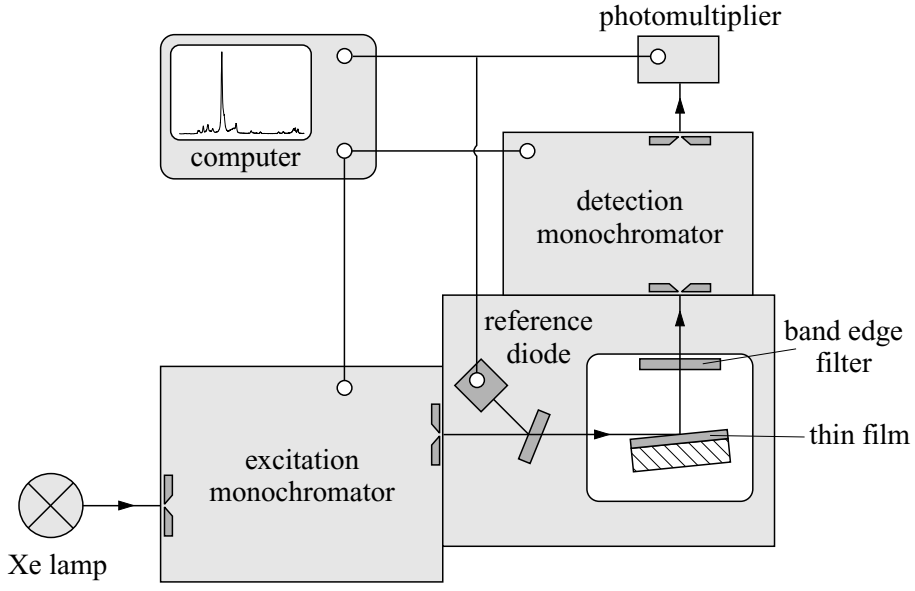

Figure 7.7: *Schematic setup of the* FLUOROLOG *spectrometer*

7.4.2 Lifetime Measurements

An excited state i of an optically active ion in a bulk crystal has the lifetime

$$\tau^V(i) = \frac{1}{k^V(i)}\,, \tag{7.19}$$

with $k^V(i)$ denoting the entire transition probability of all radiative and non-radiative transitions from state i into various destination states. Due to point defects and especially surface effects the lifetime in thin films can be reduced according to

$$\tau^F(i) = \frac{1}{k^V(i) + \sum_j k_j^Q(i)}\,. \tag{7.20}$$

Therein, $k_j^Q(i)$ is the transition probability from the excited state i due to an additional decay channel j, which does not exist in the bulk crystal. A lengthening of the fluorescence lifetime may occur in thin films whose thickness is smaller than the wavelength of the fluorescence light. In this case, the refractive index n_f of the film is influenced by the refractive indices of the neighboring media ($n_\mathrm{f} \rightarrow n_\mathrm{eff}$). Consequently, the lifetime of an electric dipole transition meets the following proportionality [Mel99]:

$$\tau \sim \frac{1}{f}\frac{\lambda^2}{\frac{n}{9}(n^2+2)^2}\,. \tag{7.21}$$

In this equation, f denotes the oscillator strength of the transition, whereas the second term is referred to as *Lorentz correction*. This term describes the increase of lifetime for decreasing refractive indices. Therefore, ultra-thin films surrounded by lower refracting materials, such as air, have a higher fluorescence lifetime in comparison to bulk material.

Experimental Setup

Lifetime measurements of thin films at room temperature were carried out at the Institute of Physical and Theoretical Chemistry, University of Tübingen[2], employing a fluorescence spectrophotometer of type Varian Cary Eclipse. The setup is very similar to the one used for fluorescence and excitation measurements (cp. figure 7.7). Instead of a cw-lamp a Xenon flashlamp ($\approx 1\,\mathrm{ms}$ FWHM) serves as excitation source here.

In order to prevent an interference with the decaying flash lamp pulse, the lifetime measurements were performed using a delay time of 0.4 ms. A gate time of 0.01 ms and a total decay time of 6 ms were used. The Eu^{3+} lifetimes are measured by excitation into the charge transfer band and detection of the hypersensitive ${}^5D_0 \rightarrow {}^7F_2$ transition. Only for aluminum garnet films the stronger ${}^5D_0 \rightarrow {}^7F_1$ transition is used.

[2]The measurements were performed by Dr. Sebastian Bär and Dr. Dmitry Khoptyar.

7.4.3 VUV Measurements

With excitation wavelengths between 58 nm and 330 nm being available, additional excitation measurements in the vacuum ultraviolet spectral region (VUV) were performed at the SuperLumi station. Synchrotron radiation of the electron-positron storage ring DORIS at DESY – Hamburg, Germany, serves as source for this wavelength region. A simplified setup of this complex platform is drawn in figure 7.8. Detailed descriptions are found in [Gür83, Kam89, Klo89, Möl86, Var94]. A primary monochromator with a spectral resolution of 0.3 nm spectrically separates the synchrotron radiation. A secondary monochromator is used to analyze the fluorescent light of the excited sample, which is detected either with a photomultiplier (excitation measurements) or with a CCD camera (emission measurements). Liquid helium is used to cool the sample holder down to 10 K.

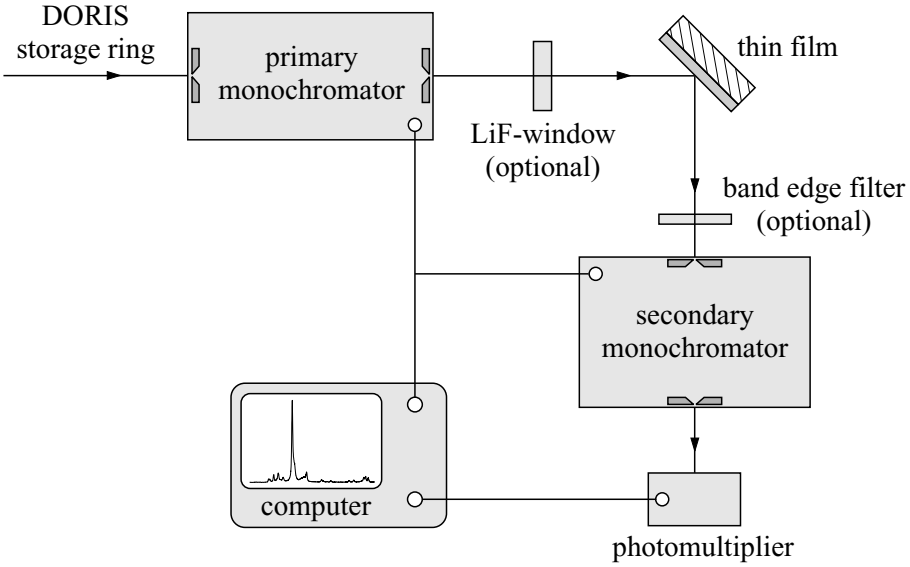

Figure 7.8: *Schematic setup of the* SuperLumi *station for VUV excitation measurements*

8 Characterization of Heteroepitaxial Thin Films

This chapter deals with the characterization of lattice matched heteroepitaxial thin film systems. In accordance with the possibilities of lattice matching presented in section 5.2 the different lattices of substrate and film material are combined in non-integer multiples (sections 8.1 and 8.2) or integer multiples (section 8.3) of the lattice constants. In addition, some measuring characteristics which are also valid in chapter 9 are introduced in this chapter.

8.1 Composite Sesquioxide Films on Sapphire

Burmester and Bär investigated yttria layers on alumina substrates with a lattice mismatch of 4.73 % [Bur02, Bär04]. An approach for a lattice mismatch reduction has been done by Rabisch with a mixture of scandia and lutetia $(Sc_{0.54}Lu_{0.46})_2O_3$ as layer material [Rab04]. These thin films were grown using the EBV technique. However, different vapor pressure coefficients of scandia and lutetia caused a composition shift of the grown 'lattice matched' films. Consisting of $(Sc_{0.81}Lu_{0.19})_2O_3$, the films had a lattice constant of $a = 9.948\,\text{Å}$ with a lattice mismatch of -1.51 % to the substrate. A major drawback of the EBV technique is that the stoichiometrical transfer depends on the boiling points and vapor pressures of the individual components used as starting material. This system was again investigated using the advantages of the PLD technique, in which the stoichiometry of the target material is preserved in the deposited film.

8.1.1 Lattice Matching

α-Y_2O_3 has a lattice constant of $a_{Y_2O_3} = 10.603\,\text{Å}$. The lattice mismatch of α-Y_2O_3 grown in $\langle 111 \rangle$ direction on the (0001) surface of an α-Al_2O_3 substrate amounts to 4.73 %. Perfect lattice matching is accomplished with the lattice constant $a_f = 10.102\,\text{Å}$. However, as there is no sesquioxide to meet this requirement, composite systems like $(Y_{1-x}Sc_x)_2O_3$ and $(Sc_{1-x}Lu_x)_2O_3$ offer a solution. It has already been set forth that these mixed sesquioxides are of the same structure as the single-component sesquioxides of scandium, yttrium, and lutetium [Bär04, Rab04]. They also crystallize in the cubic bixbyite structure, whereby the

cation sites in the lattice are occupied statistically (cp. sections 2.1 and 5.3). The lattices of substrate and film combine according to the relation $3 \times a_s = \sqrt{2}\, a_f$ (cp. section 5.2).

The lattice constants of these composite crystals are calculated from the Vegard law in equation 5.3. A film lattice constant of $a_f = 10.102$ Å can be achieved by the compositions $(Y_{0.331}Sc_{0.669})_2O_3$ and $(Sc_{0.541}Lu_{0.459})_2O_3$. From these two sesquioxide configurations the latter is preferable because of the more balanced composition between the two ionic components with x being closer to the value 0.5. The negative effect of clustering, in which domains of purely one compound are formed, is more likely to occur in $(Y_{0.331}Sc_{0.669})_2O_3$ as the amount of scandium is twice as high as the one of yttrium.

Taking additionally into account the low-concentration doping with Eu^{3+}, which is necessary for spectroscopic analysis, the lattice matching has to be slightly adjusted. Some sesquioxides like Eu_2O_3 do not normally crystallize in the bixbyite structure. As these cubic lattice constants are experimentally unknown, an ionic radii estimation has been used. According to chapter 2, the rare-earth ions are sixfold coordinated in sesquioxides, but eightfold coordinated in orthovanadates (chapter 9.2) and aluminum garnets (chapter 9.3). Figure 8.1 illustrates the dependency between the sesquioxide lattice constant and ionic radius of the incorporated trivalent rare-earth ions.

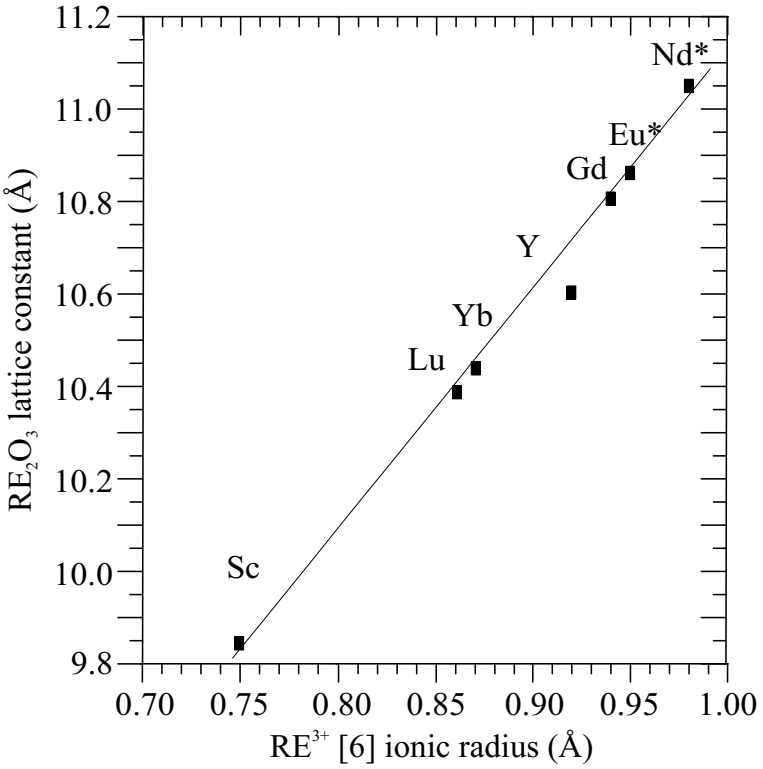

Figure 8.1: *Ionic radii of trivalent lanthanides in dependence of the lattice constants [Kam90]. The unknown lattice constants indicated with '*' are linearly extrapolated.*

First films have been deposited using a mixture of $(Eu_{0.02}Sc_{0.53}Lu_{0.45})_2O_3$, which will be referred to as composition [1]. In the progress of this work, this initial mixture was modified to $(Eu_{0.02}Sc_{0.5473}Lu_{0.4327})_2O_3$, referred to as composition [2].

8.1.2 Structural Characterization

The crystal structure of the deposited films has been examined with X-ray diffraction measurements. Average crystallite sizes $L_\perp$ perpendicular to the substrate surface have been estimated by the full width at half maximum (FWHM) of the film peaks using the Scherrer formula (equation 7.6). Lattice constants $a_\perp$ have been determined by the peak

positions (cp. chapter 7.1). A list of deposited films with the entire set of deposition parameters is given in appendix A. Due to the continuous improvement of the pulsed laser deposition setup during this work, the films are tagged in order to distinguish their fabrication characteristics. A resistive heater with no direct thermal contact to the substrate and a maximum effective temperature of 750°C has been used for films $<$ S080. Films $\geq$ S080 have been deposited using a laser-based heater with the substrates mounted on SiC or Si_3N_4 heat-spreader. In accordance with the insights gained by the work of [Gün07], pre-deposition substrate treatment in combination with atomic force microscopy has been performed in the last stage of this work as an additional preparation step for the in-situ reflection high-energy electron diffraction measurements during the deposition process. These films are tagged 'SR'.

In X-ray diffraction polarization effects, divergence, and non-perfect monochromatic radiation lead to an intensity attenuation at higher diffraction angles [Kri90, Bur02]. Because of this behavior only crystal-planes of lower diffraction order are often detected with sufficient intensity in thin films. To a certain extent the intensity at higher angles also depends on the employed X-ray device as in newer apparatuses it is boosted. The low resolution of higher-order crystal-planes in some measurements has two reasons: First, the device used at the Fachhochschule Wedel is of older age. Second, the film intensity maximum in the diffraction spectra measured with up-to-date devices at the Technische Universität Hamburg-Harburg is determined by the highest diffraction peak. All other diffraction peaks have an intensity resolution relative to this maximum, which in general belongs to the substrate. An exclusion of the substrate peak in the diffraction spectra has been avoided, as a variation in absolute measuring positions is only obtained with reference to the substrate reflections. This information is essential in order to estimate the lattice matching correctly. In agreement with this fact, the diffraction measurement analysis focuses on crystal-planes of lower order, in this case the $\{222\}$ reflection.

Although thickness series with ultra-thin films of some nanometers thickness were also fabricated in the course of this work (cp. appendix A), emphasis is laid on films with $50\,\mathrm{nm} < d_{\mathrm{film}} < 100\,\mathrm{nm}$. This is due to the fact that Burmester, Bär, and Rabisch already reported film growth effects in very thin films and assessed that crystalline bulk-like properties require film thicknesses of at least 20 nm [Bur02, Bär04, Rab04]. In addition, the analysis of lattice matching is based on pronounced and distinct reflection peaks, which necessitate a certain film thickness.

Figure 8.2 contains X-ray spectra of Eu-doped $(Sc, Lu)_2O_3$ films with (a), (b), and (c) belonging to a thickness series fabricated at identical deposition conditions from a sintered $(Sc, Lu)_2O_3$ target of composition [1]. Therein, a substrate temperature of $T = 700°C$, a constant oxygen pressure of $p_{o_2} = 7.9 \times 10^{-3}\,\mathrm{mbar}$, and a repetition rate of $\nu = 10\,\mathrm{Hz}$ were used. The collected data are summarized in table 8.1.

Besides the {0006} reflection of the α-alumina substrate at 41.75° the diffraction spectra (a) to (c) show the {222} and – in cases (a) and (b) – also the {444} film peak. The {222} reflection gains intensity with increasing film thickness, as does the {444} reflection. No diffraction peaks from atomic planes other than in ⟨111⟩ direction are present, which gives evidence to a highly textured film growth in this crystal orientation. Although, an initial shift of the {222} peak position to smaller angles with increasing film thickness is observed, the degree of crystallinity of the composite sesquioxide films is assumed to be relatively high with regard to the X-ray diffraction analysis. In comparison, the {222} reflection for the 50 nm thick film (c) resides at 30.259° leading to a film lattice constant of $a_\perp = 10.224\,\text{Å}$ with a lattice mismatch $f = 1.19\,\%$ whereas for the 200 nm thick film (b) it resides at 30.155° leading to a film lattice constant of $a_\perp = 10.258\,\text{Å}$ with a lattice mismatch $f = 1.52\,\%$. No substantial change in peak position takes place comparing the 200 nm with the 500 nm film; a deviation of 0.01° in the 2θ position can also stem from a random measuring shift [Kuz06]. Thus, the composition [1], estimated to achieve lattice matched Eu(2%):$(\text{Sc},\text{Lu})_2\text{O}_3$ films on sapphire, seems to be off-lattice with $f \leq 1.19\,\%$. The initial lattice mismatch, observed in (c) after 50 nm, may result in strain due to defects. These are compensated by elastic deformations at first. However, with increasing film thickness the stress-relaxation mechanisms result in plastic deformations and the lattice constant shift observed in (b) reflects the film lattice expansion due to non-compensable stress (cp. figure 5.4). When estimating the crystallite size $L_\perp$ it becomes apparent that the ratio of crystallite size to film thickness rapidly decreases with growing film. The size of $L_\perp = 21.2\,\text{nm}$ for the 50 nm thick film S013 increases only little for film thicknesses up to 500 nm. With this film composition and these deposition parameters the crystallite size seems to approach a limit of $\approx 25\,\text{nm}$.

In addition to the θ–2θ-scans, the out-of-plane orientation of the crystallites corresponding to atomic planes not parallel to the surface is investigated by rocking curve measurements (ω-scans), which explains the oddity of underperforming crystallite sizes with increasing film thickness. It can be seen in figure 8.3, that the ⟨111⟩ crystal axes of the 200 nm thick film are aligned along the film normal direction within 4.48° of FWHM. A strong broadening is observed due to relatively small (111) crystallites in the film, as the substrate peak has a width of 0.32° in comparison.

	Deposition		**Reflection**		**Film Properties**				**Tag**
	d_{film}(nm)	T_{sub}(°C)	peak	2θ(deg)	b_m(deg)	$L_\perp$(nm)	$a_\perp$(Å)	f(%)	
[1]	500	700	{222}	30.162	0.380	24.2	10.256	1.50	S011
[1]	200	700	{222}	30.155	0.391	23.5	10.258	1.52	S012
[1]	50	700	{222}	30.259	0.434	21.2	10.224	1.19	S013
[2]	100	975	{222}	30.439	0.258	35.9	10.165	0.62	S084
[2]	50	1050	{222}	30.571	0.225	41.3	10.122	0.12	SR06

Table 8.1: Calculation of the crystallite size and the lattice constant of $(\text{Sc},\text{Lu})_2\text{O}_3$ films determined by X-ray diffraction. Measured peak positions 2θ and peak widths b_m are fitted by a Gaussian profile. For $L_\perp$ the instrumental resolution b_a is considered. The different film compositions are indicated by [1] and [2].

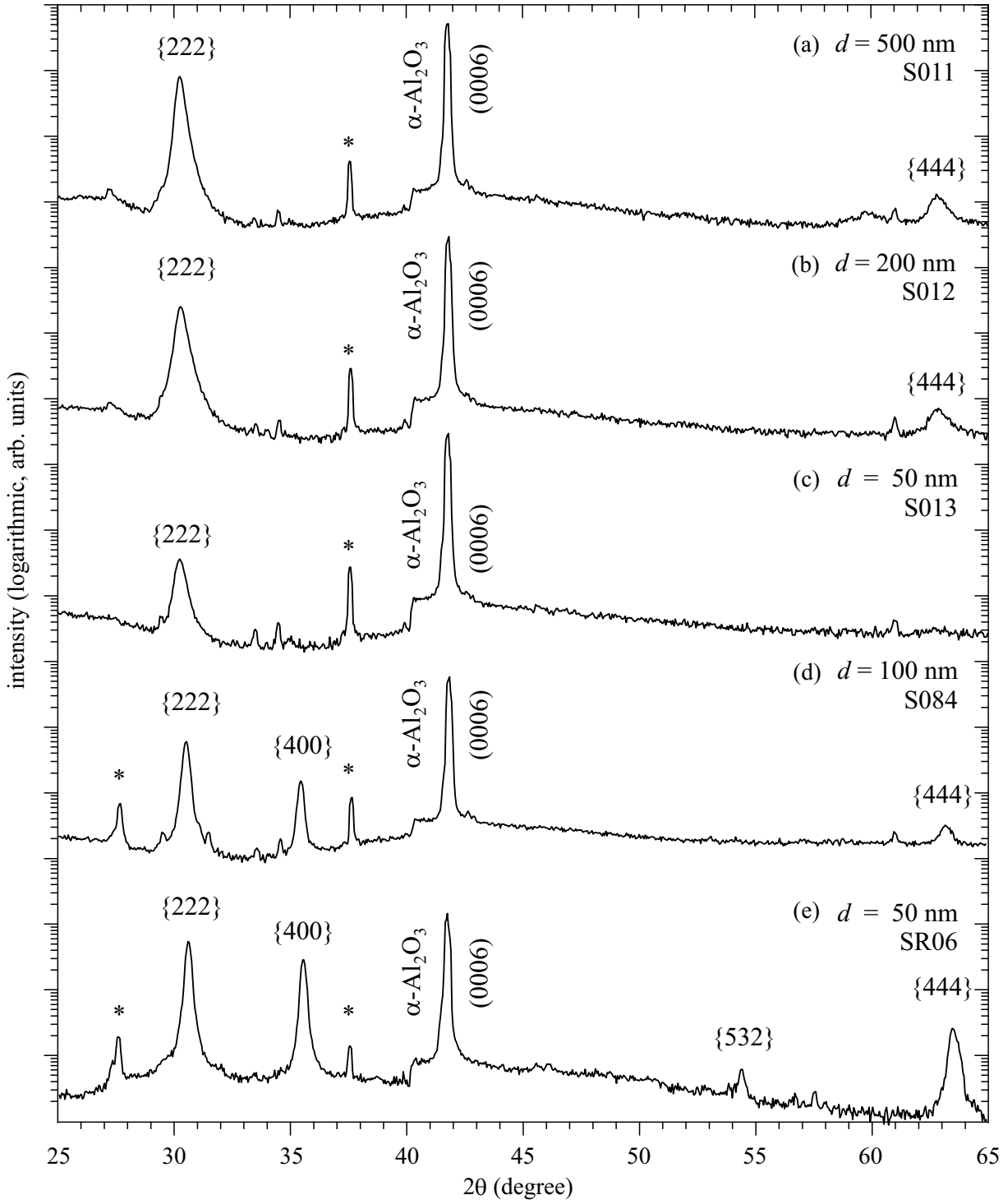

Figure 8.2: *X-ray measurements of Eu-doped $(Sc, Lu)_2O_3$ films of various thickness grown on α-Al_2O_3. Diffraction peaks indicated with '*' result from the residual Cu-K_β emission.*

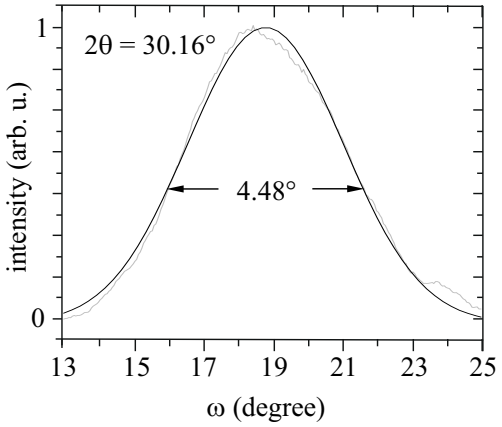

Figure 8.3: *Rocking curve fit of the S012 {222} reflection peak.*

The spectra (d) and (e) belong to thin films deposited by using the modified film composition [2]. The lattice mismatch in both cases is reduced notably, as the 100 nm thick film S084 has a lattice constant of $a_\perp = 10.165\,\text{Å}$ with a mismatch of $f = 0.62\,\%$ and the 50 nm thick film SR06 one of $a_\perp = 10.122\,\text{Å}$ with a mismatch of $f = 0.12\,\%$. For these films, the substrate temperature was raised to $\approx 1000°\text{C}$. S084 has been deposited with an oxygen pressure of $p_{o_2} = 1 \times 10^{-2}\,\text{mbar}$ from a crystalline target, SR06 has been deposited with an oxygen pressure of $p_{o_2} = 9 \times 10^{-3}\,\text{mbar}$ from a sintered target. The repetition rate was $\nu = 1\,\text{Hz}$ for both films. Apart from the lattice matching increase due to the modified composition [2], bigger crystallite sizes could be obtained. In S084 the crystallites ($L_\perp = 35.9\,\text{nm}$) constitute more than one-third of the film thickness whereas the crystallite size $L_\perp = 41.3\,\text{nm}$ of SR06 is nearly the film thickness. However, in contrast to the previous spectra the diffraction patterns of (d) and (e) indicate polycrystalline film character, as an additional reflection is seen. Being roughly one order of magnitude smaller for the 100 nm film (d), it almost reaches the same intensity as the characteristic {222} peak in the 50 nm film.

Although Zhang et al. attributed the shift in Y_2O_3 from ⟨111⟩ to ⟨100⟩ orientation with increasing oxygen gas pressure to a change in oxygen vacancies [Zha98], the rise of this additional peak at 35.45° – temporarily referred to as $(Sc, Lu)_2O_3$ {400} reflection – may also be due to subplantation effects of high-energy plasma species which hit the substrate surface. These effects have already been observed by S. Bär for pulsed laser deposition of Y_2O_3 films on α-Al_2O_3 [Bär04]. A second phase in the films could be identified as orthorhombic $YAlO_3$ (cp. chapter 2.3), which had been initially interpreted as {400} reflection of Y_2O_3. This phase resulted from subplantation of yttrium particles. Orthorhombic $LuAlO_3$ has the lattice constants $a = 5.11\,\text{Å}$, $b = 5.33\,\text{Å}$, and $c = 7.33\,\text{Å}$ and its {200} reflection would result in $2\theta = 35.1°$. No $ScAlO_3$ exists due to the comparably small ionic radius of Sc^{3+}, however a mixture of (Sc,Lu)AlO_3 may be possible due to the compensating influence of Lu^{3+} on the lattice. The formation of a second phase with (Sc,Lu)AlO_3 due to subplantation and interdiffusion is a possible explanation of the additional diffraction peak and would match the {200} reflection of this orthorhombic lattice. Mixtures of $Lu_x(RE)_{1-x}AlO_3$ are known in literature and have been characterized by J. Chval et. al. [Chv00].

Deposition from the crystalline target in comparison to a sintered target did not prove to be of advantage. Although (d) and (e) show similarities, and although better results regarding crystallinity and lattice mismatch have been obtained from a sintered target, this is seen in no context of the target material density. No improvements are achieved by increasing the target density from about 90 % to 100 % (cp. chapter 6). The smaller mismatch and the higher degree of crystallinity in the 50 nm film are ascribed to the substrate treatment prior to deposition (cp. chapter 6.1) and the higher deposition temperature.

Further insights are obtained by rocking curve measurements shown in figure 8.4. For the 50 nm thin film SR06 both crystal axes ⟨111⟩ of the sesquioxide phase and ⟨100⟩ of the assumed perovskite phase are aligned along the film normal direction within 0.72° FWHM peak width for the {222} and 0.74° for the assumed $(Sc, Lu)AlO_3$ {200} reflection. In addition, these peaks superimpose two much narrower peaks, each having a FWHM width of ≈0.07°. The two contributions for each peak can be related to a two layer structure within the film. Most probably an interface layer between substrate and film with a high density of structural defects has been formed at the initial growth state, which contributes to the broad peak. The extremely narrow contribution results from the above grown region with much better structural quality. However, the existence of two different phases within the grown film is not completely understood and has to be further investigated.

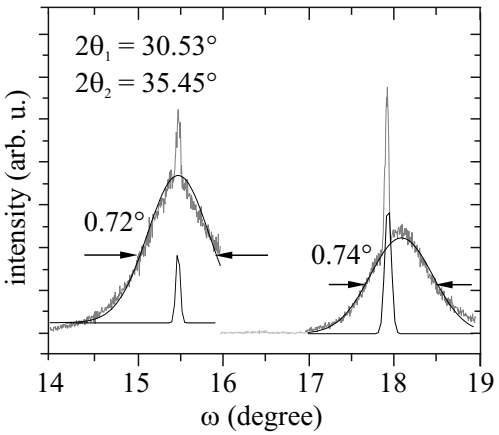

Figure 8.4: *Rocking curve fit of the SR06 {222} and {400} reflection peak.*

Comparing the deposited crystalline composite films to crystalline Y_2O_3 films also grown on sapphire [Bur02, Bär04], the properties appear to be of similar kind. As these films had a lattice mismatch of 4.7% no statements can be made on peak positions. S. Bär obtained a FWHM peak width of 0.193° from a 100 nm film and one of 0.57° from a 20 nm film. The rocking curve of a 500 nm film was estimated to be 0.74°. These films were deposited at $\nu = 10$ Hz using substrate temperatures of 700°C at oxygen pressures of 5×10^{-2} mbar [Bär04]. P. Burmester characterized a 22 nm film which had a peak width of 0.45° and was deposited at 850°C with 3 Hz and 10^{-2} mbar of oxygen atmosphere [Bur02].

The 100 nm film peak width 0.193° of Bär is comparable with the 100 nm S084 film, although the yttria film indicates a higher crystallinity than the composite film. The diffraction spectra of Bär also reveal additional reflections due to subplantation. By gradually decreasing the used pulse energies, subplantation effects should be prevented while keeping the high temperatures required for high degrees of crystallinity.

8.1.3 Surface Structure and Topography

Correlated analysis of the surface structure by RHEED measurements and surface topography by atomic force microscopy enable a better understanding of the film growth. The analysis of the X-ray diffraction measurements are strengthened by evaluation of diffraction patterns and oscillations obtained by in-situ RHEED.

Figure 8.5 shows the RHEED intensity and patterns during the growth of film SR06. In ⟨111⟩ oriented sesquioxide films with cubic structure the step height x of one monolayer (ML) is calculated from $x = a/2\sqrt{3}$ ($x = 2.92$ Å for $a = 10.102$ Å). The required number of pulses for one monolayer growth of [111] $(Sc, Lu)_2O_3$ has been estimated to be 43. No change in symmetry or spacing of the RHEED pattern occurs during the continuous

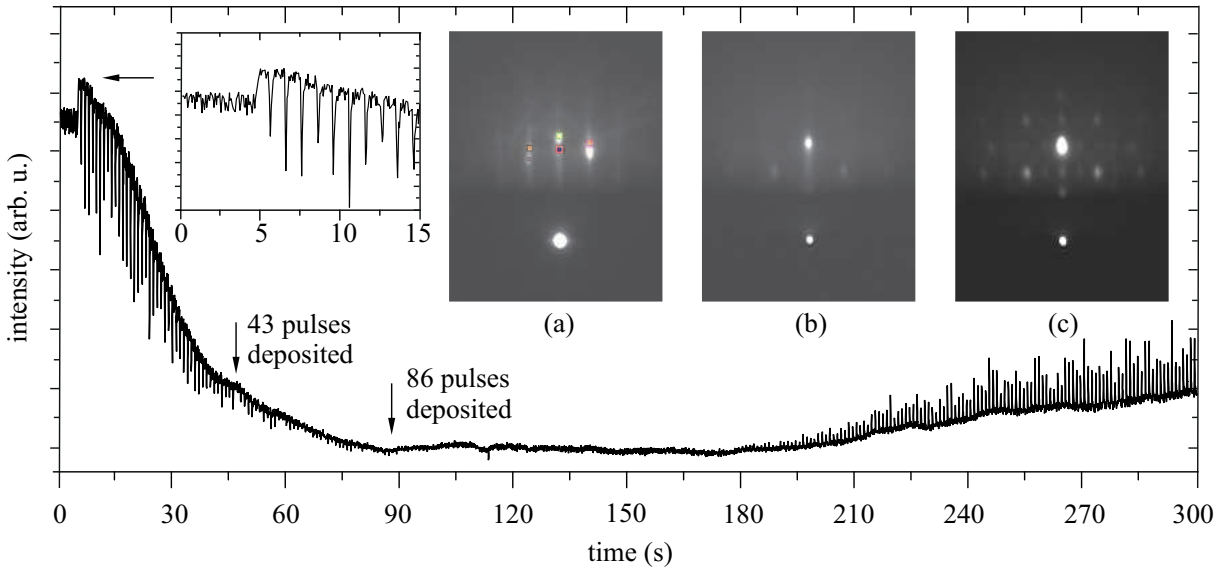

Figure 8.5: *RHEED intensity during continuous pulsed laser deposition of film SR06. Diffraction patterns after (a) 0.29 nm (43 pulses / 1 ML), (b) 10 nm (300 pulses), and (c) 50 nm are shown in the insets.*

growth at 1 Hz of the first 4 – 5 monolayers (around 180 s). The corresponding RHEED intensity decreases and almost vanishes, which indicates amorphous film growth. After the growth of around four monolayers crystallization is observed due to the constantly recovering intensity. Considering the initial diffraction pattern, the stripes shown in inset (a) indicates two-dimensional growth in the default ⟨111⟩ direction. During the following deposition of up to 10 nm a transition from two-dimensional growth to three-dimensional growth is indicated by the RHEED pattern in inset (b). This becomes more pronounced in the RHEED image in inset (c) at the end of deposition.

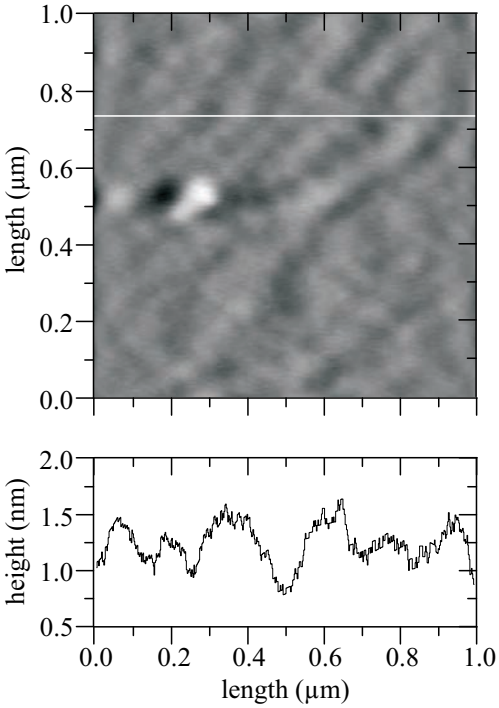

Figure 8.6: *AFM image of the 50 nm thin film SR06.*

A detailed analysis of the specularly reflected electron beam during the initial growth reveals that despite the strong intensity decrease, which indicates amorphous growth, the relaxation after each pulse (magnification in figure 8.5) is ascribed to pseudomorphically grown crystalline regimes. Another reason for this assumption is the occasional moderate rise of the RHEED intensity, first after 43 pulses as this corresponds to the growth of one monolayer (black arrow). Although this is in good agreement with the X-ray diffraction analysis, it is still not clear if the crystallization after growth of four monolayers is due to the subplantation with subsequent $(Sc, Lu)AlO_3$ formation. Other-

wise, the observed crystallization can also be interpreted as film growth of $(Sc, Lu)_2O_3$ in the preferred $\langle 111 \rangle$ direction, after an interface with much higher defect density was formed due to stress compensating reasons. As the existence of another highly crystalline phase in the film is known by evaluation of the XRD data, it is possible that the crystallization observed after four monolayer by the continuous intensity rise has two contributions and thus includes the growth of [111] $(Sc, Lu)_2O_3$ as well as [100] $(Sc, Lu)AlO_3$. In conclusion, the formation of an amorphous interface as seen by RHEED and XRD measurements, prevents a sustaining layer-by-layer growth on α-Al_2O_3.

Figure 8.6 shows the surface topography analyzed ex-situ by atomic force microscopy (AFM). In analogy to the RHEED data three-dimensional islands dominate the film surface, having an height of around 6 Å. An RMS value of 1.62 Å describes the average surface roughness of the scanned area of $1 \times 1\,\mu m^2$. Because of the pre-deposition substrate treatment the surface is still atomically flat. However, the ordered step structure has changed to a more or less disarranged island structure. The RMS value is extremely low in comparison to known literature values, which are often several nanometers high. No droplet formation could be identified over an area of $10 \times 10\,\mu m^2$.

8.1.4 Spectroscopic Analysis

Optical properties of the grown composite films were investigated by luminescence measurements (excitation and emission), VUV measurements, and lifetime measurements. In addition, the refractive indices of films were determined by ellipsometry.

Fluorescence and Excitation Measurements

In order to analyze the local crystal structure in the grown film, the luminescence properties of the deposited composite sesquioxide films have been investigated using the Fluorolog spectrometer. Important for an efficient excitation mechanism is the charge transfer band (cp. chapter 3.3), which originates from Eu^{3+} and O^{2-} interaction ranging from 200 nm to 265 nm. The interaction process consists of an electron transfer from the oxygen ligands to the europium ion $O(2p^2)Eu(4f^6) \rightarrow O(2p^1)Eu(4f^7)$. The emission spectra are measured by excitation with $\lambda_{ex} = 255$ nm into this band. Emphasis is placed on the question, whether solid solutions used for film deposition cause a peak broadening, which indicates a symmetry distortion in the local crystal structure.

A polycrystalline sample served as reference for the spectroscopic properties of Eu^{3+}-doped α-$(Sc, Lu)_2O_3$ films. This reference sample was obtained by fusing powder of 5 N purity with molar composition [2] Eu_2O_3 / Lu_2O_3 / Sc_2O_3 = 0.002 / 0.4327 / 0.5473 in a regular Czochralski crystal growth setup. Prior to characterizing the crystalline films, this polycrystalline composite sample is compared to single-component Y_2O_3. The targets in spectra (b) to (e) are all obtained by the fusion method described above and can be regarded as polycrystalline.

The emission spectra of a single-crystal Y_2O_3 (a) with narrow transition linewidths is shown in figure 8.7. The strong $^5D_0 \rightarrow {}^7F_2$ transition at 611 nm appears very sharp and

narrow, as does the comparably tiny $^5D_0 \rightarrow {}^7F_0$ transition at 580 nm. These are the characteristics of a perfect local symmetry given in a single-crystal. The peaks in emission spectra (b) of an Y_2O_3 target shows a slight broadening. A minor shift of the peak positions to shorter wavelengths is observed, due to the lower degree of crystallinity in the sample. However, all distinct features shown in (a) are present, as the local symmetry of the europium ion is not distorted. When comparing the emission spectrum of Y_2O_3 (b) with the ones of Lu_2O_3 (c) and Sc_2O_3 (d) a continuous shift of the peak positions to

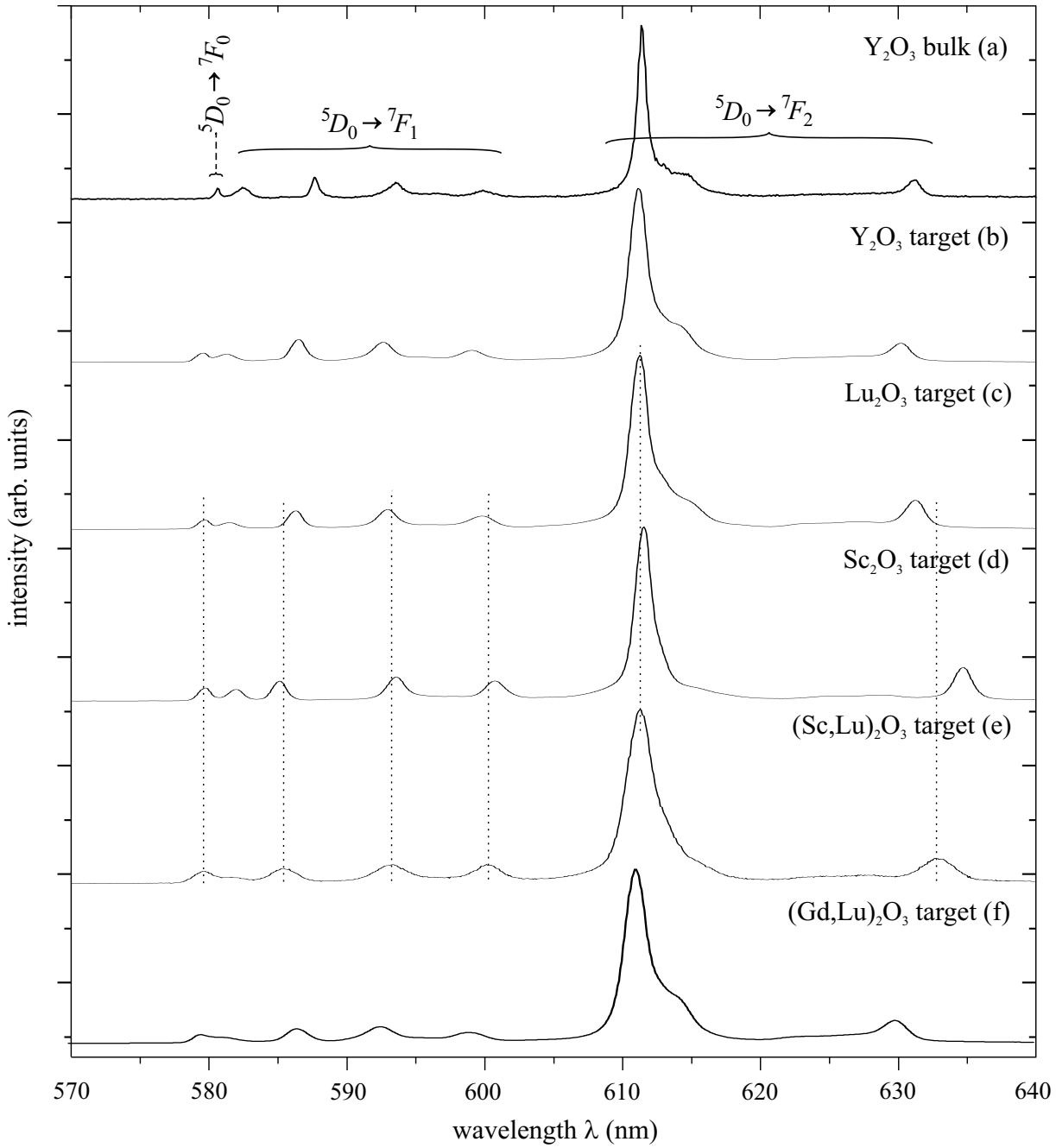

Figure 8.7: *Comparison of different Eu-doped target emission spectra.*

larger wavelengths is recognized. The right shoulder of the strong emission at 611 nm in Y_2O_3 is less pronounced in Lu_2O_3 (c) and nearly disappears in the spectrum of Sc_2O_3. These peculiarities are explained by the different ionic radii which result in crystal fields of varying strength. The emission spectrum (e) of the composite sesquioxide is basically a combination of the spectra (c) and (d). As to the slightly different transition wavelengths in lutetia and scandia, all emission peaks are broadened. This is best noticed regarding the peak at 633 nm: the wavelength in lutetia is smaller (630 nm) whereas the one in scandia is bigger (635 nm). Due to the same reason, the characteristic transition at 611 nm is broadened. The linewidth for this transition is 1.31 nm in Y_2O_3 (b), 1.25 nm in Lu_2O_3 (c), 1.28 nm in Sc_2O_3 (d), 1.86 nm in $(Sc, Lu)_2O_3$ (e), and 1.72 nm in $(Gd, Lu)_2O_3$ (f).

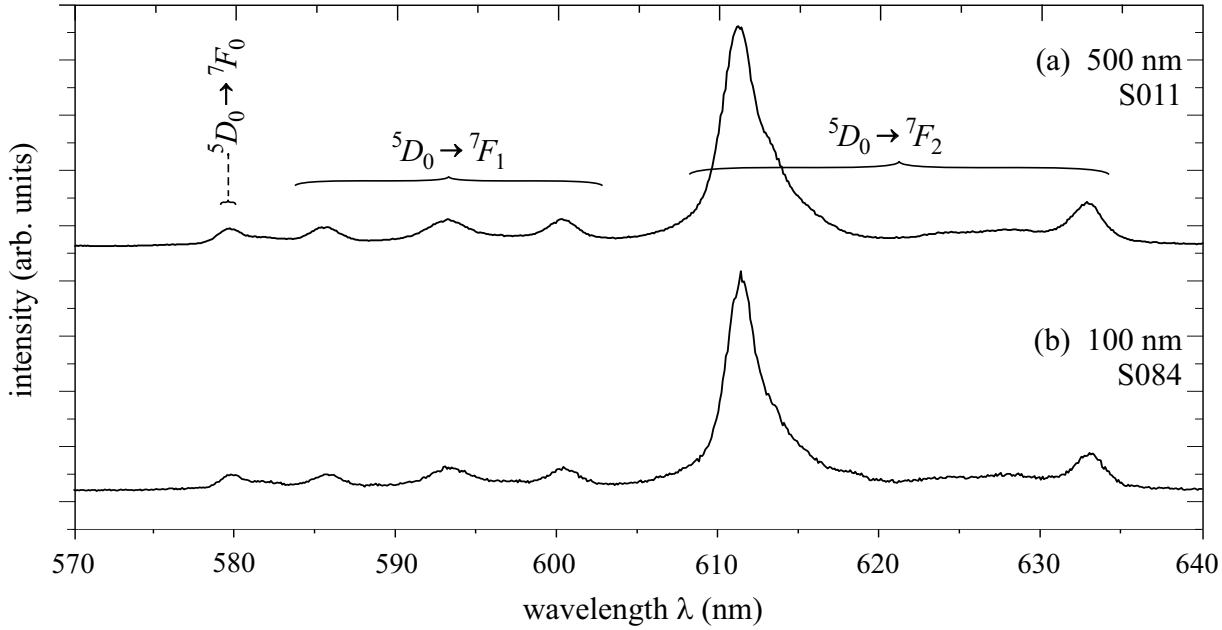

Figure 8.8: *Emission spectra of Eu(2%):$(Sc, Lu)_2O_3$ films grown on α-Al_2O_3.*

Figure 8.8 contains emission spectra of Eu(2%):$(Sc, Lu)_2O_3$ films of different thickness: 500 nm film S011 (a) and 100 nm film S084. Ultra-thin films have been excluded as the change of luminescence properties in such films below 50 nm are already investigated in literature [Bur02, Bär04, Rab04][1]. The crystalline films in (a) and (b) show spectra which are of similar shape to the reference bulk spectrum (figure 8.7e). Both spectra are dominated by the characteristic $^5D_0 \rightarrow {}^7F_2$ transition at 611 nm (cp. chapter 3.3) and are similar to the corresponding reference emission spectrum. When comparing the linewidth of the $^5D_0 \rightarrow {}^7F_2$ transition, it becomes evident that the 500 nm film has a slightly broadened structure, whereas the 100 nm film has a narrower structure. This indicates a higher degree of crystallinity and is in good agreement with the results obtained by XRD and RHEED measurements. Apart from the varying degree of crystallinity in both films, the local symmetry structure of the Eu^{3+} ion is not affected by any kind of film stress.

[1] This change is due to electronic transitions of the sevenfold coordinated Eu^{3+} in A, B, and C sites that is found in the monoclinic β-form of the sesquioxides.

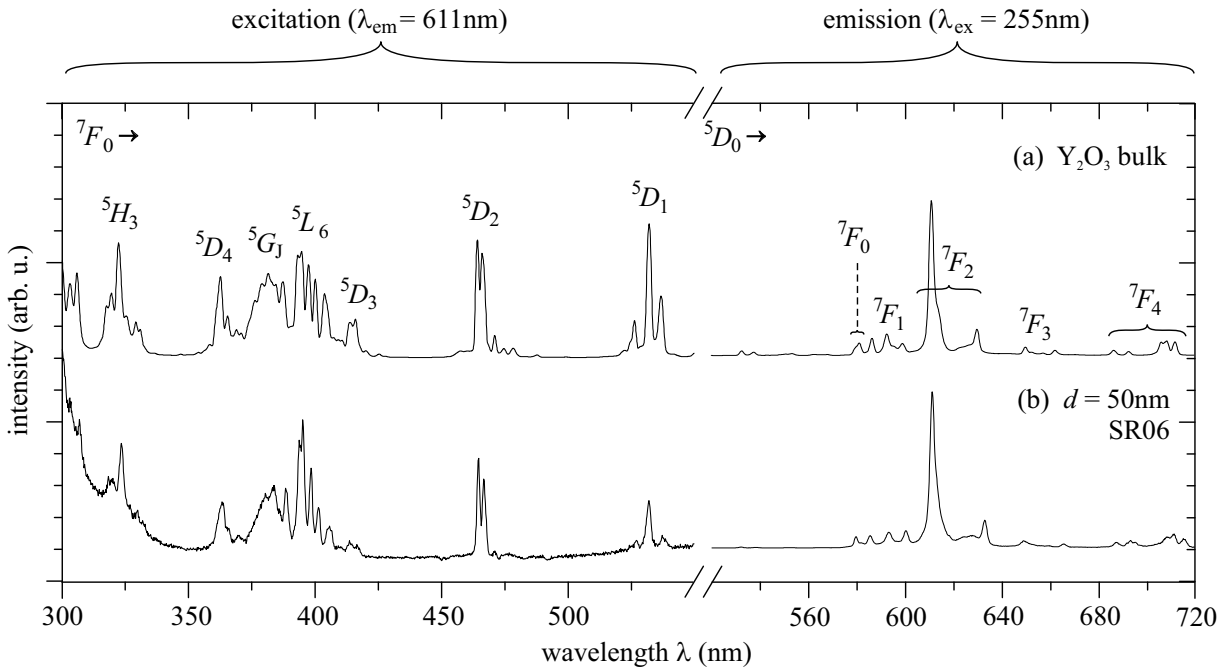

Figure 8.9: *Excitation (left) and emission spectra (right) of a 50 nm thin Eu(2%):$(Sc, Lu)_2O_3$ film in comparison to an Eu(1%):Y_2O_3 bulk crystal.*

The 50 nm thin composite sesquioxide film is compared to a bulk crystal of Y_2O_3. The excitation spectrum (b) in the left part of figure 8.9 deviates little from the bulk excitation spectrum. Only the transition into the $^5D_1$ level shows a significant intensity deviation in the 50 nm film, whereas the remaining transitions are developed in a sharp and distinct manner. Apart from the small peak position shifting due to the different sesquioxide compounds, no broadening in linewidth can be observed. If the emission spectrum (b) in the right part of figure 8.9 is considered, observations are similar. The emission peaks are resolved equally well in the 50 nm film compared to the bulk crystal. The less pronounced shoulder of the transition at 611 nm has been explained before. The composite thin film shows only a slightly broadened linewidth, which is astonishing for two reasons: Firstly, it is known, that films of thickness lower than 100 nm do not show the distinct and sharp peaks of bulk materials. Reduction of film thickness below this value is usually accompanied by changing luminescence behavior. Secondly, the peak broadening effect of composite materials should be amplified in thinner films. This is again in good agreement with the results obtained by XRD and RHEED measurements. The high degree of crystallinity in the 50 nm thin film SR06 which effects the local symmetry of the dopant ion in a positive way, can be ascribed to the pre-treatment of the substrate. The efficiency of *4f-4f* transitions is similar to the single-component bulk material.

VUV Measurements

At SuperLumi (cp chapter 7.4.3) additional excitation measurements have been performed to collect further information about the spectroscopic behavior of the composite films. Therefore, the measured spectra of a composite film are compared to the ones of

an yttria film, also deposited by PLD. These measurements were performed in the VUV spectral range at 10 K with wavelengths from 58 nm to 350 nm.

As the previous luminescence spectra revealed, the local symmetry in the composite film is well-preserved as can be seen in the emission spectrum of figure 8.10 (b). Similar to the comparison of emission spectra measured at room temperature for the 50 nm composite film (cp. figure 8.9), the 200 nm composite film is equally well-resolved as the 100 nm yttria film in (a). In the excitation spectrum (b) a lower intensity (signal to noise ratio) is apparent. The charge transfer state (CTS) which is around 240 nm (5.17 e V) is broadened in the composite film and has almost vanished. It is only indicated by a little intensity increase starting at 250 nm and continuing until the excitonic state (ES) edge around 210 nm is reached. The strong peak of the yttria spectrum (a) at 204 nm (6.08 e V), which corresponds to the ES, has much less intensity in the composite film (b). Excitation of the ES at 201 nm (6.17 e V) in the composite film (b) leads to the already known Eu:RE_2O_3 emission spectrum because of an energy transfer from the ES to the ^5D_J states of the Eu^{3+} ion. The interband transitions of Y_2O_3 (a) subsequent to the ES at around 180 nm and 150 nm vanish almost completely in the composite film (b). Only a weakly indicated structure around 190 nm (6.53 e V) is observed, which is not pronounced due to the lower intensity.

A possible explanation for the intensity loss of the ES can be found in the translation symmetry, which is ideal in a single-component system like yttria. In this case, the exciton migration is high. However, in composite films the ideal exciton migration is disturbed. This is due to the different ionic radii, in this case of the scandium and lutetium ions,

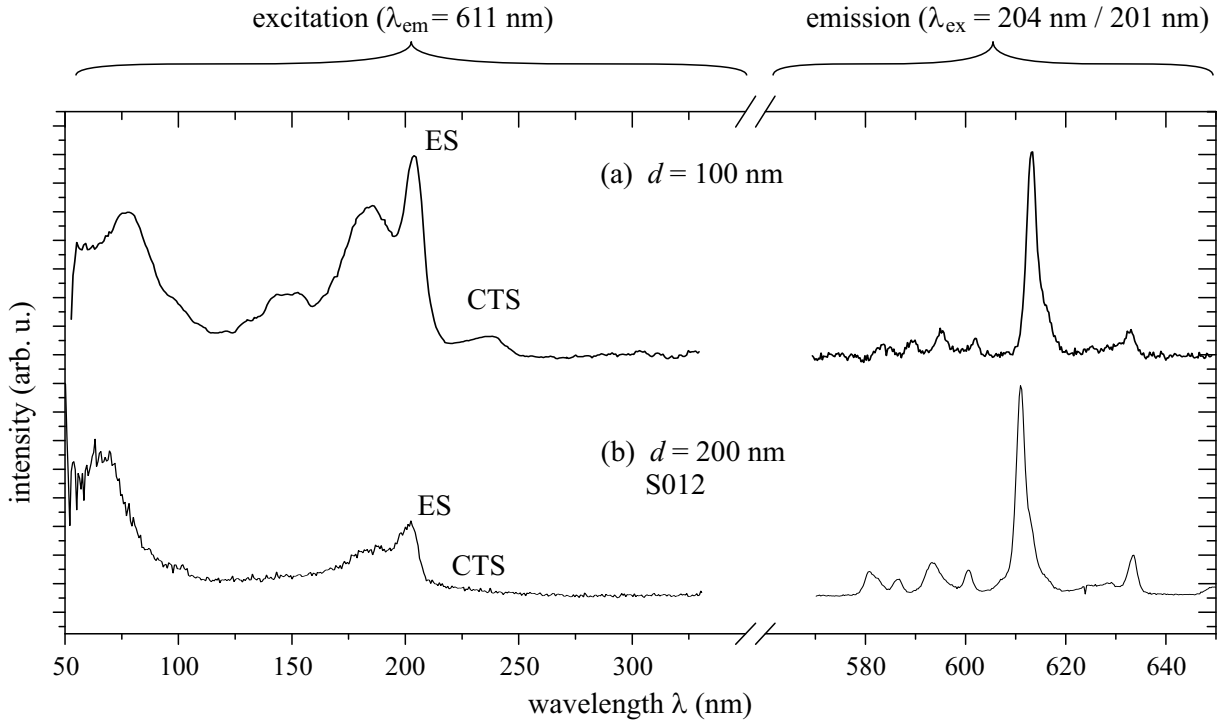

Figure 8.10: *VUV excitation (left) and emission spectra (right) of (a) Eu(4%):Y_2O_3 [Bär04] and (b) Eu:(2%):$(Sc, Lu)_2O_3$ films.*

causing a distortion of the crystal structure. As this irregularity in the lattice can function as an exciton trap, there is a higher probability for composite systems, that the created excitons do not reach the europium ions. Thus, the exciton efficiency is lower, which is indicated by the intensity loss of the ES in (b). If this causal chain is continued, the presence of the structure defects distorts the translation symmetry of the lattice, which in turn disturbs the energy band structure. In this way, the structure of the excitation spectrum (b) of the europium emission in the composite film is also affected. No distinctly resolved bands are observed.

These observations have not been made in the previous structure analysis, as by the X-ray diffraction only the average lattice structure is investigated. Therefore the VUV excitation measurements at the SuperLumi offer an important analysis method to investigate the local lattice environment of thin films.

Lifetime and Refractive Index Measurements

Lifetimes of the $^5D_0 \rightarrow {}^7F_2$ fluorescence have been determined in order to obtain additional information on the local symmetry of the Eu^{3+} centers in the deposited films[2]. Rabisch measured the lifetime of a Eu:$(Sc, Lu)_2O_3$ bulk crystal to be $\tau = 0.90\,\text{ms}$ [Rab04], which is almost equal to yttria ($\tau = 0.91\,\text{ms}$). In general, there is a tendency to increasing lifetime with decreasing film thickness. This is explained by the reduced effective refractive index in the grown thin film due to the influence of the substrate and the surrounding air, which both have lower refractive indices (Lorentz correction, cp. equation 7.21). The refractive index of the waveguiding film can be preserved by growing a cover / surface layer on top of the waveguiding film.

The measured films had thicknesses of (a) 1 000 nm, (b) 200 nm, and (c) 100 nm, with the first two being deposited with composition [1] and the latter with composition [2]. In figure 8.11 an increase in lifetime can the observed, with the 1 000 nm film having a bulk-like lifetime. The crystallite size $L_\perp$ determined by the XRD measurements seems to have little influence on the local symmetry of the Eu^{3+} ions as for the 100 nm film with improved crystallinity the lifetime increase does not stop. The luminescence measurements reveal, that the local symmetry of the considered films is not disturbed. Thus, the increase of the lifetimes can be attributed to the film thickness. Corresponding refractive index measurements were done with ellipsometry. The refractive index for a $ScLuO_3$ single-crystal at 632.8 nm has been determined by ellipsometry to be $n = 1.963$. It was proven, that the effective refractive indices of the measured films is

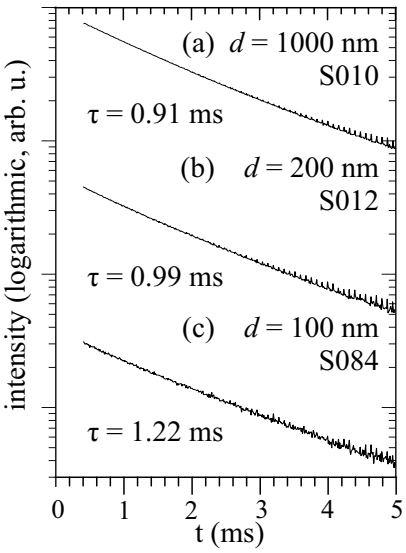

Figure 8.11: *Fluorescence lifetime of $(Sc, Lu)_2O_3$ films.*

[2] All lifetime measurements have been done at the Institute of Physical and Theoretical Chemistry, University of Tübingen by Dr. Sebastian Bär and Dr. Dmitry Khoptyar.

reduced, as predicted by the theory. The 1 000 nm Eu:$(Sc.Lu)_2O_3$ film had a refractive index of $n = 1.957$, which is almost the bulk value, whereas the 200 nm and 100 nm films show reduced refractive indices of $n = 1.955$ and $n = 1.942$, respectively. The resulting $\Delta n = 0.2$ for this substrate–film system is suited for waveguide applications.

8.2 Sapphire Films on Composite Sesquioxide

In this section the growth of sapphire films on a composite sesquioxide substrate is investigated. It is the reverse experiment of section 8.1. Although the analysis of the composite sesquioxide films in the previous section showed highly textured crystalline growth in the preferred {111} direction, it was not possible to achieve continuous layer-by-layer growth. Consequently this section investigates whether layer-by-layer film growth can be obtained using a composite sesquioxide material as substrate with a single-component film.

Due to the ionic radii difference between aluminum and europium (cp. table 3.1), with the europium ion having almost twice the radius of aluminum in sixfold coordination, it is not possible to use a Eu-doping in this case. Thus, in order to investigate the luminescence properties of the grown films, chromium is used as dopant ion. Consequently, the film layer consists of Al_2O_3 doped with Cr^{3+} whereas the substrate material is $ScLuO_3$ with equal amount of each sesquioxide component. The mixed sesquioxide substrates were prepared from a bulk crystal grown at the Institute of Laser Physics by the HEM growth technique (cp. page 8) and have a (111) orientation of the surface.

8.2.1 Lattice Matching and Structural Characterization

In this case the sesquioxide solid solution offers a threefold symmetry axis (hexagonal structure) in the cubic {111}-planes. The Al_2O_3 film can grow in vertical direction forming a (0001) surface. Similar to section 8.1 the lattices of substrate and film combine according to the relation $3 \times a_\mathrm{f} = \sqrt{2}\, a_\mathrm{s}$ (cp. section 5.2). By using equation 5.3 the lattice constant of the $(Sc_{0.5}Lu_{0.5})_2O_3$ substrate is determined to be $a_{ScLuO_3} = 10.124\,\text{Å}$. With a Cr^{3+}-doping of 0.5% the lattice constant[3] of the $(Cr_{0.05}Al_{0.95})_2O_3$ film is estimated to be $a_{Cr:Al_2O_3} = 4.772\,\text{Å}$ and $c_{Cr:Al_2O_3} = 13.024\,\text{Å}$. This leads to a theoretical lattice mismatch of $f = -0.01\,\%$ relative to the substrate, which is considerably small.

Figure 8.12 shows the diffraction measurements for two 100 nm thin Cr(0.5%):Al_2O_3 films deposited under different conditions. Primarily, the temperature of the substrate was varied from 700°C (a) to 950°C (b), whereas the oxygen pressure was almost identical with 8.5×10^{-3} mbar in the first deposition and 1×10^{-2} mbar in the second one. The deposition was carried out with 3 Hz (a) and 1 Hz (b). Table 8.2 summarizes the data obtained by the diffraction measurements.

Besides the {222} reflection of the sesquioxide substrate at 30.55°, a distinct {0006} reflection at 41.805° can be seen in (a). The intensity of this film reflection is not as high

[3] The lattice constants of hexagonal α-Cr_2O_3 are $a = 4.953\,\text{Å}$ and $c = 13.578\,\text{Å}$ [Bel03].

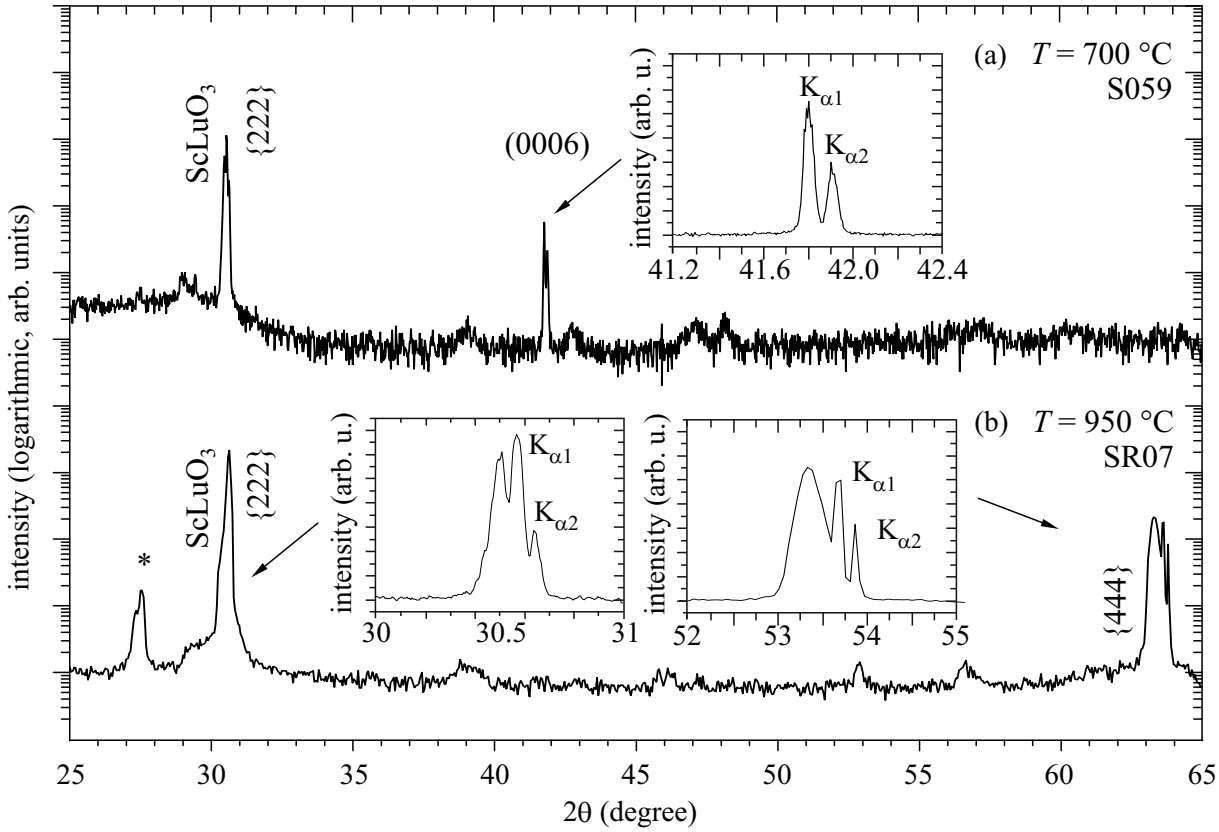

Figure 8.12: *X-ray diffraction patterns of 100 nm Cr:Al_2O_3 films deposited at different temperatures. The insets show additional high resolution scans. A residual Cu-K_β diffraction peak is indicated with '*'.*

as the reflection of the substrate, but is one order of magnitude smaller. However, the film reflection shows no broadening effect. With a high resolution scan (first inset), in which even the $K_{\alpha1}$ and $K_{\alpha2}$ lines are resolved, the peak width of this (0006) reflection is determined to be 0.044°. In comparison, the {222} reflection of the $ScLuO_3$ substrate has a peak width of 0.055°, whereas single-crystals of lutetia and scandia have peak widths of 0.042° each. For these very narrow diffraction peaks the Scherrer equation does no longer deliver correct crystallite sizes, as it is only valid for crystallite sizes of up to 150 nm [Sch18]. Thus, the estimated value $L_\perp = 210.1$ nm is more than twice as high

Deposition		**Reflection**		**Film Properties**				**Tag**
d_{film}(nm)	T_{sub}(°C)	peak	2θ(deg)	b_m(deg)	$L_\perp$(nm)	$c_\perp$(Å)	f(%)	
100	700	{0006}	41.805	0.044	210.1	12.954	−0.54	S059
100	950	—	—	—	—	—	—	SR07

Table 8.2: Calculation of the crystallite size and the lattice constant of Al_2O_3 films determined by X-ray diffraction. Measured peak positions 2θ and peak widths b_m are fitted by a Gaussian profile. For $L_\perp$ the instrumental resolution b_a is considered.

as the grown film thickness. Due to the very distinct shape of the (0006) reflection, its linewidth, and no indication of broadening, it can be assumed that the deposited Cr:Al_2O_3 film is entirely crystalline. Estimating the lattice constant in c-axis of the film delivers $c = 12.954\,\text{Å}$ which is -0.54% smaller than the substrate value.

Unfortunately, no (0006) reflection is seen in the spectrum (b). This is contrary to what was expected, as the deposition parameters thought to be optimal with regard to the repetition rate and the temperature. A temperature of 950°C should be preferable due to the higher mobility of the deposited atoms. The lower repetition rate increases the diffusion length. Both changes should effect the film growth in a positive way. However, despite pre-deposition annealing of the substrate no atomically ordered surface with terraces of atomic height could be obtained, which may indicate poor substrate quality (high miscut). The left inset in figure 8.12 (b) reveals an additional peak to the usual $K_{\alpha 1}$, $K_{\alpha 2}$-line splitting in the {222} reflection at around $2\theta = 30.5°$. Even better observable in the {444} reflection (right inset), an additional film reflection is seen at $2\theta = 63.37°$. Considering the results of the reverse substrate–film system in the previous section 8.1, the probability of subplantation leading to the same $(Sc, Lu)AlO_3$ perovskite phase is given. This reflection has a FWHM peak width of 0.33° and could correspond to the {222} reflection of $(Sc, Lu)AlO_3$ with a lattice constant of $a_{(Sc,\,Lu)AlO_3} = 5.085\,\text{Å}$. $LuAlO_3$ has an orthorhombic crystal structure with a lattice constant of $a_{LuAlO_3} = 5.11\,\text{Å}$ and $a \neq b \neq c$. As the incorporation of scandium particles would result in a smaller lattice constant this interpretation seems quite possible. Due to the very high substrate temperatures subplantation and interdiffusion of Al_2O_3 into the $ScLuO_3$ matrix is likely to occur. In addition, solid solutions like $ScLuO_3$ have reduced material hardness and melting points. This is caused by modification of the bonding forces. Apart from subplantation effects, solid-state reactions may occur at half the melting temperature. Due to these reasons, temperatures of around 700°C seem appropriate for mixed sesquioxide substrates. Further research should be invested in this system with better composite substrates using lower deposition temperatures.

8.2.2 Surface Structure and Topography

The RHEED measurements in figure 8.13(a) reveal similar yet different growth behavior compared with composite sesquioxide films on sapphire (cp section 8.1.3). Typical characteristics are the intensity fall during initial growth (amorphous interface), relaxation after each pulse (pseudomorphically grown crystalline regimes), and occasional moderate intensity rise (monolayer completion). For the Al_2O_3 film material the growth of one monolayer (2.2 Å) requires 48 pulses (black arrow). However, no crystallization is observed as the intensity does not recover. The pulse relaxation seen at initial deposition also vanishes together with the overall intensity and is less pronounced in contrast to the Eu:$(Sc, Lu)_2O_3$ RHEED oscillations for the initial deposition (cp. figure 8.5). The resulting diffraction pattern after deposition (right inset, figure 8.13) is vague and not clearly associable to the known RHEED patterns. The distinct diffraction points seen in the initial RHEED image (left inset, figure 8.13a) have almost vanished.

The post-deposition surface topography has been determined to be very smooth and

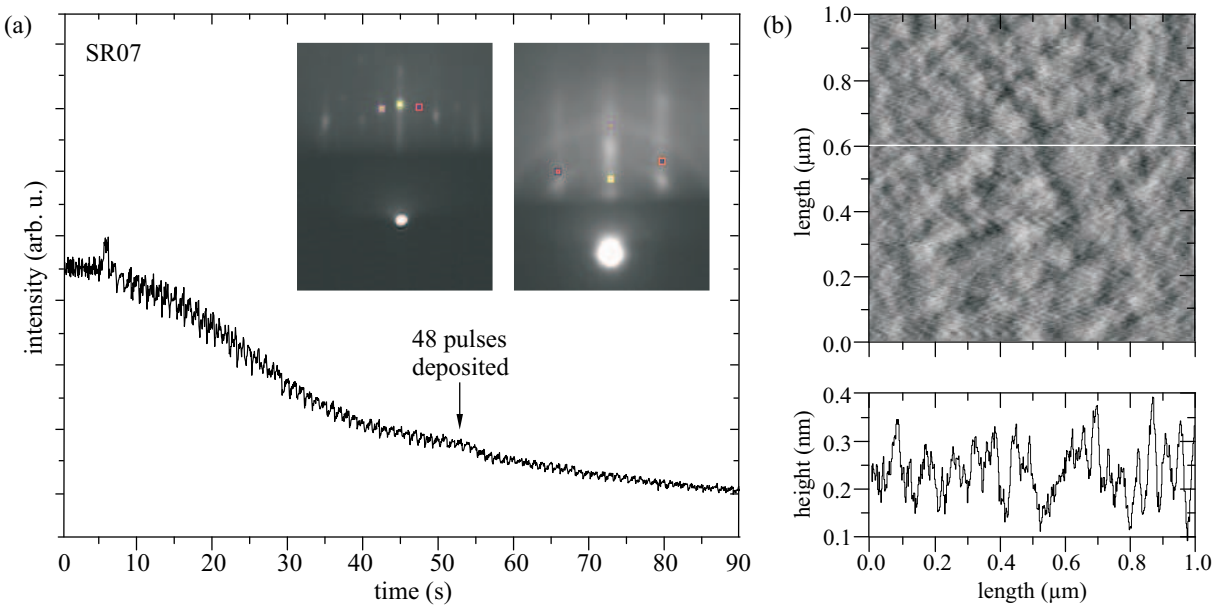

Figure 8.13: *(a) RHEED oscillations during deposition of 90 pulses at 1 Hz and corresponding diffraction patterns before (inset, left) and after deposition (inset, right). (b) Corresponding post-deposition surface topography measured by AFM.*

atomically flat (figure 8.13b). No islands or droplets are observed. The RMS roughness is estimated to be 0.6 Å, which is extremely low. The vague diffraction image after deposition as well as the intensity decrease during deposition are in agreement with the previously evaluated X-ray measurements, which did not show any film reflection. Despite the good surface properties it is concluded, that no crystalline film could be grown in this case. Unfortunately, for the monocrystalline film S059 no RHEED measurements could be done as no RHEED setup was available at that time.

8.2.3 Spectroscopic Analysis

A brief investigation of luminescence properties was done for this system. Besides the expected Cr^{3+} emission at 697 nm figure 8.14 reveals many rare-earth impurities in the $(Sc, Lu)_2O_3$ substrate. This was verified by luminescence measurements carried out using an undeposited substrate. In order to reduce this problem, powders of higher purity have to be used for the HEM growth of the substrate material. The linewidth of the spin-forbidden Cr^{3+} transition $^2E \rightarrow {}^4A_2$ at 297 nm is 1.5 nm at FWHM. The transition intensity is smaller than the substrate impurities, due to spin-forbiddance and low doping concentration (0.25%). This may also correspond to the low degree of crystallinity in the film, as already shown by X-ray and RHEED analysis.

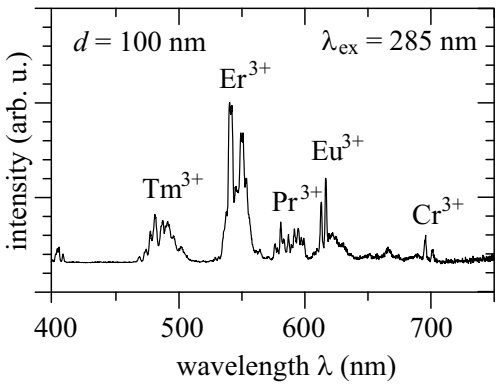

Figure 8.14: *Emission spectrum of Cr(0.25%):Al_2O_3 thin film SR07.*

8.3 Lutetia Films on Lithium Yttrium Fluoride

In this section the growth of lutetia films on ⟨100⟩ oriented $LiYF_4$ substrates is investigated. At the same time, general characteristics of oxidic layer growth on fluoride material by pulsed laser deposition are studied. Of special interest in this system is the refractive index difference with $\Delta n \approx 0.5$ (cp. table 5.2), which is advantageous for many applications.

8.3.1 Lattice Matching and Structural Characterization

$LiYF_4$ has a lattice constant of $a_{LiYF_4} = 5.16\,\text{Å}$. Therefore, the lattices of $LiYF_4$ and Lu_2O_3 combine in integer multiples of each other according to the relation $2 \times a_s \approx a_f$ (cp. chapter 5.2). Different dopant concentrations of Eu^{3+} have been used for the lutetia films. For 8% doping the lattice constant would result in 10.428 Å, with a mismatch f of 0.77% and for 2% doping in 10.400 Å with a mismatch f of 1.04%, both with respect to the substrate.

Figure 8.15 and table 8.3 contain the diffraction spectra and the corresponding data of the grown Eu:Lu_2O_3 films. The f value indicated with '*' is calculated by deriving film and substrate lattice constant from the diffraction spectra, as the diffraction measurements may shift $\pm 0.05°$ in absolute positions. Although this does not affect the measuring accuracy, the values of $a_\perp$ may not reflect the real mismatch parameter f. The films S033 and S034 have been deposited at 600°C with an oxygen pressure of 10^{-2} mbar using a repetition rate of 3 Hz, whereas for film SR09 repetition rate, temperature and oxygen atmosphere have been reduced to 1 Hz, 550°C and 5.5×10^{-3} mbar, respectively. Besides the {200} reflection of the $LiYF_4$ substrate at 34.74° the diffraction spectra (a) and (b) show the {400} film peak of Lu_2O_3 at ≈34°. In measurement (c) this {400} reflection is weaker compared to the spectra (a) and (b), but still has distinct shape (inset).

However, in all spectra a secondary film reflection arises at 32.7°, which in spectrum (c) has higher intensity than the {400} peak. Initially, it is not clear which atomic plane causes this reflection. Lu_2O_3 features a {312} reflection at 32.207° of very weak intensity. This is not very likely for various reasons. First, the considered lattice constants all shift to greater values, which indicates a certain degree of lattice expansion [Bal67]. The lattice mismatch of $f > 2\%$, exceeds the theoretically estimated value. Because of the strong lattice expansion influence, even the different dopant concentrations show negligible effects

	Deposition		**Reflection**		**Film Properties**				**Tag**
	d_{film}(nm)	T_{sub}(°C)	peak	2θ(deg)	b_m(deg)	$L_\perp$(nm)	$a_\perp$(Å)	f(%)	
Eu(8%)	100	600	{400}	34.018	0.379	24.5	10.533	2.02	S033
Eu(2%)	100	600	{400}	34.011	0.378	24.6	10.535	2.04	S034
Eu(2%)	70	550	{400}	33.920	0.334	27.9	10.563	2.13*	SR09

Table 8.3: Calculation of the crystallite size and the lattice constant of Lu_2O_3 films determined by X-ray diffraction. Peak positions 2θ and measured peak widths b_m are fitted by a Gaussian profile. For $L_\perp$ the instrumental resolution b_a is considered.

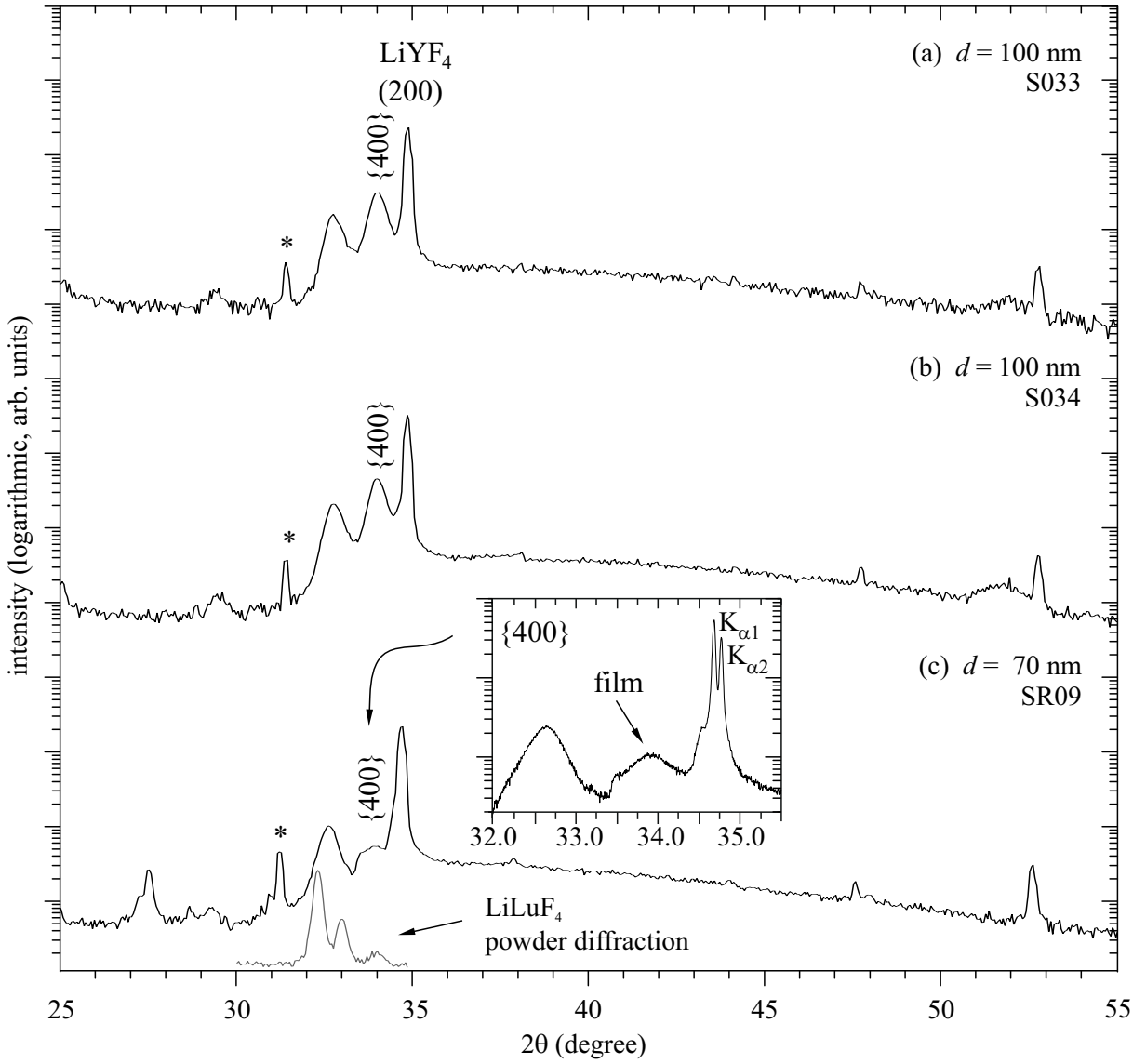

Figure 8.15: *X-ray diffraction patterns of Eu:Lu_2O_3 films grown on $LiYF_4$: (a) 8% Eu-doped 100 nm thin film, (b) 2% Eu-doped 100 nm thin film, and (c) 8% Eu-doped 70 nm thin film. The inset shows an additional high resolution scan. Residual Cu-K_β diffraction peak is indicated with '*'.*

on the resulting lattice constant. Therefore a shift of $+0.5^\circ$ which would result in smaller lattice constants in contrast to the observed expansion tendency of the lattice is unlikely to occur. Second, the films grow highly textured in $\langle 100 \rangle$ direction, because no diffraction peaks of atomic planes other than in the default orientation are present in the spectra. Therefore the formation of a single $\{312\}$ reflection is possible, though not very likely. However, most probably subplantation effects are responsible for this reflection at 32.7°. In the α-Al_2O_3–Eu:Y_2O_3 system investigated by [Bär04] subplantation effects could be observed. $LiYF_4$ has a relatively low Mohs hardness of 4-5 (cp. table 2.1). Thus, particle subplantation into the substrate could have taken place, due to the high deposition energy of 0.8 J/pulse. The comparison of film diffraction spectra with the one of $LiLuF_4$ powder

(grey spectra in figure 8.15) gives evidence to the assumption that a subplantation of the target particles resulted in a secondary phase formation of $LiLuF_4$ or $Li(Y,Lu)F_4$. This interpretation delivers a probable explanation of the additional reflection at 32.7°.

In figure 8.16 additional rocking curve measurements are shown, which reveal that the ⟨100⟩ crystal axes of Lu_2O_3 in the films are aligned along the film normal direction within 1.74° and 1.80° for the films S033 and S034, respectively. The broadened peak shape can be ascribed to the relatively small grain sizes of $L_\perp > 30\,\mathrm{nm}$. Apart from the additional $LiLuF_4$ phase, highly textured crystalline growth in ⟨100⟩ direction is indicated by these measurements, as no out-of-plane oriented crystallites can be observed.

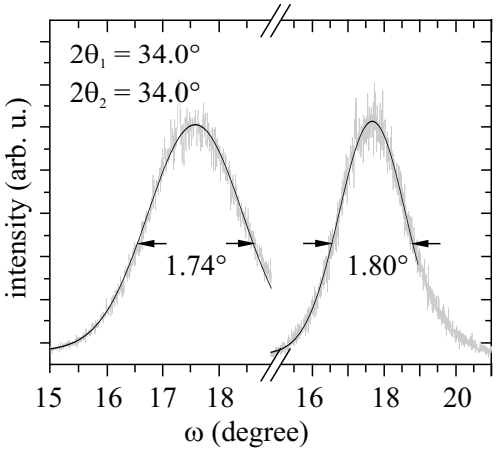

Figure 8.16: *Rocking curve scans of {400} reflection peak for films S033 (left) and S034 (right).*

8.3.2 Surface Structure and Topography

Further information on the heteroepitaxy of $Eu:Lu_2O_3$ films grown on $LiYF_4$ has been obtained by atomic force microscopy. Besides the increased surface roughness in comparison with the $Eu:(Sc,Lu)_2O_3$ and $Cr:Al_2O_3$ films, the film topography in figure 8.17 shows distinct structures. In the overview scan of $3\times3\,\mu m^2$ these structures have a maximum height of 1 nm. When performing a higher resolution scan of $0.5\times0.5\,\mu m^2$ the film surface

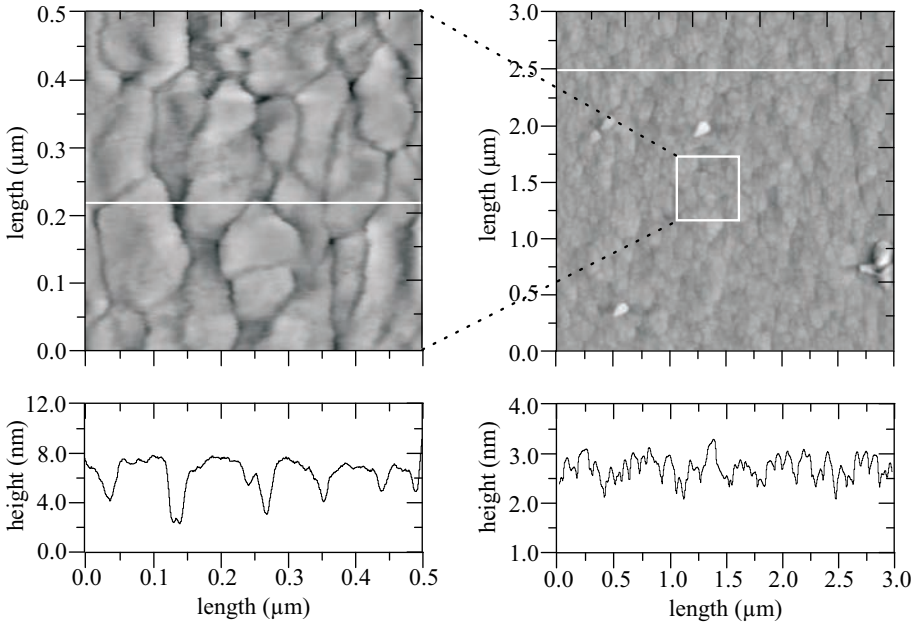

Figure 8.17: *AFM images of the 100 nm thin film SR09.*

reveals grain boundaries which have average dimensions of $100 \times 100\,\mathrm{nm}^2$. According to the X-ray analysis these grains are oriented along the $\langle 100 \rangle$ direction. The assumption can be made, that the shown film is completely stress-relaxed due to this boundary formation.

8.3.3 Spectroscopic Analysis

The optical properties of the heteroepitaxially grown Eu:Lu_2O_3 films on $LiYF_4$ were investigated by luminescence measurements (excitation and emission), VUV measurements, and lifetime measurements. The refractive indices of the films were measured by ellipsometry. No Eu-impurities were detected in the undeposited substrates.

Fluorescence and Excitation Measurements

Figure 8.18 shows the excitation and emission spectra of an Eu(1%):Y_2O_3 bulk single-crystal (a) and of a 100 nm thin Eu(8%):Lu_2O_3 film (b) grown on $LiYF_4$. The onset of the charge transfer transition which starts at around 300 nm and peaks at around 240 nm is more pronounced in the grown film. As already observed for the composite sesquioxide films grown on sapphire in section 8.1.4 the emission and excitation spectra of the Lu_2O_3 film are very similar to the bulk ones. The excitation spectrum (b) allows the assignment of each transition seen in the bulk spectrum (a). A deviation is seen in the intensity distribution in the spectra, as the excitation spectrum of the bulk is dominated by the ${}^7F_0 \rightarrow {}^5D_1$ transition. In contrast, the excitation spectrum of the film is dominated by

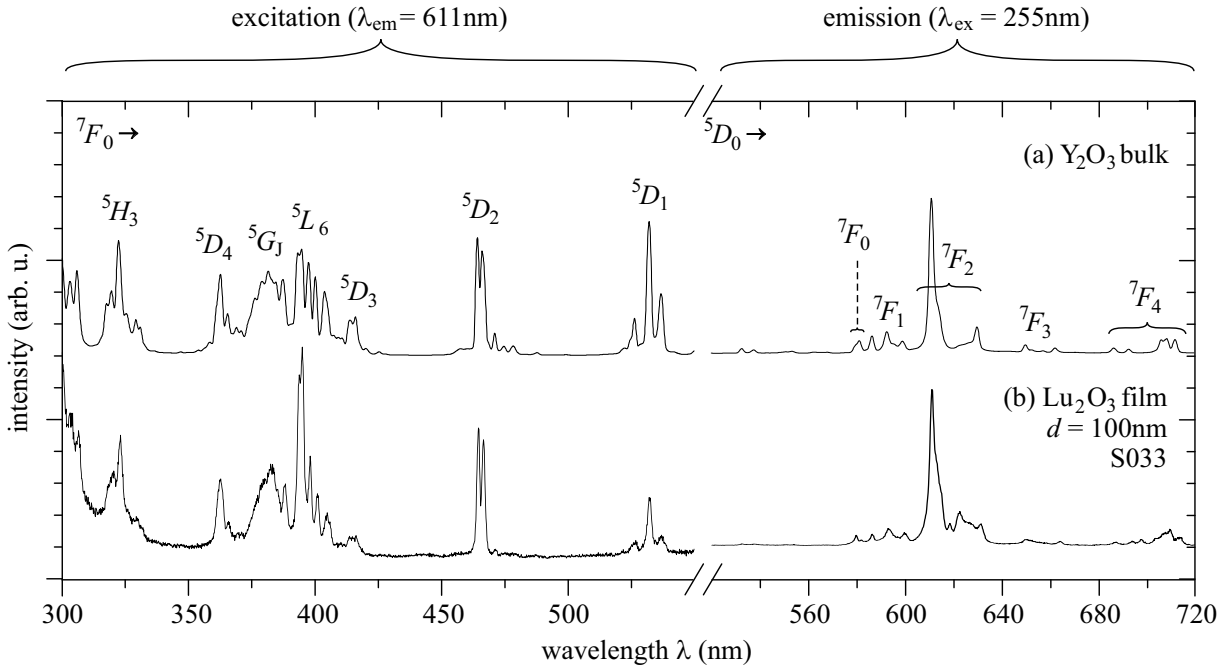

Figure 8.18: *Excitation (left) and emission spectra (right) of (a) an Eu(1%):Y_2O_3 bulk single-crystal in comparison with (b) an Eu(8%):Lu_2O_3 thin film.*

the ${}^7F_0 \rightarrow {}^5L_6$ transition. This change in transition intensities has already been observed similarly in section 8.1.4.

The emission peaks in the right part of figure 8.18(b) are resolved equally well in comparison to the bulk spectrum (a). At 622 nm of the characteristic ${}^5D_0 \rightarrow {}^7F_2$ transition the film spectrum shows an additional peak, which can be ascribed to the different properties of Y^{3+} and Lu^{3+} occupying the rare-earth lattice sites C_2 and C_{3i} (cp. figure 3.3). In the Lu_2O_3 lattice the europium emission at 622 nm from the C_{3i} symmetry site is stronger than in Y_2O_3.

When summarizing the luminescence properties of the heteroepitaxial Eu:Lu_2O_3 films at room temperature, the excitation and emission spectra have bulk-like character. This indicates a preserved local crystal structure of the Eu^{3+} ions with no symmetry distortions. The observed linewidths and transition intensities correlate to the known Eu-doped sesquioxide bulk data.

VUV Measurements

The SuperLumi VUV measurements performed at 10 K are compared to the already evaluated VUV measurements of Eu:Y_2O_3 and composite Eu:$(Sc, Lu)_2O_3$ in section 8.1.4 (figure 8.10).

It can be seen in the well-resolved emission spectrum in figure 8.19, that the local symmetry in the Eu:Lu_2O_3 film of 100 nm thickness is not disturbed. This is in good agreement with the luminescence measurements made room temperature (cp. figure 8.18), as all transitions can be identified and the linewidths and peak intensities are consistent with the known values. In contrast to the emission measurements at room temperature, the emission at 622 nm resulting from the C_{3i} symmetry site is less intense at 10 K.

The excitation spectrum has a better signal to noise ratio compared to the 200 nm composite $(Sc, Lu)_2O_3$ film. The charge transfer state (CTS) around 240 nm (5.17 eV) is pronounced, although still broadened in comparison to the yttria film. Similar to the

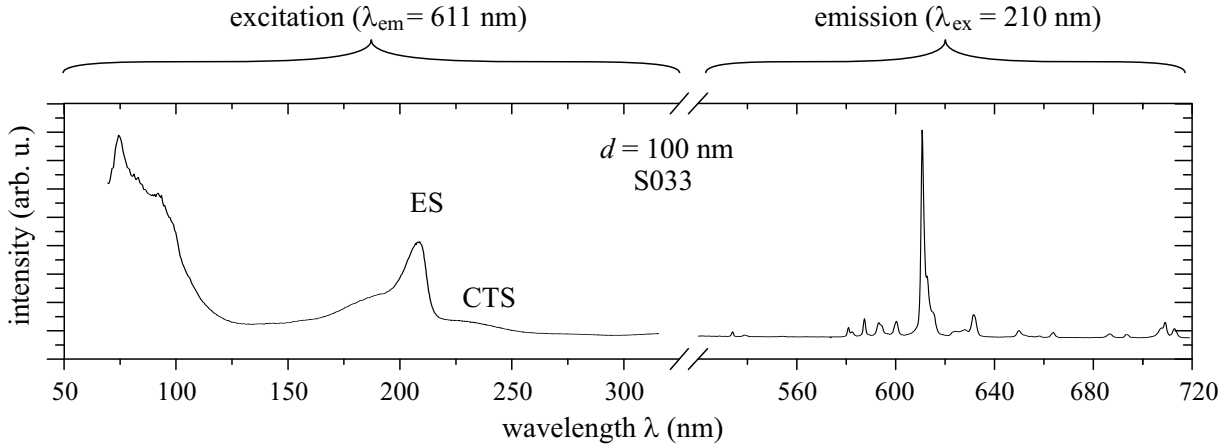

Figure 8.19: *VUV excitation and emission spectra of Eu(8%):Lu_2O_3 thin film.*

yttria spectrum, the excitonic state (ES) edge resides at around 220 nm, with the ES being of higher intensity compared to the composite film. A marginal spectral shift is also observed for the ES at around 210 nm (5.91 e V). The interband transitions are better pronounced than in the composite film and can be allocated at around 75 nm (16.54 e V), 100 nm (12.41 e V) and 180 nm (6.89 e V).

Lifetime and Refractive Index Measurements

The lifetime of the ${}^5D_0 \rightarrow {}^7F_2$ fluorescence has been estimated to obtain additional information on the local symmetry of the Eu^{3+} centers in the deposited films (cp. figure 8.20).

The lifetime of a crystalline Eu(8%):Lu_2O_3 reference sample is estimated to be $\tau = 1$ ms. For a film of 100 nm thickness the measured lifetime is 38% higher than the reference value, whereas for a ultrathin film of 4 nm thickness the lifetime increase is 63%. Both values are in good agreement with the theory, as thin films with no cover layer show higher lifetimes according to the Lorentz correction.

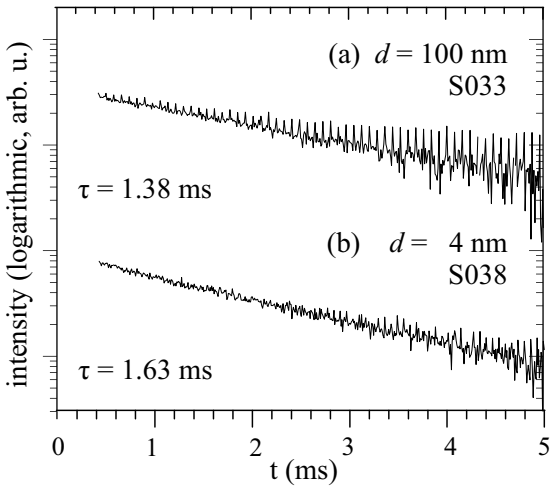

Figure 8.20: *Fluorescence lifetime of Eu:Lu_2O_3 films with different thicknesses.*

At 632.8 nm the refractive index of single-crystalline Lu_2O_3 is $n = 1.930$. A reduced effective refractive index is observed by ellipsometric measurements for both grown films, with $n = 1.912$ for the 100 nm film and $n = 1.885$ for the 4 nm film. These values correspond to the measured lifetimes. The measured refractive index difference is $\Delta n = 0.45$.

8.4 Summary and Discussion

Three heteroepitaxial systems fabricated by pulsed laser deposition have been investigated in this chapter. In general, a high degree of crystallinity with bulk-like luminescence properties and good lattice matching could be obtained. However, temperature-dependent subplantation probably occurred in every substrate–film system and is thus a major concern in pulsed laser deposition. Most probably, the upper limit for the substrate temperature of each material is half the melting point. Apart from solid-state reactions, which can take place at these temperatures, subplantation and interdiffusion of target particles into the substrate crystal matrix were always observed at substrate temperatures of roughly half the melting point. No evidence of subplantation was observed in the spectroscopic characterization, which is due to the average thickness (100 nm) of the investigated lattice matched films. Subplantation and interdiffusion effects are usually observed at film thicknesses of 20 nm and below [Bur02, Bär04].

Composite Sesquioxide Films on Sapphire

The growth on sapphire substrates requires high temperatures. Although highly textured crystalline films can be obtained at temperatures of 700°C, better film properties are achievable at higher deposition temperatures. An indicator thereof is the crystallite size which almost reaches the estimated film thickness for temperatures above 1000°C. For lower deposition temperatures the distribution of [111] oriented, but relatively small crystallites result in broad rocking curves as seen in figure 8.3. However, at temperatures above 800°C the deposited films reveal subplantation effects, which most probably resulted in the formation of a second perovskite phase as already observed for the Al_2O_3–Eu:Y_2O_3 films by S. Bär [Bär04]. Despite the high Mohs hardness of α-Al_2O_3, the high reactivity of Al^{3+} might contribute to the formation of new phases by subplantation. The additional diffraction peaks have been interpreted as [100] $(Sc, Lu)AlO_3$. These subplantation effects at higher temperatures have to be suppressed by the deposition parameters, e. g. by gradually reducing the pulse energy in a series of films to estimate a possible compromise between pulse energies required for single-crystalline deposition and pulse energies resulting in undesired subplantation effects.

Additional RHEED analysis revealed the formation of an amorphous interface at initial growth, which prevents a sustaining layer-by-layer growth on α-Al_2O_3. This has also been observed in the pulsed laser deposition of Al_2O_3–Sc_2O_3 films [Gün07]. Thus, further deposition attempts on sapphire substrates should include a buffer layer in order to prevent the initial growth of an amorphous interface and thereby realize layer-by-layer grown films.

By pre-deposition substrate treatment the surface roughness of the grown films is strongly reduced in comparison to untreated substrates [Bär04, Han07]. Further investigations regarding the in-plane characteristics of the film lattice are to be done by surface X-ray diffraction measurements.

A lattice matching of up to 99.88% could be obtained by composition [2] with luminescence properties similar to bulk single-crystals. It is difficult to assess whether the mismatch of 0.12% is caused by lattice expansion in the grown film. Otherwise, composition [2] can be improved by shifting the two-component mixture more to scandium while reducing the lutetia amount. However, the used compositions fit the estimation quite well and only fine-tuning has to be done. For laser applications the Eu^{3+} dopant could be replaced by Yb^{3+} or Er^{3+} ions, which would also result in a more homogenous lattice as the ionic radii of both laser ions are closer to the ones of Sc^{3+} and Lu^{3+}. The measured refractive index difference of $\Delta n = 0.2$ at wavelengths of 632.8 nm recommend this system for waveguiding applications.

Sapphire Films on Composite Sesquioxide

A major issue of the growth on composite sesquioxides is the substrate quality. The ⟨111⟩ oriented $ScLuO_3$ substrates contained various rare-earth impurities such as holmium, praseodymium, and erbium, which appeared in the luminescence measurements. This problem is a well-known characteristic of lanthanides, which can only be separated and

isolated to a certain degree. In the case of two lanthanide compounds as seed materials the lanthanide impurity amount is almost doubled. However, the combination of $Cr(0.5\%):Al_2O_3$ with $ScLuO_3$ resulting in a theoretical lattice matching of 99.99% is a well-suited heteroepitaxial system for PLD.

Similar to the reverse substrate–film system, subplantation was observed at substrate temperatures of 950°C. As solid solutions have reduced melting points due to bonding force modifications in the crystal matrix, 950°C was probably above half the melting temperature of $(Sc, Lu)_2O_3$. In addition, the material hardness of solid solutions is also likely to be reduced in comparison to the corresponding single-component material. Due to these factors, most probably [111] $(Sc, Lu)AlO_3$ was formed by subplantation and interdiffusion of Al_2O_3 into the $(Sc, Lu)_2O_3$ matrix.

Apart from these difficulties, a highly crystalline film could be deposited at 700°C with a crystallite size which goes beyond the Scherrer equation limits. The FWHM peak width of the (0006) film reflection was similar to the substrate values, indicating monocrystalline epitaxial film growth. With this film a lattice matching of 99.46% was achieved. Further growth of this promising systems will be performed at optimum temperatures around 700°C. As for this substrate–film system the lower refractive index is on the film-side, it would be well-suited for application as Bragg mirrors and antireflex coatings.

Lutetia Films on Lithium Yttrium Fluoride

The combination of oxide and fluoride materials incorporates some difficulties. As described before, a certain oxygen pressure is required for the pulsed laser deposition of oxidic materials. Due to this basic oxygen atmosphere, there is the danger of undesired oxyfluoride formation during deposition, e. g. an amorphous oxyfluoride interface between film and substrate. Pre-deposition substrate treatment has to be done in argon or nitrogen atmosphere to prevent oxidation. However, it has not been possible to obtain atomically flat terraces by this treatment.

The subplantation and interdiffusion of Lu_2O_3 into the $LiYF_4$ matrix probably cause a $Li(Y, Lu)F_4$ phase in the deposited thin film. This is understood due to the relatively low Mohs hardness of fluoride materials. Therefore, the deposition energy has to be reduced in further experiments in order to prevent subplantation and interdiffusion of target particles. Other parameter changes have to be considered regarding the substrate temperature and the oxygen pressure. In review, less optimal deposition parameters were used for this substrate–film system, as only few information on the pulsed laser deposition of fluorides was available. Further research in this field has to be done in future.

Despite these complications, crystalline $\langle 100 \rangle$ oriented $Eu:Lu_2O_3$ films with bulk-like luminescence properties were obtained. The obtained lattice matching of 97.98% has an observable degree of lattice expansion, as a shift to greater lattice constants than theoretically calculated took place. This system is highly suited for optical applications regarding the comparably high refractive index difference of $\Delta n = 0.45$, provided that the growth difficulties can be resolved in future.

9 Characterization of Homo- and Quasi-Homoepitaxial Thin Films

The characterization of lattice matched homo- and quasi-homoepitaxial thin film systems is subject of this chapter. Investigated materials are sesquioxides, orthovanadates, and aluminum garnets. In contrast to the heteroepitaxial systems, the lattices of substrate and film are very similar in homo- and quasi-homoepitaxy and combine directly (cp. chapter 5.2). Therefore, the epitaxy is energetically more favorable and better results are expected in regard of the film growth process and the resulting film quality.

In addition, heteroepitaxy with pulsed laser deposition may lead to subplantation effects, which disturb the growth process. In homo- and quasi-homoepitaxy the formation of additional phases due to subplantation, as observed in the previous chapter 8 for the deposition of sesquioxides on α-Al_2O_3 and $LiYF_4$ substrates, is unlikely to occur.

9.1 Sesquioxide Films on Yttria

In this section the properties of different sesquioxide films on yttria are studied. While in heteroepitaxy on sapphire only one growth direction could be investigated, the homo- and quasi-homoepitaxy will consider [111] and [100] sesquioxide films. In Eu:Y_2O_3 films the ionic radius of Eu^{3+} is bigger than that of Y^{3+}, thus the cation site in yttria is enlarged. This results in a slight lattice constant increase. The properties of these homoepitaxial films are compared to those of Eu:Lu_2O_3 films. The Lu^{3+} and Eu^{3+} ions effect the yttria lattice in compensating manner, as $r_{Lu^{3+}} < r_{Y^{3+}} < r_{Eu^{3+}}$ (cp. table 9.1). At last, lattice matching on yttria is achieved by the composite system Eu:$(Gd, Lu)_2O_3$.

9.1.1 Lattice Matching

In the above described cases of Eu:RE_2O_3 deposited on yttria the lattices combine directly $a_s \approx a_f$ (cp. chapter 5.2). Apart from the growth of homoepitaxial Eu:Y_2O_3 and quasi-homoepitaxial Eu:Lu_2O_3 films, both introducing a small lattice mismatch to yttria, it is of special interest to investigate a composite sesquioxide film to fit the substrate lattice constant $a_{Y_2O_3} = 10.603\,\text{Å}$ perfectly and obtain a higher refractive index difference as well.

As already done similarly for Eu:$(Sc, Lu)_2O_3$ films, a composition with 2 % Eu-doping is determined by the Vegard law (equation 5.3) to be $(Eu_{0.02}Gd_{0.534}Lu_{0.446})_2O_3$ [1]. This

composition was derived from the RE^{3+} ionic radii due to the reasons mentioned in chapter 8.1.1. It is the initial (Eu, Gd, Lu)-mixture that is used likewise in the lattice matched vanadate and garnet films (section 9.2 and 9.3). Later, the composition was slightly modified to $(Eu_{0.02}Gd_{0.48}\ Lu_{0.50})_2O_3$ [2]. No clustering is expected in any of the two compositions as the material amount of Lu_2O_3 and Gd_2O_3 is well balanced.

The refractive index difference between substrate and film in this lattice matched quasi-homoepitaxial system is well-suited for waveguiding. Using a linear approximation, which only delivers a tendency, the deposited thin films have a refractive index $n_f \geq 1.93$ at 1µm which results in $\Delta n = 4 \times 10^{-2}$ (cp. table 9.1).

	Y_2O_3	Lu_2O_3	Gd_2O_3	Eu_2O_3
$\boldsymbol{r}$ (Å)	0.92	0.86	0.94	0.95
$\boldsymbol{a}$ (Å)	10.603	10.391	10.813	10.859*
$\boldsymbol{n}$	1.890	1.911	1.950	1.983

Table 9.1: *Ionic radius RE^{3+}[6], lattice constant, and refractive index at 1µm of sesquioxide single-crystals. A theoretical value is indicated with '*'.*

9.1.2 Structural Characterization

The growth behavior and the lattice matching of these different sesquioxide films have been investigated on ⟨111⟩ and ⟨100⟩ oriented yttria substrates. Different sesquioxide films are compared in X-ray diffraction spectra, which are grouped according to the substrate orientation. Thus, figure 9.2 features the growth on ⟨111⟩ oriented yttria and figure 9.4 the growth on ⟨100⟩ oriented yttria. The preferred growth direction of sesquioxides is the ⟨111⟩ orientation, as crystallization in this direction occurs even on amorphous glass [Ehl05]. The pulsed laser deposition process does not take place in thermodynamic equilibrium and thus a possibly preferred growth direction may differ from regular crystal growth.

For a film composition of Eu(1.5%):Y_2O_3 the theoretically expected lattice constant is $a = 10.607\,\text{Å}$, whereas for Eu(8.0%):Lu_2O_3 and Eu(2.0%):Lu_2O_3 it is 10.428 Å and 10.400 Å, respectively. As these values are very close to the yttria lattice constant the diffraction patterns of substrate and film are not resolved distinctly and have to be approximated by superimposing Gaussian fits. Thus, the estimated values may incorporate a certain systematic error. Of course, this applies also to the composite systems and is valid in the following sections 9.2 and 9.3 as well.

Yttria Films

The above mentioned theoretically estimated lattice constant for homoepitaxial growth of Eu(1.5%):Y_2O_3 films is almost achieved by the 120 nm thin film S003. Some of the properties and deposition parameters are collected in table 9.2. This film was deposited at 668°C and 8.8×10^{-3} mbar oxygen atmosphere using a repetition rate of 10 Hz. Although the diffraction spectrum does not reveal any distinct film peak (figure 9.2a), the shoulder in the high resolution spectrum (inset) can be ascribed to the film growth. By superimposing Gaussian fits, the peak width and position, lattice constant, and crystallite size have been calculated from this {222} reflection (cp. table 9.2). Despite the strong peak broadening the crystallites have nearly half the film thickness. The lattice mismatch was estimated to

be 0.07 %. No reflections of other atomic planes are visible in the diffraction pattern. In order to investigate the out-of-plane orientation of the crystallites which are not parallel to the surface, an ω-scan was done. Figure 9.1 reveals, that the $\langle 111 \rangle$ crystal axes of the 120 nm thin film S003 are aligned along the film normal direction within 0.066°, which is similar to single-crystal bulk values of sesquioxides. However, due to the knowledge that deposition temperatures below 700°C are insufficient for crystalline sesquioxide film growth [Bur02, Bär04] and because the calculated film values are based only on approximation of the film reflex, it can be questioned whether single-crystalline growth has taken place. As no distinct film reflection was observed, the measured rocking curve most probably belongs to the substrate.

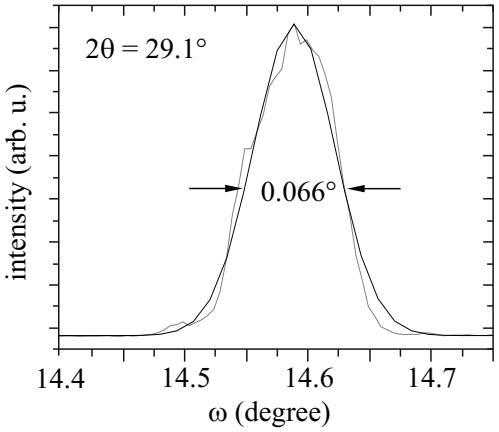

Figure 9.1: *Rocking curve fit of the S003 {222} reflection peak.*

Regardless of the almost doubled crystallite size and the narrow {400} peak width of 0.081°, the 100 nm film S008 of the same material grown on $\langle 100 \rangle$ oriented yttria has a mismatch of 0.72% to the substrate lattice (table 9.2). $L_\perp = 102$ nm was estimated from the Cu-K$_\beta$ emission of the {400} reflection, which is roughly the estimated film thickness. The value for $L_\perp$ is slightly higher than the film thickness d_{film}, which is well within the scope of measuring accuracy. The reflex intensity appears to be very low in the inset of figure 9.4 (a). This is explained by the very small measuring slit set of only 0.018°, which is normally used for single-crystal bulk material only. The mismatch f of 0.72% indicates a lattice expansion in the film, which accordingly shifts to greater lattice constants. A lattice expansion is always the result of lattice defects. However, a variety of lattice defects are distinguished. Lattice expansion due to different kinds of crystal defects are well-known in literature [Bal67] and will briefly be discussed in section 9.4.1.

Again, no additional reflections deriving from atomic planes other than in $\langle 100 \rangle$ direction can be seen, indicating a highly textured film growth. The parameters were identical to the previous film S003, except for the higher deposition temperature $T = 700$°C.

	Deposition		**Reflection**		**Film Properties**				**Tag**
	d_{film}(nm)	T_{sub}(°C)	peak	2θ(deg)	b_m(deg)	$L_\perp$(nm)	$a_\perp$(Å)	f(%)	
K$_{\alpha 1}$	120	668	{222}	29.131	0.173	54.2	10.610	0.07	S003
K$_\beta$	100	700	{400}	30.224	0.081	102.0	10.680	0.72	S008

Table 9.2: Calculation of the crystallite size and the lattice constant of Y_2O_3 films grown on [111] and [100] yttria determined by X-ray diffraction. Measured peak positions 2θ and peak widths b_m are fitted by a Gaussian profile. For $L_\perp$ the instrumental resolution b_a is considered.

Lutetia Films

Different dopant concentrations of Eu^{3+} have been applied in order to investigate the compensational influence on the lutetia lattice which is smaller than the lattice of yttria (cp. table 9.1). For 8% doping the lattice constant should result in 10.428 Å and for 2% doping in 10.400 Å. The calculated lattice mismatch f is −1.68% for Eu(8%) and −1.95% for Eu(2%), both with respect to the substrate.

Obviously, the lattice constants achieved with Eu(8%)-films have greater values and thus smaller mismatch parameters f (cp. table 9.3). For the 50 nm thin film deposited with 3 Hz at 697°C on ⟨111⟩ oriented yttria the lattice constant is 10.496 Å with a mismatch of −1.01%. The right-sided shoulder of the {222} reflection shown in figure 9.3 is ascribed to the grown film. The estimated peak width results in a crystallite size of 16.5 nm. Again, the comparatively small crystallinity stands in relation to the substrate temperature during deposition. This is demonstrated by the 50 nm thin Eu(2%)-film, which was deposited at identical conditions – the oxygen atmosphere was 10^{-2} mbar for all lutetia films – except for higher temperature of 900°C. Now the crystallite size is more than twice as high with 39.2 nm, which is nearly the film thickness. The same behavior is observed for the growth on ⟨100⟩ oriented yttria: In this case the lattice constant $a_\perp$ =10.509 Å of the film deposited at 700°C (cp. figure 9.4b) is even closer to the substrate resulting in a mismatch of −0.89%. The lattice expansion can be estimated by comparison of the resultant lattice constant with the theoretically expected value (equation 5.2). It amounts 0.77%, which must be attributed to lattice defects again. However, the crystallite size $L_\perp = 19.3$ nm of this 100 nm thin Eu(8%)-film is only about one fifth of the overall film thickness. Raising the temperature to 897°C at identical deposition parameters delivers a crystallite size of 40.9 nm in the 100 nm Eu(2%)-film, indicating that the epitaxy of Lu_2O_3 requires even higher temperatures.

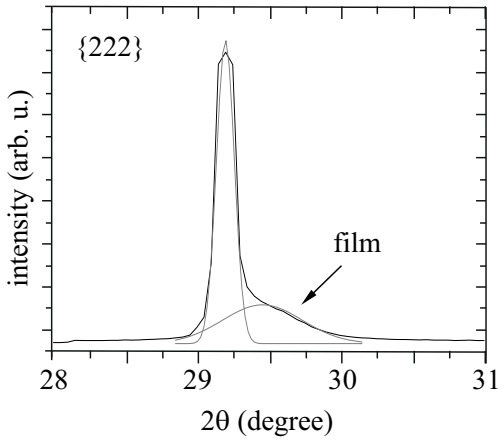

Figure 9.3: *High resolution θ–2θ-scan of the S055 {222} reflection peak.*

	Deposition		Reflection		Film Properties				Tag
	d_{film}(nm)	T_{sub}(°C)	peak	2θ(deg)	b_m(deg)	$L_\perp$(nm)	$a_\perp$(Å)	f(%)	
Eu(2%)	50	697	{222}	29.457	0.554	16.5	10.496	−1.01	S055
Eu(8%)	50	900	{222}	29.833	0.248	39.5	10.366	−2.24	S099
Eu(2%)	100	700	{400}	34.099	0.481	19.3	10.509	−0.89	S049
Eu(8%)	100	897	{400}	34.730	0.241	40.9	10.324	−2.63	S093

Table 9.3: Calculation of the crystallite size and the lattice constant of Lu_2O_3 films grown on [111] and [100] yttria determined by X-ray diffraction. Measured peak positions 2θ and peak widths b_m are fitted by a Gaussian profile. For $L_\perp$ the instrumental resolution b_a is considered.

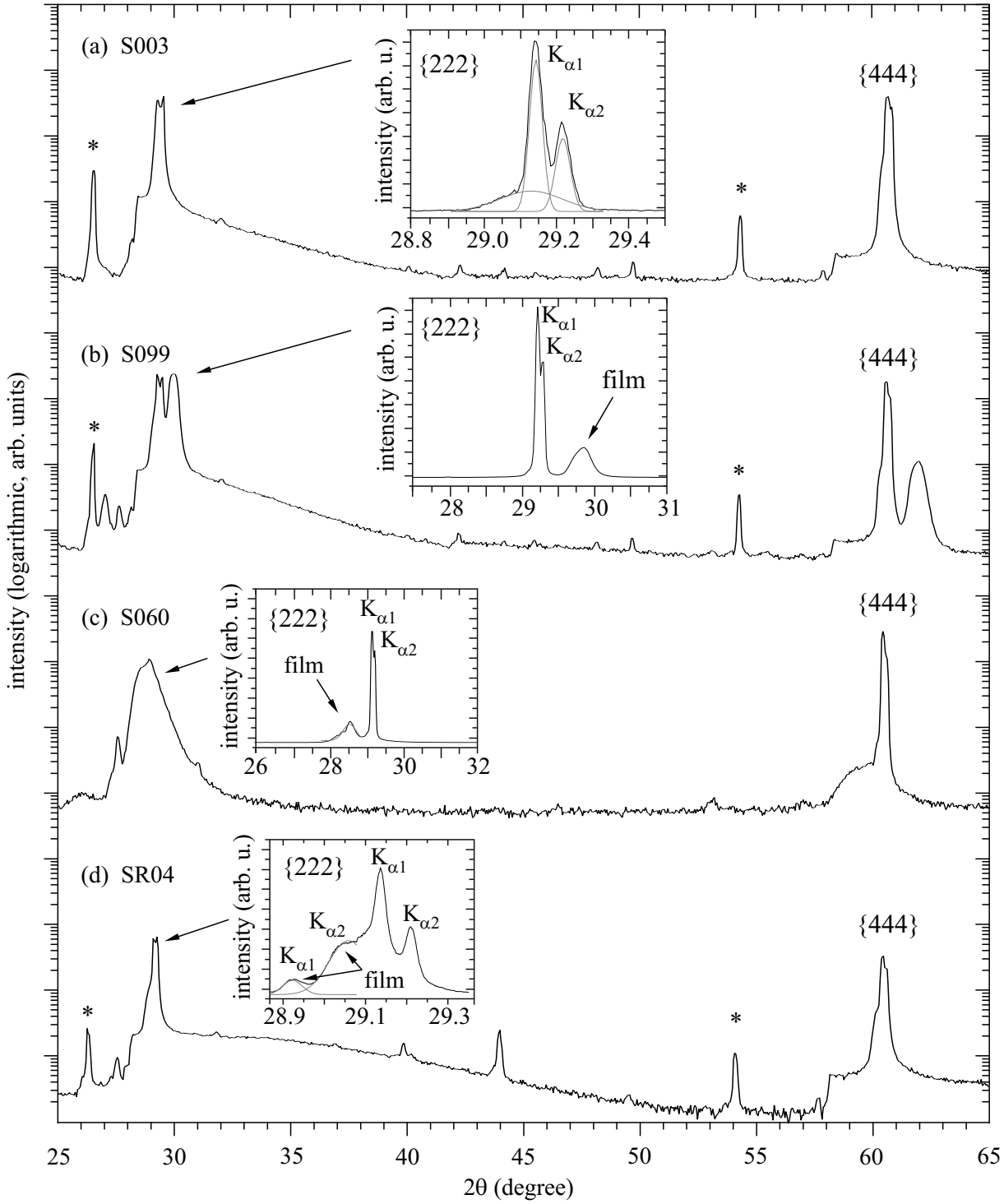

Figure 9.2: *X-ray diffraction patterns of sesquioxide films grown on* ⟨111⟩ *oriented* Y_2O_3*: (a) 120 nm Eu(1.5%):*Y_2O_3*, (b) 50 nm Eu(2%):*Lu_2O_3*, (c) 100 nm Eu(2%):*$(Gd, Lu)_2O_3$ *of composition [1], and (d) 100 nm Eu(2%):*$(Gd, Lu)_2O_3$ *of composition [2]. The insets show additional high resolution scans. Diffraction peaks indicated with '*' result from the residual Cu-*K_β *emission.*

Regarding the expected lattice constant for Eu(2%) doping, in both orientations the experimental values match very well within the measuring accuracy. Due to the higher temperature in both depositions, the crystallinity and peak width of both films are comparable in value. As no additional reflections from atomic planes other than in the default substrate direction are visible in the diffraction spectra, both films indicate highly textured crystalline growth in the substrate orientation: the 50 nm thin film in ⟨111⟩ direction (cp. figure 9.2b) and the 100 nm thin film in ⟨100⟩ direction (cp. figure 9.4c). The fact, that the film lattice constants match well with the theoretically calculated values can have different reasons. First, the lower Eu^{3+} doping in both films results in a better compensation in the lutetia lattice. It is possible, that a concentration of 2% does not disturb the lutetia lattice in a way, which would cause a lattice expansion. If the main part of the atomic plane distances diffracted by X-rays originate from undoped material due to statistically distributed europium ions throughout the lattice, a local lattice disturbance due to a single dopant ion will be of no consequence for the averaged diffraction pattern. Another explanation takes into account the higher deposition temperature for both lower doped films. A higher substrate temperature which increases the mobility of the deposited atoms can thereby amplify the ability of the lutetia lattice to compensate lower dopant concentrations without a lattice expansion. However, in both films S093 and S099 the Gaussian fit of the film reflection matches the diffraction pattern accurately and gives no evidence of a peak broadening.

No preferred film growth direction can be derived from the analyzed films. Although the measured lattice constants of the films grown in ⟨111⟩ direction are closer to the calculated values, this also can be ascribed to the film thickness. It was observed that the diffraction peaks of films with thicknesses of ≤ 50 nm shift to smaller angles (greater lattice constants) with further increasing thickness. Therefore, the reflection peaks of these thinner films may not be entirely pronounced and change their 2θ-position to smaller angles at higher thickness [Bur02, Bär04]. This behavior would relativize the above mentioned observation.

Composite Sesquioxide Films

Four composite sesquioxide films are compared, each of 100 nm thickness. Apart from the film S060, all films have been deposited at high substrate temperatures $T \geq 900$°C and an oxygen atmosphere of $8.9-9.0\times10^{-3}$ mbar using a repetition rate of 1 Hz. Only for the film SR11 the oxygen atmosphere had to be reduced to 4.6×10^{-3} mbar as the obtained RHEED diffraction images were too weak. As summarized in table 9.4 the film of composition [1] achieves a lattice constant of $a_\perp = 10.818$ Å which misses the substrate lattice constant by $f = 1.99\%$ (cp. figure 9.2c). It was deposited at 702°C and the estimated crystallite size $L_\perp = 26.8$ nm is roughly one fourth of the film thickness. Peak broadening is observed due to lattice expansion which is also caused by the mismatch f.

Despite the identical composition [2] and the similar deposition parameters a certain mismatch with respect to the substrate remains for all films. The f values in table 9.4 indicated with '*' are calculated by deriving film and substrate lattice constant from the diffraction spectra, as these diffraction measurements show a variation of $\pm 0.05°$ in absolute positions. Therefore the values of $a_\perp$ may not reflect the real mismatch

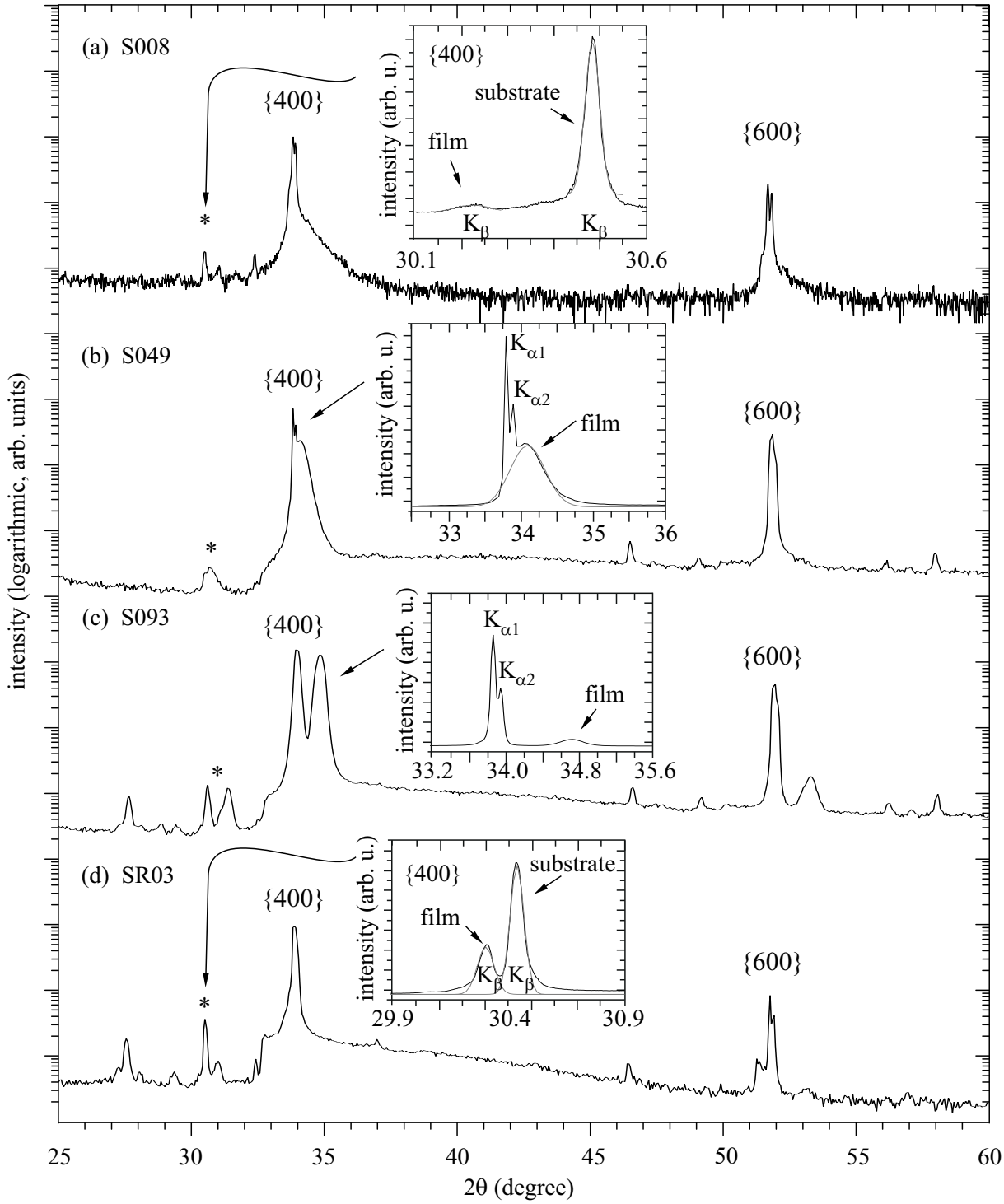

Figure 9.4: *X-ray diffraction patterns of sesquioxide films grown on ⟨100⟩ oriented Y_2O_3: (a) 100 nm Eu(1.5%):Y_2O_3, (b) 100 nm Eu(8%):Lu_2O_3, (c) 100 nm Eu(2%):Lu_2O_3, and (d) 100 nm Eu(2%):$(Gd, Lu)_2O_3$ of composition [2]. The insets show additional high resolution scans. Diffraction peaks indicated with '*' result from the residual Cu-K_β emission.*

parameter f. Within the measuring accuracy, the lattice constants of the composite films grown on ⟨111⟩ oriented yttria substrates do not show great deviation. Apparently, the oxygen pressure reduction for film SR11 had negligible influence on the film growth. It is questionable if the slightly better values for $L_\perp$ and $a_\perp$ are due to the lower oxygen pressure, as they can be ascribed to differences in the substrate surface quality as well. The composite film grown on ⟨100⟩ oriented yttria matches the substrate lattice best, with a mismatch of 0.46% (cp. figure 9.4). In comparison, the films SR04 and SR11 had lattice mismatches of 0.71% and 0.67%, respectively (cp. figures 9.2d and 9.5). The crystallite size exceeds the estimated thickness for the films of composition [2]. In the case of SR03 the difference can be explained by measuring inaccuracy. In general, film growth monitoring by in-situ reflectometry delivers only a thickness approximation based on the knowledge of the refractive indices of substrate and film. Especially for composite films the refractive index can differ from the assumed value resulting in a wrong film thickness. On the other hand the Scherrer equation only gives an estimation of the grain size $L_\perp$ within the given boundary conditions and the measuring accuracy. As the validity of the Scherrer equation has its limit at maximum grain sizes of about 150 nm [Sch18], it is concluded that the grown composite films are entirely crystalline and highly textured in the default substrate orientation.

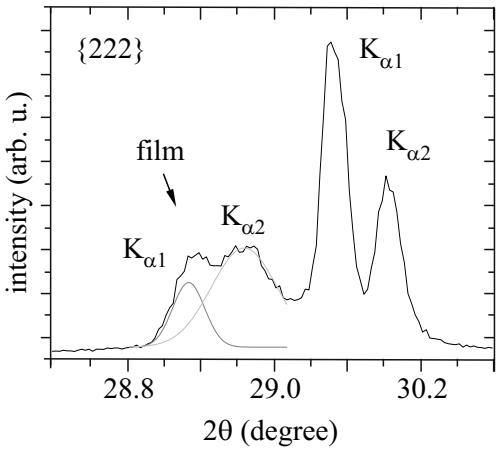

Figure 9.5: *High resolution θ–2θ-scan of the SR11 {222} reflection peak.*

In the following, the out-of-plane orientation of the crystallites corresponding to the planes not parallel to the surface are investigated by rocking curve measurements for the films SR03 and SR11. These are shown in figure 9.6. Beginning with the film grown in ⟨111⟩ direction the rocking curve (a) reveals multiple peaks of varying intensity. All reflections have narrow peak widths of $\leq 0.15°$ at FWHM. This gives evidence to a high degree of crystallinity, as polycrystalline reflections usually have much wider peaks. Rocking curves with multiple peaks indicate domain structures in the investigated film. Thus, it is

	Deposition		**Reflection**		**Film Properties**				**Tag**
	d_{film}(nm)	T_{sub}(°C)	peak	2θ(deg)	b_m(deg)	$L_\perp$(nm)	$a_\perp$(Å)	f(%)	
[1] K$_{\alpha1}$	100	702	{222}	28.560	0.350	26.8	10.818	1.99	S060
[2] K$_{\alpha1}$	100	910	{222}	28.923	0.047	194.0	10.685	0.71*	SR04
[2] K$_{\alpha1}$	100	900	{222}	28.886	0.044	207.2	10.699	0.67*	SR11
[2] K$_\beta$	100	900	{400}	30.306	0.071	116.4	10.652	0.46*	SR03

Table 9.4: Calculation of the crystallite size and the lattice constant of $(Gd, Lu)_2O_3$ films grown on [111] and [100] yttria determined by X-ray diffraction. Measured peak positions 2θ and peak widths b_m are fitted by a Gaussian profile. For $L_\perp$ the instrumental resolution b_a is considered. The different film compositions are distinguished by [1] and [2].

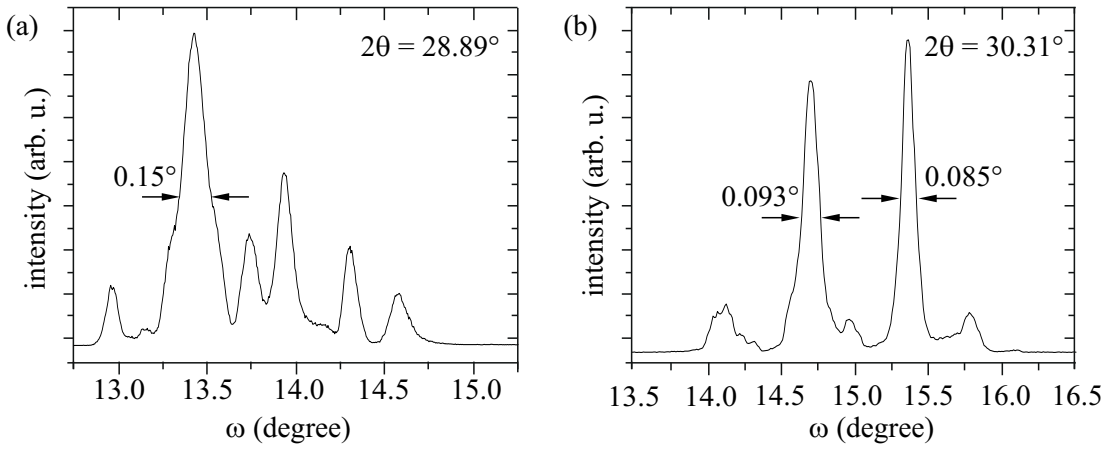

Figure 9.6: *Rocking curve measurements of (a) the SR11 {222} reflection peak and of (b) the SR03 {400} reflection peak.*

possible that lateral domains exist in the films. In agreement with the X-ray patterns and the small FWHM values of the ω-scans, these domains are monocrystalline and oriented slightly tilted to the default substrate direction in order to compensate the residual lattice mismatch while maintaining collateral cross-linking (cp. figure 9.7).

In comparison to the already discussed rocking curves, e. g. of a $(Sc, Lu)_2O_3$ film shown in figure 9.1, a broad rocking curve reveals relatively small but highly textured crystallites. Due to the large amounts and small sizes the X-ray diffraction (ω-scan) does not resolve every single-crystallite. Instead, a broad structure is observed. In contrast, the rocking curve of films SR11 and SR03 do not indicate many small crystallites but only few and large ones. As known from the θ–2θ-scans the crystallite size in both films correspond to the film thickness of 100 nm. Thus, columnar film growth is indicated with collateral cross-linked crystallites. According to the threefold symmetry axis of the [111] grown film SR11, six different crystallite types with well-defined tilting angle are observed in figure 9.6 (a). Only two main reflections are revealed in figure 9.6 (b) for the [100] grown film SR03, which have narrow FWHM widths of $\leq 0.093°$. In comparison, single-crystals of Sc_2O_3 and Lu_2O_3 have ω-scan peak widths of 0.082° and 0.15° at FWHM, respectively [Kuz06]. Most probably, both films have a 'mosaic structure' due to the residual lattice mismatch of 0.67% (SR11) and 0.46% (SR03). By gradual reduction of this residual mismatch, the multiple peaks are assumed to gradually converge until a single reflection of Gaussian shape is left (monocrystalline).

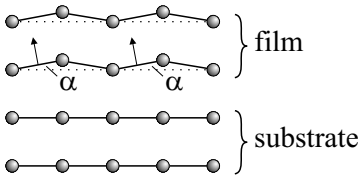

Figure 9.7: *Tilted film lattice with residual lattice mismatch* $a_f \cos\alpha = a_s$.

Despite of this possible interpretation, further investigation on the film structure has to be done. The surface X-ray diffraction (SXRD) and the transmission electron microscopy (TEM) are well-suited measuring techniques for this task. It has to be discussed whether this 'mosaic structure' is actually caused by the remaining lattice mismatch. Otherwise it could result from an inhomogeneous $(Gd, Lu)_2O_3$ solid solution. Crystal growth experiments using mixed sesquioxides of varying crystal structure incorporated some difficulties.

As Gd_2O_3 preferably crystallizes in monoclinic structure at room temperature it is possible that the ionic radius of Gd^{3+} is too large for the bixbyite structure and is responsible for the observed tilting. In the worst case a partial phase transition of Gd_2O_3 from cubic to monoclinic structure may take place, as the monoclinic structure is energetically favorable at room temperature (cp. footnote on page 14).

9.1.3 Surface Structure and Topography

The analysis of the developing surface structure during deposition by in-situ RHEED measurements and after deposition by AFM measurements delivers additional information on the film properties.

Figure 9.8 shows the in-situ RHEED analysis of the composite $Eu(2\%):(Gd,Lu)_2O_3$ film SR03 deposited at 1 Hz. The step height x of one monolayer $\langle 100 \rangle$ oriented sesquioxide film with cubic structure is half the lattice constant a ($x = 5.3$ Å for $a = 10.603$ Å). 108 pulses are required for one monolayer growth of [100] $(Gd,Lu)_2O_3$. During the continuous growth of the first 9 – 10 monolayers, no change in symmetry or spacing of the RHEED pattern is observed. Obviously, the intensity oscillation of the specularly reflected electron beam indicates two-dimensional layer-by-layer growth. The diffraction image after around 50 Å (left inset) reveals a very smooth surface, which is also confirmed by the relatively small intensity decrease at initial deposition. In comparison, figure 8.5 shows a steep intensity fall at initial deposition of heteroepitaxial $Eu:(Sc,Lu)_2O_3$. However, with continuous deposition an increase of surface roughness is indicated by the slowly decreasing oscillation amplitude. Usually, one monolayer growth is indicated by one RHEED intensity oscillation period. In this case two subsequent oscillations indicate the growth of one monolayer, with the first oscillation amplitude being strong and the second one

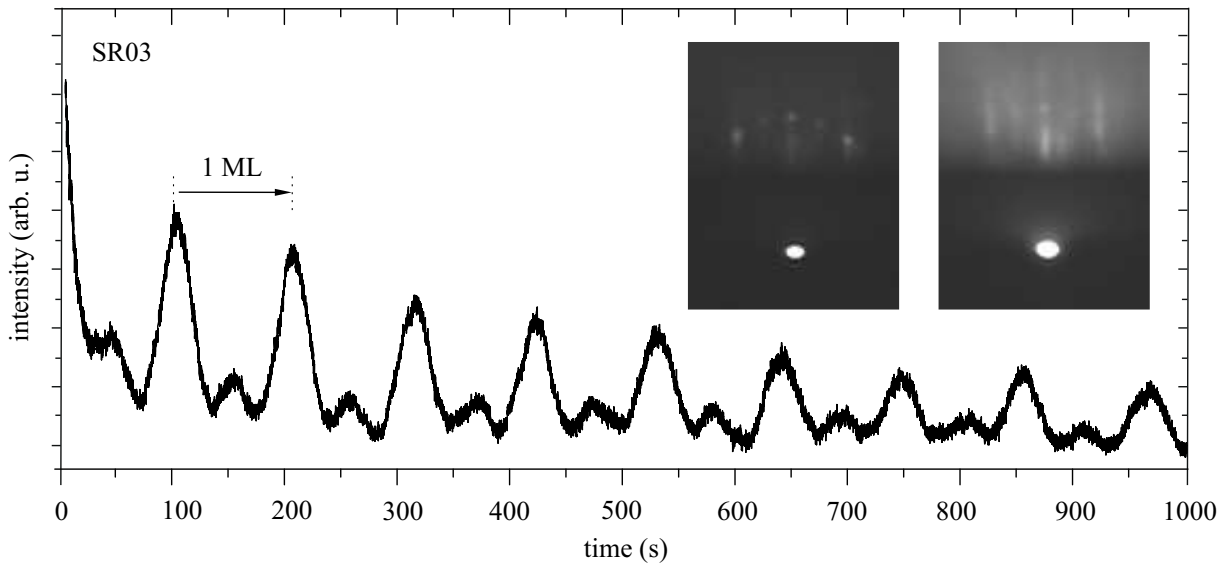

Figure 9.8: *RHEED oscillations and corresponding pattern (inset, left) during continuous deposition of around 50 Å Eu:(Gd.Lu)$_2$O$_3$ in $\langle 100 \rangle$ direction. The right inset shows the RHEED image after deposition of 100 nm.*

relatively weak. This phenomena occurs at certain incident angles and is well-known in RHEED analysis (cp. page 73). It is described by the dynamic theory. However, this different oscillation pattern does not contain additional growth information and thus no further explanation will be given here, as it would go beyond the scope of this thesis. A detailed description of this monolayer growth monitored by two oscillations is given in [Joy88]. The right inset of figure 9.8 shows the diffraction image after 100 nm film growth, for which the intensity oscillations continued until the end of deposition. According to the final diffraction image and the continuous intensity oscillations, two-dimensional layer-by-layer growth of 100 nm monocrystalline film was achieved with an atomically flat surface (RMS roughness of 1.2 Å). Although this is in agreement with the previous results of the X-ray analysis, the rocking curve measurements revealed a 'mosaic structure' for this film. This is explained in reference to the footnote remark on page 72, as the growth of slightly tilted atomic planes is not distinguishable by RHEED analysis from regular two-dimensional layer-by-layer growth without tilting.

Apart from continuous pulsed laser deposition, another way of growing monocrystalline films is the pulsed laser interval deposition (PLiD). With this technique the exact material amount which is required for the completion of a single monolayer is deposited at once. Thereby nucleation on subsequent layers is prevented. After deposition of the required material, a relaxation time is taken before the next layer is deposited. The RHEED intensity oscillation for this deposition variation is shown in figure 9.9 (a). The amount of 108 pulses, known from continuous deposition of the same substrate–film system, was deposited at the high repetition rate of 50 Hz. Thereafter a total relaxation of the RHEED intensity within 150 s is observed. If the deposited amount of material

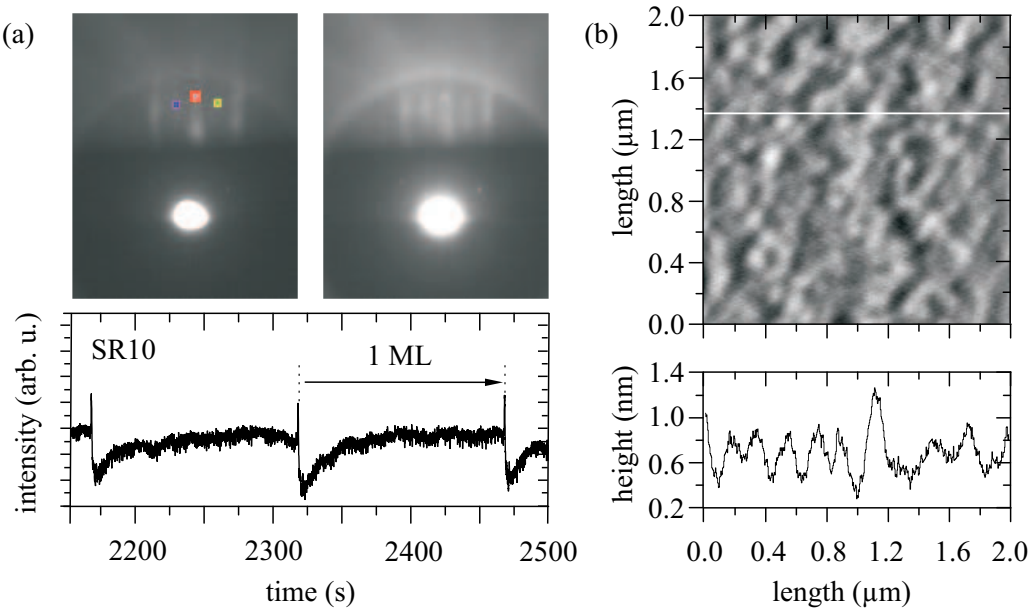

Figure 9.9: *(a) RHEED oscillations and corresponding pattern (inset, left) for pulsed laser interval deposition of Eu:$(Gd.Lu)_2O_3$ in ⟨100⟩ direction. The right inset shows the RHEED image after deposition end at 100 nm. (b) Surface topography measured by AFM.*

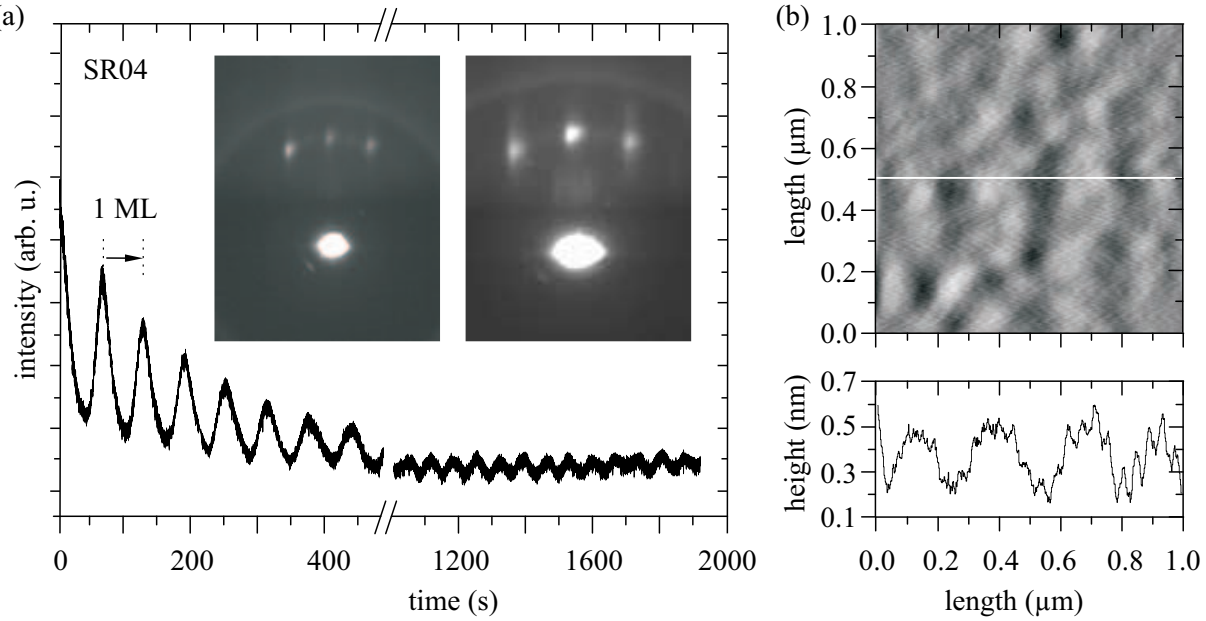

Figure 9.10: *(a) RHEED oscillations and corresponding pattern (inset, left) for continuous pulsed laser deposition of 109 Å (35 ML) Eu:(Gd.Lu)$_2$O$_3$ in* ⟨111⟩ *direction. The right inset shows the RHEED image after deposition end at 100 nm. (b) Surface topography measured by AFM.*

is not sufficient in order to complete a monolayer, the RHEED intensity will not regain its maximum value [Gün07]. Again, the final diffraction image (inset) after deposition of 100 nm which corresponds to the enduring RHEED intensity oscillations gives evidence to the monocrystalline two-dimensional layer-by-layer growth. After deposition, the surface topography was determined to be atomically flat with very low RMS roughness values of 2 Å (cp. figure 9.9b).

Similar results could be obtained in ⟨111⟩ direction as well. Figure 9.10 (a) shows the RHEED intensity oscillations for the continuous deposition at 1 Hz of the composite $(Gd, Lu)_2O_3$ film SR04 on [111] yttria. For cubic sesquioxides the step height x in [100] and [111] films is $a/2$ and $a/2\sqrt{3}$, respectively. Therefore, for the lattice constant $a = 10.6$ Å a [111] monolayer of 3.1 Å is completed after only 54 pulses whereas a [100] monolayer of 5.3 Å, requires 108 pulses. It is noticed that for increasing surface roughness, the intensity amplitude decreases. After the initial deposition of seven monolayers (21.4 Å) it remains relatively constant until the end of deposition at 100 nm film thickness. For the growth on [111] yttria the final diffraction image indicates an almost ideal surface. In comparison, the diffraction points have less tendency to form stripes. This could be an evidence of a preferred ⟨111⟩ growth direction, similar to Sc_2O_3 films [Gün07]. The surface shown in figure 9.10 (b) is again atomically flat (RMS roughness of 3 Å). In conclusion, 100 nm monocrystalline composite sesquioxide film was grown in two-dimensional layer-by-layer growth mode, which is in good agreement with the X-ray analysis results.

9.1.4 Spectroscopic Analysis

The optical properties of the grown composite films were investigated by luminescence measurements (excitation and emission), VUV measurements, and lifetime measurements. The refractive indices of the films were determined by ellipsometry. No Eu-impurities were detected in the undeposited substrates.

The luminescence properties of Eu-doped Y_2O_3 and Lu_2O_2 films fabricated by pulsed laser deposition have already been investigated by [Bur02, Bär04]. Thus, emphasis is put on the spectroscopic analysis of composite sesquioxide films and a comparison to single-component sesquioxides. Although a complete spectroscopic analysis was done for [111] and [100] grown thin films, no substantial differences exist in the optical properties. Therefore, as the optical properties of composite films grown on [111] and [100] yttria are similar and independent of the growth direction, the following spectroscopic analysis will not separately address different growth orientations.

Fluorescence and Excitation Measurements

Excitation and emission spectra of a composite $(Gd, Lu)_2O_3$ thin film (b) are compared to single-component Y_2O_3 bulk single-crystal (a) in figure 9.11. It is apparent, that the thin film has bulk-like luminescence properties. The linewidths and transition intensities are preserved in the composite thin film and very similar to the Y_2O_3 single-crystal.

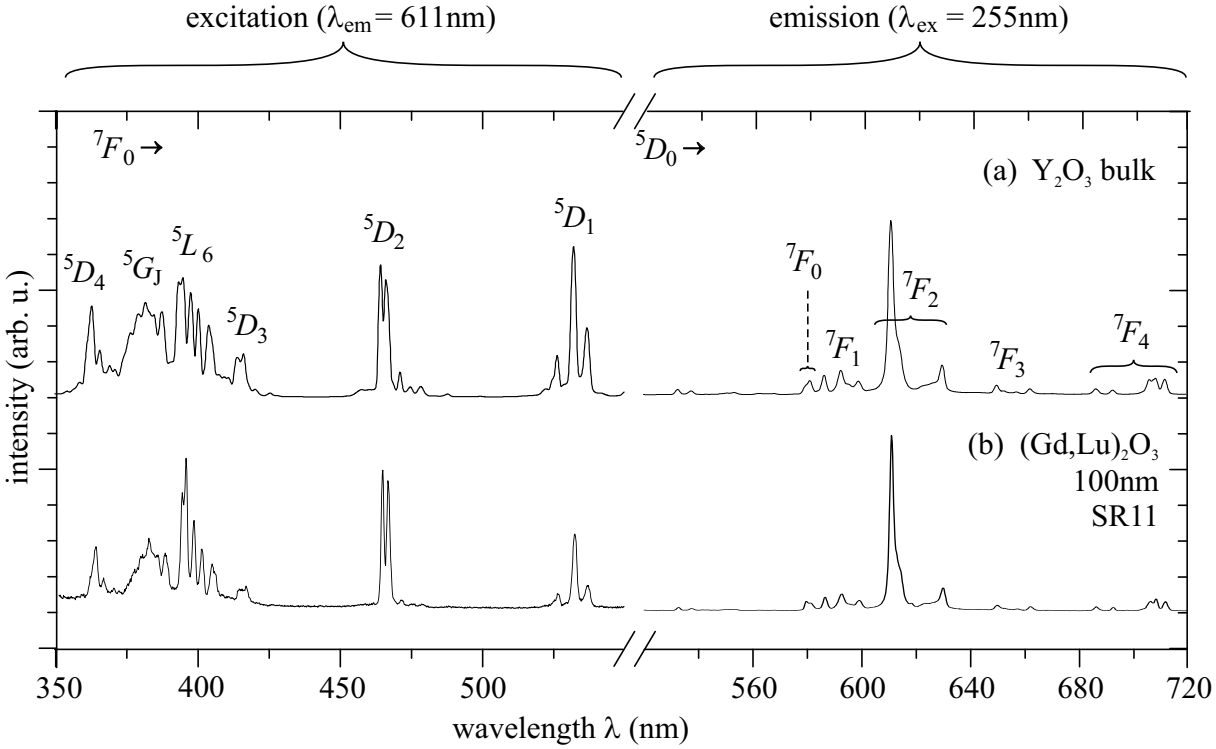

Figure 9.11: *Excitation (left) and emission spectra (right) of (a) an Eu(1%):Y_2O_3 bulk crystal in comparison to (b) an Eu(2%):$(Gd, Lu)_2O_3$ thin film.*

In detail, the emission spectrum (b) of the composite thin film shows the characteristic europium transitions with all transitions being resolved properly. The spectrum is dominated by the $^5D_0 \rightarrow {}^7F_2$ transition at 611 nm (cp. chapter 3.3), which has a linewidth of 1.56 nm at FWHM. In comparison, the transition linewidth is 1.31 nm in the Y_2O_3 bulk spectrum. This marginal linewidth difference of 0.25 nm can be ascribed to the difference between a single-component material like yttria and a composite material like $(Gd, Lu)_2O_3$. In good agreement with the spectroscopic analysis of $(Sc, Lu)_2O_3$ films in chapter 8.1.4, a small degree of broadening takes place when mixing different sesquioxides. As illustrated in figure 8.7, the small spectral shift and the marginal linewidth difference are due to the change in the crystal field. Interestingly, this figure also reveals that the broadening effect in $(Gd, Lu)_2O_3$ is smaller than in $(Sc, Lu)_2O_3$. However, the spectral shift of composite $(Gd, Lu)_2O_3$ to Y_2O_3 is negligible. The excitation spectrum of the thin film (b) shows similar fingerprints as the already evaluated sesquioxide excitation spectra in chapters 8.1.4 and 8.3.3. In short, the characteristic transitions are all well-resolved, with small intensity deviation regarding the transitions to the $^5L_6$ and the $^5D_1$ levels. This was already explained in the above mentioned sections.

VUV Measurements

Again, additional VUV excitation and emission measurements have been performed at 10 K. Figure 9.12 shows the typical Eu-spectra, similar to the ones analyzed in chapters 8.1.4 and 8.3.3. In can be seen in the well-resolved emission spectrum in figure 9.12,

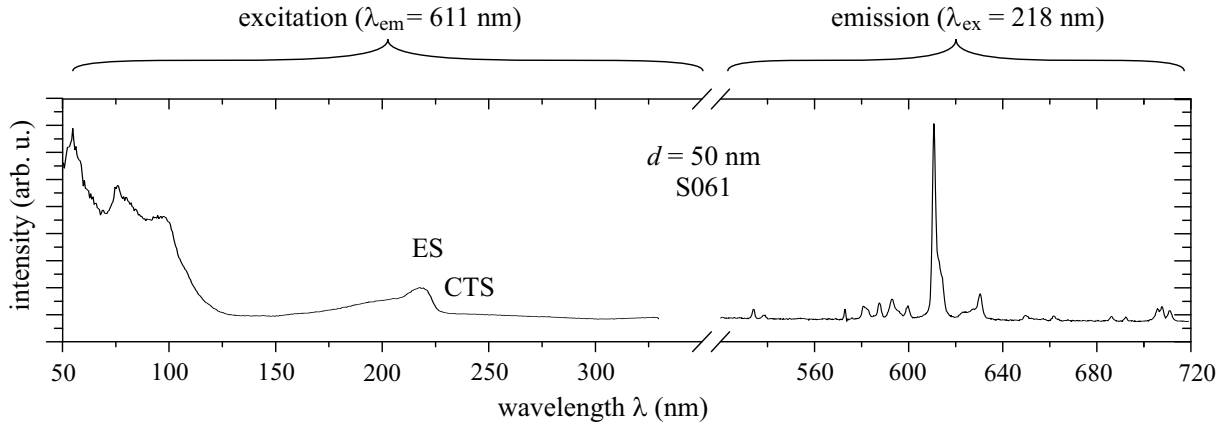

Figure 9.12: *VUV measurements of an Eu(2%):$(Gd, Lu)_2O_3$ thin film.*

that the local symmetry in the composite Eu:$(Gd, Lu)_2O_3$ film of 100 nm thickness is not disturbed. Because all transitions can be identified and the linewidths and peak intensities are consistent with the known values, this is in good agreement with the room temperature luminescence measurements (cp. figure 9.11). The excitation spectrum has a good signal to noise ratio, especially when compared with the composite $(Sc, Lu)_2O_3$ film (cp. figure 8.10). As already observed in the composite $(Sc, Lu)_2O_3$ film, the CTS around 240 nm (5.17 e V) is broadened and has almost vanished. It is still indicated by an intensity increase starting at 250 nm and continuing until the ES edge around 230 nm is reached. The ES at 218 nm (5.69 e V) is of relatively small intensity when compared to the

single-component yttria ES peak at 204 nm. Interband transitions are observed around 100 nm (12.4 e V), 75 nm (16.54 e V), and 60 nm (20.684 e V). Table 9.5 compares the optical transitions of the investigated sesquioxide materials. The most probable explanation for the weakly structured excitation spectrum with the less intense ES and CTS peaks is the disturbance of the band structure due to different ionic radii of the gadolinium and lutetium ions. Because of the similarities to composite $(Sc, Lu)_2O_3$ films it is referred to section 8.1.4 for detailed explanation. However, in comparison to $(Sc, Lu)_2O_3$ the better signal to noise ratio for the $(Gd, Lu)_2O_3$ films indicates slightly less disturbed lattices.

	CTS		ES	
	(nm)	(eV)	(nm)	(eV)
Y_2O_3	240	5.17	204	6.08
Lu_2O_3	240	5.17	210	5.91
$(Sc, Lu)_2O_3$	240*	5.17*	201	6.18
$(Gd, Lu)_2O_3$	240*	5.17*	212	5.85

Table 9.5: *Comparison of optical transitions. Values indicated with '*' are estimated (see text).*

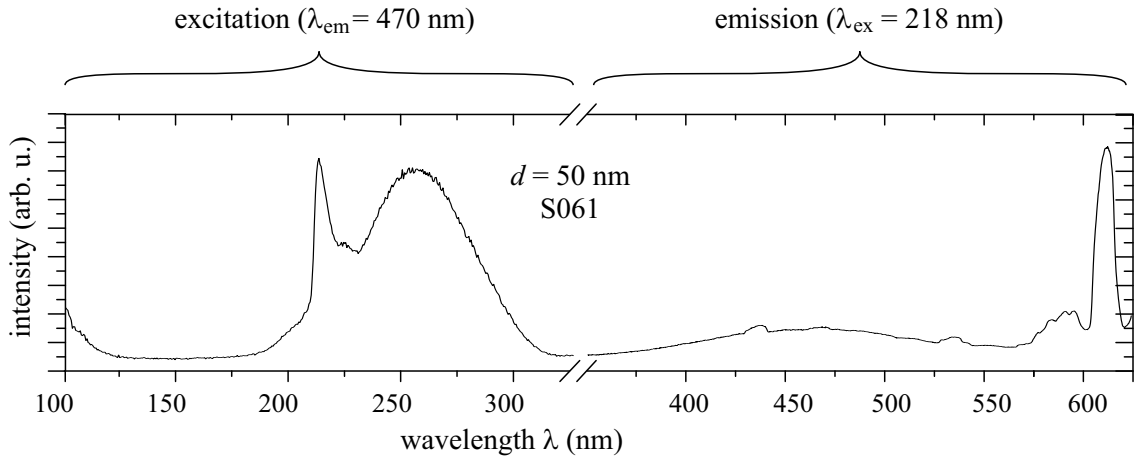

Figure 9.13: *VUV measurements of an Eu(2%):$(Gd, Lu)_2O_3$ thin film.*

In order to better investigate the CTS and ES further VUV measurements have been done using a different emission wavelength of $\lambda_{em} = 470$ nm which corresponds to a broadband CT fluorescence. Figure 9.13 shows the resulting spectra, this time with very pronounced CTS at 255 nm and ES at 212 nm (5.85 e V). Apart from the used lower resolution in order to resolve the broad CT band at 470 nm, the emission spectrum is similar to the one in figure 9.12.

Lifetime and Refractive Index Measurements

Additional ellipsometry and lifetime measurements have been performed to further investigate the local crystal structure. The fluorescence lifetimes of composite $(Gd, Lu)_2O_3$ films with thicknesses of 100 nm and 10 nm are shown in figure 9.14. The lifetimes τ of the $^5D_0 \rightarrow {}^7F_2$ fluorescence have been determined by an exponential fit of the decay curve. The polycrystalline fused sample of identical composition (cp. section 8.1.4, page 97) served as reference and had the lifetime $\tau = 0.83$ ms.

Lifetimes τ of 0.75 ms and 1.05 ms were measured for the 100 nm and the 10 nm thin film, respectively. The lifetime of the 100 nm thin film exceeds the reference sample lifetime. Besides the explanation that this indicates a higher optical quality than the polycrystalline reference probe it is also possible that the reason for the shorter lifetime is quenching. Caused by non-radiative decay processes, quenching occurs due to non-perfect films. The last interpretation would be in good agreement with the reduced quality in films S060 and S063. In the 10 nm thin film the lifetime is increased because of the Lorentz correction (cp. section 7.4.2).

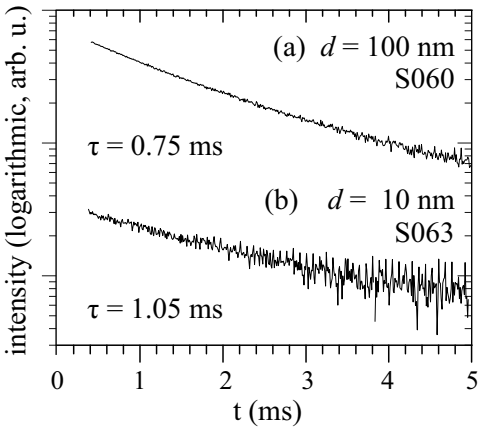

Figure 9.14: *Fluorescence lifetime of Eu:(Gd, Lu)$_2$O$_3$ films.*

The corresponding refractive indices n have been estimated by ellipsometric measurements to be 1.945 and 1.918 for the 100 nm and the 10 nm film, respectively. With the resulting refractive index difference of $\Delta n = 0.05$ waveguiding was recently achieved.

9.2 Orthovanadate Films on YVO_4

This section focuses on the characterization of rare-earth vanadate films on $\langle 100 \rangle$ oriented YVO_4. For Eu:$GdVO_4$ films the ionic radii of Eu^{3+} and Gd^{3+} are both bigger than the one of Y^{3+} in the substrate lattice (cp. table 3.1). Therefore the deposited film has a greater lattice constant in comparison. This system as well as the solid solution Eu:(Gd, Lu)VO_4, which is lattice matched with respect to the YVO_4 substrate, are investigated.

9.2.1 Lattice Matching and Structural Characterization

The lattices of Eu:$REVO_4$ films deposited on YVO_4 combine directly according to $a_s \approx a_f$ (cp. chapter 5.2). Similar to the composite sesquioxides in the previous section 9.1, two lattice matched compositions have been tried in this work: $(Eu_{0.02}Gd_{0.534}Lu_{0.446})VO_4$ [1] and $(Eu_{0.02}Gd_{0.48}\ Lu_{0.50})_2VO_4$ [2]. The ionic radii estimation of these compositions was explained in section 9.1.1. Again, the obtained refractive index difference between substrate and film is expected to be higher for the composite system.

The growth behavior and the lattice matching of these rare-earth vanadate films have been investigated on $\langle 100 \rangle$ oriented YVO_4 substrates. For a film composition of Eu(1.5%):$GdVO_4$ the theoretically expected lattice constant[1] is $a = 7.215$ Å , which would result in a lattice mismatch of 1.31% with regard to the YVO_4 substrate lattice.

In chapter 8.1.2 it has been set forth that due to the decrease in the scattering amplitude the diffraction analysis should focus on crystal-planes of lower order. However, sometimes

[1] The lattice constant of tetragonal $EuVO_4$ is $a = 7.236$ Å and $c = 6.362$ Å [Mul96].

a strong overlap of substrate and film reflections prevents a differentiated diffraction analysis. This is especially the case in homo- and quasi-homoepitaxial films. Therefore, as the diffraction spectra are widened with increasing 2θ angle, crystal-planes of higher order are analyzed in these exceptions. The f values in tables 9.6 and 9.7 indicated with '*' are calculated by deriving film and substrate lattice constants from the diffraction spectra, as the diffraction measurements may vary $\pm 0.05°$ in absolute positions. Thus, the values of $a_\perp$ do not reflect the real mismatch parameter f.

Gadolinium Vanadate Films

In figure 9.15 two diffraction spectra of Eu-doped $GdVO_4$ films are compared and the acquired film properties summarized in table 9.6. Despite having the same film composition, different degrees of lattice matching are achieved with mismatch values f of 1.72% and 0.92% for films S020 and S080. This is understood with regard to the deposition parameters. Although both films were deposited under the same oxygen atmosphere of 10^{-2} mbar, the repetition rate was varied from 11 Hz (S020) to 3 Hz (S080).

Especially the higher deposition temperature of 850°C for film S080 has strong influence

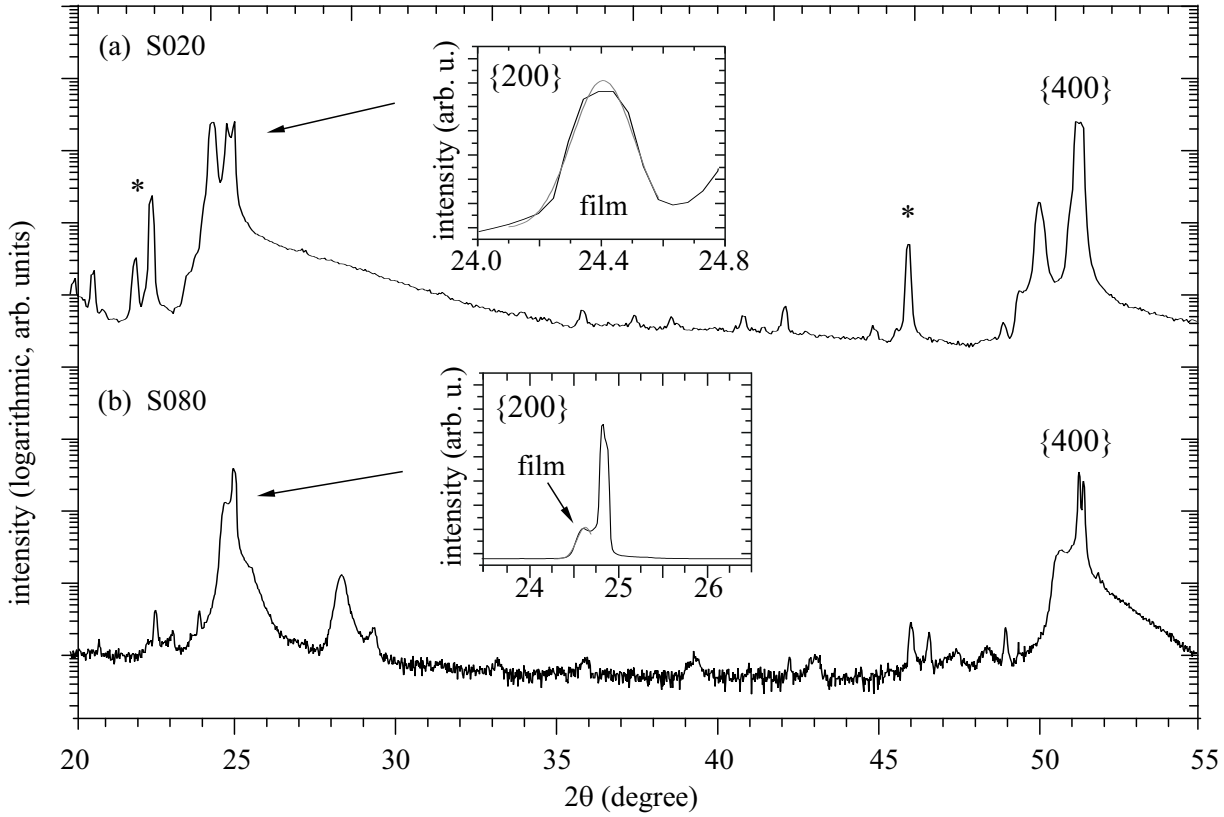

Figure 9.15: *X-ray diffraction patterns of Eu(1.5%):$GdVO_4$ films grown on ⟨100⟩ oriented YVO_4: (a) 125 nm thin film and (b) 100 nm thin film. The insets show additional high resolution scans. Diffraction peaks indicated with '*' result from the residual Cu-K_β emission.*

on the surface mobility of the deposited atoms. The mismatch of 0.92% for the film S080 is even smaller than the theoretically expected one, which can partly be ascribed to the higher temperature. Most probably, a certain degree of film stress, which is caused by the lattice mismatch, is compensated by elastic deformations. In contrast, the mismatch of 1.72% in the film S020, which lies above the estimated mismatch value of 1.31%, gives evidence to lattice expansion in this film. The film stress is not compensable by elastic deformations due to the relatively low temperature and the reduced diffusion time (repetition rate 11 Hz) during deposition of the film S020. As the ability of elastic stress-compensation during film growth is reduced, structural defects like dislocations and grain boundaries compensate the evolving stress and are responsible for the higher lattice constant [Kle89].

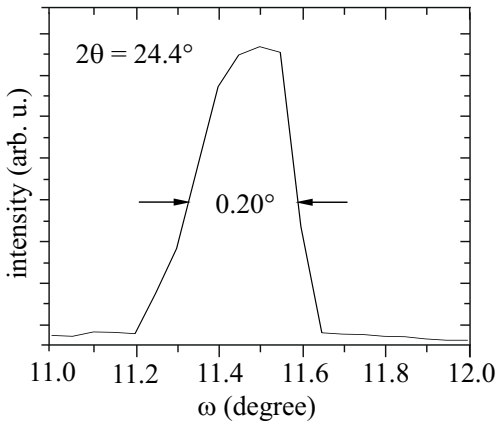

Figure 9.16: *Rocking curve fit of the S020 {200} reflection peak.*

The comparison of these two films of identical composition strongly emphasizes the influence of the deposition temperature and the repetition rate. However, the grain size of both films is almost half the film thickness with $L_\perp = 46\,\text{nm}$ in average. As no additional reflections[2] from atomic planes other than in $\langle 100 \rangle$ orientation are seen, it is concluded that the films are grown highly textured in $\langle 100 \rangle$ orientation.

An additional rocking curve measurement shown in figure 9.16 proves that the $\langle 100 \rangle$ crystal axes of the 100 nm thin film S020 are aligned along the film normal direction within 0.20°. The asymmetric broadening indicates strong lattice deformation [Hag01] due to the high mismatch. Probably, initial layers have a higher dislocation density (left-sided shoulder) in order to compensate the lattice mismatch, whereas with continuing growth the stress-relaxed film layers have less structural defects (right-sided sharp decline). The formation of an interface layer as seen in the heteroepitaxy of Eu:$(Sc, Lu)_2O_3$ is not evident and unlikely in regard of the comparably small FWHM of 0.2°.

Deposition		**Reflection**		**Film Properties**				**Tag**
d_{film}(nm)	T_{sub}(°C)	peak	2θ(deg)	b_m(deg)	$L_\perp$(nm)	$a_\perp$(Å)	f(%)	
125	730	{200}	24.416	0.209	47.2	7.285	1.72*	S020
100	850	{200}	24.845	0.216	45.4	7.162	0.92*	S080

Table 9.6: *Calculation of the crystallite size and the lattice constant of $GdVO_4$ films determined by X-ray diffraction. Measured peak positions 2θ and peak widths b_m are fitted by a Gaussian profile. For $L_\perp$ the instrumental resolution b_a is considered.*

[2] The reflection in figure 9.15, (b) at 28.44° results from the substrate. Substrate peaks are resolved with varying intensity due to the different X-ray devices used for (a) and (b).

Composite Vanadate Films

Different deposition parameters have been used for the film growth of four compared lattice matched films. An oxygen pressure of 10^{-2} mbar with a repetition rate of 11 Hz (S072, figure 9.17a) and 3 Hz (S082, figure 9.17b) have been used for the films of composition [1]. Substrate heating of 730°C (S072) and 800°C (S082) has been applied. The films of composition [2] have been fabricated in oxygen atmospheres of $7.7-8.3\times10^{-3}$ mbar at 1 Hz. The lattice mismatch of all films is below 1%, ranging from 0.95% for the film S072 of composition [1] to 0.21% for the film SR12 of composition [2]. It was observed that within both compositions one of the two film growths resulted in a larger lattice mismatch.

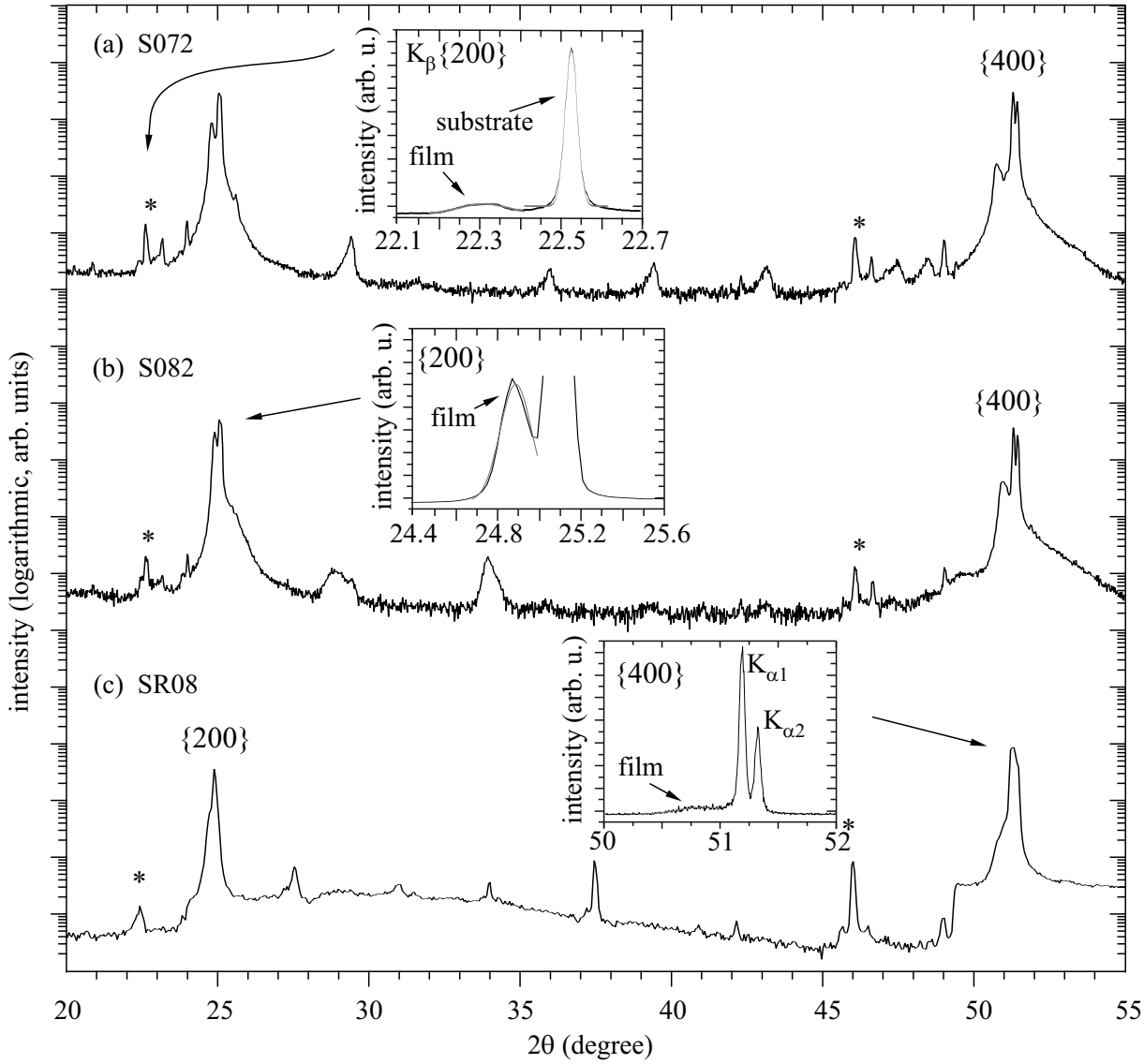

Figure 9.17: *X-ray diffraction patterns of Eu(2%):(Gd, Lu)VO_4 films of 100 nm thickness grown on ⟨100⟩ oriented YVO_4: (a) S072, (b) S082, and (c) SR08. The insets show additional high resolution scans. Diffraction peaks indicated with '*' result from the residual Cu-K_β emission.*

Although in case of composition [1] this can be explained to some extent by the deposition temperature, the influence of the substrate quality will be discussed after the X-ray analysis. When comparing the better matched film of each composition, it is obvious that an improvement in lattice matching is achieved by composition [2]. The lattice mismatch of film SR08 (figure 9.17c) is comparable with the one of S082, although different film compositions were used. A high degree of crystallinity is noticed for substrate temperatures around 730 – 800°C as the grain size $L_\perp$ is 68.7 nm for S072 and 76.3 nm for S082 which is 69- 76% of the overall film. The distinctly smaller crystallite values for films deposited at higher temperatures using a lower repetition rate may have different reasons. Probably, temperatures of 900°C are too high for vanadate materials. This hypothesis is further investigated by RHEED analysis in the following subsection. Moreover, it is possible that an evaluation of the higher order reflection {400} resulted in a systematical error for these films. The decreased scattering amplitude for these higher-order crystal-planes may result in modified peak shapes, which cause the altered grain sizes. The diffraction analysis focuses on the {400} reflection because of the strong overlap between film and substrate reflection for highly lattice matched film growth.

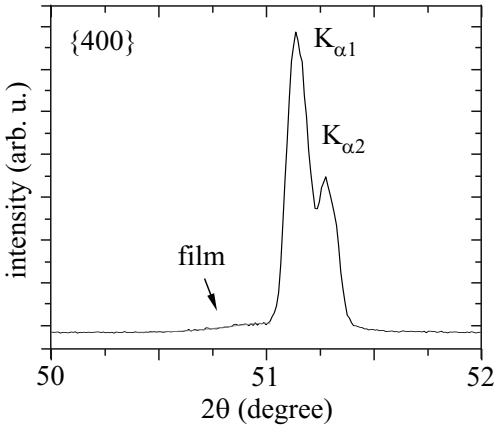

Figure 9.18: *High resolution θ–2θ-scan of the SR12 {400} reflection peak.*

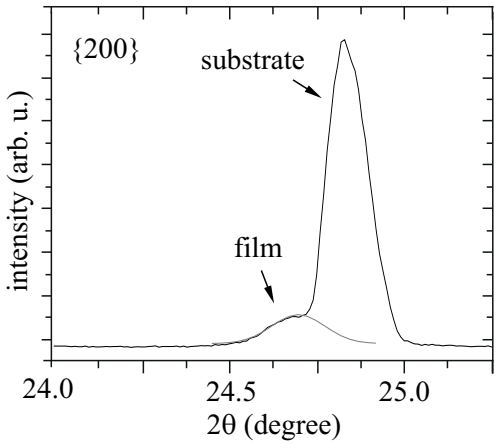

Figure 9.19: *High resolution θ–2θ-scan of the SR12 {200} reflection peak.*

Figure 9.18 depicts the {400} reflection, which was used to estimate the crystallite size of the film SR12. In order to prove the assumption of a systematic error, the {200} reflection

	Deposition		Reflection		Film Properties				Tag
	d_{film}(nm)	T_{sub}(°C)	peak	2θ(deg)	b_m(deg)	$L_\perp$(nm)	$a_\perp$(Å)	f(%)	
[1] K_β	100	730	{200}	22.315	0.125	68.7	7.195	0.95*	S072
[1] $K_{\alpha1}$	100	800	{200}	24.914	0.125	76.3	7.142	0.58*	S082
[2] $K_{\alpha1}$	100	900	{400}	50.858	0.457	21.5	7.176	0.60*	SR08
[2] $K_{\alpha1}$	100	900	{400}	51.037	0.435	22.6	7.152	0.21*	SR12

Table 9.7: *Calculation of the crystallite size and the lattice constant of $(Gd, Lu)VO_4$ films determined by X-ray diffraction. Measured peak positions 2θ and peak widths b_m are fitted by a Gaussian profile. For $L_\perp$ the instrumental resolution b_a is considered. The different film compositions are distinguished by [1] and [2].*

of film SR12 (figure 9.19) is evaluated with regard to the crystallite size. A Gaussian fit estimates the {200} peak position and width to 24.688° and 0.150°, respectively. By using these values, the grain size for SR12 is determined to be 62.5 nm. Although this grain size is indeed nearly three times higher than the one estimated by the {400} reflection, it is still smaller than the one for the films deposited at lower temperatures. By this means it is again indicated that the initial deposition parameters with temperatures of around 800°C are better suited for vanadate films. Higher temperatures seem to correspond to a reduction of the grain sizes, as observed in the films SR08 and SR12.

The out-of-plane orientation of crystallites which correspond to atomic planes not parallel to the surface are investigated by a rocking curve measurement of the {200} reflection. It is observed that the ⟨100⟩ crystal axes of the 100 nm thin film are aligned along the film normal direction with a peak width of 0.165°. The spectrum in figure 9.20 can be understood by considering the residual lattice mismatch of only 0.21%. Similar to the sesquioxide films SR11 and SR03 in section 9.1, the crystalline domains are oriented slightly tilted to the default substrate orientation to compensate the small mismatch (cp. figure 9.7). However, as the remaining mismatch is smaller than the one of the sesquioxide films SR11 and SR03, the two reflections have nearly converged into a single peak of Gaussian form. By subtracting the estimated FWHM width 0.091° of the narrow peak from the overall width 0.165°, it can be assumed that the two observed reflections in the ⟨100⟩ film normal direction have widths of 0.074° and 0.091°. This is similar to the [100] sesquioxide film SR03 rocking curve shown in figure 9.6 (b), which also had two main reflections of FWHM widths 0.085° and 0.093°.

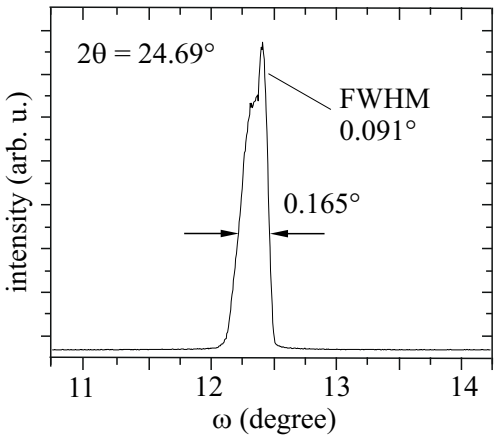

Figure 9.20: *Rocking curve fit of the SR12 {200} reflection peak.*

9.2.2 Surface Structure and Topography

Figure 9.21 (a) shows the in-situ RHEED analysis for the continuous deposition of the composite $(Gd, Lu)VO_4$ film SR08 at 1 Hz. The step height x of one monolayer in ⟨100⟩ oriented orthovanadate films with tetragonal structure is determined by $x = a/2$, which results in $x = 3.6$ Å for $a = 7.12$ Å. An amount of 118 pulses completes the growth of one monolayer [100] $(Gd, Lu)VO_4$ with 3.6 Å step height. The symmetry and spacing of the RHEED pattern changes within the continuous growth of the first five monolayers. While the pattern in inset (i) corresponds to an ideal surface with very good properties, the pattern in inset (ii) already indicates a transition from two-dimensional to three-dimensional growth after deposition of 5 Å. The diffraction points turn into stripes, which is a typical characteristic of this transition. The arrangement of the pronounced diffraction points in inset (iii) is comparable to figure 6.8 (c) and indicates three-dimensional island formation. The development of the RHEED intensity confirms this interpretation as the oscillation amplitude decreases almost exponentially during the growth of these five

monolayers. Besides indicating a fast increase in surface roughness at the initial deposition of around 50 pulses, the fast damping of the oscillations can be related to a growth mode change. In accordance, figure 9.21 (b) shows three-dimensional grains identified by AFM measurements. The RMS roughness is determined to be 2 nm. However, the smooth intensity oscillations, which indicate two-dimensional layer-by-layer growth at the deposition begin, are promising as they prove that epitaxial growth can be realized by this substrate–film system.

These results are in good agreement with the correlated X-ray analysis, especially with the moderate crystallite size of the film SR08. In conclusion, substrate temperatures of 900°C were too high for the epitaxy of orthovanadate films. This is probably due to different reasons: Although in general a high temperature is of advantage for pulsed laser deposition, this is no rule of infinite appliance. Too high substrate temperatures result in further and further increasing particle energies which consequently interact with the substrate. The high pulse energy of 0.8 J/cm^2 may have benefited the growth mode change as vanadates have comparably lower Mohs hardness. These interactions, e. g. subplantation (cp. chapter 8.3), are to be avoided in PLD. If the substrate temperature reaches half the melting temperature of the substrate material, solid-state reactions can occur. In these cases the film growth is negatively affected. The fast increase of surface roughness after only 5 Å may be a reference to solid-state reactions of the vanadate substrate due to well-known instabilities of the V^{5+} ion at high temperatures [Krä05].

However, for the grown $(Gd, Lu)VO_4$ films the ratio between crystallite size and estimated film thickness reaches a maximum for substrate temperatures of 800°C (cp. table 9.7) with

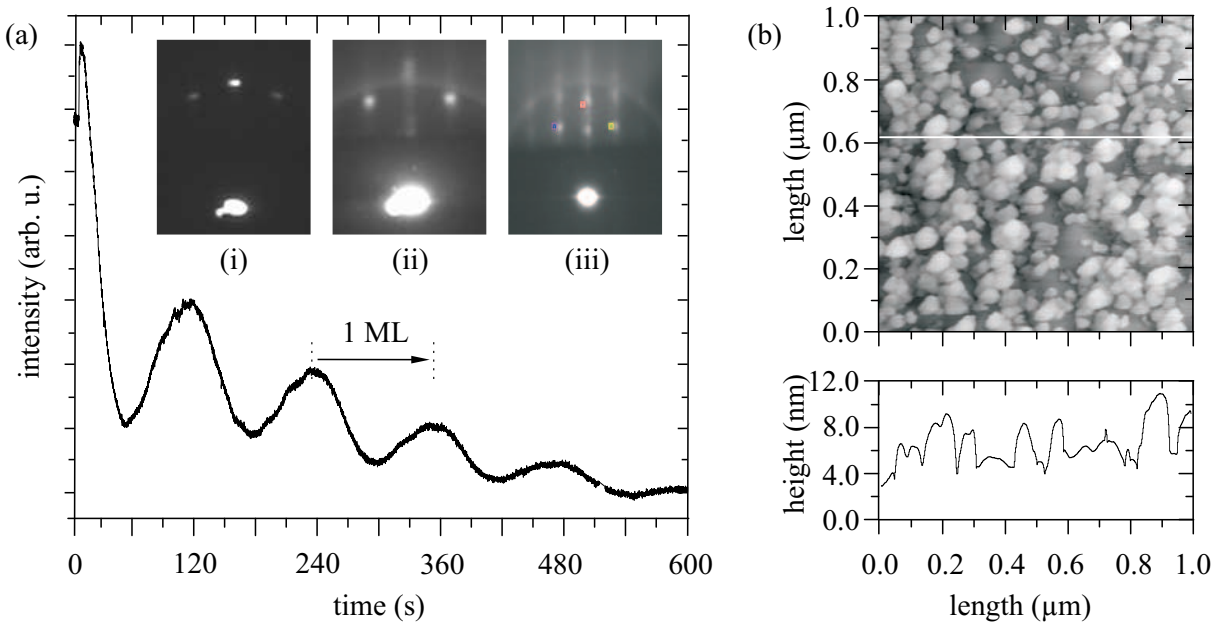

Figure 9.21: *(a) RHEED oscillations during continuous deposition of 18 Å Eu:(Gd, Lu)VO_4. The insets show the RHEED patterns before deposition (i), after growth of 5 Å (ii), and after deposition at 100 nm (iii). (b) Surface topography measured by AFM.*

76%. By this means, the temperature window for homoepitaxial pulsed laser deposition of vanadates is assumed to be around 800°C. Further growth attempts will be done in order to sustain the layer-by-layer growth mode.

Substrate Quality

YVO_4 substrates of the same charge and obtained by the same bulk single-crystal were used for the deposition of orthovanadate films. Figure 9.22 shows the surface morphology of thermally treated YVO_4 substrates used for the deposition of the films SR08 and SR12. These substrates were annealed for 1 h at temperatures of 800°C prior to deposition. By simple geometric consideration, the miscut of the used substrates was estimated to be around $\beta = 0.41°$. This is quite high in comparison to epitaxial grade polished commercially available substrates, which have miscut angles of 0.005°, e. g. the [0001] α-Al_2O_3 substrate in figure 6.5. With increasing miscut angle, the substrate surface features different step heights, which consist of multiple monolayers. These are caused as the energy of the surface atoms exceed the potential barrier of a monolayer step. Due to the additional *Schwoebel barrier* [Bar95], a drop back is not possible for these atoms. A further increasing miscut angle leads to *step-bunching* and then to uneven areas on the surface similar to 'hills' and 'valleys' due to surface tension.

The surfaces of the investigated YVO_4 substrates after thermal treatment are shown in figure 9.22. Therein, step-bunching (a) can be noticed as well as surface tension which results in 'hill' and 'valley' formation (b). Apart from these deficiencies, the existence

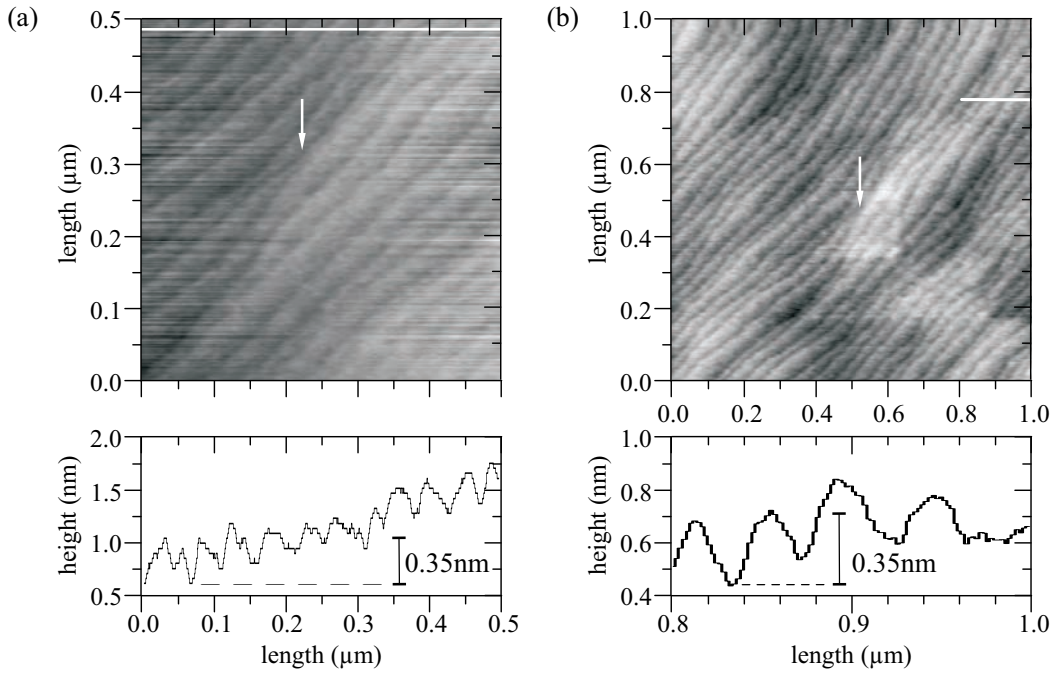

Figure 9.22: *Surface morphology of annealed [100] YVO_4 substrates. The white arrows mark (a) step-bunching and (b) indicated surface tension with a lattice defect.*

of lattice defects is indicated (b). By this means, the high miscut angles and possible lattice defects of the substrate may affect the film growth due to the comparably high step density on the substrate and the indicated surface tension [Joy88, Gün07]. Step-bunching usually causes three-dimensional island growth during the deposition process [Rij04], which would be in agreement with the growth behavior of the film SR08 observed by RHEED.

Therefore, two reasons may probably be responsible for the transition from two-dimensional to three-dimensional growth: the poor substrate quality (high miscut, step-bunching, lattice defects) and the too high substrate temperature during deposition. A correlation of both factors is possible.

9.2.3 Spectroscopic Analysis

The optical properties of the grown composite films were investigated by luminescence measurements (excitation and emission), VUV measurements, and lifetime measurements. In addition, the refractive indices of the films were determined by ellipsometry. No Eu-impurities were detected in the undeposited substrates.

Fluorescence and Excitation Measurements

Composite orthovanadate films are compared to single-component Eu:$GdVO_4$ as bulk crystal and as thin film. The charge transfer band for the investigated orthovanadates has its maximum at around 270 nm. In figure 9.23 it is apparent that the emission spectra are once again dominated by the $^5D_0 \rightarrow {}^7F_2$ transition at 619 nm with narrow linewidths of 1.2 nm at FWHM in the $GdVO_4$ bulk crystal (a), of 1.5 nm in the $GdVO_4$ film (b), and of 1.26 nm in the mixed $(Gd, Lu)VO_4$ film (c). For the emission measurements, the linewidth and transition intensities are preserved in the composite thin films and are very similar to the single-component bulk. Equally well-resolved excitation spectra (b) and (c) were measured for the thin films. Only the $^5D_1$ level at around 530 nm is less pronounced in the thin films than in the bulk crystal. Therefore, the local crystal structure of the Eu^{3+} ions is assumed to be without disturbance.

VUV Measurements

Figure 9.24 shows the VUV excitation and emission spectra which have been carried out at the SuperLumi station at 10 K. Therein, a single-component orthovanadate Eu:$GdVO_4$ thin film (a) is compared with a composite system Eu:$(Gd, Lu)VO_4$ thin film (b). The films are of comparable thickness with 125 nm for $GdVO_4$ and 100 nm for $(Gd, Lu)VO_4$. No bulk crystal was available for comparison purposes.

Basic differences are observed when comparing the excitation measurements. The band structure of Eu:$GdVO_4$ (a) reveals the charge transfer state (CTS) peaking at 265 nm (4.68 e V). No excitonic state (ES) is existent in the band structure, however at 204 nm

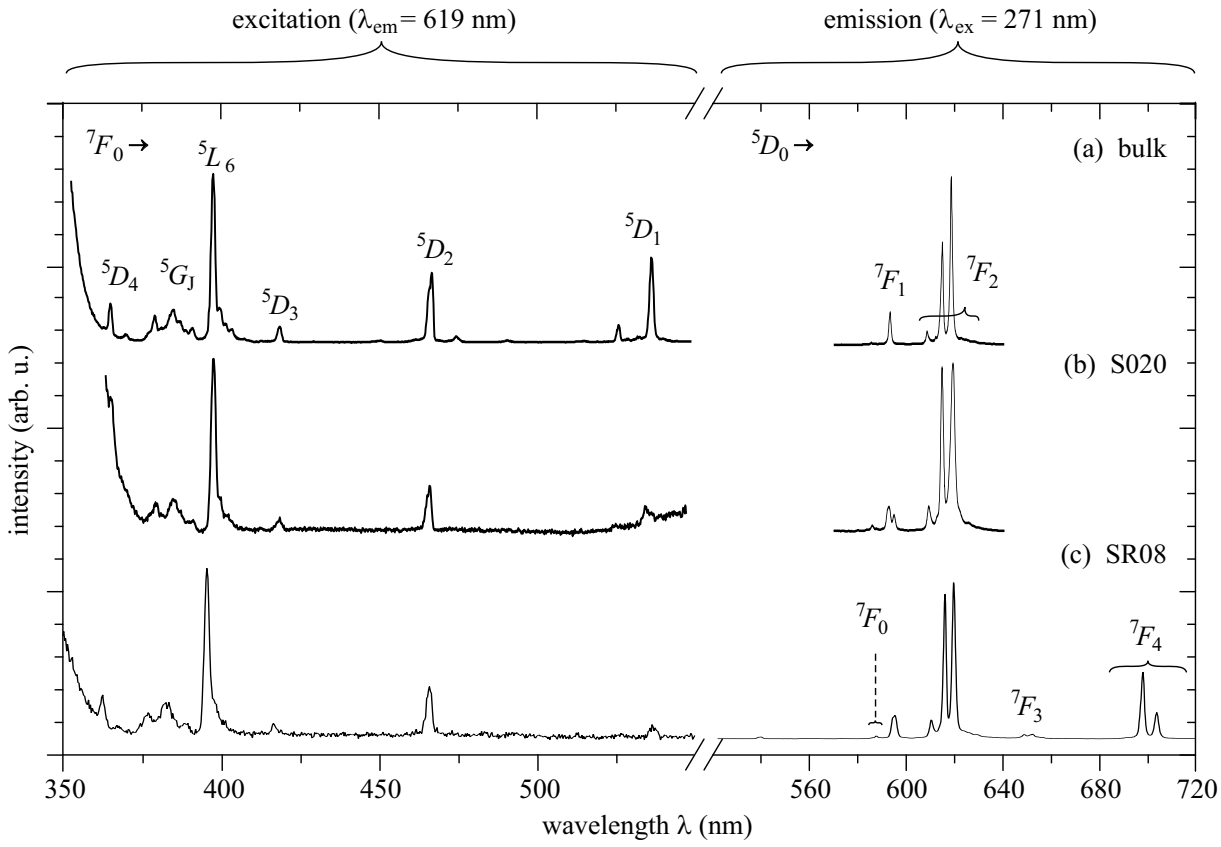

Figure 9.23: *Excitation (left) and emission spectra (right) of (a) an Eu(1%):$GdVO_4$ bulk crystal, (b) an Eu(2%):$GdVO_4$ thin 125 nm film, and an (c) Eu(2%):$(Gd, Lu)VO_4$ thin 100 nm film.*

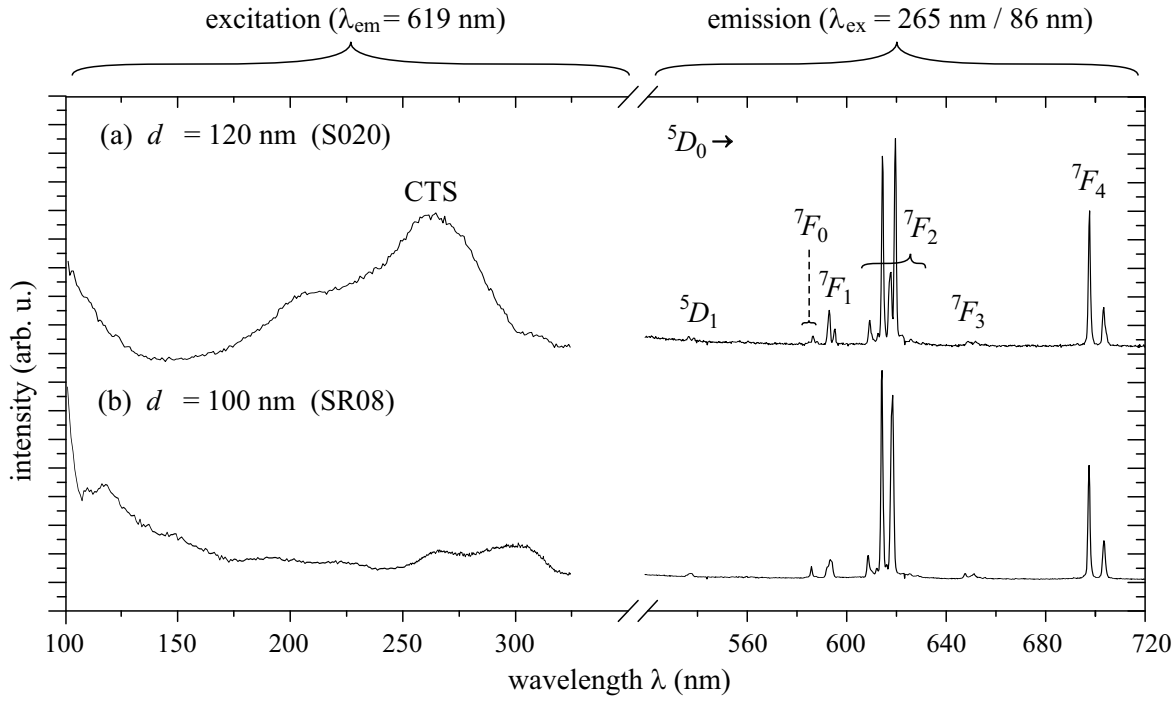

Figure 9.24: *VUV excitation and emission spectra of (a) an Eu(2%):$GdVO_4$ and (b) an Eu(2%):$(Gd, Lu)VO_4$ thin film.*

(6.08 e V) a local maximum is shown, which may be an interband transition. At 319 nm (3.89 e V) a little structural rise begins, which continues until reaching the CTS edge at 300 nm. As the band edge of YVO_4 is known to be at 337 nm (3.67 e V) having a bandgap of 3.5 e V, no strong deviation is expected for isostructural $GdVO_4$. Much of the structured band form is diminished in the spectrum (b) of the composite Eu:$(Gd, Lu)VO_4$. The highest intensity is recognized at around 300 nm (4.14 e V) which corresponds to the little structural rise in (a) at almost the same wavelength. Much of the CTS intensity has vanished with the remaining maximum peaking at 267 nm (4.65 e V). This spectral shift can be due to different bandgaps in the investigated films, which is expected to be smaller in the single-component film. At 119 nm (10.43 e V) the structure has its narrow maximum. A possible explanation for the less structured $(Gd, Lu)VO_4$ spectrum is that the crystal symmetry in the composite film is disturbed by the additional ion. The argumentation is similar to the one in chapters 8.1.4 and 9.1.4, although this time no ES is observed in the band structure. However, even without ES a distortion in the crystal structure affects the overall intensity and can be responsible for less distinct CTS. For a better understanding of the band structure (b) further VUV measurements are required.

Due to the varying band structure observed in the excitation measurements of (a) and (b), different excitation wavelength λ_{ex} have been used for the emission measurements of 265 nm and 86 nm for (a) and (b), respectively. It is apparent, that in both emission spectra (a) and (b) the linewidths and transition intensities are well-resolved in the films. There is no strong broadening observed. These indications give evidence to the assumption that the local crystal symmetry of the Eu^{3+} ions is preserved with no disturbance. The spectra are dominated by the characteristic ${}^5D_0 \rightarrow {}^7F_2$ transition. As rare-earth ions in orthovanadates occupy the lattice site D_{2d} this transition has its maximum at 615 nm and 620 nm. However, an additional peak arises in the $GdVO_4$ emission spectrum (a) at 618 nm. Most probably, this is due to a lattice defect in the $GdVO_4$ film which forms a different symmetry site at 10 K. No additional peak is seen in the corresponding room temperature measurements. Interestingly, the ${}^7F_1$ level in (b) is not as structured as for the $GdVO_4$ thin film. Also the peak intensity at 615 nm is higher than at 620 nm for the spectrum (b). Further VUV measurements are required in order to gain a better comprehension, especially in regard of the composite films.

In summary, the VUV emission measurements indicate a preserved local crystal structure in both grown films without disturbance. Similar to the VUV excitation of $(Sc, Lu)_2O_3$ shown in figure 8.10 and of $(Gd, Lu)_2O_3$ shown in figure 9.12, the existence of an additional ion in the $(Gd, Lu)VO_4$ lattice may be responsible for the structure and intensity loss in the excitation behavior of the spectrum (b).

Lifetime and Refractive Index Measurements

Additional ellipsometry and lifetime measurements have been performed to further investigate the local crystal structure. Figure 9.25 depicts the lifetime curves. Therein, the europium fluorescence lifetimes of single-component $GdVO_4$ thin films (a) are compared to the ones of composite $(Gd, Lu)VO_4$ thin films (b). The lifetime τ of the $^5D_0 \rightarrow {}^7F_2$ fluorescence was determined by an exponential fit of the decay curve. Polycrystalline samples of $GdVO_4$ and $(Gd, Lu)VO_4$, which were obtained by fusion (cp. section 8.1.4) and had the same composition as the films, served as reference in both cases.

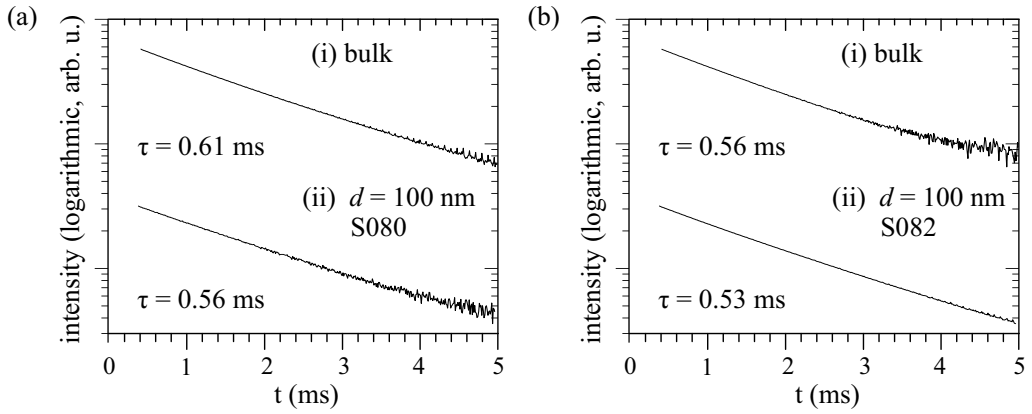

Figure 9.25: *Lifetime τ of the $^5D_0 \rightarrow {}^7F_2$ fluorescence in (a) Eu:$GdVO_4$ and (b) Eu:$(Gd, Lu)VO_4$ bulk and film material.*

The lifetimes of both grown films are similar to the corresponding bulk samples. For $GdVO_4$ (a) the lifetimes τ of bulk and film are 0.61 ms and 0.56 ms, respectively, whereas $(Gd, Lu)VO_4$ (b) bulk and film have the lifetimes 0.56 ms and 0.53 ms, respectively. In agreement with the results obtained by X-ray measurements this gives evidence to the fact that the 100 nm films are of highly crystalline character and have good optical properties. No Lorentz correction is observed at 100 nm thickness.

The corresponding refractive indices n_o have been estimated by ellipsometric measurements to be 2.059 and 2.322 at 632.8 nm for the $GdVO_4$ and the $(Gd, Lu)VO_4$ film, respectively. As the refractive index of YVO_4 is $n_o = 1.993$ at 632.8 nm (cp. appendix B) a refractive index difference of $\Delta n = 0.34$ is obtained in regard to the composite $(Gd\,Lu)VO_4$ film. In conclusion, this substrate–film system is very promising for waveguide applications.

9.3 Garnet Films on YAG

In this section the properties of different garnet films on $Y_3Al_5O_{12}$ (YAG) are studied. Due to the same reasons set forth in section 9.1, the lattice constant of Eu:YAG is slightly increased with regard to the pure YAG lattice. The properties of this homoepitaxial system are compared with the ones of the lattice matched solid solution Eu:$(Gd, Lu)_3Al_5O_{12}$.

9.3.1 Lattice Matching and Structural Characterization

The lattices of Eu:$RE_3Al_5O_{12}$ deposited on YAG substrates combine directly according to $a_s \approx a_f$ (cp. chapter 5.2). As previously for the sesquioxides (section 9.1) and vanadates (section 9.2), two lattice matched compositions have been tried in this work: $(Eu_{0.02}Gd_{0.534}Lu_{0.446})_3Al_5O_{12}$ [1] and $(Eu_{0.02}Gd_{0.48}Lu_{0.50})_3Al_5O_{12}$ [2]. The corresponding ionic radii approximation was described in section 9.1.1. Again, the obtained refractive index difference between substrate and film is expected to be higher for the composite system, referred to as (Gd, Lu)AG in short.

The growth behavior and the lattice matching have been investigated on ⟨111⟩ and ⟨100⟩ oriented YAG substrates. Different garnet films are compared in X-ray diffraction spectra, which are grouped according to the substrate orientation. Thus, figure 9.26 features the growth on ⟨111⟩ oriented YAG and figure 9.27 the growth on ⟨100⟩ oriented YAG. The preferred growth direction of YAG is the ⟨111⟩ orientation. As the pulsed laser deposition process does not take place in thermodynamic equilibrium, a possibly preferred growth direction may differ from regular crystal growth. Again, in some cases the f values are indicated with '*' (cp. explanation in section 9.2).

For the film composition of Eu(2%):$Y_3Al_5O_{12}$ the theoretically expected lattice constant is $a = 12.006\,\text{Å}$ which would result in a theoretical lattice mismatch of only 0.05% on YAG. In this calculation, the lattice constant of $Eu_3Al_5O_{12}$ is approximately $a_{EuAG} = 12.142\,\text{Å}$.

YAG Films

The deposition of garnet films requires temperatures of ≥ 800°C. Previous depositions at lower temperatures did not result in crystalline film growth (cp. appendix A). For the presented Eu:YAG films temperatures of 890°C and 860°C have been used with an oxygen

Deposition		**Reflection**		**Film Properties**				**Tag**
d_{film}(nm)	T_{sub}(°C)	peak	2θ(deg)	b_m(deg)	$L_\perp$(nm)	$a_\perp$(Å)	f(%)	
100	890	{444}	52.061	0.104	107.1	12.161	1.37	S087
100	860	{800}	60.945	0.100	118.9	12.152	1.25	S091

Table 9.8: Calculation of the crystallite size and the lattice constant of YAG films determined by X-ray diffraction. Measured peak positions 2θ and peak widths b_m are fitted by a Gaussian profile. For $L_\perp$ the instrumental resolution b_a is considered.

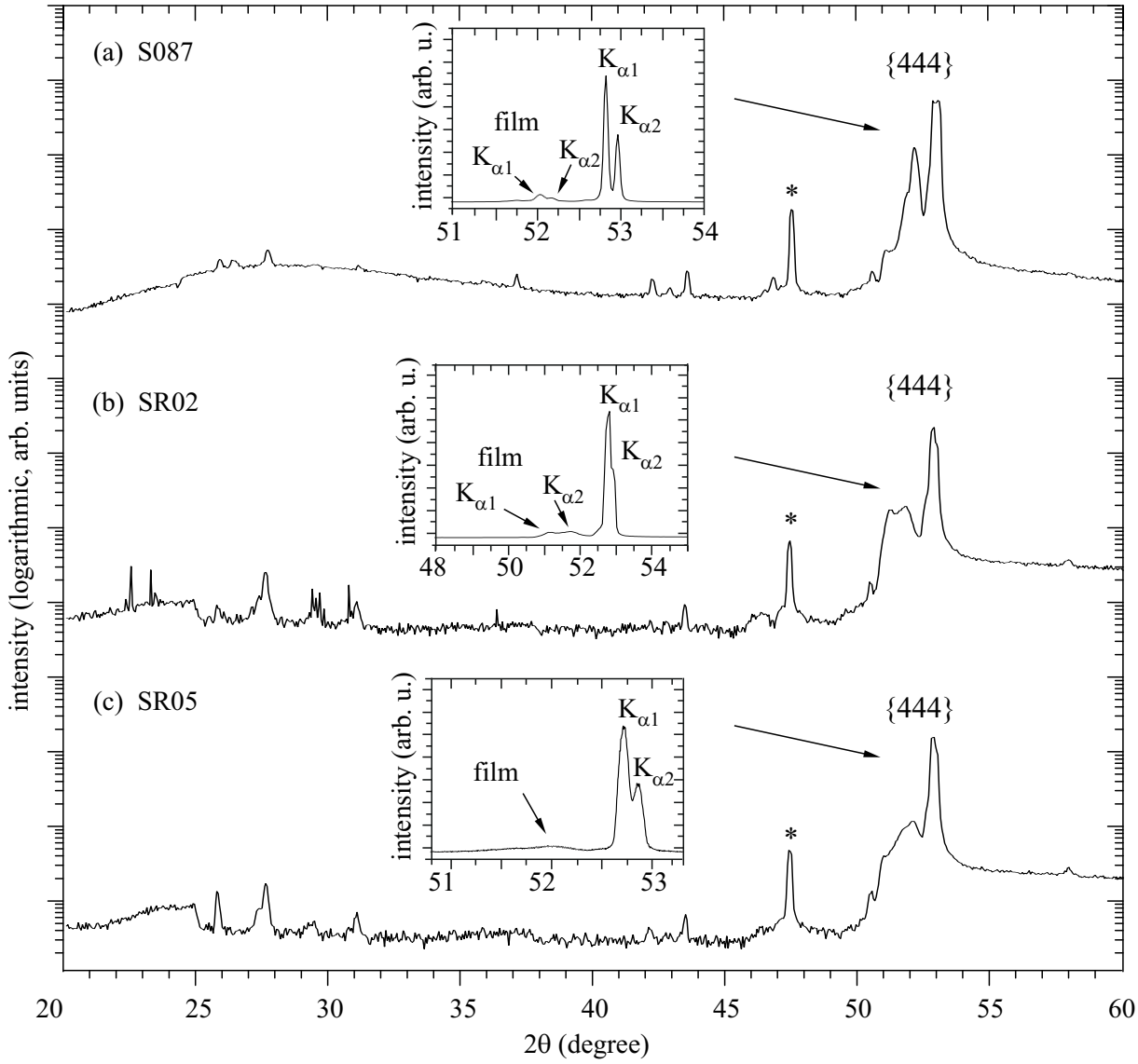

Figure 9.26: *X-ray diffraction patterns of garnet films with 100 nm thickness grown on ⟨111⟩ oriented $Y_3Al_5O_{12}$: (a) Eu(1.5%):$Y_3Al_5O_{12}$, (b) and (c) Eu(2%):$(Gd, Lu)_3Al_5O_{12}$ films. The insets show high resolution scans. Diffraction peaks indicated with '*' result from the residual Cu-K_β emission.*

pressure of 10^{-2} mbar and a repetition rate of 3 Hz. Table 9.8 summarizes the collected data. The lattice constants obtained by the diffraction spectra in figures 9.26 (a) and 9.27 (a) are 1.37% and 1.25% for the ⟨111⟩ and ⟨100⟩ grown film, respectively. None of the films reaches the predicted lattice mismatch value of 0.05% and both deposited films deviate from this value in almost equal degree. As the determined lattice constant shifts to greater values in both cases, this indicates lattice expansion due to crystal defects, which will be discussed after evaluation of the X-ray analysis for the composite garnet films. However, the (100) film has slightly better properties in regard to the lattice matching and also to the crystallite size. Despite the relatively high mismatch index f, the grain sizes indicate a high degree of crystallinity. The estimated values $L_\perp$ exceed the estimated

film thicknesses of 100 nm, but are well within the measuring accuracy. As no diffraction peaks of other orientations are seen, a single-crystalline growth of the Eu-doped garnet films is concluded.

Composite Garnet Films

Table 9.9 reviews the data for the composite garnet films grown on (111) and (100) YAG. Two compositions have been used for the deposition of composite garnet films as detailed in chapter 9.1.1. However, as no film of composition [1] has been grown in ⟨111⟩ orientation, a comparison is not possible in this orientation. A higher deposition temperature has been used for films of composition [2] as the laser heating system was upgraded. All films have been deposited by using $\nu = 1\,\mathrm{Hz}$ with a minor variation in the oxygen atmosphere (from $10^{-2}\,\mathrm{mbar}$ for film S095 to $8.8-8.9\times10^{-3}\,\mathrm{mbar}$). A strong substrate–film peak splitting for the films SR02, SR05, and SR01 is apparent in the overview θ–2θ-scans shown in figures 9.26 and 9.27. The lattice mismatch is larger in films of composition [2], and the best matching index $f = 1.07\%$ is achieved with the film S095 of composition [1]. Apart from the film composition, a dependency between the lattice mismatch and the temperature can be recognized, which will be discussed after evaluating the RHEED analysis.

Despite the usage of particularly mixed compositions in order to fit the substrate lattice, the resulting mismatch of $1.07 < f < 2.76\%$ is comparably high in garnets. Due to the fact that relatively high mismatch values were observed in the homoepitaxial Eu:YAG film as well, the reasons are most probably material related. Considering an estimated lattice expansion of 1.2% for Eu:YAG films (lattice mismatch $1.25-1.37\%$, whereas 0.05% was predicted), 'alternative' lattice mismatches for the films SR02, SR05, S095, and SR01 are 1.56%, 0.09%, −0.13% and 1.24%, respectively. In this case, best lattice matching would have been achieved with the [111] grown film SR05 of composition [2]. This confirms that apart from the unpredicted lattice expansion, composition [2] would match the YAG lattice very well.

Different from the sesquioxide and orthovanadate matrix, an additional crystal defect type occurs in garnet crystals of structure $C_3A_2D_3O_{12}$, which is referred to as *antisite*

	Deposition		**Reflection**		**Film Properties**				**Tag**
	d_{film}(nm)	T_{sub}(°C)	peak	2θ(deg)	b_m(deg)	$L_\perp$(nm)	$a_\perp$(Å)	f(%)	
[2]	100	1000	{444}	51.244	0.137	74.7	12.341	2.76*	SR02
[2]	100	986	{444}	51.986	0.267	37.2	12.177	1.29*	SR05
[1]	100	895	{400}	29.472	0.179	53.4	12.113	1.07*	S095
[2]	100	1000	{400}	29.303	0.127	75.7	12.315	2.44*	SR01

Table 9.9: Calculation of the crystallite size and the lattice constant of (Gd, Lu)AG films determined by X-ray diffraction. Measured peak positions 2θ and peak widths b_m are fitted by a Gaussian profile. For $L_\perp$ the instrumental resolution b_a is considered. The different film compositions are distinguished by [1] and [2].

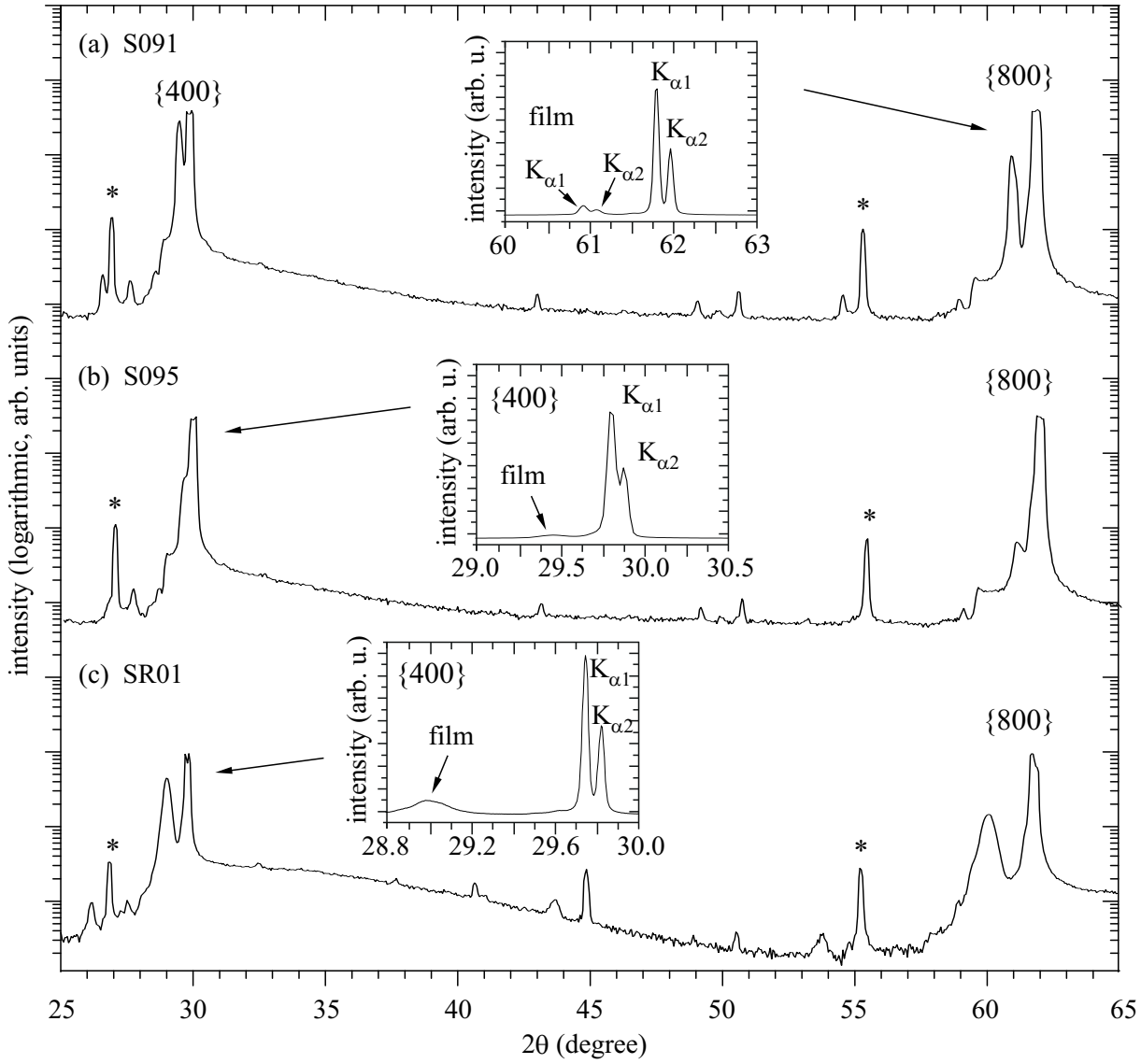

Figure 9.27: *X-ray diffraction patterns of garnet films with 100 nm thickness grown on ⟨100⟩ oriented $Y_3Al_5O_{12}$: (a) Eu(2%):$Y_3Al_5O_{12}$, (b) and (c) Eu(2%):$(Gd,Lu)_3Al_5O_{12}$ films of composition [1] and [2], respectively. The insets show high resolution scans. Diffraction peaks indicated with '*' result from the residual Cu-K_β emission.*

defect [Bab05]. This defect type refers to a site exchange between C and A cations. In case that an Y^{3+} (C-site) exchanges with an Al^{3+} (A-site), the antisite defect is denoted as 'Y^{3+}_{Al}'. By using an extended X-ray absorbtion fine structure (EXAFS) spectroscopy technique Dong et al. estimated that in several garnet crystals about two C cations exchange with two A cations per unit cell [Don91]. They further proposed that such a site exchange leads to the structural distortion from cubic $Ia3d$ to trigonal $R\bar{3}$. The site exchanges between C and A cations are accompanied by unavoidable displacements of cationic positions due to the difference in their cationic radii. In pure YAG single-crystals significant displacements of Y^{3+}_{Al} cations along the [111] direction occur due to the large

difference in cationic radii of eightfold coordinated Y^{3+} (1.02 Å) and sixfold coordinated Al^{3+} (0.54 Å) [She03]. This large difference in cationic radii is reduced by the formation of antisite defects, as sixfold coordinated Y^{3+} has a smaller cationic radius (0.92 Å). The Y_{Al}^{3+} antisite defect concentration in undoped YAG is estimated to be several tenth percent [Nik05]. A higher antisite defect concentration is observed in Eu-doped crystals [She03], as Eu^{3+} has an even larger cationic radius (1.06 Å) and thus Y_{Al}^{3+} antisite defects become energetically more favorable. Y_{Al}^{3+} antisite defects compensate the already smaller octahedral lattice site A, as the dodecahedral lattice site C in YAG is further enlarged by the Eu^{3+} ions. Interestingly, antisite defects are temperature- and energy-dependent [Kuk00, Nik05]. In YAG they occur due to high preparation temperatures of 2000°C and reach higher concentrations with increasing growth temperature (e. g. for LuAG).

Although the substrate temperature in the pulsed laser deposition process does not reach 2000°C by far, very high particle energies are used in combination with relatively high temperatures of nearly 1000°C. In agreement with the calculated formation energies of antisite defects [Kuk00], the observed lattice expansion in the homo- and quasi-homoepitaxy of garnet films is attributed to high antisite defect concentrations in the grown films. Most probably, these are responsible for the comparably high mismatch values despite the attempt of growing 'lattice matched' films. For the homoepitaxial Eu:YAG films S087 and S091 the substrate temperature was below 900°C (cp. table 9.8) and the larger Eu^{3+} ions contributed only 2% to the C-site. Probably, a slightly increased Y_{Al}^{3+} antisite defect concentration due to the Eu-doping resulted in the lattice expansion of around 1.2%. Despite this mismatch, the films are considered to be monocrystalline.

For quasi-homoepitaxial Eu:(Gd, Lu)AG films the antisite defect concentration is assumed to be higher due to the substitution of Y^{3+} with Gd^{3+} and Lu^{3+}. This is for different reasons: First, the C-site is strongly enlarged by the Gd^{3+} (1.06 Å) cations. Second, the already too small A-site must be compensated. Third, the smaller misfit between the Lu^{3+} and Al^{3+} cation radii benefits the Lu_{Al}^{3+} antisite defect formation. Fourth, the misfit between the Gd^{3+} and Lu^{3+} cation radii also benefits the Lu_{Al}^{3+} antisite defect formation. Probably, the high temperatures of 1000°C for the films SR02 and SR01 in combination with pulse energies of 0.8 J/cm² were responsible for the almost doubled mismatch values in these films. Considering the two compositions [1] and [2], it is possible that the varied Lu-amount from 45% to 50% contributed to the Lu_{Al}^{3+} antisite defect formation as well. Further investigation by microprobe analysis has to reveal the exact amount of Lu_{Al}^{3+} antisite defects. Similar to the optimization of melting compositions in regular crystal growth [İle04], this information will then be applied in a further lattice matched composition.

An additional effect has to be regarded for pulsed laser deposition of garnet materials, which is related to antisite defect formation. Figure 2.4 illustrated a unit cell of structure $C_3A_2D_3O_{12}$. In ⟨100⟩ direction the surface plane is flat with no bonds 'standing out'. However, in ⟨111⟩ direction the cations which occupy the A-site do stand out as illustrated in figure 9.28. Thus, the octahedral Al^{3+} ions occupying the A-site in ⟨111⟩ oriented growth are most

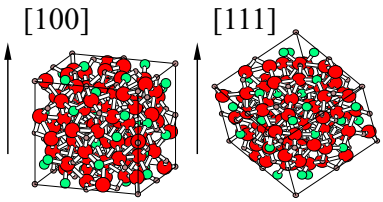

Figure 9.28: *Unit cell of YAG in different orientations*

likely to form Lu_{Al}^{3+} antisite defects, as high-energy particles which hit the substrate surface will most probably 'blast' the A-sites. This may explain the slightly increased lattice mismatch of [111] oriented garnet films compared to [100] grown films of similar substrate temperature and composition, e. g. S087 and S091, SR02 and SR01. Despite the relatively high lattice mismatch, comparable crystallite sizes $L_\perp \approx 75\,\mathrm{nm}$ were achieved for films SR02 and SR01, indicating a high degree of crystallinity.

The out-of-plane orientation in the film SR05 was investigated by a corresponding rocking curve measurement of the {444} diffraction peak. Although figure 9.29 shows excellent ordering along the ⟨111⟩ direction within a FWHM of 0.06°, the curve shows a broadening and thus deviates from the Gaussian form. The line shape can be fitted by assuming two contributions, one with a sharp peak of high crystallinity and another one with a broader structure indicating defects. A very small degree of asymmetry has to be noticed in the resultant line shape, as the maximum peak position of the assumed interface is shifted marginally to smaller angles.

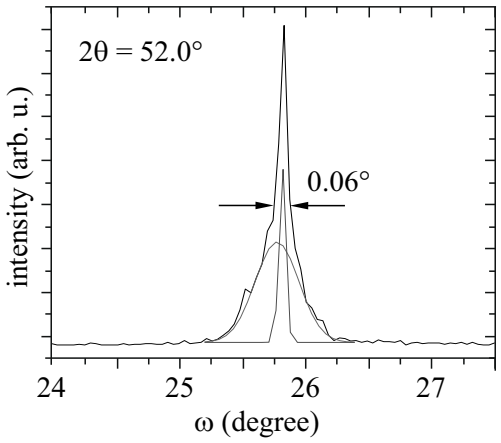

Figure 9.29: *Rocking curve of the SR05 {444} reflection peak.*

A similar out-of-plane characteristic can be observed in figure 9.30 for the {400} reflection of film SR01. Again a perfect ordering is apparent, this time along the default ⟨100⟩ direction within 0.06° at FWHM. However, the rocking curve with its maximum at 14.5° features an asymmetric broadening. The line shape complies with the Gaussian form for angles $\omega > 14.5°$, whereas for angles $\omega < 14.5°$ it deviates from the Gaussian form due to a left-sided shoulder. Again the line shape can be fitted by assuming two contributions.

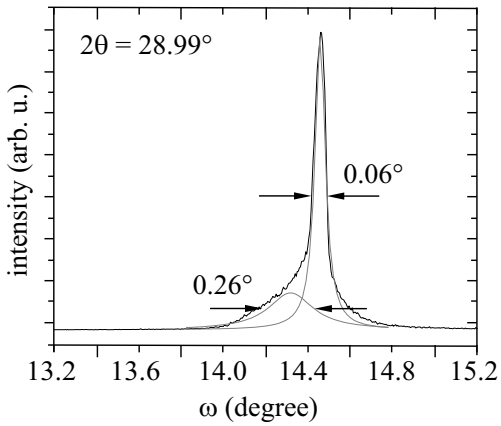

Figure 9.30: *Rocking curve of the SR01 {400} reflection peak.*

Possible explanations of the rocking curve broadening and asymmetry will be considered after evaluating the RHEED analysis for the garnet films in ⟨111⟩ and ⟨100⟩ direction.

9.3.2 Surface Structure and Topography

The RHEED analysis of the grown composite films gives further insights into the growth process. According to previous research, which was confirmed by AFM measurements for the pre-deposition substrate treatment, a unit cell of [100] YAG with the lattice constant $a = 12\,\text{Å}$ subdivides into four monolayers with a step height of 3 Å each [Gün07]. In ⟨111⟩ orientation the step height is calculated from $x = a/4\sqrt{3}$, which results in 1.73 Å.

Figure 9.31 (a) shows the intensity oscillations of the specularly reflected electron beam for the [111] garnet film SR02 deposited at 1 Hz. The required number of pulses for the growth of one monolayer has been estimated to be 44 pulses. The RHEED pattern does not change in symmetry or spacing during the entire growth process. Only a transition of the diffraction points to stripes is observed, as seen in the inset of figure 9.31 (a). A fast increase in surface roughness is indicated, as the intensity shows a steep fall within the first 10 pulses. After this initial intensity drop, the intensity oscillations remain at a relatively constant level and indicate two-dimensional layer-by-layer growth. This growth mode is sustained until the end of deposition at 100 nm film thickness, in accordance which the diffraction image and the intensity oscillations. A certain fluctuation in the intensity oscillations is apparent, when comparing these oscillations with the 'smooth' ones for ⟨100⟩ oriented growth in figure 9.32 (a). These peculiarities will be explained after analysis of the [100] growth of the same material. Figure 9.31 (b) shows the corresponding AFM image for the deposited film SR02. A structured atomically flat surface topography with indicated [111] crystallite orientation (RMS roughness of 3.4 Å) can be seen. Thus, the film normal direction is assumed to be perpendicular to the ⟨111⟩ direction.

Figure 9.32 (a) depicts the intensity oscillations of the specularly reflected electron beam for the growth of [100] (Gd, Lu)AG film SR01. An amount of 77 pulses is required for the monolayer growth in ⟨100⟩ direction with 3 Å step height. Similar to the [111] film, no change in symmetry or spacing of the RHEED pattern takes place during the entire growth process. As apparent in the left and right inset of figure 9.32 (a) only a transition of the diffraction points to stripes is observed. The intensity decrease during initial deposition of the first 10 pulses is comparably small. Two-dimensional layer-by-layer growth is indicated by the RHEED intensity oscillations. Although the intensity amplitude of the

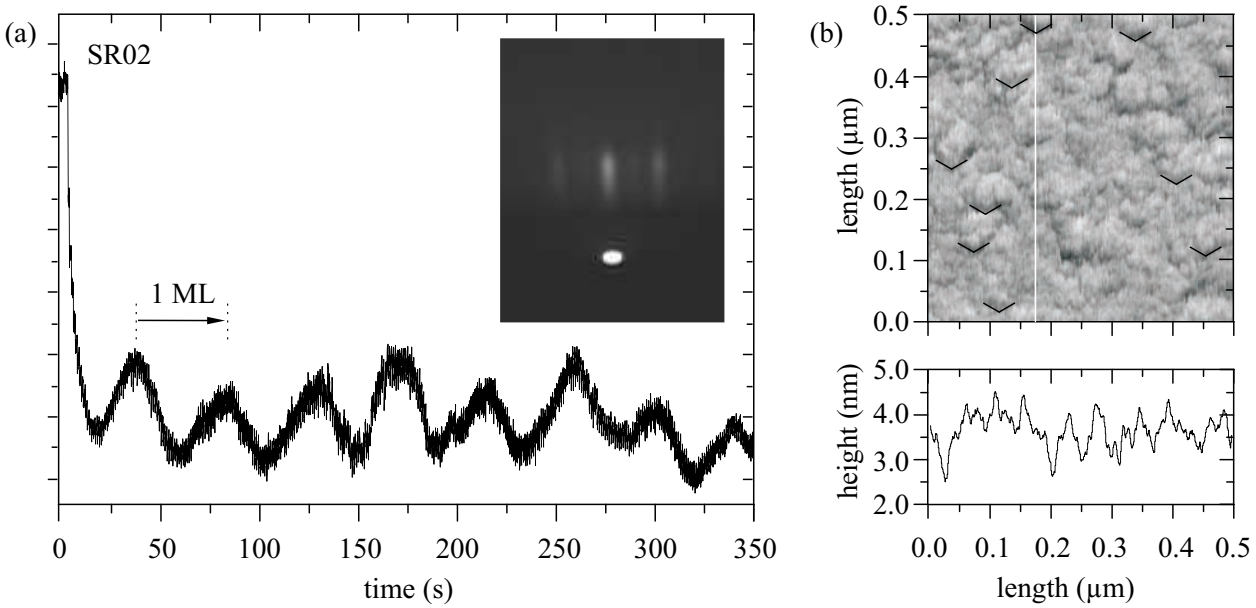

Figure 9.31: *(a) RHEED oscillations during continuous deposition of around 14 Å (8 ML) Eu:(Gd.Lu)AG in ⟨111⟩ direction. The inset shows the RHEED image after deposition of 100 nm. (b) Corresponding surface topography measured by AFM.*

oscillations slowly decreases, continuous oscillations at an almost constant intensity level remain. Pulsed laser *interval* deposition (PLiD) has been performed for the film SR01 after continuous deposition of thirteen monolayers. PLiD was applied in order to ensure layer-by-layer nucleation and prevent nucleation on subsequent layers with proceeding growth. Confirmed by the previous continuous deposition, the exact amount of pulses for complete growth of one monolayer is deposited at the high repetition rate of 50 Hz. After deposition of these 77 pulses a total relaxation of the RHEED intensity within 50 s is observed and shown in figure 9.33. The AFM analysis, shown in figure 9.32 (b), confirms the RHEED analysis as it reveals an atomically flat surface topography. A surface structure with a height of roughly 3 Å is recognized in the AFM image and correlates to one monolayer. The film has a very smooth surface as well (RMS roughness of 1.7 Å).

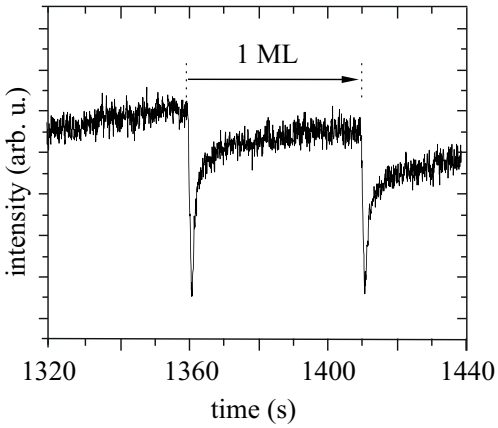

Figure 9.33: *RHEED oscillations for pulsed laser interval deposition of Eu:(Gd.Lu)AG in ⟨100⟩ direction.*

When comparing the [111] and [100] film growth of composite (Gd, Lu)AG it is recognized that after deposition, the diffraction patterns in the inset of figures 9.31 (a) and 9.32 (a) corresponds to an almost ideal surface. In both cases two-dimensional layer-by-layer growth is indicated by the diffraction stripes neighboring the elliptic (0,0)-reflex. In agreement with the X-ray diffraction analysis both films SR02 and SR01 indicate

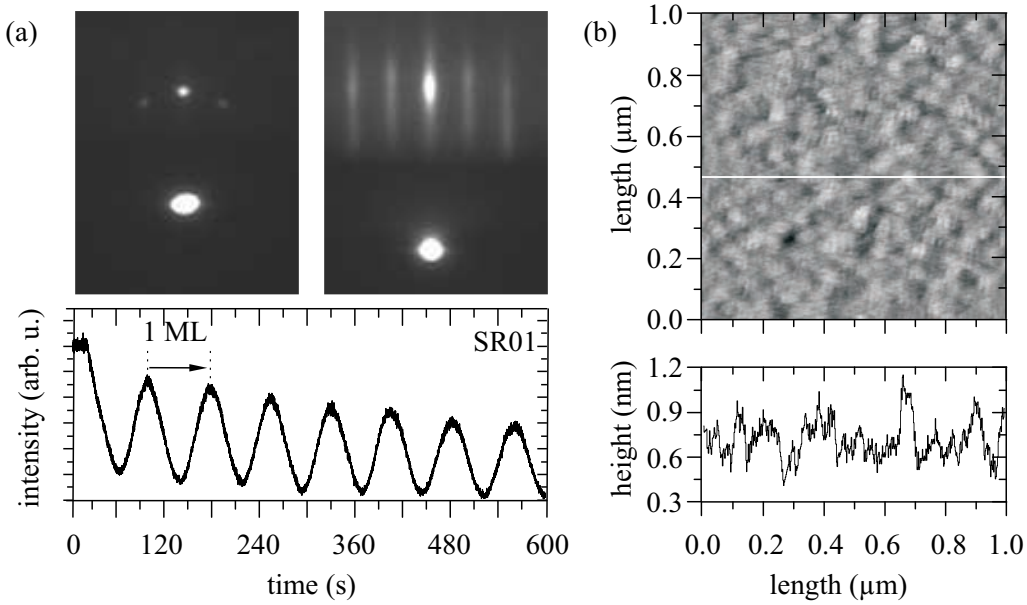

Figure 9.32: *(a) RHEED oscillations during continuous deposition of around 24 Å (8 ML) Eu:(Gd.Lu)AG in ⟨100⟩ direction. The insets show the RHEED image before (left) and after deposition of 100 nm (right). (b) Corresponding surface topography measured by AFM.*

monocrystalline character. No additional reflections from atomic planes other than in the default substrate orientation are observed in the θ–2θ-scan. The ω-scans reveal excellent alignment of the crystallites along the default substrate direction. Only the lattice mismatch due to a high antisite defect density reduced the overall film quality.

The influence of antisite defects on the film growth is indicated in various details. The initial intensity drop within the first 10 pulses for the growth of the [111] film SR02 (cp. figure 9.31a) can be attributed to the above mentioned A-site 'blasting' due to the $\langle 111 \rangle$ orientation of the substrate. Fluctuations in the intensity oscillations indicate high diffusion energies of the surface atoms 'searching' for energetically favorable positions. This may as well include site exchanging. The broadening of the rocking curves is most probably caused by these initial dislocations in the film lattice. Composition [2] does not deliver the necessary lattice constant because of the high Lu_{Al}^{3+} antisite defect concentration which further develops during the film growth. This is surely compensated by compressive stress, dislocations, and grain boundary formation (reduced crystallite size compared to the overall film thickness). Asymmetric rocking curves are often due to lattice deformation and compressive strain [Hag01]. Thus, the degree of asymmetry may be attributed to the overall lattice mismatch mainly caused by antisite defects. This is in good agreement with the rocking curves of SR05 (1.29% mismatch) and SR01 (2.44% mismatch).

In addition, it should be emphasized that the RHEED intensity oscillations do indicate epitaxial layer-by-layer growth. This would not be possible with an initial lattice mismatch between substrate and film material. For instance, it was not possible to achieve continuous RHEED oscillations for the deposition of YAG–LuAG or Y_2O_3–Lu_2O_3. In these substrate–film systems, the initial lattice mismatch prevents an epitaxial growth. It is thus assumed, that the observed lattice mismatch of up to 2.76% evolves continuously during with the film growth process.

9.3.3 Spectroscopic Analysis

In order to obtain information on the local crystal structure, the optical properties of the grown composite films were investigated by luminescence measurements (excitation and emission), VUV measurements, and lifetime measurements. In addition, the refractive indices of the films were determined by ellipsometry. No Eu-impurities were detected in the undeposited substrates. Emphasis is put on the spectroscopic analysis of composite garnet films and a comparison to the single-component YAG crystal. Although a complete spectroscopic analysis has been done for [111] and [100] grown thin films, no substantial differences exist in the optical properties. Since the optical properties of composite films grown on [111] and [100] garnet films are similar and independent of the growth direction, the spectroscopic analysis did not separately address different growth orientations.

Fluorescence and Excitation Measurements

Figure 9.34 compares the excitation and emission spectra of Eu-doped YAG bulk crystal (a) with a 100 nm lattice matched composite film (Gd, Lu)AG (b). Regarding the emission

spectra (right) the linewidths and transition intensities of the composite thin film (b) are similar to the bulk (a). Both emission spectra are dominated by the $^5D_0 \rightarrow {}^7F_1$ transition at 590 nm. A small broadening is observed for this transition, as the linewidth is 1.5 nm and 2.5 nm for the YAG bulk (a) and the (Gd, Lu)AG film, respectively. The broadening is understood because of the different ionic radii of Gd^{3+} and Lu^{3+}, which lead to crystal fields of different strength (cp. chapter 8.1.4). At 696 nm a transition arises which can not be ascribed to the known Eu-transitions. It can be identified as the $^2E \rightarrow {}^4A_2$ transition of Cr^{3+} on the Al^{3+} site. Cr-impurities in Al-materials are always existent in certain degrees. This can be explained by chromium impurities in the YAG substrate. In the excitation spectrum (b), the broad band structure peaking at around 458 nm screens the relatively weak $^5D_2$ level at 465 nm, which is resolved in spectrum (a). This broad band reveals another defect type in the composite garnet film. Most probably, the broad band can be attributed to color centers. Color centers in YAG are well-known and occur at similar wavelengths as the observed broad band. Except for this broad structure, the excitation spectrum of the (Gd, Lu)AG film (a) looks similar to the bulk spectrum of YAG (b).

In summary, with the above mentioned exceptions of the slightly broadened $^7F_1$ level and the chromium impurities, the composite thin film shows bulk-like luminescence properties. No distortions of the local symmetry of the Eu^{3+} ions are indicated.

VUV Measurements

Additional VUV excitation and emission measurements have been performed for the (Gd, Lu)AG thin films. In figure 9.35 the luminescence properties of [111] and [100] films

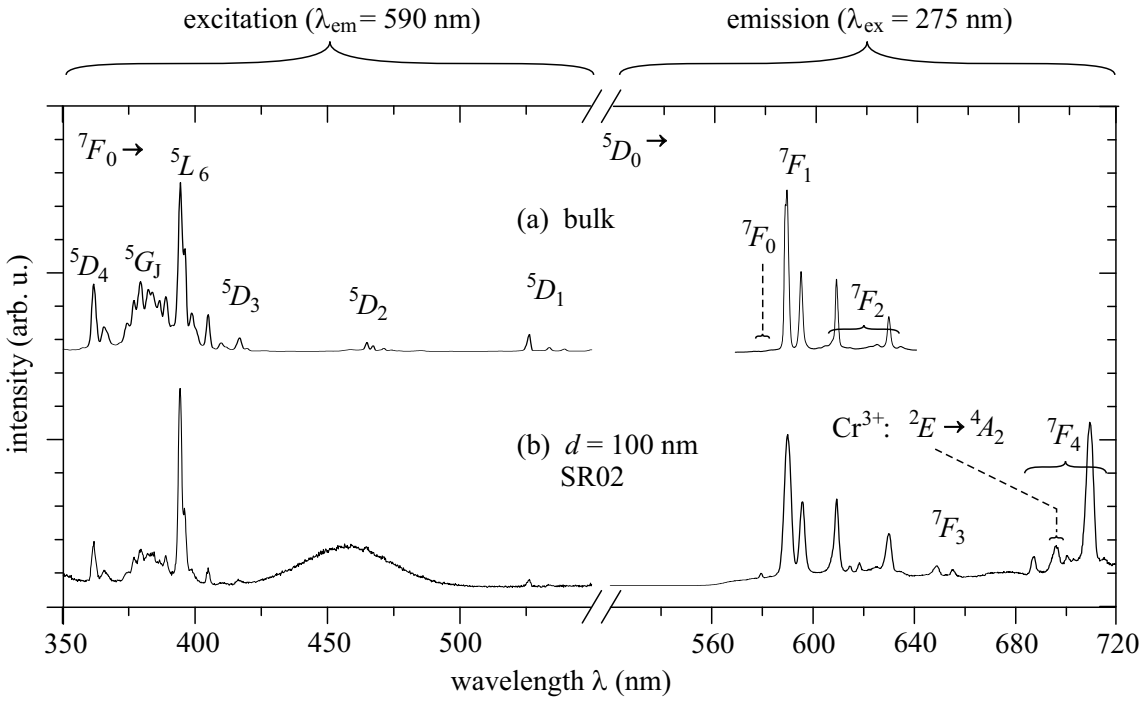

Figure 9.34: *Excitation (left) and emission spectra (right) of (a) an Eu(2%):YAG bulk and (b) an Eu(2%):(Gd,Lu)AG film of 100 nm thickness.*

are compared at 10 K. Apart from the already known and well-resolved emission spectra (right), which correspond to the luminescence room temperature measurements shown in figure 9.34, the band structure is considered. The VUV measurements of Eu:YAG single-crystals are known from literature [Pie00, Zor04, Bab05].

Both excitation spectra show a weakly pronounced charge transfer state (CTS) at around 225 nm (5.51 e V) and a strong interband transition at around 175 nm (7.09 e V). Besides these similarities, the CTS of the [111] film is less pronounced and broader in comparison to the [100] film. Also, the interband has different positions of 168 nm (738 e V) in the [111] film and 175 nm (e V) in the [100] film.

Garnet crystals such as YAG or LuAG already comes with a trapped excitonic state, due to the regular occurrence of antisite defects [Zor04]. The band edge slightly differs in YAG and LuAG from 188 nm (6.6 e V) to 180 nm (6.89 e V) [Zor05]. In these crystals the exciton is already trapped near the Lu^{3+}_{Al} or Y^{3+}_{Al} antisite defects [Zor06]. In Eu:YAG the antisite defects lead to slightly different interband positions [Pie00]. Thus, the different position of the interband in [111] and [100] composite garnet is probably related to varying Lu^{3+}_{Al} antisite defect concentrations. With increasing defect density a shift to shorter wavelengths should be observed. Under this assumption, the antisite defect concentration is higher in the [111] grown film SR02. This would be in good agreement with the previous X-ray and RHEED analysis. The [100] film SR01 has the lower amount of defects, which resulting in a comparably lower lattice mismatch. Another indication can be found in the RHEED intensity oscillations, with no initial intensity drop and 'smooth' oscillations (cp. figure 9.32).

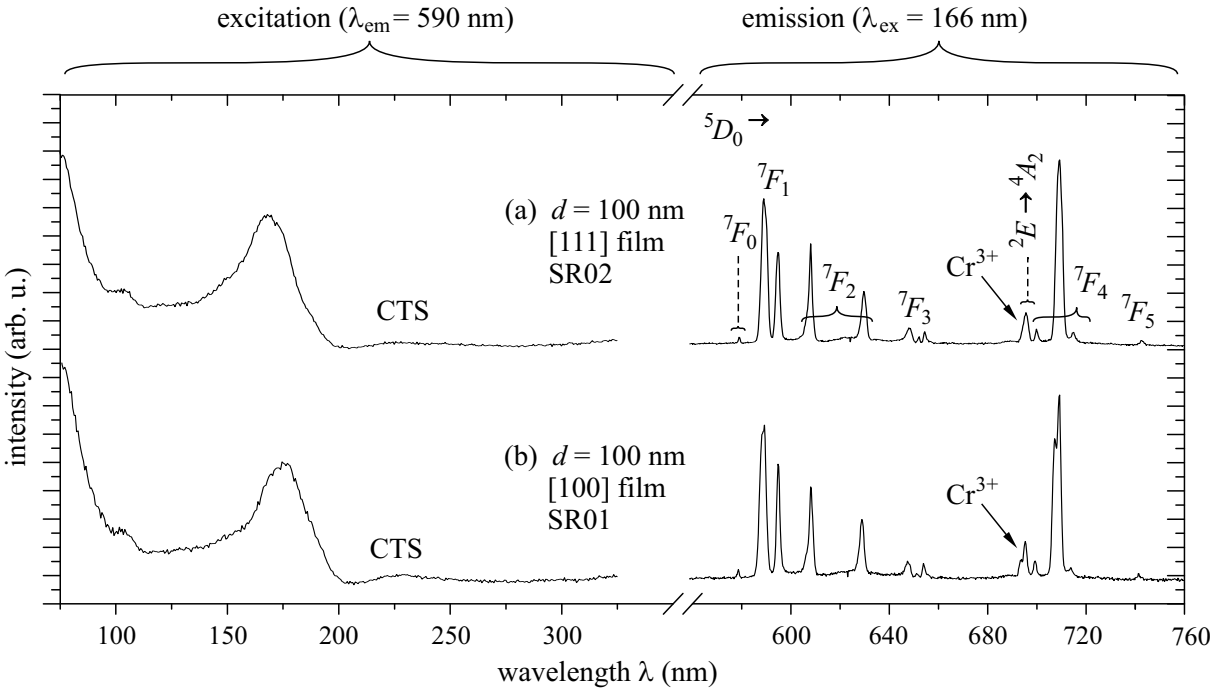

Figure 9.35: *VUV excitation and emission spectra of Eu(2%):(Gd, Lu)AG thin films (a) SR02 and (b) SR01 with different growth directions.*

However, it has to be noticed that of all investigated (Gd, Lu)-admixed systems, the band structure of the mixed garnet films suffer least from the additional ion in the lattice. No change in crystal symmetry is indicated by the excitation measurements. This has already been explained by the unavoidable antisite defects in the garnet matrix.

Lifetime and Refractive Index Measurements

Additional ellipsometry and lifetime measurements have been performed to further investigate the local crystal structure. Figure 9.36 depicts the lifetime curves. Therein, the europium fluorescence lifetimes of single-component YAG thin films (a) are compared to the ones of composite (Gd, Lu)AG thin films (b). Both films were grown in ⟨100⟩ direction. The lifetime τ of the $^5D_0 \rightarrow {}^7F_1$ fluorescence has been determined by an exponential fit of the decay curve. Polycrystalline samples of YAG and (Gd, Lu)AG which were obtained by fusion (cp. section 8.1.4, page 97) and had the same composition as the films, served as reference in both cases.

For YAG (a) the lifetimes τ of bulk and film are 1.56 ms and 0.95 ms, respectively, whereas (Gd, Lu)AG (b) bulk and film have the values 1.58 ms and 1.21 ms, respectively. In both cases the lifetime of the 100 nm thin films is shorter than the bulk lifetime. Apart from the possibility of quenching due to non-perfect film growth, the shorter lifetime in the films may indicate better optical properties compared to the polycrystalline bulk samples. This would be in good agreement with the X-ray measurements as the estimated crystallite size for the film S091 is almost twice as high as for the film S095. Thus, in comparison with the composite garnet film S095, the Eu:YAG thin film S091 has the shorter lifetime.

An estimation of the film refractive indices was done by ellipsometric analysis at 632.8 nm and compared to $n_{\mathrm{YAG}} = 1.829$. The refractive indices n were determined to be 1.838 for the Eu:YAG film S091 and 1.852 for the Eu:(Gd, Lu)AG film S095. A refractive index difference of $\Delta n = 0.023$ is realized with the composite film grown on YAG. Apart from probably being sufficient for waveguiding applications, this refractive index difference is relatively small.

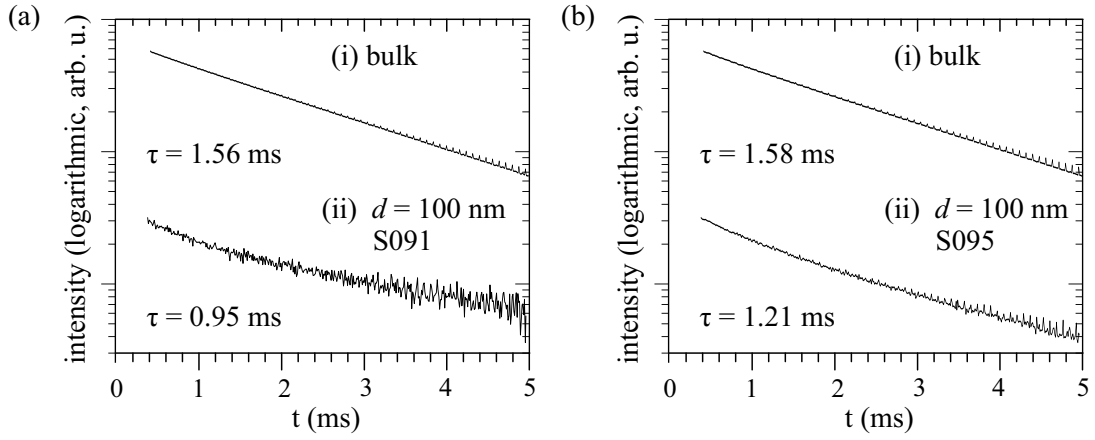

Figure 9.36: *Lifetime τ of the $^5D_0 \rightarrow {}^7F_1$ fluorescence in (a) Eu:YAG and (b) Eu:(Gd, Lu)AG bulk and film material.*

9.4 Summary and Discussion

Lattice matching of homo- and quasi-homoepitaxial films grown on Y_2O_3, YVO_4, and $Y_3Al_5O_{12}$ substrate materials has been investigated by using the pulsed laser deposition technique. The film growth behavior in the different crystal orientations $\langle 111 \rangle$ and $\langle 100 \rangle$ has been considered for sesquioxides and garnets. Except for the composite garnet films, the ionic radii approximation delivered good lattice matching of $> 99.5\%$.

Sesquioxide Films on Yttria

High substrate temperatures of $900 - 1000°C$ are required in order to realize lattice matched sesquioxide films of high crystallinity. Considering the estimated crystallite sizes in relation to the deposition temperature, Lu_2O_3 films require even higher temperatures than mixed $(Gd, Lu)_2O_3$ films. By using the solid solution $(Gd, Lu)_2O_3$ of composition [2], lattice matching of 99.54% has been achieved.

In general, the optical properties of the mixed sesquioxide films have bulk-like character. Only a marginal broadening of transition linewidths is observed for $(Gd, Lu)_2O_3$ films compared to single-component Y_2O_3 bulk crystals. However, a certain disturbance of the crystal structure was recognized by VUV excitation measurements. This is due to the additional ion, which also occupies the C_2 and C_{3i} sites in the sesquioxide matrix and results in less structured ES and CTS in the VUV excitation spectra.

Slightly tilted, highly crystalline film growth is indicated by X-ray rocking curve analysis. Probably, the tilting occurs in order to compensate stress while preserving the lateral cross-linking of the film lattice. The stress may arise because of the residual lattice mismatch. Further investigation of the in-plane lattice properties (collateral cross-linking, lattice constant $a_{\parallel}$, and crystallite size $L_{\parallel}$) by surface X-ray diffraction (SXRD) are required. The exact distribution of the Gd-, Lu-, and Eu-atoms could be investigated by high-resolution transmission electron microscopy (HRTEM). The exact determination of film stress by these techniques is crucial in order to discern whether the remaining lattice mismatch is due to lattice expansion. Otherwise, the (Gd, Lu)-mixing has to be further improved.

Another influential factor is the miscut angle of the sesquioxide substrates, as it may be responsible for varying lattice matching success at identical conditions [Joy88, Rij04, Gün07]. For instance, the miscut angles β for the Y_2O_3 [100] substrates of SR03, SR04, and SR10 have been $\beta > 1.5°$ each. These are comparably high miscut values, as epitaxial grade polished commercial α-Al_2O_3 and YAG substrates had much smaller miscut angles. In comparison, the miscut of the α-Al_2O_3 substrate shown in figure 6.5 (b) is determined to be $\beta = 0.005°$. Step-bunching and uneven surfaces (tension) have been observed for these substrates, potentially affecting the growth process.

Although slightly better lattice matching has been obtained by [100] grown films, no definite preference in growth direction could be investigated. A reason can be found in the varying substrate quality, which levels out a better growth behavior. With better oriented substrates, this analysis can be done by investigating the RHEED intensity oscillation de-

velopment for increasing deposition rates [Gün07].

Orthovanadate Films on YVO_4

The substrate temperature for orthovanadates has to be kept below 900°C. Probably, the proper temperature window for this material class lies between $730°C < T < 800°C$. For films deposited within these temperatures a high degree of crystallinity of around 76% has been achieved. For higher temperatures, three-dimensional island growth is observed, forming grains of 20 – 60 nm. The AFM analysis gave evidence to this fact, as island-like clusters are observed in figure 9.21 (b). Deposition at slightly reduced pulse energies may be beneficial as well, in agreement with the lower Mohs hardness of these materials.

A correlation between the strong RHEED oscillation damping with subsequent transition to a three-dimensional growth mode and comparably low substrate quality is assumed. After thermal substrate treatment, the miscut was determined to be 0.41°. Indications of lattice defects as well as step-bunching and surface tension were observed by AFM measurements. The initial layer-by-layer growth according to the RHEED analysis promises even better results for substrates of higher quality. Despite these complications, lattice matching of 99.79% could be realized by solid solutions $(Gd, Lu)VO_4$ of composition [2].

Besides the bulk-like luminescence properties of these mixed orthovanadate films, a disturbed crystal structure was recognized by VUV excitation measurements, which was more significant than in the solid solution sesquioxide films. Again, a possible explanation can be given by the additional ion in the orthovanadate film matrix, which also occupies the D_{2d} sites and is responsible for less pronounced band structures in the VUV excitation spectra.

Garnet Films on YAG

Of all investigated materials, the garnet crystal has the most sophisticated structure $C_3A_2D_3O_{12}$ with 160 atoms per unit cell and three different lattice sites. Garnet films showed large lattice mismatch even for homoepitaxial growth. Although the homoepitaxy of Eu(2%):YAG film should theoretically result in a lattice mismatch of marginal 0.05%, the estimated values of 1.25 – 1.37% were much higher. Accordingly, for the deposition of mixed garnet films $(Gd, Lu)_3Al_5O_{12}$, the best lattice matching of 98.93% has been achieved by composition [1], which was contrary to what was theoretically expected. These results indicate a strong, material-dependent lattice expansion in garnets. Most probably, high antisite defect concentrations of Y_{Al}^{3+} (homoepitaxy) and Lu_{Al}^{3+} (quasi-homoepitaxy) are responsible for the high mismatch.

The band structure (VUV excitation at 10 K) of the mixed garnet films did not show any difference to the well-known YAG crystal. Contrary to the solid solutions of sesquioxides and orthovanadates, the exciton migration in pure YAG single-crystals is already trapped by Y_{Al}^{3+} antisite defects. Therefore no change occurs for the additional ions. The slightly different positions of the interband transitions in dependence of the growth orientation give evidence to the assumption that the antisite defect concentration is marginally higher for [111] films. At room temperature, bulk-like luminescence properties were observed for

the mixed garnet films. Further research is necessary to resolve the difficulties of lattice matching in garnets. By microprobe analysis the exact lattice site distributions need to be investigated, which is done similarly for bulk single-crystals [İle04]. This allows a garnet-specific (Eu, Gd, Lu) composition, in which the antisite defects are already considered. By adjusting the parameters of pulse energy and substrate temperature the formation energies of antisite defects should not be reached during deposition. This presupposes a compromise between substrate temperatures required for highly crystalline films and substrate temperatures beneficial for antisite defect formation.

9.4.1 Lattice Defects and Lattice Expansion

Lattice expansion was observed in many of the deposited films. This has been attributed to possible lattice defects. As various defect types are known in literature, it is difficult to define the exact defect type and concentration in the grown films. Crystal defect categories are *point defects* (vacancies, antisite defects), *line defects* (different types of dislocations), *planar defects* (grain boundaries, antiphase boundaries), and *bulk defects* (voids, impurities) [Kle89]. Thereof, point defects are the most likely ones to occur during pulsed laser deposition.

These are defects which are not extended spatially in any dimension. Although no defined size limitation is given for point defects, the term is typically used for defects involving extra or missing atoms. In contrast to larger defects in an ordered structure (dislocations), the defective positions have no ordered structure. For historical reasons, various point defects are called 'centers', e. g. a vacancy in ionic solids is termed 'F-center' (color center). Figure 9.37 illustrates some typical point defect types. Bal et al. investigated the influence of various point defects on the crystal lattice in KCl [Bal67]. Vacancies and interstitial ions resulted in lattice expansion. It was observed that F-centers (vacancies, also called Schottky defects) in additively colored KCl caused a lattice expansion of $\Delta v/v = 0.58$ per F-center. F-centers in X-irradiated KCl with the corresponding atoms displaced to interstitial lattice sites (Frenkel pairs) caused a lattice expansion of $\Delta v/v = 1.15$ per F-center. The increasing lattice constant is calculated from $\Delta a/a = -\cot\theta \cdot \Delta\theta$. The investigated increase for KCl was $\Delta a/a = 3-5\times10^{-5}$.

Except for the garnet films with additional antisite defects, the lattice constant deviation $\Delta a/a$ for the lattice matched films was usually between $0.002-0.01$. Therefore, the defect concentration of vacancies and interstitial ions in the grown lattice matched films would be two orders of magnitude higher. Most likely, other defect types also contribute to the lattice constant increase. Further research on defect types and concentrations in the deposited films is necessary, including the growth of reference bulk single-crystals of the solid solutions for comparison purposes.

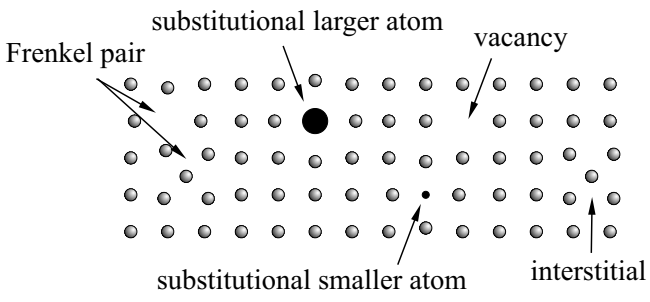

Figure 9.37: *Different point defects in a monatomic solid.*

10 Conclusions

10.1 Summary of Results

The subject of this thesis was the preparation and characterization of lattice matched crystalline rare-earth-doped oxide films for application as active or passive waveguides and optical coatings. A summary of the presented work is given in this chapter.

Lattice Matched Substrate–Film Systems

Sesquioxide, orthovanadate and aluminum garnet films were prepared because each material class offers a number of advantageous mechanical and thermal properties (high melting point, high Mohs hardness, low phonon energy, high thermal conductivity), which makes them appropriate and recommendable for integrated optical devices. Sesquioxides, orthovanadates and aluminum garnets are well-known hosts for rare-earth-doped luminescence materials (e. g. Eu:Y_2O_3 as red phosphor) and solid-state lasers (e. g. Yb:Lu_2O_3, Yb:YVO_4, Nd:YAG). An exception was the preparation of Al_2O_3 films doped with chromium instead. Cr:Al_2O_3 is known to be the first solid-state laser material [Mai60].

Proper substrates for lattice matching were found in α-Al_2O_3, sesquioxide materials (Y_2O_3 and $ScLuO_3$), YVO_4, YAG, and $LiYF_4$. Different possibilities of lattice matching were investigated by heteroepitaxy of Al_2O_3–$ScLuO_3$ and $LiYF_4$–Lu_2O_3 and by (quasi-) homoepitaxy of Y_2O_3–RE_2O_3, YVO_4–$REVO_4$ and YAG–REAG substrate–film systems. The lattice matching in the quasi-homoepitaxial systems was realized by mixing the (Eu, Gd, Lu)-amount to match the yttrium-based substrate material. Besides the lattice matching purpose this also delivered a higher refractive index difference to the substrate. In the heteroepitaxial systems the achievable refractive index difference ($0.15 < \Delta n < 0.5$ at 1µm) is still higher compared to (quasi-)homoepitaxial systems ($\Delta n \leq 0.04$ at 1µm). The film growth on Y_2O_3 and YAG was investigated in $\langle 111 \rangle$ and $\langle 100 \rangle$ direction.

Preparation

All films were fabricated by the pulsed laser deposition technique. Either pressed and sintered high purity powders or polycrystalline bulk materials obtained by fusion were used as targets in the ablation experiments. The density of the sintered targets was about 90% of the single-crystal density and no difference in the deposited films was noticed

in dependence of the used target type (sintered or crystalline). In the latter stage of this thesis, pre-deposition substrate annealing was performed to allow proper RHEED measurements and obtain additional information on the substrates. By this treatment, reconstructed atomically flat surfaces were obtained, with visible terraces by which the monolayer step height could be determined. Varying miscut angles of $\beta \leq 2.58°$ were determined.

An KrF excimer laser of 248 nm wavelength and 20 ns pulse duration was used for target ablation with material dependent laser fluences of $1.1-2.5\,\mathrm{J/cm^2}$. This resulted in material related growth rates of $0.002-0.01$ Å per pulse. The material-dependent threshold fluence was determined for ablation from sintered and crystalline targets. In order to reduce a possible droplet formation, a large ablation spot of $5-7\,\mathrm{mm^2}$ was used. With material dependent optimized deposition parameters crystalline film growth was achieved.

Structural Characterization

A number of analytical techniques were applied for a thorough characterization of the thin films. The structural analysis includes in-situ reflection high-energy electron diffraction (RHEED), ex-situ X-ray diffraction (XRD) and ex-situ atomic force microscopy (AFM).

Two-dimensional layer-by-layer growth was observed by RHEED intensity oscillations for the quasi-homoepitaxial (Gd, Lu)-admixed sesquioxide, orthovanadate and garnet systems. For these systems, the degree of lattice matching varied between $98.93-99.79\%$. The films were highly textured in the default substrate direction and had a high degree of crystallinity resulting in crystallite sizes $L_\perp$ of $66-100\%$ of the film thickness. After deposition, the film surface usually had a low roughness with RMS values of $0.12-2.0$ nm. These results are promising as smooth surfaces are important for optical applications. However, for composite sesquioxide films the out-of-plane characterization revealed multiple peaks, which indicated a 'mosaic structure' in the films. A correlation to high miscut angles of the used substrates can be assumed.

By heteroepitaxy, a highly textured and crystalline Cr:Al_2O_3 film was deposited on $ScLuO_3$ with good lattice matching of 99.46%. Unfortunately, no RHEED setup was available at that time and thus no growth monitoring had been done. The newer attempts of in-situ RHEED analysis of this system did not show a layer-by-layer growth due to poor substrate quality and too high substrate temperatures. No continuous layer-by-layer growth could be achieved with the other heteroepitaxial substrate–film systems either. Instead, for temperatures exceeding half the melting heat of the substrate, subplantation was observed in all three heteroepitaxial systems. In Al_2O_3–$(Sc, Lu)_2O_3$ and $ScLuO_3$–Al_2O_3 the target particles most probably reacted with the substrate and formed a $(Sc, Lu)AlO_3$ phase, which was identified in the XRD measurements. By subplantation and interdiffusion the lutetium particles of the $LiYF_4$–Lu_2O_3 system probably formed a $Li(Y, Lu)F_4$ phase. In heteroepitaxy, the danger of subplantation with subsequent substrate–particle reaction is a serious problem of the PLD technique. Moreover, it was not possible to obtain continuous RHEED oscillations with the substrate–film systems Y_2O_3–Lu_2O_3 or YAG–LuAG. In spite of the residual mismatch in the lattice matched films, this under-

lines the importance of lattice matched film compositions. Initial substrate–film lattice constant deviations most probably prevent layer-by-layer growth.

Additional energy dispersive X-ray (EDX) measurements proved that the target stoichiometry in the solid solution PLD-films of Eu:$(Sc, Lu)_2O_3$, Eu:$(Gd, Lu)_2O_3$, Eu:$(Gd, Lu)VO_4$, and Eu:$(Gd, Lu)_3Al_5O_{12}$ were preserved. As expected, the amount of each material in the films corresponded to the target composition within the measuring accuracy.

Spectroscopic Analysis

Information on the local crystal structure of the rare-earth-doped films were obtained by spectroscopic analysis. This included luminescence measurements (excitation and emission) at room temperature, SuperLumi VUV excitation measurements at 10 K, and lifetime measurements. The refractive indices of the films were estimated by ellipsometric analysis. As europium is a good luminescent probe emitting in the visible spectrum, and because of the main fluorescence level $^5D_0$, which is highly sensitive to the surrounding crystal field, the spectroscopic investigation focused on the Eu^{3+} ion.

A strong dependence exists between the luminescence characteristics of the dopants and the crystallinity of the host matrix. High degrees of crystallinity require high deposition temperatures. With almost no exception, the deposited films in hetero- and (quasi-) homoepitaxy had bulk-like luminescence properties when considering the linewidths and transition intensities. This was maintained down to thicknesses of ≤ 50 nm, which is an improvement to previous deposited films. For the two-component films a marginal broadening was observed in the transition linewidth. Interesting differences are revealed in VUV excitation measurements at helium temperature. Depending on the film matrix, the additional ion in (Gd, Lu)- or (Sc, Lu)-solid solutions can be responsible for a distortion in the crystal lattice. It can be assumed, that the degree of distortion is dependent on the number of different lattice sites and point group symmetries available for different ions. Therefore, the $(Gd, Lu)VO_4$ composite films are most affected whereas the $(Gd, Lu)_3Al_5O_{12}$ composite films are affected much less.

Very promising refractive index differences Δn of $0.2 - 0.5$ in heteroepitaxy and $0.02 - 0.3$ in quasi-homoepitaxy were obtained by the investigated substrate–film systems.

10.2 Résumé

The aim of the research detailed in this thesis was the investigation and epitaxy of lattice matched dielectric films for optical applications (coatings, Bragg mirrors, active and passive waveguides) by using the advantages of the pulsed laser deposition technique. The presented results demonstrate the epitaxy of high crystalline lattice matched films by PLD with correct stoichiometry and smooth surfaces. Further, it shows the possibilities of in-situ RHEED monitoring of the growth process in order to sustain controlled layer-by-layer growth.

Apparently, the lattice matched thin films investigated in this thesis have deficiencies and are by no means perfect due to drawbacks such as subplantation, tilting, antisite defects, and lattice expansion. However, it is likely that further work on lattice matching and on material specific deposition process parameters can resolve the presented problems.

10.3 Outlook and Future Work

Different analysis techniques are required in order to investigate additional film properties, such as a 'mosaic structure' or in-plane orientation of the atomic planes. The lateral crystallite sizes and the lateral lattice constants of the lattice matched films can be determined by the surface X-ray diffraction (SXRD) technique. With high resolution transmission electron microscopy (HRTEM) measurements a direct view of the atomic positions at the interface and an identification of the different components is possible. Both techniques will give further insight on the lattice matching of the films.

Another interesting idea which has not been realized in the cause of this thesis is the *gradient layer film growth* with gradually decreasing lattice matching. Similar to semiconductor film layers [Hag01], a highly lattice matched layer is grown initially on the substrate and serves as buffer layer. After a number of layers have continued the seed lattice of the substrate, the lattice matching is decreased, introducing a slightly different composition and leading over to the desired material. With such gradient film growth, high refractive index differences could be achieved while ensuring low crystal defect concentrations in the film. Gradient growth could also enable a layer-by-layer growth of heteroepitaxial systems

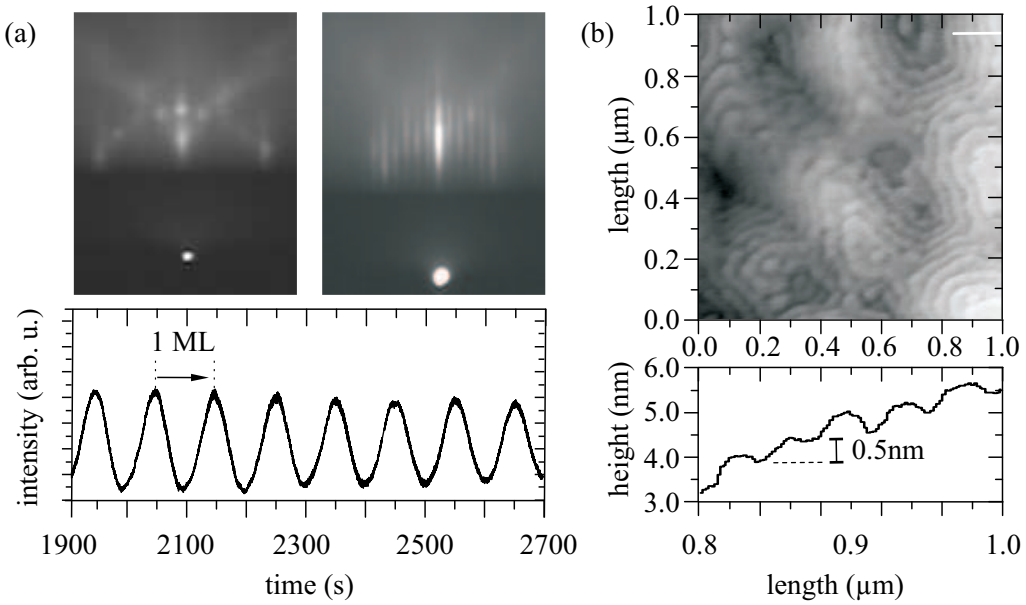

Figure 10.1: *(a) RHEED oscillations during continuous deposition of Nd:(Gd.Lu)$_2$O$_3$ in ⟨100⟩ direction on Y$_2$O$_3$. The insets show the RHEED image before (left) and after deposition end at 1 µm (right). (b) Surface topography measured by AFM.*

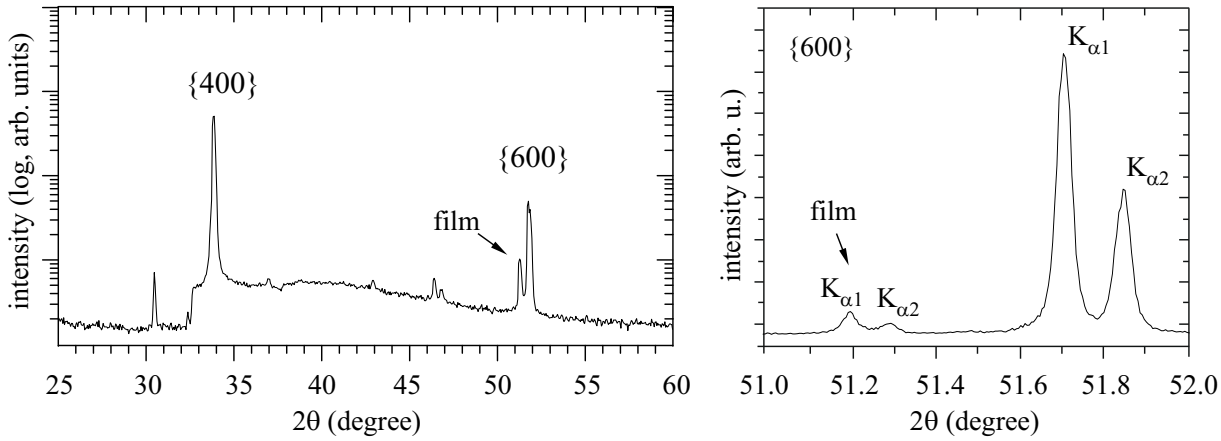

Figure 10.2: *(a) X-ray diffraction pattern of a Nd(0.5%):$(Gd, Lu)_2O_3$ film of 1 µm thickness grown on ⟨100⟩ oriented yttria. (b) High resolution scan of the {600} reflection.*

by introducing several buffer layers until finally reaching the desired film material.

The lattice matched growth of films with higher thickness and substitution of the Eu^{3+} probe ion by a laser-active ion, such as Yb^{3+}, Er^{3+} or Nd^{3+} has already been realized in our laboratory. In collaboration with T. Gün and A. Kahn a lattice matched $Nd(0.5\%):(Gd_{51.595}Lu_{47.905})_2O_3$ film of 1 µm thickness was deposited on [100] yttria. In-situ RHEED monitoring was applied during the film growth. The RHEED intensity oscillations shown in figure 10.1 (a) give evidence to two-dimensional layer-by-layer growth. Towards the designated deposition end at 1 µm the RHEED intensity oscillations indicated a change of the growth mode from layer-by-layer to step-flow (figure 10.3). The assumption of two-dimensional layer-by-layer growth is strengthened by the RHEED image after deposition, which is shown in the right inset of figure 10.1. Correspondingly, the AFM image in figure 10.3 (b) measured by T. Gün reveals a smooth atomically flat multi-level surface, in which monolayer terraces of 5 Å step height are recognized. Figure 10.2 shows the X-ray analysis measured by A. Kahn. By the 2θ positions, the lattice constants of substrate and film are determined to $a_s = 10.696$ Å and $a_f = 10.599$ Å, respectively, resulting in a lattice matching of 99.09%. The FWHM width of the {600} reflection was around 0.03° for the substrate and the film, indicating monocrystalline film growth.

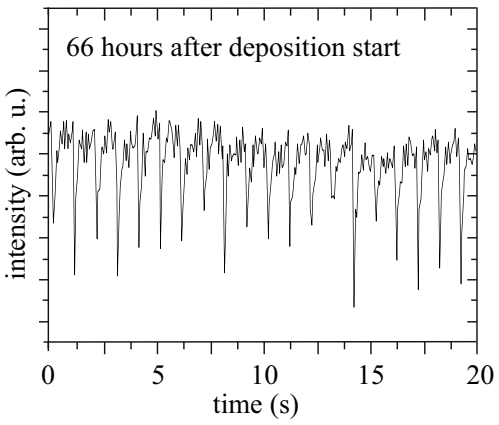

Figure 10.3: *Step flow growth of Nd:$(Gd, Lu)_2O_3$ in ⟨100⟩ direction.*

These last results emphasize that all three quasi-homoepitaxial lattice matched systems presented in this thesis are regarded as very promising laser host materials.

A List of Fabricated Films

The following table summarizes the process parameters of all films that were deposited and characterized in the course of this work.

Name	**Substrate**	**Film and Dopant** (in mol.%)	$T_{\mathbf{sub}}$ (°C)	$p_{\mathbf{O_2}}$ (mbar)	$d_{\mathbf{ts}}$ (cm)	E_p (J/pulse)	$\nu_{\mathbf{rep}}$ (Hz)	$h_{\mathbf{film}}$ (nm)
S001	Sc_2O_3	Er(1.0): Sc_2O_3	700	8.8×10^{-3}	9.0	0.8	10	
S002	SiO_2	Eu(1.5): Y_2O_3	700	8.8×10^{-3}	9.0	0.8	10	234.74
S003	Y_2O_3 (111)	Eu(1.5): Y_2O_3	668	8.8×10^{-3}	9.0	0.8	10	120
S004	Y_2O_3 (111)	Eu(1.5): Y_2O_3	668	8.8×10^{-3}	9.0	0.8	10	50
S005	Y_2O_3 (111)	Eu(1.5): Y_2O_3	668	8.8×10^{-3}	9.0	0.8	10	20
S006	Y_2O_3 (111)	Eu(1.5): Y_2O_3	668	8.8×10^{-3}	9.0	0.8	10	5
S007	Y_2O_3 (111)	Eu(1.5): Y_2O_3–Y_2O_3	668	8.8×10^{-3}	9.0	0.8	10	20–5
S008	Y_2O_3 (100)	Eu(1.5): Y_2O_3	700	8.8×10^{-3}	9.0	0.8	10	100
S009	Y_2O_3 (111)	Er(2.0): Lu_2O_3	705	8.8×10^{-3}	9.2	0.8	10	100
S010	α-Al_2O_3	Eu(2.0): $ScLuO_3$	700	7.9×10^{-3}	9.2	0.8	15	1000
S011	α-Al_2O_3	Eu(2.0): $ScLuO_3$	700	7.9×10^{-3}	9.2	0.8	10	500
S012	α-Al_2O_3	Eu(2.0): $ScLuO_3$	700	7.9×10^{-3}	9.2	0.8	10	200
S013	α-Al_2O_3	Eu(2.0): $ScLuO_3$	700	7.9×10^{-3}	9.2	0.8	10	50
S014	α-Al_2O_3	Eu(2.0): $ScLuO_3$	700	7.9×10^{-3}	9.2	0.8	10	10
S015	α-Al_2O_3	Eu(2.0): $ScLuO_3$	700	7.9×10^{-3}	9.2	0.8	10	5
S016	α-Al_2O_3	Eu(2.0): $ScLuO_3$	700	7.9×10^{-3}	9.2	0.8	10	50
S017	α-Al_2O_3	Eu(2.0): $ScLuO_3$	700	7.9×10^{-3}	9.2	0.8	10	5
S018	α-Al_2O_3	Nd(0.5): $ScLuO_3$–$ScLuO_3$	700	7.9×10^{-3}	9.2	0.8	16	8000–3500
S019	α-Al_2O_3	Eu(2.0): Y_2O_3	20	7.9×10^{-3}	9.0	0.8	31	100
S020	YVO_4	Eu(1.5): $GdVO_4$	730	1×10^{-2}	9.0	0.8	11	124.66
S021	YVO_4	Eu(1.5): $GdVO_4$	730	1×10^{-2}	9.0	0.8	11	62.33
S022	α-Al_2O_3	Eu(1.5): $GdVO_4$	730	1×10^{-2}	9.0	0.8	11	581
S023	α-Al_2O_3	Nd(0.5): $ScLuO_3$–Al_2O_3	730	1×10^{-2}	9.0	0.8	16	10000–5000
S024	YVO_4	Eu(1.5): $GdVO_4$	730	1×10^{-2}	9.0	0.8	16	20
S025	YVO_4	Eu(1.5): $GdVO_4$	730	1×10^{-2}	9.0	0.8	11	8
S026	YVO_4	Eu(1.5): $GdVO_4$	730	1×10^{-2}	9.0	0.8	11	4

Name	Substrate	Film and Dopant (in mol.%)	T_{sub} (°C)	p_{O_2} (mbar)	d_{ts} (cm)	E_p (J/pulse)	ν_{rep} (Hz)	h_{film} (nm)
S027	YVO_4	Eu(1.5): $GdVO_4$	730	1×10^{-2}	9.0	0.8	3	2
S028	YVO_4	Eu(1.5): $GdVO_4$	730	0	9.0	0.8	1	2
S029	YVO_4	Eu(1.5): $GdVO_4$	730	1×10^{-2}	9.0	0.8	1	2
S030	YVO_4	Eu(1.5): $GdVO_4$–Al_2O_3	730	1×10^{-2}	9.0	0.8	3	4–32
S031	YVO_4	Eu(1.5): $GdVO_4$	730	1×10^{-2}	9.0	0.8	3	20
S032	$LiYF_4$	Eu(8.0): Lu_2O_3	600	1×10^{-2}	9.0	0.8	3 | 7 | 1	240
S033	$LiYF_4$	Eu(8.0): Lu_2O_3	600	1×10^{-2}	9.0	0.8	3	100
S034	$LiYF_4$	Eu(2.0): Lu_2O_3	600	1×10^{-2}	9.0	0.8	3	100
S035	$LiYF_4$	Eu(2.0): Lu_2O_3	600	1×10^{-2}	9.0	0.8	3	50
S036	$LiYF_4$	Eu(2.0): Lu_2O_3	600	9.5×10^{-3}	9.0	0.8	3	20
S037	$LiYF_4$	Eu(2.0): Lu_2O_3	600	9.5×10^{-3}	9.0	0.8	1	8
S038	$LiYF_4$	Eu(2.0): Lu_2O_3	600	9.5×10^{-3}	9.0	0.8	1	4
S039	$LiYF_4$	Eu(2.0): Lu_2O_3	600	9.5×10^{-3}	9.0	0.8	1	2
S040	$LiYF_4$	—	—	—	—	—	—	—
S041	YVO_4	Eu(2.0): $GdVO_4$ buried	700	1×10^{-2}	9.0	0.8	3	20–2–20
S042	YAG	Eu(2.0): YAG	700	1×10^{-2}	9.0	0.8	3	100
S043	α-Al_2O_3	Eu(2.0): YAG	700	1×10^{-2}	9.0	0.8	15	340
S044	YAG (111)	Eu(2.0): YAG	700	1×10^{-2}	9.0	0.8	3	50
S045	YAG (111)	Eu(2.0): YAG	700	1×10^{-2}	9.0	0.8	3	20
S046	YAG (111)	Eu(2.0): YAG	700	1×10^{-2}	9.0	0.8	3	8
S047	YAG (111)	Eu(2.0): YAG	700	1×10^{-2}	8.0	0.8	3	4
S048								
S049	Y_2O_3 (100)	Eu(8.0): Lu_2O_3	700	1×10^{-2}	9.0	0.8	3	100
S050	Y_2O_3 (100)	Eu(8.0): Lu_2O_3	700	1×10^{-2}	9.0	0.8	3	50
S051	Y_2O_3 (100)	Eu(8.0): Lu_2O_3	700	1×10^{-2}	9.0	0.8	3	20
S052	Y_2O_3 (100)	Eu(8.0): Lu_2O_3	700	1×10^{-2}	9.0	0.7	3	8
S053	Y_2O_3 (100)	Eu(8.0): Lu_2O_3	700	1×10^{-2}	9.0	0.7	3	4
S054	Y_2O_3 (100)	Eu(8.0): Lu_2O_3	700	1×10^{-2}	9.0	0.8	3	2
S055	Y_2O_3 (111)	Eu(8.0): Lu_2O_3	697	1×10^{-2}	9.0	0.8	3	50
S056	Y_2O_3 (111)	Eu(8.0): Lu_2O_3	697	1×10^{-2}	9.0	0.8	28	20
S057	$ScLuO_3$ (111)	Cr(0.5): Al_2O_3	700	1×10^{-2}	9.0	0.8	3	50
S058	$ScLuO_3$ (111)	Cr(0.5): Al_2O_3	700	1×10^{-2}	9.0	0.8	3	20
S059	$ScLuO_3$ (111)	Cr(0.5): Al_2O_3	700	1×10^{-2}	9.0	0.8	3	100
S060	Y_2O_3 (111)	Eu(2.0): $(Gd, Lu)_2O_3$	702	1×10^{-2}	9.0	0.8	3	100
S061	Y_2O_3 (111)	Eu(2.0): $(Gd, Lu)_2O_3$	705	1×10^{-2}	9.0	0.7	3	50
S062	Y_2O_3 (111)	Eu(2.0): $(Gd, Lu)_2O_3$	705	1×10^{-2}	9.0	0.7	3	25
S063	Y_2O_3 (111)	Eu(2.0): $(Gd, Lu)_2O_3$	705	1×10^{-2}	9.0	0.8	3	10
S064	Y_2O_3 (111)	Eu(2.0): $(Gd, Lu)_2O_3$	705	1×10^{-2}	9.0	0.8	3	5
S065	YAG (100)	Eu(2.0): (Gd, Lu)AG	645	1×10^{-2}	9.0	0.8	3	100

Name	**Substrate**	**Film and Dopant** (in mol.%)	$T_{\mathbf{sub}}$ (°C)	$p_{\mathbf{O_2}}$ (mbar)	$d_{\mathbf{ts}}$ (cm)	E_p (J/pulse)	$\nu_{\mathbf{rep}}$ (Hz)	$h_{\mathbf{film}}$ (nm)
S066	YAG (100)	Eu(2.0): (Gd, Lu)AG	666	1×10^{-2}	9.0	0.8	3	50
S067	YAG (100)	Eu(2.0): (Gd, Lu)AG	659	1×10^{-2}	9.0	0.8	3	25
S068	YAG (100)	Eu(2.0): (Gd, Lu)AG	665	1×10^{-2}	9.0	0.8	3	10
S069	α-Al_2O_3	Eu(2.0): (Gd, Lu)AG	715	1×10^{-2}	9.0	0.75	11	498
S070	α-Al_2O_3	Eu(2.0): $(Gd, Lu)_2O_3$	750	1×10^{-2}	9.5	0.75	11	738
S071	α-Al_2O_3	Eu(2.0): (Gd, Lu)VO_4	730	1×10^{-2}	9.0	0.75	11	334
S072	YVO_4	Eu(2.0): (Gd, Lu)VO_4	730	1×10^{-2}	9.0	0.75	11	100
S073	YVO_4	Eu(2.0): (Gd, Lu)VO_4	730	1×10^{-2}	9.0	0.75	11	50
S074	YVO_4	Eu(2.0): (Gd, Lu)VO_4	730	1×10^{-2}	9.0	0.75	11	25
S075	YVO_4	Eu(2.0): (Gd, Lu)VO_4	730	1×10^{-2}	9.0	0.75	3	10
S076	YVO_4	Eu(2.0): (Gd, Lu)VO_4	730	1×10^{-2}	9.0	0.75	3	25
S077	$LiYF_4$	Eu(8.0): Lu_2O_3	600	9.2×10^{-3}	9.0	0.4	11	100
S078	$LiYF_4$	Eu(8.0): Lu_2O_3	600	1×10^{-2}	9.0	0.4	3	100
S079	$LiYF_4$	Eu(8.0): Lu_2O_3	600	1×10^{-2}	8.0	0.4	3	100
S080	YVO_4	Eu(2.0): $GdVO_4$, *cryst*	850	1×10^{-2}	9.5	0.8	3	100
S081	YVO_4	Eu(2.0): $GdVO_4$, *cryst*	800	1×10^{-2}	9.5	0.8	3	5
S082	YVO_4	Eu(2.0): (Gd, Lu)VO_4, *cryst*	800	1×10^{-2}	9.5	0.8	3	100
S083	YVO_4	Eu(2.0): (Gd, Lu)VO_4, *cryst*	800	1×10^{-2}	9.5	0.8	3	5
S084	α-Al_2O_3	Eu(2.0): $ScLuO_3$, *cryst*	975	1×10^{-2}	9.5	0.8	1 | 3	100
S085	α-Al_2O_3	Eu(2.0): $ScLuO_3$, *cryst*	940	1×10^{-2}	9.5	0.8	1	5
S086	$LiYF_4$	Eu(2.0): Lu_2O_3, *cryst*	600	1×10^{-2}	9.5	0.8	3	100
S087	YAG (111)	Eu(2.0): YAG, *cryst*	890	1×10^{-2}	9.5	0.8	3	100
S088	YAG (111)	Eu(2.0): YAG, *cryst*	875	1×10^{-2}	9.5	0.8	1	5
S089	YAG (100)	Eu(2.0): YAG, *cryst*	865	1×10^{-2}	9.5	0.8	1	5
S090	YAG (100)	Eu(2.0): YAG, *cryst*	885	1×10^{-2}	9.5	0.8	1	50
S091	YAG (100)	Eu(2.0): YAG, *cryst*	860	1×10^{-2}	9.5	0.8	3	100
S092	Y_2O_3 (100)	Eu(2.0): Lu_2O_3, *cryst*	900	1×10^{-2}	9.5	0.8	3	10
S093	Y_2O_3 (100)	Eu(2.0): Lu_2O_3, *cryst*	898	1×10^{-2}	9.5	0.8	3	100
S094	Y_2O_3 (100)	Eu(2.0): Lu_2O_3	905	1×10^{-2}	9.5	0.8	3	10
S095	YAG (100)	Eu(2.0): (Gd, Lu)AG, *cryst*	895	1×10^{-2}	9.5	0.8	1	100
S096	YAG (100)	Eu(2.0): (Gd, Lu)AG, *cryst*	895	1×10^{-2}	9.5	0.8	1	5
S097	YAG (111)	Eu(2.0): (Gd, Lu)AG, *cryst*	870	1×10^{-2}	9.5	0.8	1	5
S098	Y_2O_3 (111)	Eu(2.0): $(Gd, Lu)_2O_3$, *cryst*	900	1×10^{-2}	9.5	0.8	1	5
S099	Y_2O_3 (111)	Eu(2.0): Lu_2O_3, *cryst*	900	1×10^{-2}	9.5	0.8	1 | 3	50
S100	Y_2O_3 (111)	Eu(2.0): Y_2O_3, *cryst*	900	1×10^{-2}	9.5	0.8	1	20
E101	Y_2O_3 (111)	Eu(2.0): $(Gd, Lu)_2O_3$	470	4×10^{-5}	—	—	—	100
E102	Y_2O_3 (100)	Eu(2.0): $(Gd, Lu)_2O_3$	470	4×10^{-5}	—	—	—	100
E103	Y_2O_3 (100)	Eu(2.0): $(Gd, Lu)_2O_3$	470	4×10^{-5}	—	—	—	100
E104	YVO_4	Eu(2.0): (Gd, Lu)VO_4	470	4×10^{-5}	—	—	—	100

Name	Substrate	Film and Dopant (in mol.%)	T_{sub} (°C)	$p_{\mathrm{O_2}}$ (mbar)	d_{ts} (cm)	E_p (J/pulse)	ν_{rep} (Hz)	h_{film} (nm)
E105	YAG (100)	Eu(2.0): (Gd, Lu)AG	430	4×10^{-5}	—	—	—	150
E106	YAG (100)	Eu(2.0): (Gd, Lu)AG	430	4×10^{-5}	—	—	—	150
E107	YAG (100)	Eu(2.0): (Gd, Lu)AG	430	4×10^{-5}	—	—	—	150
E108	YAG (111)	Eu(2.0): (Gd, Lu)AG	430	4×10^{-5}	—	—	—	150
SR01	YAG (100)	Eu(2.0): (Gd, Lu)AG	1000	8.8×10^{-3}	9.7	0.8	1	100
SR02	YAG (111)	Eu(2.0): (Gd, Lu)AG	1000	8.9×10^{-3}	9.7	0.8	1	100
SR03	Y_2O_3 (100)	Eu(2.0): (Gd, Lu)$_2O_3$	900	8.9×10^{-3}	9.7	0.8	1	100
SR04	Y_2O_3 (111)	Eu(2.0): (Gd, Lu)$_2O_3$	910	8.9×10^{-3}	9.7	0.8	1	100
SR05	YAG (111)	Eu(2.0): (Gd, Lu)AG	986	8.9×10^{-3}	9.7	0.8	1	100
SR06	α-Al_2O_3	Eu(2.0): (Sc, Lu)$_2O_3$	1050	9×10^{-3}	9.7	0.8	1	50
SR07	$ScLuO_3$ (111)	Cr(0.25): Al_2O_3	950	8.5×10^{-3}	9.7	0.8	1	100
SR08	YVO_4	Eu(2.0): (Gd, Lu)VO_4	900	8.3×10^{-3}	9.7	0.8	1	100
SR09	$LiYF_4$	Eu(2.0): Lu_2O_3	550	5.5×10^{-3}	9.7	0.8	1	70
SR10	Y_2O_3 (100)	Eu(2.0): (Gd, Lu)$_2O_3$	920	9×10^{-3}	9.7	0.8	1	100
SR11	Y_2O_3 (111)	Eu(2.0): (Gd, Lu)$_2O_3$	905	4.6×10^{-3}	9.7	0.8	1 | 0.5	100
SR12	YVO_4	Eu(2.0): (Gd, Lu)VO_4	900	7.7×10^{-3}	9.7	0.8	1	100
K047	Y_2O_3 (100)	Nd(0.5): (Gd, Lu)$_2O_3$	900	8.8×10^{-3}	9.6	0.8	1	10^3

Table A.1: *List of fabricated films. A resistive heater with no direct thermal contact was used for films < S080. Films ≥ S080 were deposited using a laser-based heater with the substrates mounted on a SiC or Si_3N_4 heat-spreader. Pre-deposition substrate treatment in combination with atomic force microscopy were performed as a preparation for the in-situ reflection high-energy electron diffraction measurements during the deposition process for films SR01 – SR12. In addition to films denoted with 'SR', the film K047 was manufactured in the same manner in collaboration with T. Gün and A. Kahn. Further results regarding this film will soon be published. Films which were fabricated by D. Barlösius using the EBV technique are tagged 'E'.*

B Sellmeier Equations

Material	**Refractive Index** (λ in μm)	**Reference**
Sc_2O_3	$n = \sqrt{3.83252 + \frac{0.0492688}{\lambda^2 - 0.0237987} - 0.014094\lambda^2}$	[Mix99]
Y_2O_3	$n = \sqrt{3.5387 + \frac{0.0421725}{\lambda^2 - 0.0243226} - 0.00914896\lambda^2}$	[Mix99]
Lu_2O_3	$n = \sqrt{3.62004 + \frac{0.0412526}{\lambda^2 - 0.0239454} - 0.0086344\lambda^2}$	[Mix99]
Gd_2O_3	$n = \sqrt{1 + \frac{\lambda^2}{0.364402\lambda^2 - 0.0075356}}$	[Liu07]
α-Al_2O_3	$n_o = \sqrt{1.5586 + \frac{1.52365\lambda^2}{\lambda^2 - 0.01097} + \frac{5.36043\lambda^2}{\lambda^2 - 325.66}}$ $n_e = \sqrt{1.78106 + \frac{1.27616\lambda^2}{\lambda^2 - 0.01242} + \frac{0.33939\lambda^2}{\lambda^2 - 17.03}}$	[Kuz06]
YAG	$n = \sqrt{1 + \frac{2.282\lambda^2}{\lambda^2 - 0.01185} + \frac{3.27644\lambda^2}{\lambda^2 - 282.734}}$	[Zel98]
YVO_4	$n_o = \sqrt{3.77834 + \frac{0.069736}{\lambda^2 - 0.04724} - 0.0108133\lambda^2}$ $n_e = \sqrt{4.59905 + \frac{0.110534}{\lambda^2 - 0.04813} - 0.0122676\lambda^2}$	[Bri07]
$GdVO_4$	$n_o = \sqrt{3.8987165 + \frac{0.05990622}{\lambda^2 - 0.0514395} - 0.011319\lambda^2}$ $n_e = \sqrt{4.734369 + \frac{0.1216149}{\lambda^2 - 0.0523664} - 0.013927\lambda^2}$	[Foc07]
$LiYF_4$	$n_o = \sqrt{1.38757 + \frac{0.70757\lambda^2}{\lambda^2 - 0.00931} + \frac{0.18849\lambda^2}{\lambda^2 - 50.99741}}$ $n_e = \sqrt{1.31021 + \frac{0.84903\lambda^2}{\lambda^2 - 0.00876} + \frac{0.53607\lambda^2}{\lambda^2 - 134.9566}}$	[Bro07]

Table B.1: *Sellmeier equations of the used materials. The equations for the sesquioxides apply to the cubic bixbyite structure.*

Bibliography

[Abr78] V. N. Abramov and A. I. Kuznetsnov, *Fundamental absorption of Y_2O_3 and $YAlO_3$*, Soviet Physics of Solid State **20** (3), 399 (1978).

[Abr83] V. N. Abramov, A. N. Ermoshkin and A. I. Kuznetsnov, *Optical properties and electron energy structure of Y_2O_3 and Sc_2O_3*, Soviet Physics of Solid State **25** (6), 981 (1983).

[And94] F. Anderson, P. Summers, H. Weidner, P. Hong and R. Peale, *Interpretive crystal-field parameters: Application to Nd^{3+} in $GdVO_4$ and YVO_4*, Physical Review B **50** (20) (1994).

[And96] S. Andrieu and P. Frechard, *What information can be obtained by RHEED applied on polycrystalline films?*, Surface Science **360** (1), 289 (1996).

[And98] A. A. Anderson, *Crystalline planar waveguide lasers fabricated by pulsed laser deposition*, Dissertation, Faculty of Science, Department of Physics, University of Southampton (1998).

[Ani83] S. I. Anisimov, Y. B. Zel'dovich, N. A. Inogamov and M. F. Ivanov, *Shock Waves, Explosions, and Detonations*, in: *Progress in Astronautics and Aeronautics, Series 87*, 218 (Washington, DC, 1983).

[Ash76] N. W. Ashcroft and N. D. Mermin, *Solid State Physics* (Saunders College Publishing, Fort Worth, 1976).

[Atk87] P. W. Atkins, *Physikalische Chemie* (VCH Verlag, 1987).

[Auc88] O. Auciello, A. R. Krauss, J. Santiago-Aviles, A. F. Schreiner and D. M. Gruen, *Surface compositional and topographical changes resulting from excimer laser impacting on $YBa_2Cu_3O_2$ single phase superconductors*, Applied Physics Letters **52** (3), 239 (1988).

[Bab05] V. Babin, K. Blazek, A. Krasnikov, K. Nejezchleb, M. Nikl, T. Savikhina and S. Zazubovich, *Luminescence of undoped LuAG and YAG crystals*, Physica Status Solidi C **2** (1), 97 (2005).

[Bal62] C. J. Ballhausen, *Introduction to Ligand Field Theory* (McGraw-Hill Book Company, Inc., New York, 1962).

[Bal67] R. Balzer, H. Peisl and W. Waidelich, *Gitterfehlordnung in KCL mit Farbzentren*, Zeitschrift für Physik **204**, 405 (1967).

[Bar57] C. Barta, F. Petru and B. Hájek, *Über die Darstellung des Einkristalls von Scandiumoxyd*, Die Naturwissenschaften **45**, 36 (1957).

[Bar69] W. P. Barr, *The production of low scattering dielectric mirrors using rotating vane particle filtration*, Journal of Physics E **2** (2), 1112 (1969).

[Bar74] B. D. Bartolo, *Optical properties of ions in solids* (Plenum Press, New York, 1974).

[Bar95] A.-L. Barabasi and H. E. Stanley, *Fractal concepts in surface growth* (Cambridge University Press, 1995).

[Bar01] S. J. Barrington, *Planar Waveguide Devices fabricated by Pulsed Laser Deposition*, Dissertation, Faculty of Science, Department of Physics, University of Southampton (2001).

[Bär04] S. Bär, *Crystalline, Rare-Earth-doped Sesquioxide PLD-Films on α-Alumina*, Dissertation, Fachbereich Physik, Universität Hamburg (2004).

[Bär05] S. Bär, H. Scheife and G. Huber, *Rare-earth-doped GVO films grown by pulsed laser deposition*, Optical Materials **28** (6-7), 681 (2005).

[Bas95] M. Bass, *Handbook of optics* (McGraw-Hill Book Company, Inc., New York, 1995), 2nd edition.

[Bat82] I. P. Batra, *Electronic structure of α-Al_2O_3*, Journal of Physics: Condensed Matter **15**, 5399 (1982).

[Bau58] E. Bauer, *Wachstum dünner Schichten*, Zeitschrift für Kristallographie **110**, 372 (1958).

[Bäu00] D. Bäuerle, *Laser Processing and Chemistry* (Springer-Verlag, Berlin, Heidelberg, New York, 2000).

[Bec88] C. H. Becker and J. Pallix, *Laser ablation of bulk $YBa_2Cu_3O_{7-\delta}$ and cluster emission*, Journal of Applied Physics **64** (10), 5152 (1988).

[Bee88] J. L. Beeby, in: P. K. Larsen and P. J. Dobson (editors), *Reflection High-Energy Electron Diffraction and Reflection Electron Imaging* (Plenum, New York and London, 1988).

[Bel03] E. L. Belokoneva and Y. K. Shcherbakova, *Electron density in synthetic escolaite Cr_2O_3 with a corundum structure and its relation to antiferromagnetic properties*, Zhurnal Neorganicheskoi Khimii **48**, 960 (2003).

[Ber66] L. Bergmann and C. Schäfer, *Lehrbuch der Experimentalphysik, Ausgabe III* (Walter de Gruyter & Co, 1966).

[Ber74] H. Bergmann, *Gmelin Handbuch der Anorganischen Chemie, Seltenerdelemente, Teil C1* (Springer-Verlag, Berlin, Heidelberg, New York, 1974).

[Bin86] G. Binning, C. Quate and C. Gerber, *Atomic Force Microscope*, Physical Review Letters **56** (9), 930 (1986).

[Blo74] N. Bloembergen, *Laser-Induced Electric Breakdown in Solids*, IEEE Journal of Quantum Electronics **QE-10** (3), 375 (1974).

[Böl88] B. Bölger, P. K. Larsen and G. Meyer-Ehmsen, in: P. K. Larsen and P. J. Dobson (editors), *Reflection High-Energy Electron Diffraction and Reflection Electron Imaging* (Plenum, New York and London, 1988).

[Bon00] C. L. Bonner, *Multi-watt, diode-pumped planar waveguide lasers*, Dissertation, Faculty of Science, Department of Physics, University Southampton (2000).

[Bor27] M. Born and J. R. Oppenheimer, *Zur Quantentheorie der Moleküle*, Annalen der Physik **84**, 457 (1927).

[Bor75] M. Born and E. Wolf, *Principles of Optics,* 5^{th} edition (Pergamon Press, Oxford, 1975).

[Bra92] S. Brandt, *Datenanalyse,* 3. Auflage (BI Wissenschaftsverlag, Mannheim, 1992).

[Bra99] W. Braun, *Applied RHEED* (Spinger Tracts in Modern Physics, Springer-Verlag, Berlin, Heidelberg, New York, 1999).

[Bre62] F. Breech and L. Cross, Applied Spectroscopy **16** (1962).

[Bri07] I. Brightcrystal, http://www.brightcrystals.com/english/readnew.asp?NewsID=4914 (2007).

[Bro95] I. N. Bronstein, K. A. Sememdjajew, G. Musiol and H. Mühling, *Taschenbuch der Mathematik* (Verlag Harry Deutsch, Frankfurt am Main, 1995).

[Bro07] I. Broadband, http://www.bblaser.com/bbl_item/0156aotk_ndylf.html (2007).

[Bul95] A. V. Bulgakov and N. M. Bulgakova, *Dynamics of laser-induced plume expansion into an ambient gas during film deposition*, Journal of Physics D: Applied Physics **28** (8), 1710 (1995).

[Bul98] A. V. Bulgakov and N. M. Bulgakova, *Gas-dynamic effects of the interaction between a pulsed laser-ablation plume and the ambient gas: analogy with an underepanded jet*, Journal of Physics D **31**, 693 (1998).

[Bün89] J.-C. G. Bünzli and G. R. Choppin, *Lanthanide Probes in Life, Chemical and Earth Sciences* (Elsevier Science Publishing Company Inc., New York, 1989).

[Bur62] G. Burns, *Shielding and Crystal Fields at Rare-Earth Ions*, Physical Review **128** (5), 2121 (1962).

[Bur02] P. Burmester, *Optisch aktive, kristalline, Selten-Erd-dotierte Y_2O_3-PLD-Schichten auf α-Al_2O_3*, Dissertation, Fachbereich Physik, Universität Hamburg (2002).

[Che88] J. T. Cheung and H. Sankur, *Growth of thin films by laser-induced evaporation*, CRC Critical Reviews in Solid State and Material Sciences **14** (1), 63 (1988).

[Che01] R. Chety, E. Millon, A. Boudrioua, J. C. Loulergue, A. Dahoun and J. Perrière, *Growth of $GdCa_4O(BO_3)_3$ thin films by pulsed-laser deposition for nonlinear optical applications*, Journal of Materials Chemistry **11**, 657 (2001).

[Che04] T. Chen, X. M. Li, S. Zhang and H. R. Zeng, *Oxygen dependence of the crystallinity of MgO films grown on $Si_{(100)}$ by PLD*, Journal of Crystal Growth **270**, 553 (2004).

[Chi99] W. Y. Ching and Y.-N. Xu, *Nonscalability and nontransferability in the electronic properties of the Y-Al-O system*, Phys. Rev. B **59**, 12815 (1999).

[Cho99] M. H. Cho, D. H. Ko, K. Jeong, I. W. Lyo, S. W. Whangbo, H. B. Kim, S. Choi, J. H. Song, S. Cho and C. N. Whang, *Temperature dependence of the properties of heteroepitaxial Y_2O_3 films grown on Si by ion assisted evaporation*, Journal of Applied Physics **86** (1), 198 (1999).

[Chr94] D. B. Chrisey and G. K. Hubler, *Pulsed laser deposition of thin films* (Wiley & Sons, New York, 1994).

[Chv00] J. Chval, D. CleHment, J. Giba, J. Hybler, J.-F. Loude, J. Mares, E. Mihokova, C. Morel, K. Nejezchleb, M. Nikl, A. Vedda and H. Zaidi, *Development of new mixed $Lu_x(RE^{3+})_{1\ x}AP$:Ce scintillators*, Nuclear Instruments and Methods in Physics Research A **443**, 331 (2000).

[Coh86] P. I. Cohen, P. R. Pukite, J. M. van Hove and C. S. Lent, *Reflection high-energy electron diffraction studies of epitaxial growth of semiconductor surfaces*, Journal of Vacuum Science & Technology A: Vacuum, Surfaces, and Films **3** (4), 1251 (1986).

[Coh91] A. Cohen, P. Allenspacher, M. M. Brieger and H. O. I. Jeuck, *Beam target interaction during growth of $YBa_2Cu_3O_{7-x}$ by the laser ablation technique*, Applied Physics Letters **59** (17), 2186 (1991).

[Con28] E. U. Condon, *Nuclear motions associated with electron transitions in diatomic molecules*, Physical Review **32**, 858 (1928).

[Con51] E. U. Condon and H. G. Shortley, *Theory of Atomic Spectra* (Cambridge University Press, 1951).

[Con69] B. H. Connor and T. M. Valentine, *A Neutron Diffraction Study of the Crystal Structure of the C-form of Yttrium Sesquioxide*, Acta Crystallographica 2140 (1969).

[Cul78] B. D. Cullity, *Elements of X-ray diffraction, 2^{nd} edition* (Addison Wesley, London, 1978).

[Cze02] C. Czeranowsky, *Resonatorinterne Frequenzverdopplung von diodengepumpten Neodym-Lasern mit hohen Ausgangsleistungen im blauen Spektralbereich*, Dissertation, Institut für Laser-Physik, Universität Hamburg (2002).

[Dav21] C. J. Davisson and C. H. Kunsman, *The scattering of electrons by Nickel*, Phys. Rev. **19**, 253 (1921).

[Dav27] C. J. Davisson and L. H. Germer, Phys. Rev. **30**, 705 (1927).

[Die68] G. H. Diecke, *Spectra and Energy Levels of Rare Earth Ions in Crystals* (Interscience Publishers, John Wiley & Sons, New York, 1968).

[Die92] J. Dieleman, E. van de Riet and J. C. S. Kools, *Laser ablation deposition: Mechanism and application*, Jpn. J. Appl. Phys. **31**, 1964 (1992).

[Dij87] D. Dijkamp, T. Venkatesan, X. D. Wu, S. A. Shaheen, N. Jisrawi, Y. H. Min-Lee, W. L. McLean and M. Croft, *Preparation of Y-Ba-Cu oxide superconductor thin films using pulsed laser evaporation from high T_c bulk material*, Applied Physics Letters **51** (8), 619 (1987).

[DIN78] DIN 4761, Deutsche Norm, *Oberflächencharakter, Geometrische Oberflächentextur-Merkmale, Begriffe und Kurzzeichen* (Beuth-Verlag, Berlin / Köln, 1978).

[Don88] E. E. Donaldson, J. T. Dickinson and S. K. Bhattacharya, *Production and properties of ejecta released by fracture of materials*, Journal of Adhesion **25**, 281 (1988).

[Don91] J. Dong and K. Lu, *Noncubic symmetry in garnet structures studied using extended x-ray-absorption fine-structure spectra*, Physical Review B **43**, 8808 (1991).

[Dup89] H. Dupendant, J. P. Gavigan, D. Givord, A. Lienard, J. P. Rebouillat and Y. Souche, *Velocity distribution of microsized particles in thin film laser ablation deposition (LAD) of metals and oxide superconductors*, Applied Surface Science **43**, 369 (1989).

[Dye91] R. C. Dye, R. E. Muenchause and N. S. Nogar, *Laser ablation of Y_2O_3*, Chemical Physics Letters **181** (6), 531 (1991).

[Egg19] J. Eggert, *Über den Dissoziationszustand der Fixsterngase*, Physikalische Zeitschrift **20**, 570 (1919).

[Ehl05] S. Ehlert, *Herstellung und Charakterisierung ultradünner PLD-Sesquioxidschichten auf Quarz*, Diplomarbeit, Fachbereich Physik, Universität Hamburg (2005).

[Eph26] F. Ephraim and R. Bloch, Chemische Berichte **59**, 2692 (1926).

[Erd72] P. Erdös and J. H. Kang, *Electronic Shielding of Pr^{3+} and Tm^{3+} in Crystals*, Phys. Rev. B **6**, 3393 (1972).

[Flo04] F. Flory and L. Escoubas, *Optical properties of nanostructured thin films*, Progress in Quantum Electronics **28**, 89 (2004).

[Foc07] I. Foctek, http://www.foctek.com/products/crystals/Nd_GdVO4.htm (2007).

[For99a] L. Fornasiero, *Nd^{3+}- und Tm^{3+}-dotierte Sesquioxide*, Dissertation, Institut für Laser-Physik, Universität Hamburg (1999).

[For99b] L. Fornasiero, E. Mix, V. Peters, E. Heumann, K. Petermann and G. Huber, *Efficient laser operation of Nd:Sc_2O_3 at 966 nm, 1082 nm, and 1486 nm*, Conference on Advanced Solid-State Lasers, Boston, USA, technical digest 89–90 (1999).

[Fra59] F. C. Frank and H. J. van der Merwe, *One-dimensional dislocations*, in: *I. u. II. Proc. Royal Soc.*, 205–225 (London, 1959).

[Fre90] R. H. French, *Electronic Structural of α-Al_2O_3, with Comparison to AlON and AlN*, J. Am. Chem. Soc. **73**, 477 (1990).

[Fri93] D. Fried, T. Kushida, G. P. Reck and E. W. Rothe, *The yttrium oxide chemiluminescence from the 308 nm excimer laser ablation of $YBa_2Cu_3O_{7-X}$, Y_20_3, and YCl_3*, Journal of Applied Physics **73** (11), 7810 (1993).

[Fuk89] H. Fukumoto, T. Imura and Y. Osaka, *Heteroepitaxial growth of Y_2O_3 films on silicon*, Applied Physics Letters **55** (4), 360 (1989).

[Geo95] D. B. Geohegan and A. A. Puretzki, *Dynamics of laser ablation plume penetration through low pressure background gases*, Applied Physics Letters **67**, 197 (1995).

[Gre87] J. E. Greedan, *Rare Earth Elements and Materials*, in: K. A. Gschneider Jr and L. Eyring (editors), *Encyclopedia of Physical Science & Technology*, volume **12**, chapter 1, 18–39 (Academic Press Inc., Orlando, 1987).

[Gri04] C. Grivas, T. C. May-Smith, D. P. Shepherd and R. W. Eason, *On the growth and lasing characteristics of thick Nd:GGG waveguiding films fabricated by pulsed laser deposition*, Appl. Phys. A **79**, 1203 (2004).

[Gün07] T. Gün, *Charakterisierung von mittels PLD hergestellten epitaktischen Sesquioxid- und YAG-Schichten*, Diplomarbeit, Universität Hamburg (2007).

[Gür83] P. Gürtler, E. Roick and G. Z. und M. Poey, *Superlumi: A high flux VUV spectroscopic device for luminescence measurement*, Nuclear Instruments and Methods **208**, 835 (1983).

[Hag01] P. R. Hageman, S. Haffouz, V. Kirilyuk, A. Grzegorczyk and P. K. Larsen, *High Quality GaN Layers on Si(111) Substrates: AlN Buffer Layer Optimisation and Insertion of a SiN Intermediate Layer*, Physicus Status Solidi A **188** (2), 523 (2001).

[Hai01] N. Hairston, *Lithograpgy Aids Integration of Optics*, Laser Focus World **37**, 93 (2001).

[Han07] N.-O. Hansen, *Mikroskopische und strukturelle Eigenschaften Selte-Erd-dotierter Sesquioxid-PLD-Schichten*, Diplomarbeit, Universität Hamburg (2007).

[Heb70] J. Heber, K. H. Hellwege, U. Köbler and H. Murmann, *Energy levels and interaction between Eu^{3+}-ions at lattice sites of symmetry C_2 and symmetry C_{3i} in Y_2O_3*, Zeitschrift für Physik **237**, 189 (1970).

[Hen76] M. Henzler, *Atomic steps on single-crystals: Experimental methods and properties*, Appl. Phys. **9**, 11 (1976).

[Hen89] B. Henderson and G. F. Imbusch, *Optical Spectroscopy of Inorganic Solids* (Clarendon Press, Oxford, 1989).

[Hen91] M. Henzler and W. Göpel, *Oberflächenphysik des Festkörpers* (Teubner-Taschenbücher, 1991).

[Her83] I. Hernández-Calderon and H. Höchst, *New method for the analysis of reflection high-energy electron diffraction: α-Sn(001) and InSb(001) surfaces*, Phys. Rev. B **27**, 4961 (1983).

[Hoe66] H. R. Hoekstra, *Phase Relationships in the Rare Earth Sesquioxides at High Pressure*, Inorganic Chemistry **5** (5), 754 (1966).

[Hoe75] H. E. Hoefdraad, *The charge transfer absorption band of Eu^{3+} in oxides*, Journal of Solid State Chemistry **15**, 175 (1975).

[Hoe92] T. H. Hoekstra, L. T. H. Hilderink, P. V. Lambeck and T. J. A. Popma, *Photoluminescence and attenuation of spray-pyrolysis-deposited erbium.doped Y_2O_3 planar optical waveguides*, Optics Letters **17** (21), 1506 (1992).

[Hof03] W. A. Hofer, *Theories of scanning probe microscopes at the atomic scale*, Reviews of modern physics **75**, 1287 (2003).

[Hol92] E. Holland-Moritz, Z.Phys. B: Condens. Matter **89**, 285 (1992).

[Hos77] T. Hoshina, S. Imanaga and S. Yokono, *Charge transfer effects on the luminescent properties of Eu^{3+} in oxysulfides*, Journal of Luminescence **15**, 455 (1977).

[Hu96] W. S. Hu and Z. G. Liu, *Pulsed-laser deposition and optical properties of completely (001) textured optical waveguiding $LiNbO_3$ films upon SiO_2/Si substrates*, Optics Letters **21** (13), 946 (1996).

[Hub04] G. Huber, *Scientific notations and material properties on the work objectives*, Private talk (2004).

[İle04] B. İleri, *Nd-dotierte Granat-Laserkristalle für satellitengestütztes Wasserdampf DIAL*, Diplomarbeit, Universität Hamburg (2004).

[Iva75] I. A. Ivanova, A. M. Morozov, M. A. Petrova, I. G. Podkolzina and P. P. Feofilov, *Preparation and properties of single crystals of double fluorides of lithium and the rare earths*, Inorganic Materials **11** (12), 1868 (1975).

[Jør64] C. Jørgensen, R. Pappalardo and E. Rittershaus, *Reflection Spectra of Lanthanides in Thorium(IV) Oxide and the Large Nephelauxetic Effect of Oxide Ligands or Vacancies*, Zeitschrift für Naturforschung **19A**, 424 (1964).

[Jør70] C. K. Jørgensen, *Electron Transfer Spectra*, Progress in Inorganic Chemistry **12**, 101 (1970).

[Jør77] C. K. Jørgensen and R. Reisfeld, *Lasers and Excited States of Rare Earths* (Springer-Verlag, Berlin, Heidelberg, New York, 1977).

[Joy88] B. A. Joyce, J. H. Neave, J. Zhang and P. J. Dobson, in: P. K. Larsen and P. J. Dobson (editors), *Reflection High-Energy Electron Diffraction and Reflection Electron Imaging* (Plenum, New York and London, 1988).

[Jud62] B. R. Judd, *Optical Absorption Intensities of Rare-Earth Ions*, Physical Review **127** (3), 750 (1962).

[Kai02] N. Kaiser, *Review of the fundamentals of thin-film growth*, Applied Optics **41** (16), 3053 (2002).

[Kam89] S. Kampf, *Bildung und Zerfall der heteronuklearen Edelgasexzimere KrAr, KrNe, XeKr und XeAr*, Dissertation, Fachbereich Physik, Universität Hamburg (1989).

[Kam90] A. A. Kaminskii, *Laser Crystals. Their Physics and Properties* (Springer-Verlag, Berlin, Heidelberg, New York, 1990), 2. edition.

[Kap62] A. A. Kaplyanskii and P. P. Feofilov, *The spectra of divalent rare earth ions in crystals of alkaline earth fluorides*, Opt. Spec. **13**, 129 (1962).

[Kaw88] T. Kawamura, in: P. K. Larsen and P. J. Dobson (editors), *Reflection High-Energy Electron Diffraction and Reflection Electron Imaging* (Plenum, New York and London, 1988).

[Kei97] B. Keiper, *Ionengestützte Laserpulsabscheidung von Oxidschichten für optische Anwendungen*, Dissertation, Fakultät E-Technik und Inform.-Technik, Technische Universität Chemnitz (1997).

[Kel85] R. Kelly, J. J. Cuomo, P. A. Leary, J. E. Rothenberg, B. E. Braren and C. F. Aliotta, *Laser sputtering, Part 1, On the existence of rapid laser sputtering at 193 nm*, Nuclear Instruments and Methods B **9**, 329 (1985).

[Kel92] R. Kelly, *Gas dynamics of the pulsed emission of a perfect gas with applications to laser sputtering and to nozzle expansion*, Physical Review A **42** (2) (1992).

[Kik28] S. Kikuchi, *Diffraction of Cathode Rays by Mica*, Jpn. J. Phys. **5**, 83 (1928).

[Kir03] M. Kirm, *unveröffentlichte Messungen* (Fachbereich Physik, Universität Hamburg, 2003).

[Kit86] C. Kittel, *Introduction to Solid State Physics* (John Wiley and Sons, 1986).

[Kle89] H. Kleinert, *Gauge Fields in Condensed Matter, Vol. II, Stresses and Defects* (World Scientific, Singapore, 1989).

[Klo89] T. Kloiber, *Erosion fester Edelgase durch photonenstimulierte Desorption neutraler Edelgasatome und -moleküle*, Dissertation, Fachbereich Physik, Universität Hamburg (1989).

[Klu98] A. Klust, H. Pietsch and J. Wollschläger, *Growth of CaF_2 on $Si_{(111)}$: Imaging of the CaF_2 interface by friction force microscopy*, Appl. Phys. Lett. **86**, 51901 (1998).

[Kor89] G. Koren, A. Gupta, R. J. Basemann, M. I. Lutwyche and R. Laibowitz, *Laser wavelength dependent properties of $YBa_2Cu_3O_{7-\delta}$ thin films deposited by laser ablation*, Applied Physics Letters **55** (23), 2450 (1989).

[Kor01] M. B. Korzenski, P. Lecoeur, B. Mercey, P. Camy and J. L. Doualan, *Low propagation losses of an $Er:Y_2O_3$ planar waveguide grown by alternate-target pulsed laser deposition*, Applied Physics Letters **78** (9), 1210 (2001).

[Krä05] C. Kränkel, *HEM-Züchtung und Charakterisierung des neuen Lasermaterials $Yb^{3+}:YVO_4$*, Diplomarbeit, Fachbereich Physik, Universität Hamburg (2005).

[Kri90] H. Krischner, *Einführung in die Röntgenstrukturanalyse* (Friedr. Vieweg & Sohn, Braunschweig, 1990).

[Kuk00] M. Kuklja, *Defects in yttrium aluminium perovskite and garnet crystals: atomistic study*, Journal of Physics: Condensed Matter **12**, 2953 (2000).

[Kuz03] Y. Kuzminykh, *not published* (Fachbereich Physik, Universität Hamburg, 2003).

[Kuz06] Y. Kuzminykh, *Crystalline, Rare-Earth-Doped Sesquioxide and YAG PLD-Films*, Dissertation, Fachbereich Physik, Universität Hamburg (2006).

[Lan04] J. Lancock, C. Garapon, C. Martinet, J. Mugnier and R. Brenier, *Influence of the PLD-parameters on the crystalline phases and fluorescence of Eu:*Y_2O_3 *planar waveguides*, Appl. Phys. A **79**, 1263 (2004).

[Lan05] J. Lancock, C. Garapon, M. Jelinek, J. Mugnier and R. Brenier, *Optical and structural properties of Pr:GGG crystalline thin film waveguides grown by pulsed-laser deposition*, Appl. Phys. A **81**, 1477 (2005).

[Lar88] P. K. Larsen and P. J. Dobson, *Reflection High-Energy Electron Diffraction and Reflection Electron Imaging* (Plenum, New York and London, 1988).

[Lec02] P. Lecoeur, M. B. Korzenski, A. Ambrosini, B. Mercey, P. Camy and J. L. Doualan, *Growth of Er:*Y_2O_3 *thin films by pulsed laser ablation from metallic targets*, Applied Surface Science **186**, 403 (2002).

[Len84] C. S. Lent and P. I. Cohen, *Diffraction from stepped surfaces I: Reversible surfaces*, Surface Science **137** (4), 121 (1984).

[Lif03] G. Lifantes, *Integrated Photonics: Fundamentals* (Wiley CVH Verlag GmbH, Weinheim, Germany, 2003).

[Lit99] D. Litvinov, T. O'Donnell and R. Clarke, *In-situ thin-film texture determination*, Journal of Applied Physics **85** (4), 2151 (1999).

[Liu07] L. Liu and X. Chen, *Energy levels, fluorescence lifetime and Judd-Ofelt parameters of* Eu^{3+} *in* Gd_2O_3 *nanocrystals*, Nanotechnology **18**, 1 (2007).

[Loh69] E. Loh, *Ultraviolet-absorption spectra of europium and ytterbium in alkaline earth fluorides*, Phys. Rev. **84** (2), 184 (1969).

[Loh73] E. Loh, *Strong-field assignment of* $4f^{13}5d$ *levels of* Yb^{2+} *in* $SrCl_2$, Phys. Rev. B **7**, 1864 (1973).

[Lou01] L. Lou, W. Zhang, A. Brioude, C. Le Luyer and J. Mugnier, *Preparation and characterization of sol-gel* Y_2O_3 *planar waveguides*, Optical Materials **18**, 331 (2001).

[Mae97] T. Maeda, M. Yoshimoto, T. Ohnishi, G. H. Lee and H. Koinuma, *Orientation - defined molecular layer epitaxy of* α-Al_2O_3 *thin films*, J. Cryst. Growth **177**, 95 (1997).

[Mah90] J. E. Mahan, K. M. Geib, G. Y. Robinson and R. G. Long, *A review of the geometricla fundamentals of reflection high-energy electron diffraction with application to silicon surfaces*, J. Vac. Sci. Technol. A **8** (5), 3692 (1990).

[Mai60] T. Maiman, *Stimulated Optical Radiation in Ruby*, Nature **27**, 2319 (1960).

[Mai83] L. I. Maissel and R. Glang, *Handbook of Thin Film Technology* (McGraw-Hill, New York, 1983).

[Man63] M. Mandel, *Paramagnetic resonance of Yb^{3+} in yttrium oxide*, Applied Physics Letters **2** (10), 197 (1963).

[Mat89] E. Mathias and R. W. Dreyfus, *From laser induced desorption to surface damage*, in: P. Hess (editor), *Topics in Current Physics*, volume **47**, 89–128 (Springer-Verlag, Berlin, Heidelberg, New York, 1989).

[McK00] J. McKittrick, C. F. Bacalski and G. A. Hirata, *Characterization of Photoluminescent ($(Y_{1-x}Eu_x)_2O_3$) Thin Films Prepared by Metallorganic Chemical Vapor Deposition*, Journal of the American Ceramic Society **83** (5), 1241 (2000).

[McN97] A. D. McNaught and A. Wilkinson, *Compendium of Chemical Terminology*, in: International Union of Pure and Applied Chemistry (IUPAC) (editor), *http://www.iupac.org* (Blackwell Science, London, 1997).

[Mel99] R. S. Melzer, S. P. Feofilov, B. Tissue and H. B. Yuan, Physical Review B **60** (20) (1999).

[Men28] G. Menzer, Z. Krstallogr. **69** (1928).

[Mes90] A. Messiah, *Quantenmechanik*, volume **2** (Walter de Gruyter & Co., Berlin, 1990), 3 edition.

[Met94] S. M. Metev and V. P. Veiko, *Laser-Assisted Microtechnology* (Springer-Verlag, Berlin, Heidelberg, New York, 1994).

[Mio95] A. Miotello and R. Kelly, *Critical assessment of thermal models for laser sputtering at high fluences*, Applied Physics Letters **67** (24), 3535 (1995).

[Mix99] E. Mix, *Kristallzüchtung, Spektroskopie und Lasereigenschaften Yb-dotierter Sesquioxide*, Dissertation, Institut für Laser-Physik, Universität Hamburg (1999).

[Moi97] B. Moine, C. Dujardin, H. Lautesse, C. Pedrini, C. Combes, A. Belski, P. Martin and J. Gesland, *Spectroscopic and scintillation properties of cerium-doped LuF_3 single crystal*, Materials Forum **239-241**, 245 (1997).

[Möl86] T. Möller, P. Gürtler and E. R. und G. Zimmerer, *The experimental station superlumi: A unique setup for time- and spectrally resolved luminescence under state selective excitation with synchrotron radiation*, Nuclear Instruments and Methods A **246**, 461 (1986).

[Mor82] C. A. Morrison and R. P. Leavitt, *Spectroscopic properties of triply ionized lanthanides in transparent host crystals*, in: K. A. Gschneider Jr and L. Eyring (editors), *Handbook on the physics and chemistry of rare earths*, volume **5**, chapter 46, 461–692 (North-Holland, Amsterdam, 1982).

[Mor02] S. Morita, R. Wiesendanger and E. Meyer, *Non-contact Atomic Force Microscopy* (Springer-Verlag, Berlin, Heidelberg, New York, 2002).

[Mul96] D. F. Mullica, E. L. Sappenfield, M. M. Abraham, B. C. Chakoumakos and L. A. Boatner, *Structural investigations of several $LnVO_4$ compounds*, Inorganica Chimica Acta **248**, 85 (1996).

[Nak79] E. Nakazawa, *Charge transfer type Luminescence of Yb^{3+} ions in RPO_4 and R_2O_2S (R=Y, La, and Lu)*, Journal of Luminescence **18/19**, 272 (1979).

[Nik05] M. Nikl, E. Mihokova, J. Pejchal, A. Vedda, Y. Zorenko and K. Nejezchleb, *The antisite Lu_{Al} defect-related trap in $Lu_3Al_5O_{12}$:Ce single-crystal*, Physica Status Solidi B **242** (14), R119 (2005).

[Ofe62] G. S. Ofelt, *Intensities of Crystal Spectra of Rare-Earth Ions*, Journal of Chemical Physics **37** (3), 511 (1962).

[Pal85] E. D. Palik, *Handbook of Optical Constants of Solids* (Academic Press, New York, 1985).

[Pea75] R. D. Peacock, *The Intensities of Lanthanide f↔f Transitions,* Bd. 22 (Springer-Verlag, Berlin, Heidelberg, New York, 1975).

[Pet01] V. Peters, *Growth and Spectroscopy of Ytterbium-Doped Sesquioxides*, Dissertation, Institut für Laser-Physik, Universität Hamburg (2001).

[Pet02a] K. Petermann, L. Fornasiero, E. Mix and V. Peters, *High melting sesquioxides: crystal growth, spectroscopy, and laser experiments*, Opt. Mater. **19**, 67 (2002).

[Pet02b] V. Peters, A. Bolz, K. Petermann and G. Huber, *Growth of highly-melting sesquioxides by the heat-exchanger method*, J. Cryst. Growth **237** (9), 879 (2002).

[Pet05] L. Petit, A. Svane, Z. Szotek and W. Temmerman, Phys. Rev. B **72** (2005).

[Pet07] R. Peters, C. Kränkel, K. Petermann and G. Huber, *Broadly tunable high-power Yb:Lu_2O_3 thin disk laser with 80% slope efficieny*, Optics Express **15** (11), 7075 (2007).

[Pie00] L. Pieterson, M. Heeroma, E. de Heer and A. Meijerink, *Charge transfer luminescence of Yb^{3+}*, Journal of Luminescence **91**, 177 (2000).

[Pie01] L. Pieterson, *Charge transfer and $4f^n \leftrightarrow 4f^{n-1}5d$ luminescence of lanthanide ions*, Proefschrift, Faculteit Scheikunde, Universiteit Utrecht (2001).

[Pon02] O. Pons-Y-Moll, J. Perriere, E. Million, R. M. Defourneau, D. Defourneau, B. Vincent, A. Essahlaoui and A. Boudrioua, *Structural and optical properties of rare-earth-doped Y_2O_3 waveguides grown by pulsed-laser deposition*, Journal of Applied Physics **92** (9), 4885 (2002).

[Puk88] P. R. Pukite, P. I. Cohen and S. Batra, in: P. K. Larsen and P. J. Dobson (editors), *Reflection High-Energy Electron Diffraction and Reflection Electron Imaging* (Plenum, New York and London, 1988).

[Rab04] L. Rabisch, *Ultradünne, Eu-dotierte, thermisch aufgedampfte Sesquioxid-Schichten auf α-Al_2O_3*, Dissertation, Fachbereich Physik, Universität Hamburg (2004).

[Rao96] R. P. Rao, *Growth and characterization of Y_2O_3:Eu^{3+} phosphor films by sol-gel process*, Solid State Communications **99** (6), 439 (1996).

[Ray63] D. K. Ray, *Investigations into the Origin of the Crystalline Electric Field Effects on Rare Earth Ions - II. Contributions from the Rare Earth Orbitals*, Proceedings of the Physical Society **82**, 47 (1963).

[Rea63] J. F. Ready, *Development of plume of material vaporized by giant-pulse laser*, Applied Physics Letters **3** (4), 11 (1963).

[Rij04] G. Rijnders and D. H. A. Blank, *Enhanced surface diffusion through termination conversion growth during epitaxial $SrRnO_3$ growth*, Applied Physics Letters **84**, 505 (2004).

[Rös90] A. Röseler, *Infrared spectroscopic ellipsometry* (Akademischer Verlag Berlin, 1990).

[Rot60] R. S. Roth and S. J. Schneider, *Phase Equilibria in Systems Involving the Rare-Earth Oxides. Part I. Polymorphism of the Oxides of the Trivalent Rare-Earth Ions*, Journal of Research of the National Bureau of Standards-A **64** (4), 309 (1960).

[Sae89] K. L. Saenger, *Time-resolved optical emission during laser ablation of Cu, CuO, and high-T_c superconductors: $Bi_{1.7}Sr_{1.3}Ca_2Cu_3O_x$ and $Y_1Ba_{1.7}Cu_{2.7}O_y$*, Journal of Apllied Physics **66** (9), 4435 (1989).

[Sae93a] K. Saenger, *Pulsed laser depostion (Part I) - A review of process characteristics and capabilities*, Processing of Advanced Materials **3**, 1 (1993).

[Sae93b] K. Saenger, *Pulsed laser depostion (Part II) - A review of process mechanisms*, Processing of Advanced Materials **3**, 63 (1993).

[Sah21] M. N. Saha, *Versuch einer Theorie der physikalischen Erscheinungen bei hohen Temperaturen mit Anwendungen auf die Astrophysik*, Zeitschrift für Physik **6**, 40 (1921).

[Sam82] G. V. Samsonov, *The Oxide Handbook* (IFI / Plenum Press, New York, 1982).

[San85] H. Sankur and R. Hall, *Thin-film deposition by laser-assisted evaporation*, Applied Optics **24** (20), 3343 (1985).

[Sas00] A. Sasahara, H. Uetsuka and H. Onishi, *Reflection High-Energy Electron Diffraction and Reflection Electron Imaging*, Jpn. J. Appl. Phys. **39** (20), 3773 (2000).

[Sch18] P. Scherrer, *Bestimmung der Größe und der inneren Struktur von Kolloidteilchen mittels Röntgenstrahlen*, Nachrichten von der Gesellschaft der Wissenschaften zu Göttingen 98–100 (1918).

[Sch67] H. L. Schläfer and G. Gliemann, *Einführung in die Ligandenfeldtheorie* (Akademische Verlagsgesellschaft, Frankfurt am Main, Germany, 1967).

[Sch70] G. Schnaack and J. Konigstein, *Phonon and Electron Raman Spectra of Cubic Rare-Earth Oxides and Isomorphous Yttrium Oxide*, J. Opt. Soc. Am. **60**, 1110 (1970).

[Sch73] P. Schuster, *Ligandenfeldtheorie, Band 19, Chemische Taschenbücher* (Verl. Chemie, Weinheim / Bergstr., 1973).

[Seo02] S. Y. Seo, S. Lee, H. D. Park, N. Shin and K. Sohn, *Luminescence of pulsed laser deposited Gd_2O_3:Eu^{3+} thin film phosphors on quartz glass substrates*, Journal of Applied Physics **92** (9), 5248 (2002).

[Ser99] R. Serna, M. Jiménez de Castro, J. A. Chaos and C. N. Afonso, *The role of Er^{3+}-Er^{3+} separation on the luminescence of Er-doped Al_2O_3 films by pulsed laser deposition*, Applied Physics Letters **75** (26), 4073 (1999).

[Sha76] R. D. Shannon, *Revised Effective Ionic Radii and Systematic Studies of Interatomic Distances in Halides and Chalcogenides*, Acta Crystallographica **A32**, 751 (1976).

[Sha93] R. N. Sharma and A. C. Rastogi, *Compositional and electronic properties of chemical-vapor-deposited Y_2O_3 thin film-Si(1O0) interfaces*, Journal of Applied Physics **74** (14), 6691 (1993).

[She03] Y. Shen, C. Li, V. Costa and K. Bray, *Laser site-selective excitation spectroscopy of Eu^{3+}-doped yttrium aluminum garnet*, Physical Review B **68**, 1 (2003).

[Shi92] T. Shitara, D. D. Vvedensky, M. R. Wilby, J. Zhang, J. H. Neave and B. A. Joyce, *Step-density variations and reflection high-energy electron-diffraction intensity oscillations during epitaxial grown on vinical GaAs(001)*, Physical Review B **46** (11), 6815 (1992).

[Sin66] S. P. Sinha, *Complexes of the rare earths* (Pergamon Press, London, 1966).

[Sin90] R. K. Singh and J. Narayan, *Pulsed-laser evaporation technique for deposition of thin films: Physics and theoretical model*, Physical Review B **41** (13), 8843 (1990).

[Sin92] R. K. Singh, D. Bhattacharya, P. Tiwari, J. Narayan and C. B. Lee, *Improvement in the properties of high T_c films fabricated in situ by laser ablation of $YBa_2Cu_3O_7$-Ag targets*, Applied Physics Letters **60** (2), 2022 (1992).

[Smi65] H. M. Smith and A. F. Turner, *Vacuum Deposited Thin Films Using a Ruby Laser*, Applied Optics **4** (1), 147 (1965).

[Sob79] I. I. Sobelman, *Atomic Spectra and Radiative Transitions* (Springer-Verlag, Berlin, 1979).

[Ste66] R. M. Sternheimer, *Shielding and Antishielding Effects for Various Ions and Atomic Systems*, Physical Review **146** (1), 140 (1966).

[Sto88] S. Stoyanov and N. Michailiv, *Non-Steady State Effects in MBE: Oszillations of the Step Density at the Crystal Surface*, Surface Science **202**, 109 (1988).

[Stu96] B. C. Stuart, M. D. Feit, S. Herman, A. M. Rubenchik, B. W. Shore and M. D. Perry, *Nanosecond-to-femtosecond laser-induced breakdown in dielectrics*, Physical Review B **53** (4), 1749 (1996).

[Tan98] Z. K. Tang, G. K. L. Wong, P. Yu, M. Kawasaki, A. Ohtomo, H. Koinuma and Y. Segawa, *Room-temperature ultraviolet laser emission from self-assembled ZnO microcrystallite thin films*, Applied Physics Letters **72** (25), 3270 (1998).

[Tar96] E. J. Tarsa, E. A. Hachfeld, F. Quinlan, J. S. Speck and M. Eddy, *Growth related stress and surface morphology in homoepitaxial $SrTiO_3$ films*, Applied Physics Letters **68**, 490 (1996).

[Tho28] G. P. Thomson, Proc. Roy. Soc. A **117**, 600 (1928).

[Thu99] A. Thum-Jäger and K. Rohr, *Angular emission distributions of neutrals and ions in laser ablated particle beams*, Journal of Physics D: Applied Physics **32**, 2827 (1999).

[Tom86] T. Tomiki, J. Tamashiro, Y. Tanahara, A. Yamada, H. Fukutani, T. Miyahara, H. Kato, S. Shin and M. Ishigame, *Optical Spectra of Y_2O_3 Single Crystals in VUV*, Journal of the Physical Society of Japan **55** (12), 4543 (1986).

[Tyu98] M. Tyunina, J. Levoska and S. Leppavouri, *Experimantal studies and modeling of Pb-Zr-Ti-O film growth in pulsed laser deposition*, Journal of Applied Physics **83**, 5489 (1998).

[Ugl77] A. A. Uglov and A. N. Kokora, *Thermophysical and hydrodynamic effects in laser-beam processing of materials*, Soviet Journal of Quantum Electronics **7**, 671 (1977).

[Var94] D. Varding, *Luminiszenzspektroskopische Untersuchung dynamischer Eigenschaften freier Exzitonen in festen Edelgasen Krypton und Xenon*, Dissertation, Fachbereich Physik, Universität Hamburg (1994).

[Veg21] L. Vegard, *Die Konstitution der Mischkristalle und die Raumfüllung der Atome*, Zeitschrift für Physik **5** (27), 17 (1921).

[Ven00] J. A. Venables, *Introduction to surfaced and thin film processes* (Cambridge University Press, Cambridge, 2000).

[Vin00] L. T. Vinh, V. Yam, Y. Zeng and D. Bouchier, *Nucleation and growth of self-assembled Ge/Si(001) quantum dots in single and stacked layers*, Thin Solid Films **380**, 2 (2000).

[Web82] M. J. Weber, *Lasers and Masers*, in: *CRC Handbook of Laser Science and Technology*, volume **1** (CRC Press Inc., Boca Raton, Florida, 1982).

[Win81] G. Winkler, *Magnetic Garnets* (F. Vieweg & Sohn Verlagsgesellschaft mbH, Braunschweig, 1981), 1. edition.

[Win07] M. Winter, *WebElements*, University of Sheffield and WebElements Ltd. (UK) (2007).

[Wyc86] R. W. G. Wyckoff, *Crystal Structures Vol.2, 2^{nd} edition* (Interscience Publishers, New York, 1986).

[Xu91] Y. Xu and W. C. Ching, *Self-consistent band structures, charge distributions, and optical-absorption spectra in MgO, Al2O3 and $MgAl_2O_4$*, Physical Review B **43**, 4461 (1991).

[Xu97] Y. Xu, Z. Gu and W. Y. Ching, *Electronic, structural, and optical properties of crystalline yttria*, Physical Review B **56** (23), 14993 (1997).

[Xu99] Y.-N. Xu and W. Y. Ching, *Electronic structure of yttrium aluminum garnet ($Y_3Al_5O_{12}$)*, Phys. Rev. B **59**, 10530 (1999).

[Yan76] P. P. Yaney and L. G. DeShazer, *Spectroscopic studies and analysis of the laser states of Nd^{3+} in YVO_4* **66** (12), 1405 (1976).

[Yos94] M. Yoshimoto, K. Yoshida, H. Maruta, Y. Hishitani, H. Koinuma, S. Nishio, M. Kakihana and T. Tachibana, *Pulsed Laser Deposition of Thin Films*, Nature **399**, 340 (1994).

[Yos95] M. Yoshimoto, T. Maeda, T. Ohnishi, H. Koinuma, O. Ishiyama and M. Shinohara, *Atomic-scale formation of ultrasmooth surfaces on sapphire substrates for high-quality thin-film fabrication*, Applied Physics Letters **67**, 2615 (1995).

[Zel98] D. E. Zelmon, D. L. Small and R. Page, *Refractive-index measurements of undoped yttrium aluminum garnet from 0.4 to 5.0 μm*, Applied Optics **37**, 4933 (1998).

[Zha98] S. Zhang and R. Xiao, *Yttrium oxide films prepared by pulsed laser deposition*, Journal of Applied Physics **83** (7), 3842 (1998).

[Zhe89] J. P. Zheng, Z. Q. Huang, D. T. Shaw and H. S. Kwok, *Generation of high-energy atomic beams in laser-superconducting target interactions*, Applied Physics Letters **54** (3), 280 (1989).

[Zho03] Y. Zhou, J. Lin, M. Yu, S. Han, S. Wang and H. Zhang, *Morphology control and luminescence properties of YAG:Eu phosphors prepared by spray pyrolysis*, Materials Research Bulletin **38**, 1289 (2003).

[Zor04] Y. Zorenko, A. Voloshinovskii, I. Konstankevych, V. Kolobanov, V. Mikhailin and D. Spassky, *Luminescence of excitons and antisite defects in the phosphors based on garnet compounds*, Radiation Measurements **38** (4-6), 677 (2004).

[Zor05] Y. Zorenko, V. Gorbenko, A. Voloshinovskii, G. Stryganyuk, V. Mikhailin, V. Kolobanov, D. Spassky, M. Nikl and K. Blazek, *Exciton-related luminescence in LuAG:Ce single crystals and single crystalline films*, Physica Status Solidi A **202** (6), 1113 (2005).

[Zor06] Y. Zorenko, A. Voloshinovskii, M. Nikl, K. Nejezchleb, V. Mikhailin, V. Kolobanov and D. Spassky, *Exciton and anti-site defect related luminescence in $Lu_3Al_5O_{12}$ and $Y_3Al_5O_{12}$ garnets*, Europhysical Conference on Defects in Insulating Materials, Milan **10**, 25 (2006).

[Zyc02] E. Zych, *Concentration dependence of energy transfer between Eu^{3+} ions occupying two symmetry sites in Lu_2O_3*, Journal of Physics: Condensed Matter **14**, 5637 (2002).

List of Publications

Publications in Journals

1. R. Treichel, C. Czeranowsky, B. İleri, K. Petermann and G. Huber, *Mixed garnet laser-crystals for water vapor DIAL transmitter*, in: Proceedings of the 5th International Conference on Space Optics (Toulouse, France, March 30 - April 2, 2004).

2. S. G. P. Strohmaier, H.J. Eichler, C. Czeranowsky, B. İleri, K. Petermann, G. Huber, *Diode pumped Nd:GSAG and Nd:YGG laser at 942 and 935 nm*, Opt. Comm. **275**, 170 (2007).

3. F. Kallmeyer, M. Dziedzina, X. Wang, H.J. Eichler, C. Czeranowsky, B. İleri, K. Petermann, and G. Huber, *Nd:GSAG-pulsed laser operation at 943 nm and crystal growth*, Applied Physics B **89**, 305 (2007).

4. B. İleri and G. Huber, *Epitaxy and characterization of lattice matched Eu^{3+}-doped sesquioxide films on Y_2O_3 substrates*, HasyLab Annual Report (2007), *submitted*.

5. B. İleri and K. Petermann and G. Huber, *Epitaxy and Characterization of Lattice Matched, Monocrystalline, Dielectric Oxide Films Fabricated by Pulsed Laser Deposition*, Nature Photonics (2008), *in preparation*.

International Conference Contributions

1. B. İleri, C. Czeranowsky, K. Petermann, and G. Huber, *Mixed garnet laser crystals for water vapor detection*, Conference on Lasers and Electro-Optics / Europe (CLEO/Europe - IQEC) (Munich, Germany, June 12 - 17, 2005), oral presentation.

2. B. İleri, S. Bär, and G. Huber, *Annealing and lattice matching of crystalline rare-earth doped garnet PLD-films*, Conference on Lasers and Electro-Optics / Europe (CLEO/Europe - IQEC) (Munich, Germany, 2007), oral presentation.

3. B. İLERI, S. BÄR, AND G. HUBER, *Lattice matching of crystalline, rare-earth doped PLD-films demonstrated using Ortho-Vanadates*, European Materials Research Society Spring Meeting (Strasbourg, France, May 28 - June 1, 2007), oral presentation.

4. B. İLERI, T. GÜN, K. PETERMANN, AND G. HUBER, *Epitaxy and Characterization of Lattice Matched, Crystalline, Dielectric Oxide Films Fabricated by Pulsed Laser Deposition*, Conference on Lasers and Electro-Optics (CLEO - QELS) (San Jose, USA, May 4 - 9, 2008), *submitted*.

5. A. KAHN, T. GÜN, B. İLERI, H. KÜHN, K. PETERMANN, G. HUBER, J. D. B. BRADLEY, F. AY, K. WÖRHOFF, M. POLLNAU, Y. LUO AND P. HOFFMANN, *Monocrystalline Rare Earth doped (Gd, Lu)$_2O_3$ Waveguiding Films Produced by Pulsed Laser Deposition and Structured by Reactive Ion Etching*, Conference on Lasers and Electro-Optics (CLEO - QELS) (San Jose, USA, May 4 - 9, 2008), *submitted*.

National Conference Contributions

1. B. İLERI, C. CZERANOWSKY, K. PETERMANN, AND G. HUBER, *Verschiebung der Emissionswellenlänge in Nd-dotierten Granat-Kristallen von 946 bis 935 nm*, 14. Norddeutscher Lasertag, (Braunschweig, Germany, December 13, 2003), poster presentation.

2. B. İLERI, C. CZERANOWSKY, K. PETERMANN, AND G. HUBER, *Verschiebung der Emissionswellenlänge in Nd-dotierten Granat-Kristallen von 946 bis 935 nm*, Verhandlungen der DPG, Frühjahrstagung FG Quantenoptik und Photonik (Munich, Germany, March 21 - 26, 2004), poster presentation.

3. S. G. P. STROHMAIER, H. J. EICHLER, B. İLERI UND C. CZERANOWSKY, *Quasi-3-Niveau Laseremission aus kristallinen und keramischen Medien um 940 nm*, Verhandlungen der DPG, Frühjahrstagung FG Quantenoptik und Photonik (Munich, Germany, March 4 - 9, 2005), oral presentation.

4. B. İLERI, S. BÄR, AND G. HUBER, *Gitteranpassung von kristallinen, SE-dotierte PLD-Schichten am Beispiel YVO_4*, Verhandlungen der DPG, Frühjahrstagung FG Thin Films (Regensburg, Germany, March 26 - 30, 2007), oral presentation.

Meetings, Seminars

1. B. İLERI, *Schichtherstellung mit Pulsed Laser Deposition und neue Anwendungen*, Workshop of the Graduiertenkolleg "Spektroskopie an lokalisierten atomaren Systemen" (Stade, Germany, 2004), oral presentation.

2. B. İLERI, *Verschiebung der Emissionswellenlänge in Nd-dotierten Granat-Kristallen von 946 nm bis 935 nm*, Seminar über Festkörperlaser (Hamburg, Germany, 2004), oral presentation.

3. K. PETERMANN, B. İLERI, C. CZERANOWSKY, AND G. HUBER, *Growth of Nd-doped GSAG Laserboules: 2nd Phase of the ESA / Astrium Mixed Garnet Laser Studies*, ESA Project Meeting, Institute of Laser-Physics (Hamburg, Germany, 2005), oral presentation.

4. B. İLERI, *Gitteranpassung von kristallinen, Selten-Erd-dotierten PLD-Schichten*, Seminar of the Graduiertenkolleg "Spektroskopie an lokalisierten atomaren Systemen" (Hamburg, Germany, 2006), oral presentation.

Acknowledgement

The presented work of the years 2004 to 2007 at the Institute of Laser-Physics – University of Hamburg would not have been possible without the support of many people who dedicated their precious time, knowledge, assistance and guidance.

Therefore first, I would like to express my gratitude to my supervisor Prof. Dr. Günter Huber for the opportunity to carry out my PhD studies in his "Solid-State Lasers"-group, the interesting work in a promising field of research, and his enduring support throughout the time of accomplishing this thesis.

Dr. Klaus Petermann has been a constant source of inspiration through never ending discussions, numerous advice and explanations whether related to physics or other interesting areas of life. Great credit should also be given to his innumerable contacts that have been an invaluable help during this period and for the daily work.

I have to thank Dr. Sebastian Bär for the introduction to the field of 'thin films', the help and support throughout the years. Your ideas and advice were very helpful as were your encouragement when all went wrong again.

The entire group 'F' has an extraordinary and outstanding working atmosphere that makes work a pleasure. Thanks a lot to my former and current room mates of 'room 114' Dr. Michael Mond, Dr. Juan José Romero, Jens Johannsen, Nicolaie Pavel, Teoman Gün, Andreas Kahn, Malte Posewang, and Nicky Thilmann - "hey, what about tea time?" Special thanks to Dr. Yury Kuzminykh for the expertise and introduction to the HEM growth as well as for last minute updating of the X-ray data converter program to rescue my measurements. You rule! Also I have to thank Dr. Lutz Rabisch for the hints in performing ellipsometric measurements as well as Friedjof Tellkamp for his astonishing abilities in building and/or repairing anything (especially the PLD 'monster')- there are some who call him MacGyver. Greetings to Teoman Gün for the nice weekends at the institute, his RHEED expertise, and the AFM advice concerning the NCM. Thanks a lot for the interesting discussions about RHEED patterns, intensity oscillation, and deformed rocking curves as well. - Teşekkürler! Kendine iyi bak, arkadaş. For the technical and logistical support I want to express my gratitude to Robert Fischer, Stefan Garbers, Silke Frömmig and Victoria Romano.

Thanks goes out to the patient proofreaders of this thesis Dr. Klaus Petermann, Dr. Sebastian Bär, Christian Kränkel, Teoman Gün, and Alex Bepple. Special thanks goes out to the Anglistics expert Mr. André Pawlitzki for covering the void regarding proper English style. Very special thanks and gratitude to my wife Silvia for not only proofreading but also correcting the LaTeX documents. Found a mistake? - Keep it!

I also would like to thank

- ... Dr. Andriy Zolotaryov for the interesting weekend measurements at the SXRD, that turned out to be a non-functioning XRD. As well thank you very much for the scientific discussions and advice.
- ... Dr. Gregory Stryganyuk and Prof. Dr. Georg Zimmerer at SuperLumi for the opportunity to use the station and Dr. Gregory Stryganyuk for interesting discussions on luminescence spectra and for mutual help.
- ... Prof. Dr. Rainer Anton for the possibilities of EDX measurements.
- ... Dr. Sebastian Bär for the lifetime measurements at the University of Tübingen.
- ... Michael Pfeifers, Christian Krug and Prof. Dr. Christoph Platte at the Fachhochschule Wedel for XRD measurements.
- ... Rainer Behn for additional XRD-measurements at the TU Hamburg-Harburg.
- ... Dieter Barlösius for the preparation of the EBV-films (at least we tried...).
- ... Nicky Thielmann and Malte Posewang for all the favors, especially for the last-minute luminescence measurements.
- ... Nils-Owe Hansen for the AFM introduction, Jörn Siebenmorgen for the refreshing Linux and LaTeX chats, Teoman Gün for advanced AFM techniques, Susanne Teruko Fredrich-Thornton for the Nuno-CDs (Arigato!), and André Richter for the years of mutual study and work since October 1999.
- ... Alex Bepple for the wonderful cooking sessions, Sven Blissenbach, and Nick Nowak for endless friendship and support.
- ... Marcus Deml for inspiring music, Dr. mult. Thomas Schirrmacher for inspiring theological writing during the time of working at this thesis.
- ... All the great bands for providing the soundtrack to this thesis.

Last but not least, I would like to thank my parents Dres. Esin and Muhlis İleri for all that I am. Very special thanks to my precious wife Silvia for her love, friendship, support, encouragement, advice, and understanding in the last years and especially for the last month of 2007!

This work was funded by the Deutsche Forschungsgemeinschaft through the Graduiertenkolleg "Physik mit neuartigen kohärenten Strahlungsquellen" no. 1355 and "Spektroskopie an lokalisierten atomaren Systemen" no. 463.

Index

alumina (α-form), 10
antisite defect, 145
atomic force microscopy (AFM), 83
avalanche ionization, 34

Born-Oppenheimer approximation, 25
Bragg-diffraction-law, 76

central field approximation, 19
charge transfer, 24
configurational coordinate model, 25
corundum, 10

Eggert–Saha-equation, 39
Einstein diffusion law, 64
electron-phonon-coupling, 25
ellipsometry, 80
Europium, 28
    energy level scheme, 30
    fluorescence, 29
ex-site techniques
    optical spectroscopy, 84
ex-situ techniques, 75
    atomic force microscopy, 83
    ellipsometry, 80
excitation, VUV
    experimental setup (SuperLumi), 87

fluorescence
    experimental setup (Fluorolog), 85
fluorides
    lithium yttrium fluoride $LiYF_4$, 13
fracto-emission, 38
Franck-Condon principle, 27
Frank-van-der-Merwe growth, 48
free-carrier-absorption, 34

gadoliniumoxide Gd_2O_3, 9
gadoliniumvanadate $GdVO_4$, 12
garnets
    YAG $Y_3Al_5O_{12}$, 11
growth modes
    island (Volmer-Weber), 48
    layer-by-layer (Frank-van-der-Merwe), 48
    layer-plus-island (Stranski-Krastanov), 48
    step-flow, 48

heteroepitaxy, 46
homoepitaxy, 46

in-situ techniques, 75
    reflectometry, 61, 81
    RHEED, 67
inverse bremsstrahlung, 40
island growth, 48

Kramers degeneration, 21

lanthanide contraction, 7
laser fluence, 34
    threshold, 36
laser-induced breakdown, 33
lattice mismatch, 49
layer-by-layer growth, 48
layer-plus-island-growth, 48
ligand-field theory, 23
lithium yttrium fluoride $LiYF_4$, 13
Lorentz correction, 86
lutetiumoxide Lu_2O_3, 8

Miller indices, 76
multi-phonon relaxation, 27
multi-photon absorption, 34

nephelauxetic effect, 9, 18

optical spectroscopy, 84

fluorescence and excitation, 85
lifetime, 86
VUV excitation, 87

plasma
angular distribution, 43
expansion, 40
in background gas, 41
point defects, 156
pseudomorph growth, 49
pulsed laser deposition (PLD), 31

quasi-homoepitaxy, 46

reflectometry, 61, 80
RHEED, 67
Russell-Saunders-coupling, 20

sapphire, 10
scandiumoxide Sc_2O_3, 8
Schwoebel barrier, 137
selection rules
Laporte selection rules, 22
sesquioxides
gadoliniumoxide Gd_2O_3, 9
lutetiumoxide Lu_2O_3, 8
scnadiumoxide Sc_2O_3, 8
yttriumoxide Y_2O_3, 8
splashing-effect, 38
step density model, 73
step-bunching, 66, 137
step-flow growth, 48
Stokes shift, 27
Stranski-Krastanov growth, 48
stress
compressive, 49
tensile, 49
structure factor, 77
structure zone model, 47
superheating, 36
symmetry
centrosymmetric C_{3i}, 7, 11
non-centrosymmetric C_2, 7

target morphology, 37
target outgassing, 38
thermal diffusion length, 35
thermal diffusivity, 35
Thomson scattering, 75
transitions
charge transfer, 24
non-radiative, 27

vanadates
gadolinium-vanadate $GdVO_4$, 12
yttrium-vanadate YVO_4, 12
Vegard law, 54
Volmer-Weber growth, 48

X-ray diffraction (XRD), 75
rocking-curve measurement, 76

Young's equation, 48
yttrium aluminum garnet $Y_3Al_5O_{12}$, 11
yttriumoxide Y_2O_3, 8
yttriumvanadate YVO_4, 12